Development of Novel Synthetic Methodologies, Characterization and Studies on Magnetic and Surface Properties of Some Binary and Ternary Transition Metal Nitrides

THESIS

Submitted in partial fulfillment
of the requirements for the degree of
DOCTOR OF PHILOSOPHY

by

PRAGNYA PARAMITA MISHRA

Under the Supervision of

Prof. Rabi Narayan Panda

BITS Pilani
Pilani | Dubai | Goa | Hyderabad

BIRLA INSTITUTE OF TECHNOLOGY AND SCIENCE, PILANI
2018

To my Mother…

BIRLA INSTITUTE OF TECHNOLOGY AND SCIENCE, PILANI

CERTIFICATE

This is to certify that the thesis entitled **"Development of Novel Synthetic Methodologies, Characterization and Studies on Magnetic and Surface Properties of some Binary and Ternary Transition Metal Nitrides"** and submitted by **Pragnya Paramita Mishra** ID No **2013PHXF0005G** for award of PhD degree of the institute embodies original work done by her under my supervision.

Signature in full of the Supervisor: Rabi narayan Panda

Name in capital letters: **Prof. RABI NARAYAN PANDA**

Designation: Associate Professor

Department of Chemistry

Date: 12/07/2018

ACKNOWLEDGEMENTS

I take this opportunity to express my earnest gratitude towards my supervisor, Prof. Rabi Narayan Panda for his constant encouragement, valuable suggestion and guidance throughout the PhD work. I got to learn a lot from him, not only the bare scientific facts but also the beauty and interpretation of science. I am thankful to have him as my mentor and truly appreciate everything that he has taught me and will treasure them as I go through my life.

My special thanks to Prof. Souvik Bhattacharyya, Vice-Chancellor, BITS Pilani, Prof. Raghurama G, Director, BITS Pilani, K K Birla Goa Campus, Prof. Sunil Bhand, Dean, Sponsored research and consultancy division (SRCD), Prof. Prashanta Kumar Das, Associate Dean, Academic research division (ARD), Prof. A. P. Koley, Associate Dean, Instruction division, Prof. Neena Goveas, Associate Dean, Academic Registration and Counselling BITS Pilani, K K Birla Goa Campus for providing necessary facilities.

I express my gratitude to the members of doctoral advisory committee, Dr K. P. Jayadevan and Dr. Ram Shankar Patel for their useful suggestions and periodical reviews of my PhD work. I am thankful to Prof. Mainak Banerjee, Convenor, doctoral research committee and members of DRC Prof. Anjan Chattopadhyay, Prof. Raghunath Behera, Prof. Halan Prakash, Prof. P. Bhavna and Prof. N. N Ghosh for their help in academic matters during PhD. I also express my sincere thanks to Prof. Raghunath Behera, former Head and Prof. Anjan Chattopadhyay, Head, Department of Chemistry for their support and cooperation.

The financial support provided by department of science and technology (DST) India as fellowship for Project Assistant-II during March, 2013 to Nov, 2014 is greatly acknowledged.

I acknowledge Dr. M. Manivel Raja, senior scientist, Defence metallurgical research laboratory (DMRL) Hyderabad for doing magnetic measurements. I also acknowledge SAIF IIT Bombay, SAIF IIT Madras, Anna University, Chennai and Karunya University, Coimbatore for carrying out magnetic, microscopic and analytical measurements.

I thank Mr Pratap Kumar Behera, Ms Veena Naik, office staff ARD and SRCD for their assistance in official matters. I also thank Ms. Princy Johnson, Mr Digambar Waingankar, technical staff, Chemistry department for their help during laboratory work. I am very thankful to

my senior colleague Dr. Shankar Balu Dalavi for his assistance in routine laboratory work during my PhD. I am grateful to all my friends and lab mates in chemistry department for their help and support at the time of need. I wish to thank Dr Arunashree Panda for her valuable suggestions, affectionate behaviour and caring attitude during the stay.

No words can express my gratefulness towards my parents Mr. Ganga Narayan Mishra and late Ms. Sunita Mishra. I also express my gratitude towards my grandmother Ms. Hemalata Mishra and Uncle Mr. Ganesh Kumar Rath for their encouragement and motivation for doing my PhD.

I am thankful to my parent-in-laws for their support and patience during the PhD work. Words fail to express my profound gratitude towards my husband Mr. Biswa Ranjan Tripathy, who has been a pillar of strength beside me, a source of inspiration, motivation and encouragement as well. His commitment and persistence have helped me to realize my aspirations, without which I would not have been able to get this far.

Finally, thanks to almighty God for his grace and blessings.

Pragnya Paramita Mishra

Abstract

Development of Novel Synthetic Methodologies, Characterization and Studies on Magnetic and Surface Properties of some Binary and Ternary Transition Metal Nitrides

Transition metal nitrides are technologically important because of their unique physical and chemical properties. Research on metal nitrides is scanty, due to their synthetic difficulty. Also, the stability of the metal nitrides is a matter of concern, as most nitrides are sensitive to oxygen and form oxides in air atmosphere. Therefore, studies on metal nitrides are not explored much. The present study investigates novel synthesis, characterization techniques, surface and magnetic properties study of nitrides such as: ε- $Co_xFe_{3-x}N$ ($0 \leq x \leq 0.4$), γ′-$Ni_xFe_{4-x}N$ (x = 0.2, 0.4, 0.6, 0.8), VN, γ-Mo_2N, γ-$Co_xMo_{2-x}N$(x= 0.25), β-W_2N and $CoWN_2$ materials. Various novel synthetic routes have been developed and adopted to obtain the above mentioned nitrides as pure phase nano-structures. The observed properties have been correlated to the size, shape and structure of the materials. Size and surface effects become predominant at nano scale leading to variation in intrinsic properties, which is evident in our research findings.

ε-Fe_3N and γ′- Fe_4N materials have been synthesized via citric acid assisted sol-gel method. The effect of Co substitution on structural and magnetic properties of ε-phase iron nitride has been studied in detail. ε- $Co_xFe_{3-x}N$ ($0 \leq x \leq 0.4$) materials crystallize in hexagonal crystal structure with values of lattice parameters in the range of a = 4.772 -4.783 Å and c = 4.413 - 4.423 Å. The crystallite sizes of the products are estimated to be in the range of 44 - 55 nm. For ε-$Co_{0.1}Fe_{2.9}N$ nitride, γ′-Fe_4N phase along with ε-Fe_3N phase was observed in the XRD pattern. With gradual increase of Co content (x) to 0.2 at wt%, ε-Fe_3N phase was stabilized. However, with further increase of Co content (x) upto 0.3 and 0.4 at wt%, small amount of α-Fe precipitation in the nitride product as impurity phase was obtained. It is observed that with increasing Co substitution, the lattice parameters as well as the crystallite sizes of ε- $Co_xFe_{3-x}N$ ($0 \leq x \leq 0.4$) system increases in a systematic manner. The average SEM particle sizes are found to be in the range of 110-155 nm with spherical

morphology indicating possible agglomeration of crystallites due to their magnetic nature. The values of saturation magnetization, M_s and coercivity, H_c, of ε-$Co_xFe_{3-x}N$ ($0 \leq x \leq 0.4$) system of nitrides were found to be in the range of 8-39 emu/g and 199-219 Oe, respectively. The values of M_s are found to increase with slight initial decrease with progressive increase in Co content. γ′-$Ni_xFe_{4-x}N$ ($0.2 \leq x \leq 0.8$) materials have been synthesized in nanocrystalline pure phase. The effect of Ni substitution on the structural and magnetic properties of γ′-Fe_4N nitrides has been investigated. The crystallite sizes of nano-crystalline γ′-$Ni_xFe_{4-x}N$ ($0.2 \leq x \leq 0.8$) are found to be in the range of 31– 45 nm. Insertion of Ni atoms into the host lattice expands the lattice due to nano size and strain effect, dominantly. There is an increasing trend in the values of lattice parameter up to x= 0.6 of the materials with progressive increase in the Ni substitution and are found to be in the range of 3.792 Å- 3.795 Å. The average SEM particle sizes are estimated to be in the range of 155 - 250 nm. A maximum value of M_s, i.e. 181emu/g, was obtained for γ′-$Ni_{0.6}Fe_{3.4}N$ material. The observed values of H_c are in the range of 76-109 Oe.

Nanocrystalline vanadium nitride materials have been synthesized using citric based sol-gel method. Various oxide precursors are prepared with alteration of reaction parameters and are subjected to nitridation using two different routes, i.e. urea route and ammonia route. The structural, morphological and surface properties of the products are studied in detail in correlation to the type of precursor and nitridation source, used. The crystallite sizes of the products are in the range of 7 - 28 nm. The estimated lattice parameters are in the range of 4.112 Å – 4.126 Å. Electron microscopy study reveals spherical and elongated rod like morphology for the products obtained via ammonia and urea routes, respectively. The average SEM particle sizes are in the range of 68-111 nm obtained via ammonia route. The dimensions of products are in the range of 540 nm X 72 nm – 1266 nm X 261 nm for urea route, obtained from TEM microscopy study. The estimated BET surface area of the VN products are found to be in the range of 11-57 m^2/g. A maximum surface area of $57m^2/g$ was obtained for VN obtained via urea route from the precursor V_2O_5 obtained at 350^oC. The average pore sizes are in the range of 4-189 nm. The products show mesoporous kind of behaviour with type IV isotherm and H2 hysteresis loop.

γ-Mo_2N and γ-$Co_{0.25}Mo_{1.75}N$ have been synthesized by using various precursor routes and using solid urea and gaseous ammonia as nitridation agents. Hydrazine and potassium borohydride have been used for the synthesis of precursors of γ-Mo_2N and γ-$Co_{0.25}Mo_{1.75}N$, respectively followed by nitridation using ammonia route. Ethylenediamine has been used as organic source for the precursor synthesis of γ-Mo_2N synthesized via urea route. The nitride products are studied for structural, morphological, surface and magnetic properties. The average crystallite sizes of γ-Mo_2N and γ-$Co_{0.25}Mo_{1.75}N$, synthesized via ammonia route and γ-Mo_2N, synthesized via urea route are estimated to be 6 nm, 11±0.5 nm and 5±0.4 nm, respectively. The obtained lattice parameter values are 4.193(5) Å, 4.198(2) Å and 4.162(17) Å for γ-Mo_2N and γ-$Co_{0.25}Mo_{1.75}N$ synthesized via ammonia route and γ-Mo_2N synthesized via urea route, respectively. The surface properties study for γ-Mo_2N and γ-$Co_{0.25}Mo_{1.75}N$ nitride materials synthesized via ammonia route indicate high and moderate surface areas, i.e. 53 and 12 m^2/g, respectively. Room temperature VSM study (M vs. H) indicates weak ferromagnetic behaviour of γ-Mo_2N and γ-$Co_{0.25}Mo_{1.75}N$ (ammonia route) and γ-Mo_2N (urea route) materials having coercivity values of 2838 Oe, 880 Oe and 296 Oe, respectively.

Pure phase β-W_2N and ternary $CoWN_2$ materials have been synthesized using citric acid based sol-gel method followed by nitridation using urea and ammonia route, respectively. The structural, morphological, surface and magnetic properties of the synthesized products have been investigated. The average crystallite size for β-W_2N is 3±0.2 nm and 11-16 nm for $CoWN_2$ materials, prepared at two different temperatures i.e. 700°C and 750°C, respectively. β-W_2N material crystallizes in fcc structure with lattice parameter value 4.155(4) Å. The synthesized $CoWN_2$ materials crystallize in hexagonal structure. The lattice parameter values are estimated to be a = 2.876(7) Å, b = 2.876(6) Å, c = 15.372(48) Å and a = 2.872(3) Å, b = 2.872(2) Å, c = 15.381(21) Å for the products obtained at 700°C and 750°C, respectively. The average SEM particle size for β- W_2N materials is estimated to be 234±17 nm and 97±5 nm and 67±4 nm for $CoWN_2$ materials synthesized at 700°C and 750°C, respectively. The specific surface areas of β- W_2N materials obtained via urea route are estimated to be 6 m^2/g and 13 m^2/g synthesized at 700°C and 750°C, respectively. The values of saturation magnetization, M_s and coercivity, H_c, are estimated to be 0.031emu/g

and 759 Oe, respectively for crystalline β-W_2N synthesized at 750°C. The values of M_s and H_c of $CoWN_2$ synthesized at 750°C are estimated to be 1.71emu/g and 375 Oe, respectively.

In brief, several transition metal nitrides have been synthesized using novel chemical synthetic methodology and their structural, morphological, magnetic and surface properties etc. have been investigated in the present work. The effect of substitution of transition metal on various properties of a binary transition metal nitride has been studied. Ternary transition metal nitride has been synthesized and characterized for various physical properties study. The variation of different properties such as structural, surface and magnetic properties at nanoscale have been investigated in detail. Use of various precursors and nitridation routes such as: solid urea and gaseous ammonia have been explored and the effects on product properties have been studied. High surface materials with nanosize, useful for catalytic application have been synthesized. Nanocrystalline materials with high value of saturation magnetization and moderate coercivities, useful for recording media application have been prepared in the present work.

Contents

Title	Page No
Acknowledgement	...iv
Abstract	…vi
List of figures	…xviii
List of tables	…xxiv
List of symbols and abbreviations	…xxvii
1. Introduction	
1.1 General introduction	…01
1.2 Potential technological applications	…03
1.3 Crystal structure	…04
1.3.1 Crystal structure of iron nitrides	…04
1.3.1.1Crystal structure of γ′-Fe_4N	…05
1.3.1.2 Crystal structure of ε-Fe_3N	…06
1.3.2 Crystal structure of VN	…07
1.3.3 Crystal structure of molybdenum nitrides (β- and γ-Mo_2N)	…08
1.3.4 Crystal structure of β-W_2N	…09
1.3.5 Crystal structure of $CoWN_2$	…10
1.4 Synthesis methods	…11
1.5 Advanced characterization tools	…13
1.5.1 Elemental analysis	…13
1.5.1.1 Atomic absorption spectroscopy (AAS)	…13
1.5.1.2 Energy dispersive X-ray (EDX)	…14
1.5.2 Powder X-ray diffraction (PXRD)	…14
1.5.3 Electron microscopy (SEM/TEM)	…14
1.5.4 Sorption measurements	…15
1.6 Magnetism in solid materials	…17
1.6.1 Magnetism in bulk materials	…18
1.6.1.1 Diamagnetism	…18
1.6.1.2 Paramagnetism	…18

1.6.1.3 Ferromagnetism …20
1.6.2 Magnetism in nano materials …21
1.6.2.1 Nanomagnetic effects …21
1.6.2.1.1 Coercivity (H_c) …24
1.6.2.1.2 Anisotropy energy (K) …25
1.6.2.1.3 Saturation magnetization (M_s) …26
1.6.2.1.4 Curie temperature (T_c) …27
1.7 Literature survey …27
1.8 Gaps in the existing research …30
1.9 Aim of the study …31

2. Material and methods …42

2.1 Synthesis methods …42
2.1.1 Synthesis of precursor …43
2.1.1.1 Sol-gel method …43
2.1.1.2 Co-precipitation method …44
2.1.1.3 Borohydride reduction route …45
2.1.1.4 Other precursor methods: Use of metal and organic/inorganic chelator …45
2.1.2 Nitridation of precursors …46
2.1.2.1 Solid-gas nitridation reactor …47
2.1.2.1.1 Nitridation using gaseous ammonia …47
2.1.2.1.2 Nitridation using solid urea in N_2 (g) atmosphere …48
2.2 Elemental analysis …49
2.2.1 Atomic absorption spectroscopy (AAS) …49
2.2.2 Energy dispersive X-ray (EDX) …50
2.3 Characterization techniques …51
2.3.1 Powder X-ray diffraction …51
2.3.1.1 Basic principle …51
2.3.1.2 Powder X-ray diffractometer …52
2.3.1.3 Determination of structural parameters by using powder XRD …53

2.3.1.3.1 Determination of crystalline phase(s) and Lattice parameters …53
2.3.1.3.2 Crystallite size measurement …54
2.3.2 Electron microscopy …54
2.3.2.1 Scanning electron microscopy (SEM) …55
2.3.2.1.1 Basic principle and instrumentation …55
2.3.2.1.2 Sampling and determination of morphology and particle size ..56
2.3.2.2 Transmission electron microscopy (TEM) …57
2.3.2.2.1 Basic principle and instrumentation …57
2.3.2.2.2 Sampling and determination of morphology and TEM particle size …57
2.3.2.2.3 Interpretation of structural parameters from SAED pattern …58
2.4 Instrumental techniques for studying materials properties …59
2.4.1 BET surface area analyzer …59
2.4.1.1 Instrumentation …59
2.4.1.2 Experimental procedure …60
2.4.1.3 Interpretation of data for surface area and porosity …61
2.4.2 VSM measurement …61
2.4.2.1 Basic principle and instrumentation …61
2.4.2.2 Sampling and measurement of magnetic parameters …62
2.4.3 Electrochemical analysis …63
2.4.3.1 Basic principle and instrumentation …63
2.4.3.2 Sampling and measurement of electrochemical parameters …63

3. Magnetic Properties of ε-$Co_xFe_{3-x}N$ ($0 \leq x \leq 0.4$) and γ′-$Ni_xFe_{4-x}N$ ($0 \leq x \leq 0.8$) Nitride Systems …68

3.1 Introduction …68
3.2 Materials and methods …69
3.2.1 Synthesis of ε-$Co_xFe_{3-x}N$ ($0 \leq x \leq 0.4$) and γ′-$Ni_xFe_{4-x}N$ ($0.2 \leq x \leq 0.8$) materials by direct nitridation of solid precursors …69
3.2.1.1 Synthesis of iron based oxide and mixed metal oxide precursor(s) …69
3.2.1.2 Nitridation of oxide precursor …70

3.2.1.2.1 Nitridation of Co substituted Fe based mixed metal precursors …70
3.2.1.2.2 Nitridation of Ni substituted Fe based mixed metal precursors …71
3.2.2 Instrumental characterization ...71
3.3 Results and discussion …72
3.3.1 X-ray diffraction analysis …72
3.3.1.1 Precursor characterization …72
3.3.1.2 Solid state reactivity study …74
3.3.1.3 XRD study of ε-$Co_xFe_{3-x}N$ ($0 \leq x \leq 0.4$) …75
3.3.1.4 XRD study of γ′-$Ni_xFe_{4-x}N$ ($0.2 \leq x \leq 0.8$) materials …78
3.3.2 Elemental analysis of Fe-Co-N and Fe-Ni-N nitrides …81
3.3.2.1 Atomic absorption spectroscopy of ε- $Co_xFe_{3-x}N$ …81
3.3.2.2 EDX analysis of γ′-$Ni_xFe_{4-x}N$ ($0.2 \leq x \leq 0.8$) materials …82
3.3.3 Electron Microscopy Studies of ε-$Co_xFe_{3-x}N$ ($0 \leq x \leq 0.4$) and γ′-$Ni_xFe_{4-x}N$ ($0.2 \leq x \leq 0.8$) materials …83
3.3.3.1 SEM Studies of ε-$Co_xFe_{3-x}N$ ($0 \leq x \leq 0.4$) and γ′-$Ni_xFe_{4-x}N$ ($0.2 \leq x \leq 0.8$) materials …83
3.3.3.1.1 SEM Studies of ε-$Co_xFe_{3-x}N$ ($0 \leq x \leq 0.4$) …83
3.3.3.1. 2 SEM Studies of γ′-$Ni_xFe_{4-x}N$ ($0 \leq x \leq 0.8$) materials …85
3.3.3.1.3 EDX Studies of ε-Fe_3N and γ′-$Ni_{0.4}Fe_{3.6}N$ nitride materials …87
3.3.3.2 TEM studies of ε-Fe_3N and γ′-$Ni_xFe_{4-x}N$ ($0.2 \leq x \leq 0.8$) materials …88
3.3.4 Magnetic properties study …91
3.3.4.1 Magnetic properties of ε-$Co_xFe_{3-x}N$ ($0 \leq x \leq 0.4$) …91
3.3.4.2 Magnetic properties of γ′-$Ni_xFe_{4-x}N$ ($0.2 \leq x \leq 0.8$) materials …95
3.4 Conclusion …99

4. Structural Characterization and Surface Properties Study of vanadium nitride Synthesized using Novel Chemical Method ...103

4.1 Introduction …103
4.2 Materials and methods …105
4.2.1 Preparation of V_2O_5 precursor by citric acid based sol-gel method …105
4.2.2 Synthesis of VN by urea route …105

4.2.3 Synthesis of VN by nitridation using NH_3(g) …106
4.2.4 Instrumental characterization …106
4.3 Results and discussions …107
4.3.1 X-ray diffraction studies …107
4.3.1.1 Precursor characterization …107
4.3.1.2 Solid state reactivity study …109
4.3.1.2.1 Solid state reactivity study of VN formation via urea route …109
4.3.1.2.2 Solid state reactivity study of VN formation via NH_3(g) route …111
4.3.1.3 X-Ray diffraction study of VN synthesized by urea and ammonia routes …111
4.3.2 Electron microscopy study …114
4.3.2.1 SEM study of VN …114
4.3.2.2 TEM study of VN …115
4.3.2.3 EDX study of VN …121
4.3.3 BET adsorption and desorption studies …122
4.3.3.1 BET surface area study …122
4.3.3.2 Sorption isotherm and porosity …124
4.3.4 Electrochemical properties of VN Nitride …126
4.4 Conclusion …127
5. Novel synthesis, Characterization and Studies on Nanocrystalline γ-Mo_2N and γ-$Co_{0.25}Mo_{1.75}N$ Nitrides …131
5.1 Introduction …131
5.2 Material and methods …132
5.2.1 Synthesis of γ-Mo_2N and γ-$Co_{0.25}Mo_{1.75}N$ nitrides via nitridation using NH_3(g) …133
5.2.1.1 Synthesis of molybdenum oxide via hydrazine route …133
5.2.1.2 Synthesis of Co-Mo based bimetallic oxides via borohydride route …133
5.2.1.3 Synthesis of γ-Mo_2N and γ-$Co_{0.25}Mo_{1.75}N$ via

ammonia route …133
5.2.2 Synthesis of γ-Mo_2N nitrides via nitridation using solid urea …134
5.2.2.1 Synthesis of molybdenum- ethylene diamine complex …134
5.2.2.2 Synthesis of γ-Mo_2N via urea route …134
5.2.3 Instrumental characterization …135
5.3 Results and discussions …135
5.3.1 γ-Mo_2N synthesized via ammonia route …135
5.3.1.1 XRD studies of γ-Mo_2N …135
5.3.1.1.1 Precursor characterization …135
5.3.1.1.2 Solid state reactivity study on formation of γ-Mo_2N …137
5.3.1.1.3 X-ray diffraction studies of γ-Mo_2N …139
5.3.1.2 Electron microscopic studies of γ -Mo_2N synthesized via ammonia route …140
5.3.1.2.1 TEM studies of γ -Mo_2N …140
5.3.1.2.2 HRTEM studies of γ- Mo_2N …141
5.3.1.3 BET surface area study of γ -Mo_2N …142
5.3.1. 4 Magnetic studies of γ -Mo_2N …143
5.3.2 γ-$Co_{0.25}Mo_{1.75}N$ synthesized via ammonia route …145
5.3.2.1 X-ray diffraction studies of γ-$Co_{0.25}Mo_{1.75}N$ …145
5.3.2.1.1 Precursor characterization …145
5.3.2.1.2 XRD study of γ-$Co_{0.25}Mo_{1.75}N$ …147
5.3.2.2 Microstructural characterization of γ-$Co_{0.25}Mo_{1.75}N$ synthesized via ammonia route …148
5.3.2.2.1 TEM studies of γ-$Co_{0.25}Mo_{1.75}N$ …148
5.3.2.2.2 HRTEM studies of γ-$Co_{0.25}Mo_{1.75}N$ …150
5.3.2.3 BET surface area study of γ-$Co_{0.25}Mo_{1.75}N$ …151
5.3.2.4 VSM studies of γ-$Co_{0.25}Mo_{1.75}N$ …152
5.3.3 γ -Mo_2N synthesized via urea route …153
5.3.3.1 X-ray diffraction studies of γ –Mo_2N …154
5.3.3.2 Structural characterization of Mo_2N synthesized via urea route …155
5.3.3.2.1SEM and EDX studies of γ –Mo_2N …155

5.3.3.2.2 HRTEM studies of γ -Mo_2N …156
5.3.3.3 VSM studies of γ-Mo_2N synthesized via urea route …157
5.4 Conclusion …158
6. Novel Synthesis, Characterization and Properties Study of W and Co-W based Binary and Ternary Nitride Materials …162
6.1 Introduction …162
6.2 Materials and methods …163
6.2.1 Synthesis of β-W_2N …163
6.2.1.1 Precursor synthesis …163
6.2.1.2 Nitridation of precursor via urea route …164
6.2.2 Synthesis of $CoWN_2$ …164
6.2.2.1 Synthesis of $CoWO_4$ precursor …164
6.2.2.2 Nitridation of precursor via ammonia route …165
6.2.3 Instrumental characterization …165
6.3 Results and discussions …166
6.3.1 β- W_2N synthesized via urea route using WO_3 precursor …166
6.3.1.1X- ray diffraction analysis of β-W_2N …166
6.3.1.1.1 Precursor characterization …166
6.3.1.1.2 Solid state reactivity and XRD study of β-W_2N …168
6.3.1.2Microstructural characterization of β-W_2N …170
6.3.1.2.1 SEM studies of β-W_2N synthesized at various temperatures …170
6.3.1.2.2 HRTEM studies of β-W_2N synthesized at 750^0C …171
6.3.1.2.3 EDX study of β-W_2N synthesized via urea route …172
6.3.1.3 BET surface area study of β-W_2N synthesized via urea route …173
6.3.1.4 Magnetic studies of β-W_2N …175
6.3.2 $CoWN_2$ synthesized via nitridation of $CoWO_4$ using NH_3(g) …175
6.3.2.1 X- ray diffraction analysis of $CoWN_2$ …176
6.3.2.1.1 Precursor characterization …176
6.3.2.1.2 Solid state reactivity study and XRD study …177
6.3.2.2 Microstructural (SEM and EDX) characterization of $CoWN_2$ …180

6.3.2.2.1 SEM studies of $CoWN_2$ …180
6.3.2.2.2 EDX studies …181
6.3.2.3 Magnetic studies of $CoWN_2$ …182
6.4 Conclusion …183
7. Summary and future scope …186
7.1 Summary …186
7.2 Future prospects …191
Appendix i
Appendix ii
Appendix iii

List of Figures

Sl. No	Figure caption	Page No.
1.1	Crystal structure of γ′-Fe_4N. The site occupancies of Fe and N are indicated.	…06
1.2	Hexagonal structure of ε-Fe_3N indicating arrangements of Fe and N atoms in hcp lattice.	…07
1.3	Crystal structure of VN indicating arrangement of V and N in the cubic lattice.	…08
1.4	Crystal structure of γ-Mo_2N showing positions of Mo and N in the fcc lattice.	…09
1.5	Crystal structure of β-W_2N showing positions of W and N atoms in the fcc lattice.	…10
1.6	Layered crystal structure of $CoWN_2$.	…11
1.7	Different types of adsorption isotherms; (a) I, (b) II, (c) III, (d) IV, (e) V and (f) VI [78].	…16
1.8	Different Types of adsorption Hysteresis; (a) H1, (b) H2, (c) H3 and (d) H4.	…17
1.9	(a) Field dependent magnetization and (b) Temperature dependent inverse susceptibility of a typical diamagnetic material.	…18
1.10	(a) Field dependent magnetization and (b) temperature dependent inverse susceptibility of a paramagnet showing (1) Curie and (2) Curie-weiss behaviour.	…19
1.11	Magnetic characteristics of a typical ferromagnet; (a) field dependent magnetization (M vs H) and (b) temperature dependent inverse susceptibility ($1/\chi$) [80].	…20
1.12	Hysteresis loop of a typical ferromagnet	…21
1.13	Representation of (a) super paramagnetic domains and (b) hysteresis loop showing zero coerciviy of a superparamagnetic assembly of nano particles.	…23
1.14	Variation of coercivity as a function of particle diameter.	…24
1.15	Variation of anisotropy energy, K_{eff}, as a function of grain diameter.	…26
2.1	Schematic block diagram of vertical nitridation reactor. Enlarged view of the sample chamber is shown for clarity reason.	…48
2.2	Schematic block diagram of horizontal nitridation reactor.	…49
2.3	Block diagram illustrating experimental set up of atomic absorption	

spectroscope (AAS) set up. …50
2.4 Representation of constructive interference of two parallel X-ray beams A and B, subjected to condition, when the path difference is a multiple of wavelength, λ. …52
2.5 Block diagram of X-ray powder diffractometer. …53
2.6 Block diagram of scanning electron microscope. …56
2.7 Block diagram of transmission electron microscope. …57
2.8 Block diagram of a BET surface area analyzer [48]. …60
2.9 Schematic diagram representing principle involved in vibrating sample magnetometer [49]. …62
2.10 Block diagram of a typical electrochemical cell. …63
3.1 Indexed XRD patterns of various precursor materials; (a) α-Fe_2O_3, (b) $Co_{0.6}Fe_{2.4}O_4$ spinel and (c) α-$Ni_{0.5}Fe_{1.5}O_3$. …72
3.2 Indexed XRD patterns of products obtained via nitridation of α-Fe_2O_3 precursors at various temperatures; (a) 550˚C, (b) 600˚C and (c) 700˚C. …74
3.3 Indexed XRD patterns of products obtained via nitridation of α- $Ni_{0.2}Fe_{1.8}O_3$ precursor at various temperatures; (a) 550˚C, (b) 600˚C and (c) 700˚C. …75
3.4 Indexed XRD patterns of ε-$Co_xFe_{3-x}N$ ($0.0 \leq x \leq 0.4$) materials synthesized at 700˚C; (a) x = 0, (b) x = 0.1, (c) x = 0.2, (d) x = 0.3 and (e) x = 0.4. Minor impurity phases corresponding to α-Fe and γ′-Fe_4N are marked with * and +, respectively. …76
3.5 Variation of lattice parameters (a, c) with Co at. wt% in ε-$Co_xFe_{3-x}N$ (x=0, 0.2,0.3 and 0.4) materials. Inset figure shows the variation of c/a ratios with various at. wt% of Co. …77
3.6 Indexed XRD patterns of γ′-$Ni_xFe_{4-x}N$ materials synthesized at 700˚C; (a) x = 0.2, (b) x = 0.4, (c) x = 0.6 and (d) x = 0.8. The impurity phase, ε-Fe_3N has been marked as asterisk (*). …79
3.7 Composition dependent lattice parameters of γ′-$Ni_xFe_{4-x}N$ ($0.2 \leq x \leq 0.8$) materials. Inset figure shows change in (111) peak positions with various Ni content in γ′-$Ni_xFe_{4-x}N$ ($0.2 \leq x \leq 0.8$); x= (a) 0.2, (b) 0.4, (c)0.6 and (d)0.8 …80
3.8 SEM micrographs of ε-Fe_3N ((a), (b)) and ε-$Co_xFe_{3-x}N$ ($0.2 \leq x \leq 0.4$)

materials for x=0.2 ((c),(d)), x=0.3 ((e),(f)) and x=0.4 ((g),(h)). …84

3.9 SEM micrographs of γ′-$Ni_xFe_{4-x}N$ ($0.2 \leq x \leq 0.8$) materials; ((a), (b)) x = 0.2, ((c), (d)) x = 0.4, ((e), (f)) x = 0.6 and ((g),(h)) x = 0.8. …86

3.10 EDX spectra of (a) ε-Fe_3N and (b) γ′-$Ni_{0.4}Fe_{3.6}N$ Nitrides. …88

3.11 TEM micrograph of (a) ε -Fe_3N and γ′-$Ni_xFe_{4-x}N$ ($0.2 \leq x \leq 0.8$) materials; (b) x = 0.2, (c) x = 0.4, (d) x = 0.6 and (e) x = 0.8. …89

3.12 Selected area electron diffraction patterns of γ′-$Ni_xFe_{4-x}N$ ($0.2 \leq x \leq 0.8$); (a) x= 0.4 and (b) x = 0.6 materials. …90

3.13 Plot of specific magnetization as a function of field for (a) ε-Fe_3N and ε-$Co_xFe_{3-x}N$ ($0.2 \leq x \leq 0.4$) materials; (b) x=0.2, (c) x=0.3 and (d) x=0.4. …92

3.14 Plot of specific magnetization as a function of H^{-1} for ε-$Co_xFe_{3-x}N$ materials; (a) x=0, (b) x = 0.2, (c) x = 0.3 and (d) x = 0.4. …93

3.15 Plot of saturation magnetization vs. Co at.wt% of ε-$Co_xFe_{3-x}N$ (x=0, 0.2, 0.3, 0.4). Inset figure shows plot of coercivity vs. Co at.wt%. …94

3.16 Plot of specific magnetization as a function of field for γ′-$Ni_xFe_{4-x}N$ ($0.2 \leq x \leq 0.8$) materials for (a) x = 0.2, (b) x = 0.4, (c) x = 0.6, (d) x = 0.8 materials. Inset shows zoom in plots near 0 kOe for clarity reason. …96

3.17 Plot of specific magnetization as a function of H^{-1} for γ′-$Ni_xFe_{4-x}N$ (a) x=0.2, (b) x= 0.4, (c) x =0.6,(d) x= 0.8 materials. …97

3.18 Plot of Ni at. wt% vs. saturation magnetization and coercivity of γ′-$Ni_xFe_{4-x}N$($0.2 \leq x \leq 0.8$) materials. …98

4.1 Indexed XRD patterns of V_2O_5 precursor materials synthesized by citric acid–assisted sol–gel method at various temperatures; (a) 350 °C and (b) 550 °C. ..108

4.2 Indexed XRD patterns of products obtained via nitridation of V_2O_5 precursor synthesized at 550˚C via urea route at (a) 650˚C and V_2O_5 : urea = 1:18 (b) 700˚ C temperature and V_2O_5 : urea = 1:18 (c) 650˚C and V_2O_5 : urea = 1:15 (d) 700˚C and V_2O_5 : urea = 1:15. ..110

4.3 Indexed XRD patterns of VN synthesized at 700˚C from V_2O_5 precursor obtained at (a) 350˚C and (b) 550˚C via urea route. ..112

4.4 Indexed XRD patterns of VN synthesized at 700˚C from V_2O_5 precursor obtained at (a) 350˚C and (b) 550˚C via ammonia route. ..113

4.5 SEM micrographs of VN synthesized via urea route ((a), (c)) and ammonia route ((b) and (d)) obtained by nitridation of V_2O_5 precursors heat treated at 350 °C and 550°C, respectively. ..115

4.6 TEM micrographs of VN nitrides at different magnifications synthesized via urea route from V_2O_5 precursors obtained at 350°C ((a), (b)) and 550°C ((c), (d)). ..116

4.7 TEM micrographs of VN nitrides at different magnifications synthesized via ammonia route from V_2O_5 precursors obtained at 350°C ((a), (b)) and 550°C ((c), (d)). ..117

4.8 TEM particle size distributions of VN nitrides synthesized via ammonia route from V_2O_5 precursors obtained at different temperatures; (a) 350˚C and (b) 550˚C. ..118

4.9 SAED patterns of VN nitrides synthesized via urea ((a), (b)) and ammonia ((c) and (d)) routes. The patterns ((a), (c)) and ((b) and (d)) are recorded from VN nitride synthesized via V_2O_5 precursors heat treated at 350°C (V_2O_5 (350)) and 550 °C (V_2O_5 (550)), respectively. ..120

4.10 EDX spectra of VN synthesized at 700˚C via (a) urea route and (b) ammonia route from V_2O_5 precursor obtained at 350°C. ..122

4.11 Adsorption–desorption isotherms and pore-size distribution plots of VN materials prepared via urea route from V_2O_5 precursors obtained at 350˚C ((a), (b)) and 550˚C ((c), (d)), respectively. ..124

4.12 Adsorption–desorption isotherms and pore-size distribution plots of VN materials prepared via ammonia route from V_2O_5 precursors obtained at 350˚C ((a), (b)) and 550˚C ((c), (d)), respectively. ..125

4.13 Cyclic voltametry plot of VN prepared via ammonia route from precursor V_2O_5 (350). ..127

5.1 Indexed XRD patterns of precursors, heat treated at (a) 300˚C and (b) 500˚C for 2hrs duration. The precursors were prepared via hydrazine route. ..136

5.2 Indexed XRD patterns of nitridation products obtained at various temperatures; (a) 650˚C, (b) 680˚C and (c) 700˚C. * and # indicate minute impurity phases present in the materials. ..138

5.3 Indexed XRD pattern of γ-Mo_2N synthesized via ammonia route at 700°C. * indicates presence of minute amount of δ-MoN phase in the product. ..139
5.4 TEM micrographs at various magnifications (a)-(c) and SAED pattern (d) of γ-Mo_2N. ..140
5.5 TEM particle size distributions for γ-Mo_2N materials. ..141
5.6 HRTEM micrograph of γ-Mo_2N synthesized via ammonia route at 700˚ C ..142
5.7 (a) Adsorption - desorption isotherm and (b) pore size distribution plots of γ-Mo_2N measured at 77K. ..143
5.8 Plot of specific magnetization vs field of γ-Mo_2N measured at room temperature. ..144
5.9 XRD patterns of the α-$Co_{0.12}Mo_{0.88}O_3$ precursors obtained via borohydride route and heated at different temperatures (a) 80^oC (as prepared) and (b) 200^oC. ..146
5.10 Indexed XRD pattern of γ-$Co_{0.25}$ $Mo_{1.75}$ N synthesized at 700˚C. * indicates minute MoO_3 as impurity phase. ..147
5.11 TEM micrographs with various resolutions ((a), (b) and (c)) and SAED pattern (d) of γ-$Co_{0.25}Mo_{1.75}N$ ..148
5.12 TEM particle size distributions for γ-$Co_{0.25}Mo_{1.75}N$ material. ..150
5.13 HRTEM image of γ-$Co_{0.25}Mo_{1.75}N$. ..151
5.14 Plots of adsorption - desorption isotherm (a) and pore size distribution (b) for γ- $Co_{0.25}$ $Mo_{1.75}$ N material. ..152
5.15 Plot of specific magnetization vs. applied field of γ-$Co_{0.25}Mo_{1.75}N$ materials synthesized at 700^oC. ..153
5.16 Indexed XRD pattern of γ –Mo_2N synthesized at 700˚C via urea route. ..154
5.17 SEM micrographs of γ-Mo_2N synthesized via urea route at 700° C with different magnifications(X); (a) 10000X, (b) 20000X, (c) 40000X and (d) 55000X. ..155
5.18 EDX spectrum of γ-Mo_2N synthesized via urea route at 700° C. ..156
5.19 HRTEM image (a) and corresponding SAED pattern (b) of γ -Mo_2N synthesized via urea route at 700°C. ..157
5.20 Field dependent magnetization plot of γ-Mo_2N synthesized via urea route

measured at room temperature. ..158

6.1 XRD patterns of precursor heat treated at various temperatures; (a) 150°C, (b) 300°C, (c) 400°C and (d) 500°C in air atmosphere. The XRD pattern recorded for 500^{o}C heat treated sample has been indexed. ..167

6.2 Indexed XRD patterns of nitridation products obtained from prefired amorphous precursor, WO_3 , at (a) 700^{o}C and (b), (c) 750 ^{o}C ..169

6.3 SEM micrographs of β-W_2N synthesized at various temperatures; (a)700°C, (b)750°C (run 1) and (c) 750°C (run 2). ..171

6.4 (a), (b) and (c) HRTEM micrographs of β-W_2N nitride synthesized at 750^{o}C and (d) SAED pattern of β-W_2N ..172

6.5 EDX spectra of β-W_2N synthesized at various temperatures (a) 700°C and (b), (c) 750°C. ..173

6.6 BET adsorption - desorption isotherms of β-W_2N synthesized at (a) 700°C and (b) 750°C. Inset shows corresponding pore size distribution plots. ..174

6.7 Field dependent magnetization plot of crystalline β-W_2N material synthesized at 750°C(Run 1). ..175

6.8 XRD pattern of precursor material heat treated at various temperatures (a) as dried at 90^{o}C and (b) 400°C in air atmosphere. ..176

6.9 Indexed XRD pattern of β-W_2N synthesized at 700°C via ammonia route from commercial WO_3 precursor. ..178

6.10 Indexed XRD pattern of nitridation products heat treated at various temperatures (a) 650°C (b) 700°C and (c) 750°C. * indicates Co as impurity phase. ..179

6.11 SEM micrographs of $CoWN_2$synthesized at 700°C (a), (b) and 750°C(c),(d) with various magnifications. ..181

6.12 EDX spectra of $CoWN_2$ synthesized at (a) 700°C and (b) 750°C. ..181

6.13 Field dependent magnetization plot of $CoWN_2$ measured at room temperature. ..182

List of Tables

Sl. No	Table caption	Page No
3.1	Materials, stoichiometric amount of reagents, nitridation temperature and heating ramp.	…70
3.2	Materials, stoichiometric amount of reagents, nitridation temperature and heating ramp.	…71
3.3	Materials, Metal atom ratios, Phase, interplanar distance (d), Miller indices (hkl), relative intensities and crystallite sizes of various precursors.	…73
3.4	Materials phase, Miller indices (hkl), observed (d_{obs}) and calculated interplanar distance (d_{cal}) lattice parameters (a, c) and c/a ratios of ε-$Co_xFe_{3-x}N$ ($0 \leq x \leq 0.4$) materials.	…78
3.5	Materials phase, Miller indices (hkl), observed (d_{obs}) and calculated interplanar distance (d_{cal}) and lattice parameters of γ′-$Ni_xFe_{4-x}N$ (x=0.2, 0.4, 0.6, 0.8) nitrides.	…81
3.6	Materials, Elements, Weight % calculated experimentally using AAS and theoretically.	…82
3.7	Materials, Elements, Atoms % calculated experimentally using EDX and theoretically.	…83
3.8	Materials, Co at.wt% (x), Average crystallite sizes and SEM sizes of ε-Fe_3N (x=0) and ε-$Co_xFe_{3-x}N$ ($0.2 \leq x \leq 0.4$) materials.	…85
3.9	Materials, Ni at. wt%, Average crystallite size, SEM particle sizes of γ′-$Ni_xFe_{4-x}N$($0.2 \leq x \leq 0.8$) materials.	…86
3.10	Materials, interplanar distance ‘d’, Miller indices and lattice parameters calculated from XRD and SAED patterns of γ′-$Ni_xFe_{4-x}N$(x = 0.4, 0.6) materials.	…91
3.11	Material, Co at.wt%, saturation magnetization (M_s) and coercivity (H_c) of ε-$Co_xFe_{3-x}N$ ($0.2 \leq x \leq 0.4$) nitrides.	…95
3.12	Material, Ni at.wt%, Saturation magnetization (M_s) and Coercivity (H_c) of γ′-$Ni_xFe_{4-x}N$ ($0.2 \leq x \leq 0.8$) nitrides	…96
4.1	Summary of nitridation process.	…106

4.2 Materials, Miller indices, observed interplanar distance and calculated lattice parameters for V_2O_5 precursors synthesized at 350°C and 550°C. …109

4.3 Materials, precursors, routes, Miller indices, observed and calculated interplanar spacing and lattice parameters of VN nano materials. …114

4.4 Materials, precursors, routes, average crystallite sizes, TEM and SEM particle sizes of VN materials synthesized via different routes. …119

4.5 Materials, Synthesis routes, Precursors, Interplanar Spacings and Miller indices (hkl) of VN Materials. …120

4.6 Materials, precursors, route, pore volume, BET surface area, BET particle size and average pore size of VN materials. …123

5.1 Materials, Miller indices (hkl), observed and calculated interplanar spacings (d_{obs} and d_{cal}) and lattice parameters of α-MoO_3 synthesized via hydrazine route and heat treated at 500^{o}C. …137

5.2 Material, Miller indices, observed and calculated interplanar distance, lattice parameter and average crystallite size of γ-Mo_2N. …140

5.3 Average TEM particle size, interplanar distance, Miller indices and lattice parameters observed from SAED pattern of γ-Mo_2N. …141

5.4 Material, Miller indices (hkl), observed and calculated interplanar spacings ($d_{obs,}$ d_{cal}), lattice parameter and average crystallite size of γ-$Co_{0.25}Mo_{1.75}N$ nitride. …148

5.5 Material, Average TEM particle size, interplanar distance calculated from SAED and XRD, Miller indices and lattice parameter calculated from SAED and XRD pattern of γ-$Co_{0.25}Mo_{1.75}N$ material. …149

5.6 Material, miller indices, observed and calculated interplanar distance, lattice parameter and average crystallite size of γ -Mo_2N synthesized via urea route. …155

5.7 Materials, average SEM particle size, interplanar distance from SAED pattern, Miller indices and corresponding lattice parameters of γ-Mo_2N material synthesized via urea route. …157

6.1 Material, Phase, Average crystallite size, Miller indices (hkl), interplanar spacings (d) and lattice parameters of WO_3 precursor. …168

6.2 Material, Phase, Miller indices, observed and calculated interplanar spacings, crystallite sizes and lattice parameter of β- W_2N. …170

6.3 Materials, Nitridation temperature, BET surface area, pore volume and average pore size of β-W_2N materials. …174

6.4 Material, Miller indices (hkl), observed interplanar distance (d), lattice parameter and average crystallite size of $CoWO_4$. …177

6.5 Materials, Nitridation temperature, Miller indices, observed and calculated interplanar distances, lattice parameters and average crystallite size of $CoWN_2$ materials synthesized at various temperatures. …180

List of symbols and Abbreviations

Abbreviation / symbols	Description
A	Exchange stiffness / Ampere
Å	Angstrom
a, b, c	Lattice parameters
a.u.	Arbitrary unit
AAS	Atomic absorption spectroscopy
AX	Alkaline earth halide
AN	Alkaline earth nitride
aq.	aqueous
at. wt%	Atomic weight percentage
at.%	Atomic percentage
Avg.	Average
bcc	Body centered cubic
BET	Brunauer–Emmett–Teller
BJH	Barrett-Joyner-Halenda
C	Curie constant
cc	Cubic centimeter
CHN	Carbon Hydrogen Nitrogen
CRT	Cathode ray tube
CV	Cyclic voltametry
D_c	Critical diameter
d_{cal}	Calculated interplanar distance
deg	Degree
dia	Diameter
d_{obs}	Observed interplanar distance
e.g.	For example
EDX	Energy dispersive X-ray
emu	Electromagnetic unit
et al.	And others

etc	etcetera
fcc	Face centred
Fg^{-1}	Faraday per gram
FWHM	Full width at half maximum
g	Gram/ gas
h	Hour
H_c	Coercivity
hcp	Hexagonal close packed
HDN	Hydrodenitrogenetion
HDS	Hydrodesulphurization
hex	hexagonal
hkl	Miller indices
hrs	Hours
HRTEM	High resolution transmission electron microscopy
i.e.	That is
ICDD	International centre for diffraction data
IUPAC	International Union of Pure and Applied Chemistry
JCPDS	Joint Committee on Powder Diffraction Standards
K	Kelvin
k_B	Boltzmann constant
K_{eff}	Effective anisotropy constant
keV	Kilo electron volt
kJ	Kilo Joule
kOe	Kilo Oersted
LED	Light emitting diode
M	Molar
MX	Metal halide

min	Minute
MN	Metal nitride
M_R	Remnant magnetization
M_s	Saturation magnetization
mV	Mili volt
N	Normal
nm	Nano meter
NMP	N-Methyl-2-pyrrolidone
^{o}	degree
^oC	Degree centigrde
P/P_o	Relative pressure
ppm	Parts per million
PVDF	Polyvinylidene difluoride
PXRD	Powder X-ray diffraction
r_M	Radius of metal
r_X	Radius of nonmetal
RS	Rock salt
RT	Room temperature
s	Second
SAED	Selected area electron diffraction
SC	Specific capacitance
SEM	Scanning electron micrography
SSM	Solid state metathesis
t	Thickness of magnetic inactive layer
t	Average crystallite size
T_B	Blocking temperature
T_c	Curie temperature
TEM	Transmission electron microscopy
TM	Transition metal
TPR	Temperature programmed reaction

V	Volt
vs	Versus
VSM	Vibrating sample magnetometer
wt.%	Weight percentage
XRD	X-ray diffraction
ZB	Zinc blende
γ	Critical exponent of correlation length
λ	Wavelength
μ_0	Permeability
μ_B	Bohr magneton
μm	Micro meter
ρ	Density
σ_{bulk}	Electronic conductivity of bulk material
χ	Magnetic susceptibility
Ω^{-1}	Ohm^{-1}, electrical unit of conductance
Θ	Weiss constant, angle

Chapter 1

Introduction

This chapter deals with general introduction to transition metal nitrides including their potential technological applications. The structural aspects, common synthesis methods and advanced characterization techniques used for nitride materials have been described. A general discussion on magnetism in bulk and nanoform has been presented. Extensive literature survey has been done to find out the gaps in the existing research. The objectives of the thesis have been defined based on the existing gaps and a layout of the thesis structure has been presented in the current chapter.

1.1 General introduction

Nitrogen is a versatile element that forms compounds with most of the metallic elements listed in the periodic table. The bonding between nitrogen and a less electronegative element such as a transition metal brings up very stable compounds, namely metal nitrides. Significant, rapid progress has been made in nitride chemistry in recent decades because of their wide range of applications in various fields. The potential applications are based on their interesting properties; such as: electronic, optical, thermal and magnetic properties [1-6]. Some of the notable properties include: metallic to insulating or superconducting behaviour, absorption/ emission bands ranging from UV to visible and/or near infrared region, low to high thermal conductivity, paramagnetic to ferromagnetic characteristics, soft to extreme hardness etc. In addition, they possess high chemical and thermal stability and show excellent catalytic properties. The bonding scheme in nitrides is richer compared to oxides, as more number of electrons are in bonds than localized on the anion lattice [7, 8]. This feature is reflected in their electronic and optical properties. Nitrides, such as AlN, GaN and InN can be semiconductors, whereas many corresponding oxides are insulators (e.g. Al_2O_3) [2]. Nitrides are less readily sintered than oxides and have higher conductivity than oxides [9]. The combination of their properties places them between high performance ceramics and metals [10].

Interstitial nitrogen has a potential to alter the properties of iron-based alloys in a useful sense suitable for particular applications [11]. Many theoretical studies establish the relation between structural and magnetic parameters [11-13]. The early transition metal nitrides adopt rock salt structure whereas the late transition metal nitrides adopt zinc blende structure with the crossover at MnN. It is noted that the tendency towards magnetism is stronger in the rock salt phase than in the zinc blende phase. The lattice constant of zincblende (ZB) structure is always larger than that of the rock salt (RS) structure. FeN has a high magnetic moment in RS structure, while in ZB it becomes magnetic at very large lattice expansion. CoN stays nonmagnetic in ZB structure. Similarly, MnN becomes magnetic above a certain value of lattice constant in ZB structure. CrN has a gradual increasing magnetic moment as a function of the lattice constant. VN shows a very weak magnetism and TiN and ScN are nonmagnetic [12]. Studies on Fe_xN_y type interstitials show that the magnetization of the compound increases with decrease in nitrogen content [11, 13, 14.].

Nitrogen plays an important role in modification of magnetic properties in 3-d metal/alloys (Fe-N, Fe-Ni-N etc.) including 3d-4f intermetallic compounds (Nd_2Fe_{17}, SmCo etc.) [15,16]. In fact, several magnetic parameters, such as: saturation magnetization, M_s, Curie temperature, $T_{c,}$ coercivity, H_c, and blocking temperature,T_B, etc., change upon insertion of atomic nitrogen in the host crystal structure. The presence of nitrogen in the interstitial positions provokes expansion of the lattice, majorly. The influence of nitrogen on tailoring of magnetic properties can be well understood from the fact that certain iron based alloys can change their magnetic states from weak ferromagnet to strong one [11].

On a global scale, the operation of the Haber-Bosch process for the production of ammonia, currently consumes 1-2% of the world's energy demand [17]. Hence the development of more active catalysts which would allow a reduction in the reaction temperature and the stringent conditions of operation is of significant interest. In this context, catalytic activity of binary and ternary metal nitrides is very promising. The nitrides include those of molybdenum, vanadium, uranium, rhenium and cerium nitrides [18-20].

These interstitial nitrides are often found to exhibit group VIII noble metal like properties. This was first pointed out by Levy and Boudart [21]. It is deduced that introduction of nitrogen atom into the metal lattice results in combination of sp electrons of

N with metal 'spd' bands. This leads to an increase in the d-electron density of the metal at the Fermi level and induces noble metal like properties to the nitrides [22].

The synthesis of nitride is very complex which involves breaking and making of N≡N bond, having bond dissociation energy of 945 kJ/mol. This is comparatively greater than the bond dissociation energy of oxides, i.e. 498 kJ/mol [23]. Therefore, higher temperature is required for nitride synthesis. Some of the nitrides are air sensitive, so they can easily form oxides and hydroxides upon exposure to atmosphere [24, 25]. The nitrides are mostly used in bulk form or micron sized powders due to an intrinsic difficulty in synthesizing them as nanoparticles in a scalable fashion. These factors contribute towards the less abundance of studies on nitrides compared to other ceramics and nanomaterials.

1.2 Potential technological applications

Most of the nitride materials are referred as refractory materials [26]. In recent years, different phases of ferromagnetic iron nitride compounds have attracted great attention over pure iron by virtue of their excellent magnetic properties and high corrosion and wear resistance [27, 28]. The metastable and unstable group VII and VIII nitrides, mainly those of iron, are of extreme importance in steel hardening. Acicular γ'-Fe_4N particles are regarded as potential candidate for magnetic recording applications [29]. Iron nitride can also be used as magnetic fluid active damper, spintronic devices and magnetic sensor [30, 31]. A good number of nitride materials are significant as catalysts for various reactions. These materials have been particularly successful with reactions in a hydrogen environment like hydrogenation, dehydrogenation, HDN, HDS, hydrogenolysis, ammonia synthesis, hydride activation, fisher-tropsch reactions and hydrocarbon isomerization etc. [9, 32-39]. Another noteworthy catalytic application of nitrides includes use of molybdenum nitride and tungsten nitride as substitutes of iridium for the catalysts in microthruster, used for space communication [40]. Group III – V transition metal nitrides are promising candidates for electronics and device applications. Group III semiconductors are used for short wavelength LED and semiconducting lasers [1-3]. The transition metal nitrides are superhard materials used for coating and cutting tools [41, 42].

1.3 Crystal structure

Transition metal nitrides are close packed metallic structures in which nitrogen atoms occupy interstitial sites due to their smaller size than the metallic atoms [43]. Nitrogen, a diatomic gas can form compounds with every transition metal except for the late elements of second and third row. The crystal structures of the nitrides show a considerable variation. Towards the left of the periodic table the structures tend to be simple, very often resembling the parent transition metal. However, towards the right of the periodic table, the structures adopted, tend to be more complicated. These trends were first systematized by Hagg's rule, which states that the structure formed depends upon the radius ratio $r = r_X/r_M$. r_X and r_M represent radii of nonmetal and metal, respectively. When the ratio 'r' is less than 0.59, the common structures formed are: face centered cubic (fcc), hexagonal close packed (hcp) and simple hexagonal (hex). In these structures the nonmetal atoms are placed in the large interstitial sites of octahedral or cubic prismatic geometry. When 'r' is greater than 0.59, the metallic arrangement distorts to accommodate the larger nonmetal atom and to preserve metal- metal interactions [44]. It has been already established that early transition metal nitrides, ScN-CrN, possess rock salt (RS) structure whereas later ones, i.e. MnN-CoN, prefer zinc blende (ZB) type structure with the cross over occurring at MnN [12]. These TMNs can be classified into ionic, covalent and metallic on the basis of their structural bonding. The chemical bonding in transition metal nitride is due to the mixing of d-orbitals of metal atom with p-orbitals of nitrogen atom [45]. Group I and group II metals form nitride compounds essentially containing ionic bonds. For example: Li forms an ionic nitride, i.e. Li_3N, having high value of ionic conductivity. Elements of Group III and Group IV form covalently bonded nitrides. Some of the important crystal structures related to Fe-N, VN, W_2N, Mo_2N and $CoWN_2$ materials systems are described in the following subsections.

1.3.1 Crystal structure of iron nitrides

Atomic nitrogen can be dissolved in the body centered cubic (bcc) lattice of α-Fe to a concentration of 0.4 at.% N without much distortion of the lattice. When more than 2.4 at.% of N is dissolved in pure Fe, the bcc lattice undergoes a tetragonal deformation [46]. In the composition range up to 11 at.% N the iron nitride compound is called nitrogen martensite α′ phase. At saturation, nitrogen martensite has the Fe_8N composition. The α′-Fe_8N can

transform into the α″-$Fe_{16}N_2$ phase. Depending upon the nitrogen concentration there exist a series of binary Fe−N compounds: γ″-FeN_y (y = 0.9−1.0) with ∼50 atomic % N, ζ-Fe_2N with ∼33% of N, ε-Fe_3N_{1+y} (y = 0−0.33) with ∼25% N, γ′-Fe_4N with ∼20% N, and Fe_8N (or α″- $Fe_{16}N_2$) with ∼11% N [47]. However, in this thesis ε-Fe_3N_{1+y} and γ′-Fe_4N phases were dealt with and their structural elucidations are mentioned in the subsequent sub-sections.

1.3.1.1 Crystal structure of γ′-Fe_4N

The simplest ordered Fe-N compound is cubic γ′-Fe_4N. This is a cubic antiperovskite which can be described as a face centered cubic lattice of iron metal (γ-Fe) with N atom located at the body center site (figure 1.1). γ′-Fe_4N structure crystallizes in $Pm\bar{3}m$ space group [11,47,48]. The fcc lattice of γ-Fe is expanded by 33% by interstitial nitrogen in the 1b body centre position, giving a value of lattice parameter of 3.795Å against the value of 3.450Å for γ-Fe. There are two non-equivalent iron sites; the body corner 1a site with cubic symmetry having 12 iron neighbours at 2.68 Å and the 3c face centre site with two nitrogen neighbours at 1.90 Å and 12 iron second neighbours at 2.68 Å. When another transition metal such as Co, Ni, Sn or Mn is substituted in the γ′-Fe_4N lattice then the structure of the host lattice changes due to various site occupancies. The substitution of Co for Fe is random but Ni has a preference for corner sites. Sn substitutes Fe at the corner sites rather than the face centered sites, whereas Mn can occupy both the lattice sites of γ′-Fe_4N lattice [49-51].

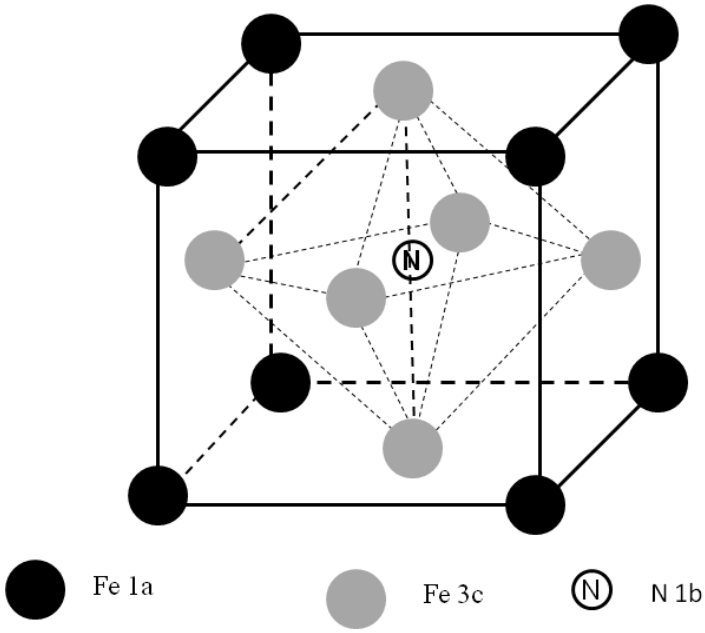

Figure 1.1 Crystal structure of γ′-Fe_4N. The site occupancies of Fe and N are indicated.

1.3.1.2 Crystal structure of ε-Fe_3N

ε-Fe_3N phase crystallizes with hexagonal close packed (hcp) structure with alternate stacking of Fe and N layers (figure 1.2). The epsilon phase exists over a wide range of composition in the iron- nitrogen (Fe-N) phase diagram ranging from 25-33 at. % of N. The upper limit of the nitrogen concentration for ε-phase is 49.3N atoms / 100 Fe atoms [52]. In this hexagonal lattice, all Fe sites are equivalent as are the N sites. In ε-Fe_3N, Fe atoms form an hcp arrangement with N atoms occupying voids inside Fe_6 octahedra. One third of the octahedral voids in an hcp arrangement of Fe are occupied by N in the ideal structure of ε-Fe_3N resulting in NFe_6 octahedra sharing only common vertices. The structure can be regarded as optimized in terms of avoiding close N-N contacts which correspond to NFe_6 octahedra sharing common edges and faces [13]. In the Co and Ni substituted ε-Fe_3N system, metal atoms randomly replace Fe atoms and occupy [1/3, 2/3, 1/4] and [2/3, 1/3, 3/4] positions, while the N atoms occupy regular positions [0,0,0] and [1/3, 2/3, 1/2] positions [48, 53].

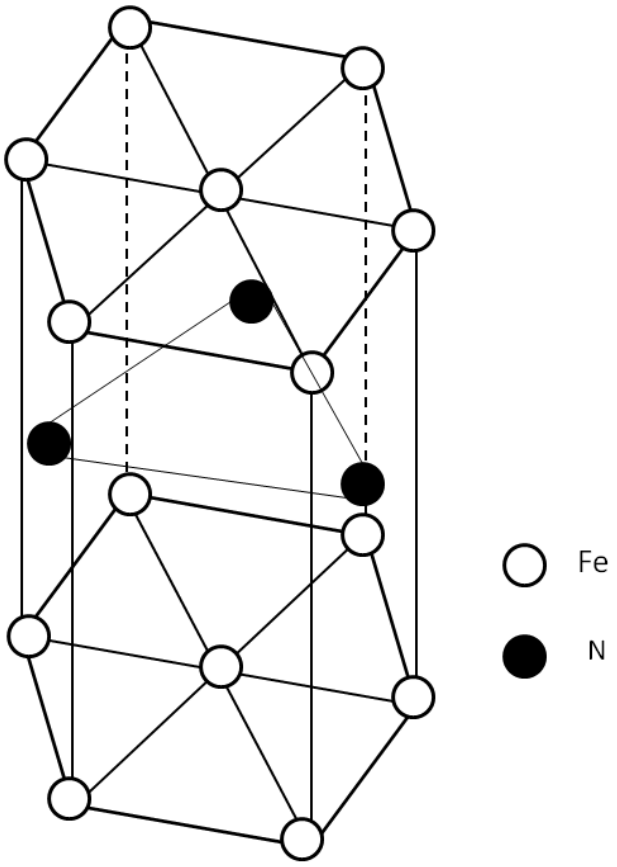

Figure 1.2 Hexagonal structure of ε-Fe_3N indicating arrangements of Fe and N atoms in hcp lattice.

1.3.2 Crystal structure of VN

Vanadium nitride has a cubic rock salt structure with space group *Fm3m* having point symmetry *m3m*. V and N atoms occupy (0, 0, 0) and (1/2, 1/2, 1/2) atomic positions, respectively [24]. The bond distance between nearest V and N atoms is found to be 2.069 Å. The lattice parameter is found to be 4.13 Å for stoichiometric cubic VN structure [24, 54].

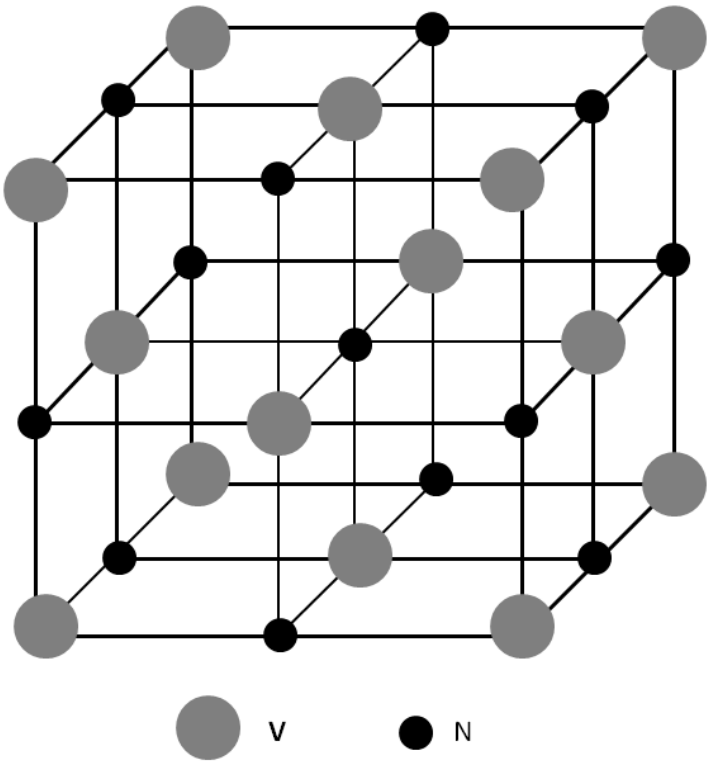

Figure 1.3 Crystal structure of VN indicating arrangement of V and N in the cubic lattice.

1.3.3 Crystal structure of molybdenum nitrides (β- and γ-Mo_2N)

The crystalline phases appearing in molybdenum – nitrogen (Mo-N) systems are very complex. Different forms of molybdenum nitrides widely differing in crystal structure result, depending upon N content. Three different stable molybdenum nitride phases, i.e. β- , γ-Mo_2N and Mo_3N_2, result in the binary phase diagram of Mo-N, when the N content is slightly greater than the stoichiometric values. $Mo_2N_{1\pm x}$, with lower values of covalencies crystallize in two different structures which are deduced from the bcc Mo structure [43, 55]. At low temperature, tetragonal β-$Mo_2N_{1\pm x}$ is formed by occupation of octahedral interstices by N atoms. γ-$Mo_2N_{1\pm x}$ crystallizes in rock salt structure (NaCl-B1-type) and can be described as a face centered cubic array of Mo atoms with N atoms randomly occupying one half of the octahedral interstices of the host metal (*Fm3m* space group) (figure 1.4) [43]. Tagliazucca *et al*. have reported another structure for γ-$Mo_2N_{1\pm x}$ having space group *Pm* $\bar{3}$*m* with ordered vacancies, distinguished from *Fm3m* structure by presence of superstructure

reflection [56]. With excess of nitrogen, molybdenum nitride also crystallizes in a structure similar to γ-Mo_2N having stoichiometric formula as Mo_3N_2 [43].

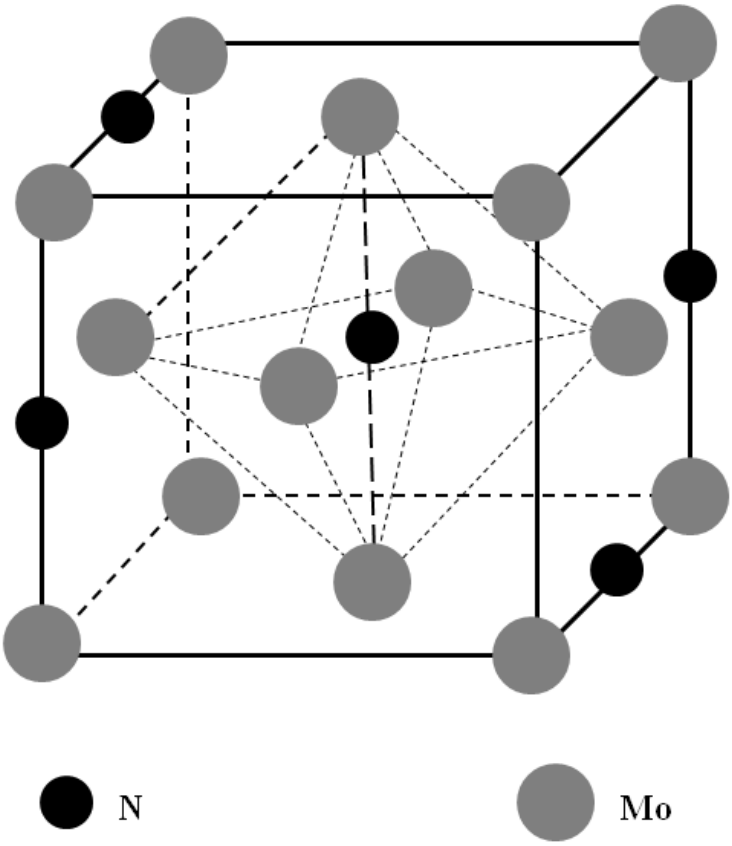

Figure 1.4 Crystal structure of γ-Mo_2N showing positions of Mo and N in the fcc lattice.

1.3.4 Crystal structure of β-W_2N

The first crystallographic analysis of tungsten nitride was made by Hagg in 1930 [56]. He identified β- tungsten nitride phase which has the composition W_2N. A new γ-phase of tungsten nitride was also postulated in 1951 [57]. Tungsten nitride also exists in tetragonal (WN), hexagonal (δ-WN) and rhombohedral (WN_2) phase [57, 58]. A cubic γ-phase of stoichiometry W_3N_4 has also been synthesized [57]. Figure 1.5 shows the unit cell of β-W_2N structure which is structurally similar to γ-Mo_2N except Mo atom positions are replaced by W (see figure 1.4). β-W_2N crystallizes in a cubic structure with space group *Fm3m* and B1 structural type. W atoms are located in 4a (0,0,0) sites and N atoms occupy half of 4b (1/2,1/2,1/2) sites. The calculated reported value of lattice parameter of β-W_2N is 4.199Å (reported value: 4.128 Å), whereas the lattice parameter of cubic WN is 4.362Å [58].

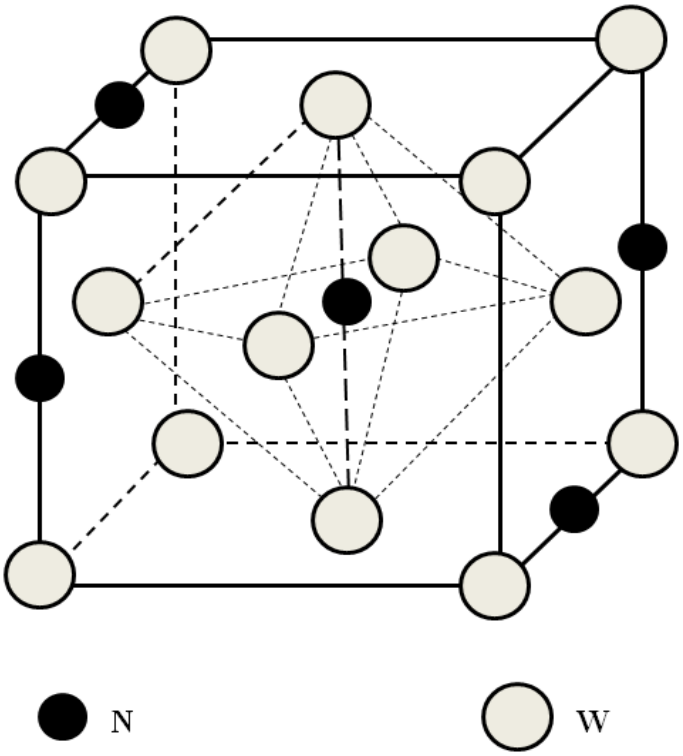

Figure 1.5 Crystal structure of β-W_2N showing positions of W and N atoms in the fcc lattice.

1.3.5 Crystal structure of $CoWN_2$

The compound $CoWN_2$ crystallizes in typical layered structures with W in trigonal prismatic coordination by nitrogen. It has a structure of ABN_2 (A = Co, B = W), as illustrated in figure 1.6. These polyhedra are connected to each other forming layers, which are stacked together, so that the second transition metal occupies octahedral voids between the layers [59]. The structure consists of alternating layers of trigonal W-N prisms and triangular lattice layers of Co- site atoms [60].

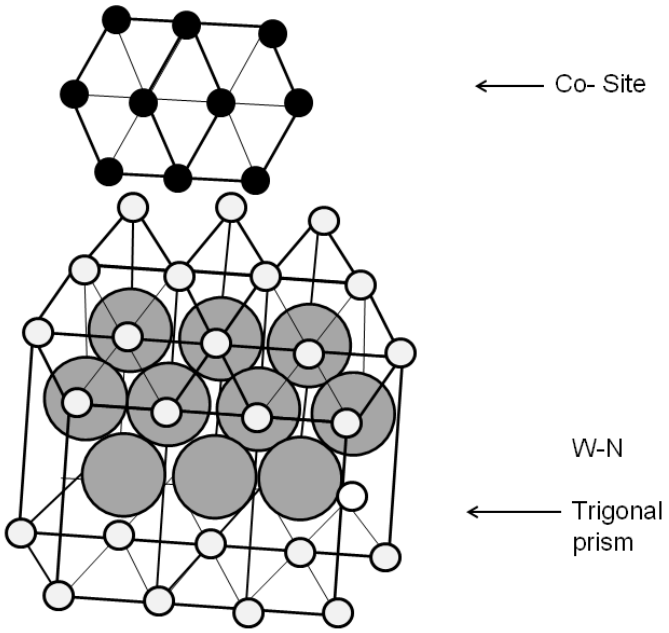

Figure 1.6 Layered crystal structure of $CoWN_2$ [59]

1.4 Synthesis methods

The synthesis methods can be sub-divided into two categories: (1) physical methods and (2) chemical methods. Among the physical approaches, the most frequently used ones are arc melting, solid state methods, physical vapor deposition, plasma and laser methods etc.. On the other hand, several chemical approaches are adopted for synthesis which includes sol-gel, co-precipitation, molecular precursor method, solid state metathesis and solvothermal synthesis etc. These methods are more versatile and allow production of a broader range of compounds with high purity and homogeneous distribution of constituent atoms [33]. As important functional properties of the nanomaterials depend on the shape, size and morphology of the particles, use of chemical synthesis for preparing materials has become important topic of investigation [34, 61].

In the past several decades, great efforts have been made to synthesize nitrides and the available routes contain a wide range of synthesis techniques such as nitridation of metal or metal oxides, using urea or azide as reductant, use of reactive hard template, chemical vapor deposition, molecular beam epitaxy, sputtering, solid state metathesis route etc. [10, 34, 45, 62-66]. The nitride materials can be produced in the form of thin films, coatings and nanopowder at low to moderate and high temperature of preparation.

Polycrystalline nitride samples are prepared by powder metallurgy. The metal or the oxide powder is reacted with gaseous nitrogen or ammonia. The direct nitridation of metal powder with nitrogen is the most common laboratory method for preparing nitrides. The preparation of high purity materials with homogeneous distribution of nitrogen atoms is quite a difficult task. Very high temperature, highly purified gas and inert atmosphere are generally required. The preparation conditions also vary according to the alloy system. Sixth group elements cannot be effectively nitrided in N_2(g). They form nitrides at low temperature only in an NH_3(g) atmosphere and require longer reaction times [26].

Nitridation of oxide precursor is one of the commonest routes to nanocrystalline nitrides. Volpe and Boudart developed the temperature programmed reactions (TPR) which involve heating the metal oxide in flowing ammonia gas with slow heating and cooling ramps. Although, the methodology has its own impact, it is limited due to non-availability of crystalline metal/mixed metal oxides of particular stoichiometry. In addition, it leads to precipitation of non-removable oxide impurities in some cases. The synthesis of a series of early transition metal nitride catalyst from oxide precursors through TPR reaction has been investigated by Claridge *et al.* [67].

Solid state metathesis reactions are also used to prepare alkali and alkaline earth metal nitrides [34]. The SSM reaction for the synthesis of nitrides typically involves a metal halide (MX) and an alkali or alkaline earth nitride (AN) compound and the reaction can be described by an ion exchange scheme.

$$MX + AN \rightarrow MN+AX \qquad \text{---------- (1.1)}$$

The common drawbacks of conventional SSM reaction include uncontrollable reaction process, poor crystallinity and non-stoichiometric product formation [68].

The preparation of nitrides is more challenging than oxides as the later can be prepared in air but the former usually requires exclusion of air and water or an inert environment for the synthesis. Also, transition metal nitrides are often refractory and the constituent elements have low diffusion rates. Thus, at moderate temperature long reaction times are often required to produce a pure product [25].

Based on the above facts, there is an increasing interest in developing alternative chemical approaches to metal nitrides using tailored molecular precursors to lower the

synthesis temperature and to achieve molecular control over the crystal growth and the processing of the materials [69, 70]. Numerous efforts have been focused on various methods like organometallic compounds and direct nitridation of the metal etc. The organometallic route is expensive, toxic, extremely unstable and very difficult to synthesize and handle [71]. Similarly, complex nitride phases (ternary, quarternary) are difficult to obtain and unstable, phase separated products are obtained using the direct nitridation of metal elements or inter metallic compounds [25]. Hence there is a need to develop a method that uses inexpensive precursor materials and is applicable to synthesis of various metal nitrides. In this context, nitridation using oxide precursor obtained via chemical routes by using NH_3(g) and solid urea as nitrogen sources can be used as alternative useful methods of nitride preparation. The advantages for using both the routes are described here with. In oxides, the fractional difference in M-O and M′-O bond strength is much smaller (where M and M′ represent two different transition metals). Therefore, it is possible to prepare complex nitride phases (M-M′-N) at lower temperature from the oxide precursors [25, 67]. Urea route involves preparation of the metal - urea complex precursor, which is a chemically stable and inexpensive compound, compared to other precursors such as organometallic materials or anhydrous chloride [62]. Urea replaces the coordinated water around the metal atom and decomposes at elevated temperatures leaving metal oxide particles or metal chloride in case of metal-urea nitrate or metal-urea chloride, respectively. Finally the complex transforms into metal nitride under a flowing N_2(g) atmosphere [71].

1.5 Advanced characterization tools

Various advanced characterization techniques are used to probe the structural, morphological, catalytic and magnetic properties of nanomaterials. The details of the instrumental techniques, experimentation and analysis of results are presented in this section.

1.5.1 Elemental analysis

1.5.1.1 Atomic absorption spectroscopy (AAS)

This analytical application is based on the fact that metal atoms absorb strongly at discrete characteristic wavelengths, which coincide with the emission spectral line of the particular metal. The atoms are atomized first and then irradiated by optical radiation. The

atomization is done using passing the liquid sample through nebulizer and thermal treatment is done employing suitable fuel/oxidant pair, e.g. acetylene/oxygen which can produce a temperature up to 3150^{o}C. The radiation passes through a monochromator in order to separate element specific radiation, which is detected by a detector [72].

1.5.1.2 Energy dispersive X-ray (EDX)

Energy dispersive X-ray (EDX) is another analytical technique to determine the trace elements present in the materials. This equipment is generally attached with a scanning electron microscope (SEM). The number and energy of the X-rays emitted from the specimen are detected by an energy dispersive spectrometer. The energy of X-rays emitted represents characteristic of the difference of energy between two shells and atomic structure of an atom. Thus, the detection of the X-rays emitted allows the determination of elements present in the materials [73].

1.5.2 Powder X-ray diffraction (PXRD)

X-ray diffraction is an important tool for the structural characterization of the inorganic solid materials. The technique deals with the diffraction of X-rays from the crystal planes stacked in a parallel manner. It gives information about the structural properties like phase(s), crystallite sizes, lattice parameters, inter planar distance and space group of the crystal etc. Rietveld refinement can give additional information based on the XRD data. The refinement can solve an unknown crystal structure and quantitatively determine the percentage of different phases in the sample including spatial arrangement of atoms in crystal structure.

1.5.3 Electron microscopy (SEM/TEM)

Microscopy using wave properties of X-rays is an essential characterization technique for investigation of micro structure of materials. In particular, probing crystallographic information and composition at nanometer scale can be achieved by using SEM/TEM [74]. SEM technique is based on secondary electron emission from the surface of a solid specimen in reflection mode which can provide imaging. The basis of technique used for TEM is the transmission of X-rays in a submicron specimen producing imaging along with diffraction patterns. Scanning electron microscopy can provide morphological information at sub-micron scale and elemental information at micron scale of a material.

Conventional TEM and related spectroscopic techniques, such as: EDX are common tools for investigating shape, size, crystal structure and composition of the materials at < 1nm scale (see subsection, 1.5.1.2) [75].

1.5.4 Sorption measurements

Physisorption is the technique to study the specific surface area and pore characteristics of solid materials [76]. The technique accurately determines the amount of gas adsorbed by the solid, which is a direct measure of porous properties and structure of the material. Different probe gases (e. g. N_2, Ar and CO_2) are frequently used as adsorptive, depending upon the nature of the material (defined as adsorbent) and the information required. N_2 (g) adsorption at 77 K is a well known measurement technique for routine investigation of new materials. The isotherms obtained from the adsorption measurements provide information about surface area, pore volume and particle size distribution. If applied over a wide range of relative pressure (P/P_0), N_2 (g) adsorption isotherms provide information on size distributions in the micro-, meso- and macro- porosity range (~ 0.5 – 200 nm) [77].

There are six types of isotherms and four types of hysteresis loops as per IUPAC classification [78]. The types of isotherms are shown in figure 1.7 (a) - (f). Type I isotherm is concave to the P/P_o axis (figure 1. 7 (a)). Pores are typically microporus with the exposed surface residing almost exclusively inside the micropores, which once filled with adsorbate, leave little or no external surface for further adsorption. Type II isotherm is most frequently found when adsorption occurs on nonporous or macroporous adsorbent. Inflection point occurs near the completion of the first adsorbed monolayer (figure1. 7 (b)). Type III isotherm is convex to the P/P_o axis over its entire range (figure 1. 7 (c)). Isotherms of this type are not common, but there are a number of systems (e .g. nitrogen on polyethylene) which give isotherms with such kind of gradual curvature. Type IV isotherm can be easily identified by its characteristic hysteresis loop, which is due to capillary condensation taking place in mesopores. Inflection point typically occurs near completion of the first monolayer like type II (figure 1. 7(d)). Type V isotherm is uncommon; it is related to the type III isotherm in that the adsorbent-adsorbate interaction is weak, but is obtained with certain porous adsorbents (figure 1.7 (e)). Type VI isotherm represents stepwise multilayer adsorption on a uniform non-porous surface in which the sharpness of the steps depends on

the system and the temperature (figure 1.7 (f)). The step-height represents the monolayer capacity for each adsorbed layer and, it remains nearly constant for two or three adsorbed layers.

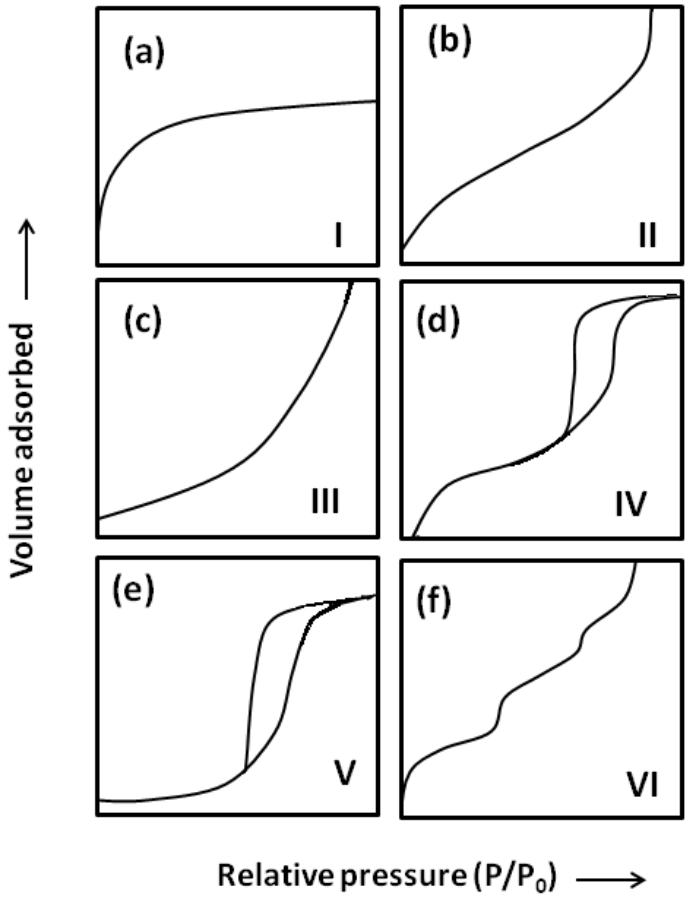

Figure 1.7 Different types of adsorption isotherms; (a) I, (b) II, (c) III, (d) IV, (e) V and (f) VI [78].

There are 4 types of hysteresis loops, i.e. H1, H2, H3 and H4, represented in figure 1.8. In H1 the two branches are almost vertical and nearly parallel over an appreciable range of gas uptake whereas in the H4 they remain nearly horizontal and parallel over a wide range of P/P_o. In certain respects types H2 and H3 may be regarded as intermediate between these two extremes [78].

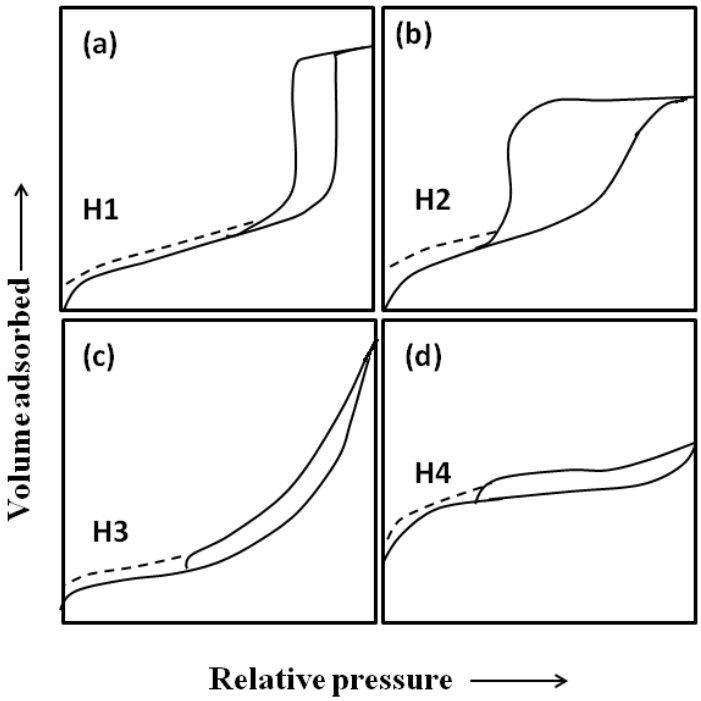

Figure 1.8 Different Types of adsorption Hysteresis; (a) H1, (b) H2, (c) H3 and (d) H4.

1.6 Magnetism in solid materials

Magnetism in solids arises due to spin of the electrons, orbital angular momentum about the nucleus and the change in orbital moment due to applied field. The first two effects give paramagnetic contributions and the third gives a diamagnetic contribution [79]. Although, several electrons are arranged in different energy levels inside the atoms, only those electrons which are unpaired can contribute towards magnetic moments in atoms/ions. This is due to electrons combining into pairs with opposite magnetic moment as a result of Pauli's exclusion principle or combining into a filled subshell with net orbital moment zero.

Magnetic behaviour can be majorly distinguished into 5 types; namely: (i) diamagnetic, (ii) paramagnetic, (iii) ferrimagnetic, (iv) ferromagnetic and (v) antiferromagnetic. In this thesis work, we will be dealing with diamagnetism, paramagnetism and ferromagnetism of solids with bulk and nano-particle forms. Therefore, the following subsections will be focused on basic theories and phenomena on the above stated five types of magnetic behaviours in bulk and nano-form.

1.6.1 Magnetism in bulk materials

1.6.1.1 Diamagnetism

Diamagnetism can be regarded as the result of shielding currents induced in an ion's filled electron shells by an applied field. According to Lenz's law, the induced currents give rise to an induction flux opposite to the change in the applied field [79]. Diamagnetic substances have weak magnetization induced by the field and the direction is opposite to the field. Ideal diamagnetism is characterized by a negative temperature independent magnetic susceptibility (χ). Diamagnetism is observed (atleast in part) in all magnetic substances, which arises due to absence of unpaired electrons. Diamagnetic substances have filled orbitals with no net magnetic moment (figure 1.9) [80]. Examples include: Cu and NaCl in crystalline form and SiO_2 in amorphous form.

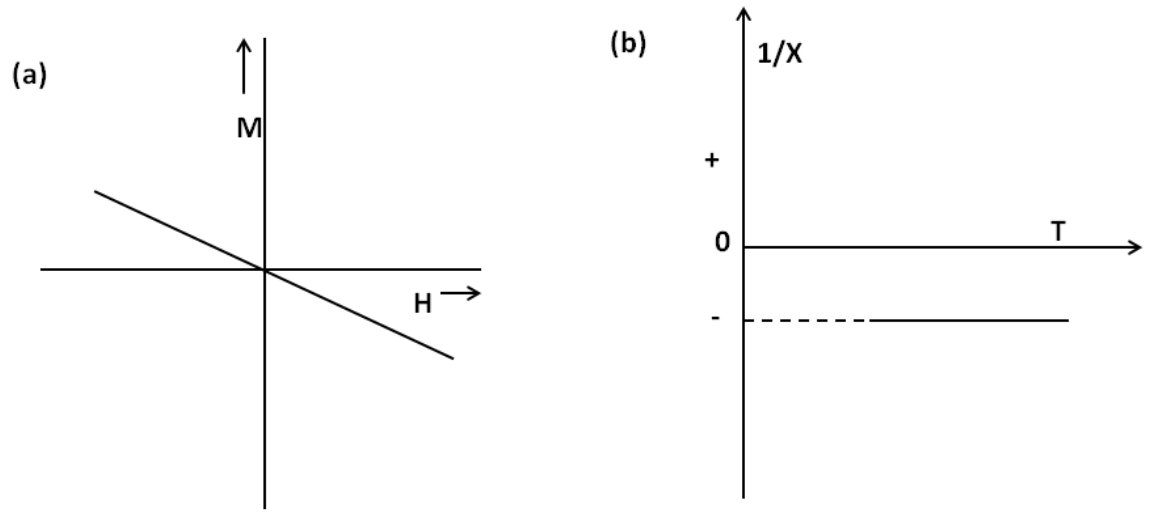

Figure 1.9 (a) Field dependent magnetization and (b) Temperature dependent inverse susceptibility of a typical diamagnetic material [80.]

1.6.1.2 Paramagnetism

This type of magnetism arises from spontaneous moments of unpaired electrons present in the atoms, e.g. transition metals. The orientation of each moment is randomized by its thermal energy, k_BT, and is aligned by an externally applied magnetic field. Ideal paramagnetism is characterized by susceptibility, χ , which varies inversely as temperature T

(χ = C/T, where C is the Curie constant). But ideal paramagnetism is an exception to the law as there is an appreciable inter-ionic coupling between the ionic moments in a solid. The temperature dependent susceptibility is given by Curie-Weiss law [80] which is defined as follows:

$$X = C/ (T-\Theta) \qquad \text{---------- (1.2)}$$

Θ is a constant which expresses the interionic coupling and termed as 'Weiss constant'.

The temperature dependent inverse susceptibility demonstrating Curie and Curie-Weiss law has been shown in figure 1.10.

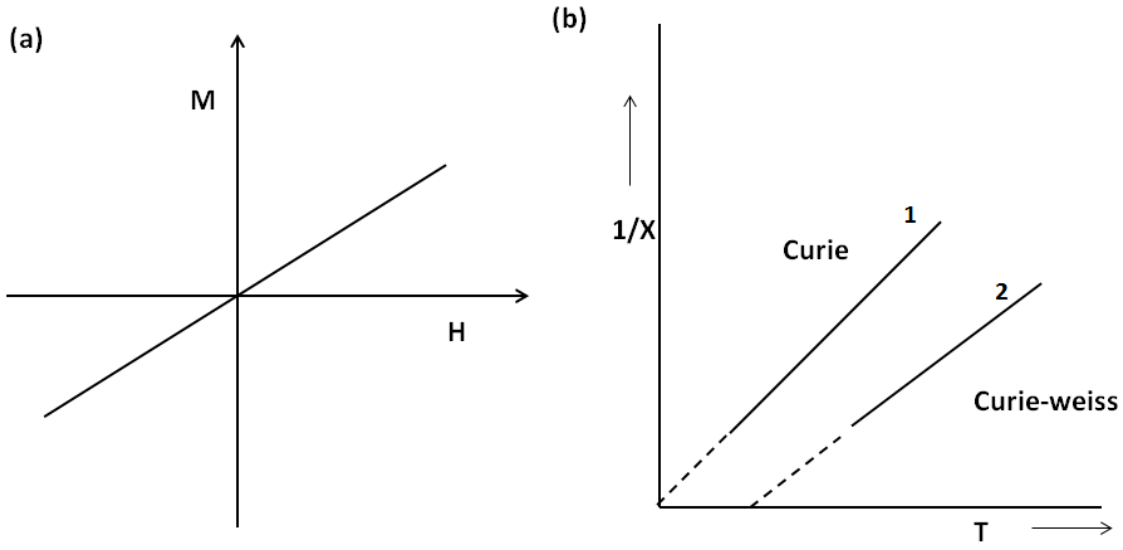

Figure 1.10 (a) Field dependent magnetization and (b) temperature dependent inverse susceptibility of a paramagnet showing (1) Curie and (2) Curie-weiss behaviour.

The magnetization vs. applied field, (M vs. H) plot of the paramagnet follows a linear relationship with a positive slope and positive magnetization. Langevin theory is applicable to the materials with non-interacting localized electrons. This theory states that each atom has a magnetic moment which is randomly oriented due to thermal agitation [81]. Application of external magnetic field produces slight alignment and thus low magnetization in the same direction of applied field. As the temperature increases, thermal agitation disturbs the alignment and the decrease in susceptibility is described by Curie law [81].

1.6.1.3 Ferromagnetism

This kind of magnetism leads to long range collinear alignment of all the moments in the system. Thus, there exists a spontaneous magnetization even in the absence of an applied magnetic field. The field dependent magnetization and temperature dependent inverse susceptibility of ferromagnet have been shown in figure 1.11 (a) and (b). The magnetization of a ferromagnet sharply rises at lower fields as the domains with more favourable alignments expand at the expense of others and get saturated when maximum domain alignment is achieved.

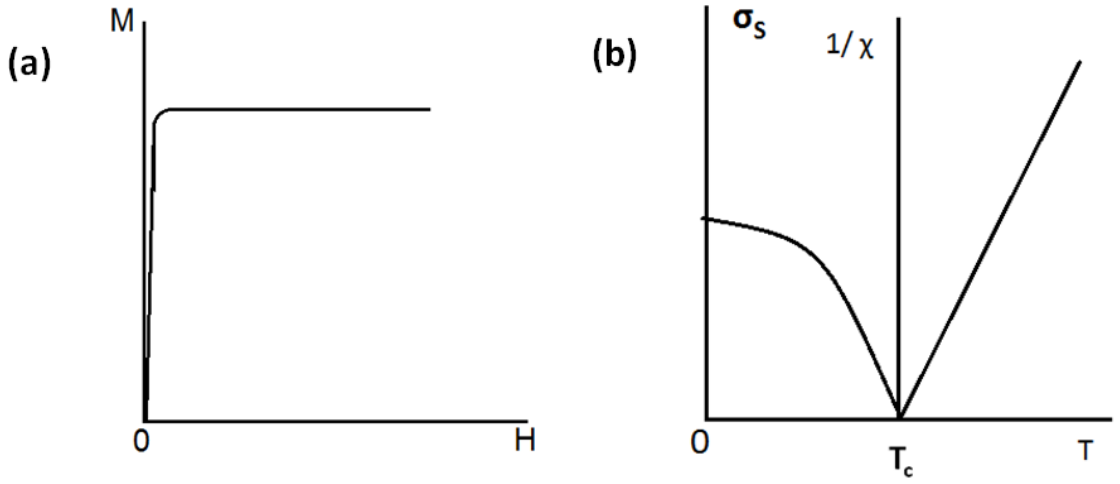

Figure 1.11 Magnetic characteristics of a typical ferromagnet; (a) field dependent magnetization (M vs. H) and (b) temperature dependent inverse susceptibility (1/χ) [80].

The properties of these substances are in good accord with the Weiss theory. With the increase in temperature, a point is reached where the thermal energy of the ferromagnet becomes comparable and eventually exceeds the exchange energy (which in turn depends upon anisotropy energy). At this temperature value of magnetization becomes null and is known as Curie temperature (T_c). Above T_c an ideal ferromagnet becomes a paramagnet and obeys Curie- Weiss law [80].

The full hysteresis plot of magnetization vs. field characteristics of a typical ferromagnetic material has been shown in figure 1.12. When magnetic field is applied, alignment of magnetic domains along the field direction takes place. In a large enough magnetic field, magnetization tends to saturate. If the applied field is changed continuously

between two extremes $\pm$ H_0, the magnetization process is not reversible and follows a hysteresis loop shown in figure 1.12.

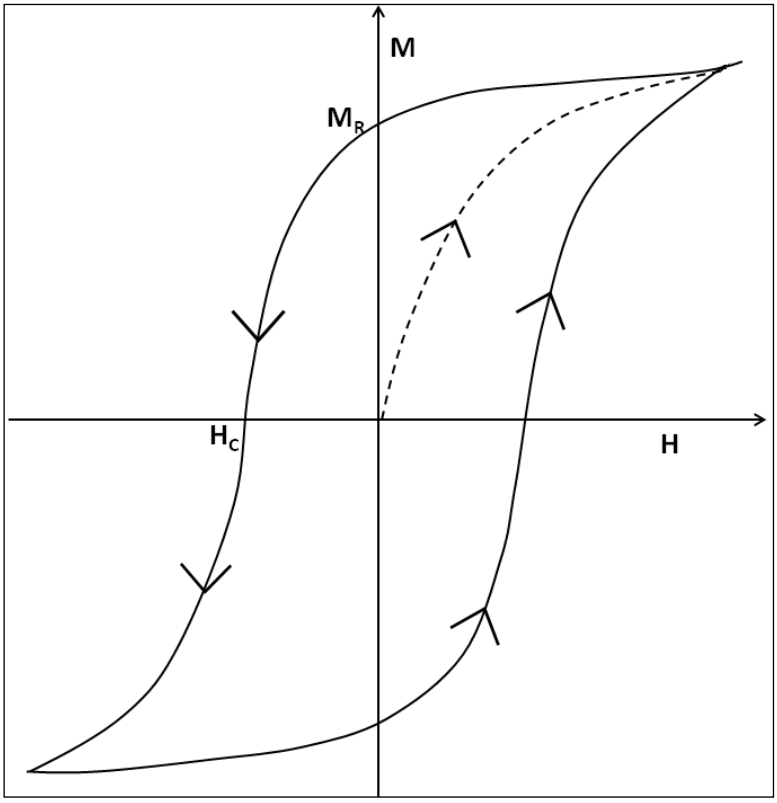

Figure.1.12 Hysteresis loop of a typical ferromagnet.

1.6.2 Magnetism in nanomaterials

Nanomagnetic materials exhibit interesting magnetic behaviour that is distinct from those of the bulk form of the same substance [82]. These characteristics are important for their various potential technological applications [6, 83]. This is because the reduced materials dimensions are comparable to the critical length of one or more of various phenomena such as the size of magnetic domains. Critical length is the maximum length below which, at given temperature the particle is single domain in nature and behaves as superparamagnetic [84]. The details of the specific magnetic phenomena occurring in the nano-magnetic systems are presented in the following sub-sections.

1.6.2.1 Nanomagnetic effects

The subdivision of magnetic structure of materials into distinct magnetic domains is the origin of many unique behaviours in magnetic materials. Based on the theory of

magnetism, the total energy of an ellipsoid is contributed by three types of energies, i.e. exchange, anisotropy and magnetostatic energy [85]. As the size of the magnet increases the number of domain walls also increase. This results in reduction of magnetostatic energy. While the numerous domain walls increase the exchange and anisotropic energies. Therefore, the size of a magnet has a great influence on the magnetic behaviour (popularly known as size effect). In addition, due to large volume to surface ratio because of small size of the nanomaterials surface effects get pronounced. The size and surface effects are described as follows [84].

(I) Size effect in nanomaterials : superparamagnetism

A single domain particle is uniformly magnetized with all the spins aligned in the same direction. The magnetization is reversed by spin rotation as there are no domain walls to move. This is the reason for very high saturation magnetization in nanomagnetic systems. In such a system coercivity increases from the bulk value, attains a maximum and then reduces further to zero value with the decrease of particle size. However, another source for the high coercivity in nanoparticles is the shape anisotropy which may result from particulate shape [5].

Magnetic crystallites below the threshold size or critical diameter at a particular temperature show superparamganetism. The temperature is referred as blocking temp (T_B), above which a particle is superparamagnetic [84]. The thermal energy (k_BT) overcomes the magnetic energy barrier ($K_{eff}V$) with decreasing particle size and the system behaves like a paramagnet. Instead of atomic magnetic moments, there is now a giant (super) moment inside each particle. This system is named as super-paramagnet. Such a system has no hysteresis (figure 1. 13) [5, 84].

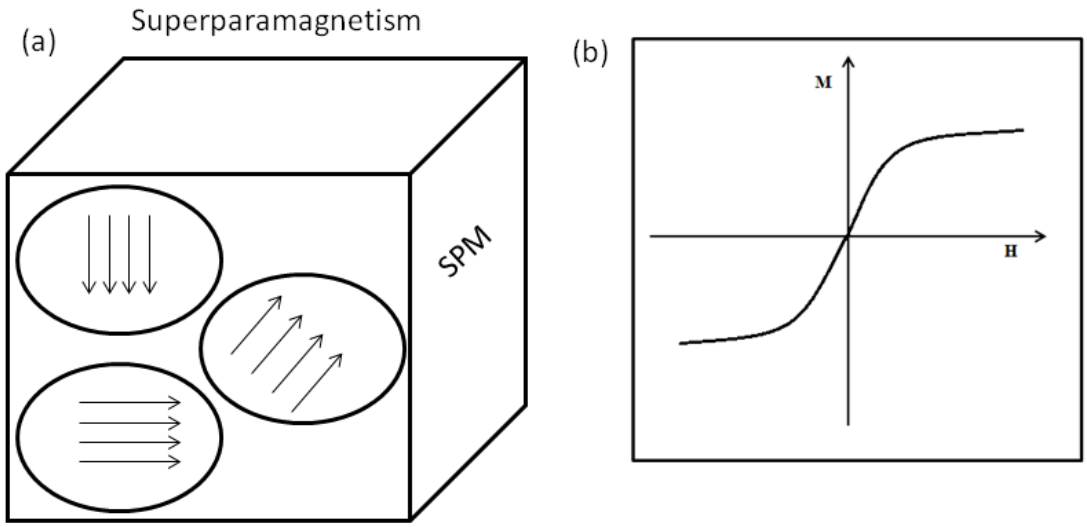

Figure 1.13 Representation of (a) super paramagnetic domains and (b) hysteresis loop showing zero coerciviy of a superparamagnetic assembly of nanoparticles.

(II) Surface effects in nanomaterials : spin canting

As the particle size decreases, a large percentage of all the atoms in a nanoparticle are surface atoms, which implies that surface and interface effects become more important. Due to the large surface atoms, bulk atoms ratio the surface signs contribute more towards the magnetizations. The local breaking of symmetry might lead to change in the band structure, lattice constant and atom coordination [5].

One of the interesting properties of transition metals and transition metal compounds is the occurrence of magnetism due to the establishment of a spontaneous (local) spin polarization of the electrons. Electronic paramagnetism arises from atoms, molecules and lattice defects possessing an odd number of electrons, causing a nonzero total spin [81]. Free atoms and ions with a partially filled inner shell (e.g. transition elements and rare earths) have unpaired electrons which lead to nonzero spin. Electrons occupied in 3d and 4f orbitals are highly localized on the atoms and correlations between electronic spins are very important. This is the cause of magnetism in late transition elements like Co, Ni and Fe. The elements Fe, Co and Ni show ferromagnetism due to parallel alignment of magnetic moments in terms of an exchange interaction between neighboring moments [86]. This argument is also extended while explaining magnetism in metal nitrides, such as: Fe_4N, Mn_4N, Fe_3N etc., except the contribution from spin pairing of N p states with TM 3d states.

The second group of magnetic materials is formed by strongly covalent compounds and alloys and are weakly ferromagnetic in nature. In this group the electrons are itinerant but the magnetic moment is localized in many of these materials [81, 86-89].

1.6.2.1.1 Coercivity (H_c)

With the reduction of size, there is a critical volume below which it costs more energy to create a domain wall than to support the external magnetostatic energy of a single domain state [88, 90]. The critical diameter of a spherical particle below which it exists in a single domain state is given by the following equation:

$$D_c \approx 18 \frac{\sqrt{AK_{eff}}}{\mu_0 M^2} \qquad \text{------- (1.3)}$$

Where, A is the exchange constant, K_{eff} is the anisotropy constant, μ_0 is the magnetic permeability and M is the saturation magnetization [88]. For instance, critical diameter of Fe particles for behaving as single domain is estimated to be 15 nm, using the above relation [85].

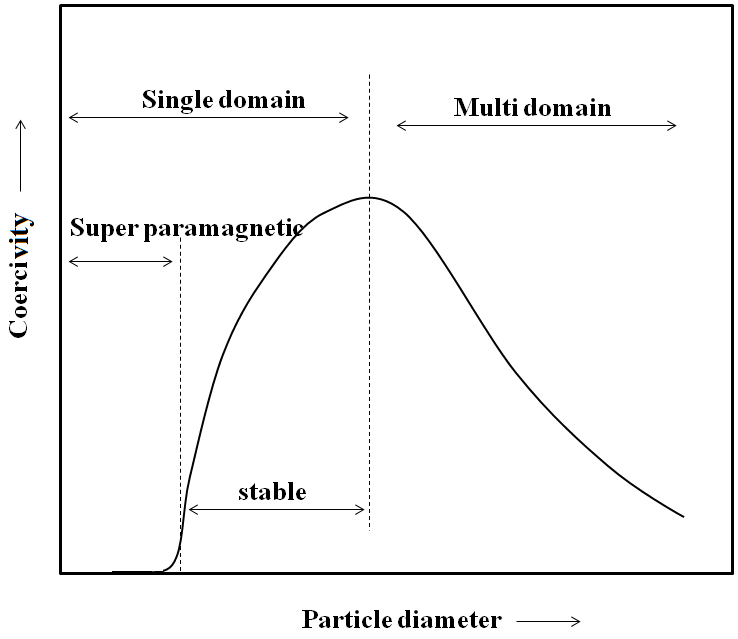

Figure 1.14 Variation of coercivity as a function of particle diameter [86]

Figure 1.14 represents the variation of coercivity as a function of particle diameter along with the assigned magnetic states; e. g. superparamagnetic etc. Below a critical size the magnet shows super paramagnetic behaviour and coercivity (H_c) becomes zero. The

value of coercivity is maximum at the critical diameter. With further increase in particle diameter multi domain regions begin to appear and the coercivity reduces [84]. Another source for high coercivity in a system of small particles is the shape anisotropy. Any departure from the sphericity of a single domain particle has an influence on coercivity [5].

1.6.2.1.2 Anisotropy energy (K)

In nano-particle systems crystal anisotropy (K) which is a measure of strength of the magnetization changes with particle dimensions. The change in anisotropy energy affects magnetic parameters; such as: M_s, H_c and T_c etc. [80, 81]. It is already well known that magnetic anisotropy energy in nanomaterials can be best described by effective anisotropy constant (K_{eff}) rather than K. The magnetic anisotropy energy per particle, responsible for holding the magnetic moments along certain direction can be expressed as:

$$E(\theta) = K_{eff}V\mathrm{Sin}^2\theta \qquad \text{--------- (1.4)}$$

Where, 'V' is particle volume, 'K_{eff}' is anisotropy constant and 'θ' is angle between the magnetization and the easy axis [5].

The energy barrier, $K_{eff}V$, favours the collinear arrangements of net spins corresponding to particulates in an assembly. With decreasing particle size the thermal energy, k_BT, exceeds the energy barrier, $K_{eff}V$ and the magnetization is easily flipped (i.e. tendency towards non-collinearity). For $k_BT > K_{eff}V$, the system behaves like a paramagnet and there is a giant magnetic moment inside each particle. This system is named as a super paramagnet. Such a system has no hysteresis [5, 80].

Size dependence of average anisotropy energy, K_{eff}, may be given by the following literature reported equation.

$$\langle K_{eff} \rangle = K_1^4 \cdot D^6/A^3 \qquad \text{-------- (1.5)}$$

Where $\langle K_{eff} \rangle$ is the average anisotropy energy, 'D' is the particle diameter and 'A' is the exchange stiffness [91]. It has been estimated that for a particle having diameter D in the range of 10- 20 nm, a relatively small increase in 'D' can give rise to drastic increase in the value of magnetic anisotropy energy, K_{eff}. The figure below illustrates the trend of 'K' in kJ/m^3 vs 'D' in nm.

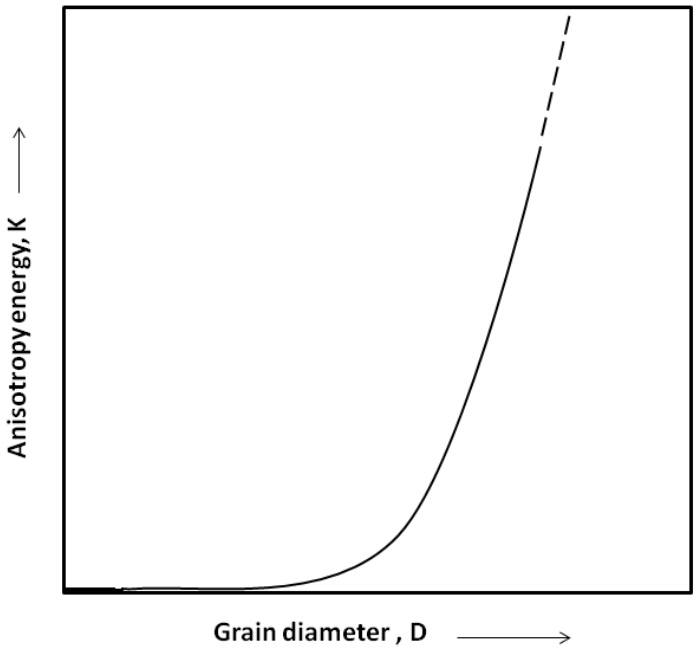

Figure 1.15 Variation of anisotropy energy, K_{eff}, as a function of grain diameter.

1.6.2.1.3 Saturation magnetization (M_s)

The saturation magnetization of nanoparticle decreases with decrease in particle size. The size dependent saturation magnetizations have been investigated in the literature extensively [92-95]. As the particle size decreases, there is an increase in surface to volume ratio which may lead to reduction in saturation magnetization, remarkably.

The saturation magnetization (M_s) in nano-materials can be expressed by the equation:

$$M_s = M_s\,(\text{Bulk})\ \left(1-\frac{6\,t}{d}\right) \qquad \text{------- (1.6)}$$

Where '*t*' is the thickness of magnetically inactive layer, 'd' is particle diameter and 'M_s' is the saturation magnetization. The thickness (*t*) of the magnetically inactive layer can be calculated by linear fitting of Saturation magnetization plotted against 1/d [91, 92].

The energy of a magnetic particle in an external field is proportional to size or volume via the number of magnetic molecules in a single magnetic domain. When magnetic energy becomes comparable to thermal energy, k_BT, thermal fluctuations of spins significantly reduce the magnetic moment at a given field strength [94]. The decrease in M_s

can also be attributed to spin canting (i.e. non-collinear arrangement of spins at or near the surface of the particle) [95].

1.6.2.1.4 Curie temperature (T_c):-

It is well known that Curie temperature (T_c) decreases with the decrease in size of the particle below a critical size [93]. The decline in the value of Curie temperature may be due to either finite size scaling or surface effects. The finite size scaling theory predicts that the shift in transition temperature from that of the bulk should depend on the particle size of the system as per the following relation.

$$\frac{T_C(\infty)-T_C(d)}{T_C(\infty)} = \left({}^{d}/_{d_0} \right)^{\frac{-1}{\gamma}} \qquad \text{--------- (1.7)}$$

Where, $T_c(d)$ is Curie temperature as a function of particle size 'd', $T_c(\infty)$ is bulk Curie temperature, 'd_0' is a constant, 'γ' is critical exponent of correlation length [90]. The change in 'T_c' may be positive or negative depending upon the boundary conditions, geometry and interaction. The finite size scaling effect is evident in two dimensional systems such as transition metal thin films [96].

It is also possible that decrease in T_c can have its origin from surface effect. For ultrafine particles a significant fraction of particles are on the surface. Since the ratio of surface to bulk atoms in a system is proportional to d^{-1}, such an effect if linearly dependent on specific surface area might also yield a change in Curie temperature (T_c), proportional to d^{-1}. This is mathematically equivalent to eq. (1.7) mentioned above for critical exponent of correlation length, $\gamma = 1$[93, 97].

1.7 Literature survey

Mazumder *et al.* and Ningthoujam *et al.* have reviewed the synthetic methods available for the preparation of transition metal nitrides [9, 45]. K. T. Jacob *et al.* have reported a comprehensive thermodynamic study for the synthesis of nitrides from various precursors like oxides, sulfides and chlorides using nitriding agents like ammonia and hydrazine [98]. B. Vaidhyanathan *et al.* have reported simple microwave assisted combustion procedure for the synthesis of a number of metal nitrides [99]. Synthesis methodologies, structural and magnetic properties of Fe based binary, substituted binaries

and ternary nitrides in the form of nano-structures, thin films and bulk materials have been reported [29, 47, 48]. Lei *et al.* and Song *et al*. have reported solid state metathesis reaction as a synthetic route to metal nitrides [34, 68]. A low-temperature approach to synthesize iron nitride from amorphous iron has been reported [100].

Magnetic properties of nanocrystalline ε-Fe_3N and Co_4N phases synthesized from a new precursor route have been studied by Theerthagiri et al. [101]. Synthesis, structural and magnetic properties of ε-Fe_xN ($2 \leq x \leq 3$) submicron particles and diffusion mechanism of nitrogen atoms have been studied by Minagawa *et al*. [102]. Magnetic and electrical properties of iron nitride films containing both amorphous matrices and nanocrystalline grains have been reported [103]. The effect of cooling procedure on the lattice parameters of hexagonal ε- iron nitride powder has been studied and new relations between lattice parameters and nitrogen content was given [104]. Many theoretical studies are also available on electronic structure of ε-Fe_3N and γ′-Fe_4N nitrides in order to explain the origin of magnetism [105,106]. Effects of substitution of transition metals and rare earth elements (Co, Ni, Mn and Ce, Pr, Nd, Sm, Gd etc.) on magnetic properties of iron nitrides have been extensively studied in the literature [16, 28, 49]. γ′-Fe_4N nanocrystals and epitaxial thin films have been synthesized by DC magnetron sputtering and reactive sputtering [107,108]. There are literature reports on synthesis, magnetic and Mössbauer properties study of Co and Ni substituted ε-Fe_3N and γ′-Fe_4N system [109-113]. Electronic structure and magnetism of nanocrystalline γ′-$Fe_{4-x}Ni_xN$ has been studied by L. Chen [114]. Total energy and electronic structure calculation for γ′-Fe_4N and γ′-$CoFe_3N$ crystal structure have been performed to understand the structural stability and magnetism using first principle computational method [15].

VN has been synthesized using vanadium tetrachloride and urea as nitrogen source [69]. Giordano *et al.* have reported a urea based soft path way at relatively low temperature for synthesis of a number of nitrides and carbides of metals like Ti, V, Nb, Ga, Mo, W and Cr [33]. Glushenkov *et al*. have synthesized VN by temperature programmed ammonia reduction of V_2O_5 and the structural and capacitive properties of VN have been studied [115]. Roldan *et al*. have reported mechanochemical synthesis of VN [116]. Crystalline VN foam has been prepared by Hong *et al.* [117]. Mesoporous VN has been prepared by solid-solid phase separation [118]. High performance super capacitor properties of coaxial TiN-

VN fibers of core shell structures have been reported [119]. VN holds a great promise as anode material for asymmetric supercapacitor due to its large specific capacitance, high electrical conductivity and wide operation window in negative potential [120]. VN supported Pd catalyst exhibited significant catalytic activity for formic acid oxidation [121]. VN nanofiber membrane performs as a highly stable support for Pt catalyzed oxygen reduction reaction with much higher durability [122]. VN catalysts show higher stability under typical hydroprocessing conditions compared to vanadium sulphide [123].

Molybdenum nitride has been prepared via various synthetic routes such as thermal reduction, nitridation of oxide precursor, high pressure synthesis and urea route etc. [56,124-126]. There are reports on selective catalytic activities of molybdenum nitride in various reactions such as hydrogenation of aromatic nitro- compounds and dehydrogenation of aromatic alcohols [127,128]. Cobalt molybdenum nitride has been used as a highly active and stable electrocatalyst for hydrogen evolution reaction [129]. A series of binary and ternary molybdenum nitrides for the catalytic synthesis of ammonia has been compared. The activities in the order Co_3Mo_3N > Fe_3Mo_3N >> Ni_2Mo_3N for ternary nitrides and γ-Mo_2N ~ β-$Mo_2N_{0.78}$ >> δ-MoN for binary nitrides has been found [130]. The catalytic activities of ternary nitrides are found to be much higher than binary nitirides [130]. A nitrogen rich molybdenum nitride, MoN_2 rhombohedral structure has been newly discovered. This nitride adopts a rhombohedral R3m structure isotypic with MoS_2 and exhibits catalytic activities three times more than traditional MoS_2 catalyst for the hydrodesulfurization of dibenzothiophene and more than twice as high in the selectivity to hydrogenation [131].

Synthesis using solid state ion exchange, crystal structure and elastic properties of novel tungsten nitride has been reported by Wang *et al.* [132]. A novel pseudo-morphotactic (shape of the precursor transforms into final product) synthesis route has been reported by Chen *et al.* [133]. Yin *et al.* have reported improved performance for methanol electro-oxidation by adopting tungsten nitride supported Platinum (Pt-WN/C) as catalysts. The tungsten nitride supported Pt catalysts exhibit significantly improved performance towards methanol electrooxidation in acidic aqueous solutions in comparision with other catalysts [134]. Tungsten nitride holds great promise as anode for lithium ion batteries due to its moderately high capacity, good electrical conductivity, high rate cycling performance due to low transport resistance and high lithium ion diffusion coefficient [135, 136]. Villaseca *et al.*

have reported β-W_2N as a promising candidate for electrode materials in electrochemical devices operating in high corrosive environments [137]. Tungsten nitride nanorod arrays grown on carbon cloth act as efficient hydrogen evolution cathode material [138]. The nitrides VN, Mo_2N and W_2N have been successfully used as catalysts for NO reduction with hydrogen [139].

1.8 Gaps in the existing research

Despite the wide range of potential applications, there are not so many ways to prepare metal nitrides in a systematic and scalable fashion, especially as compared to the metal oxides. Some metal nitride systems are indeed very difficult to make. There is still lack of work reporting the synthesis of tailored systems for selective process. One can imagine that this is due to an intrinsic difficulty to prepare these materials in a sustainable way, on the nanoscale and as a pure phase. In order to synthesize nitride nanoparticles with nano-size single domain range with narrow particle size distributions, stabilization of metastable nitride phases and homogeneous distribution of nitrogen in the nitride materials, there is a potential need for developing new synthetic routes. Incorporation of suitable chemical substituents by suitable chemical method may give good technological properties such as high surface area, single domain particles etc. and may be worthy of investigation and is therefore, a gap in existing research.

The materials in nanoscale dimension behave in a different manner than the bulk material. Extensive characterization and study of different properties of these nanomaterials have many useful applications in industrial and technological field. As we are developing new synthetic routes for the aforesaid materials, it may be possible that alteration of size, shape, surface and chemical modifications may result. It would be challenging in order to characterize the nano-materials with advanced techniques for crystal structure and morphology study etc. These will be a new aspect/contribution in the topic while analyzing the characterization results.

Although, studies have been done on magnetic properties of nano-materials (oxide, metal alloys etc.), relatively, fewer studies have been reported on size, shape and surface structure dependence on magnetic parameters for nitride material systems. This is probably due to difficulties in synthesis of materials in well defined nano-structures. In the nanometer scale,

saturation magnetization, coercive field, anisotropy, spin related phenomena etc., can be correlated to materials structure produced by adopting different synthetic methodology and processing techniques. Ternary nitride materials show very interesting magnetic properties in terms of their long range magnetic order. Investigation of substituted binary and ternary transition metal nitrides are mostly unexplored to-date.

The synthesis of nitride materials with high surface area has many potential applications including catalysis and bio-medical applications e.g. drug delivery. It is well known that V, W and Mo based binary and ternary materials show very high surface area. However, the high surface area depends on precursors employed during nitride synthesis along with nitridation parameters. There is an urge for developing high surface area materials with porous structures. Very little research has been done regarding this aspect.

The structure-properties correlation aspects of the above said nitride materials will be of new and interesting applications and the gap is understood.

From the extensive literature survey the following gaps in the existing research have been found.

i. There is lack of research for the synthesis of nitride in nanoscale pure form with controlled shape and size using novel synthesis technique.
ii. Characterization of the nanoscale pure nitride materials merits further investigation for structure dependent property studies.
iii. The excellent magnetic properties of binary, substituted binary and ternary transition metal nitrides are still to be exploited.
iv. The synthesis and surface properties study of high surface area nitride materials for catalytic applications merits further research.
v. The structure property correlation of the nitride materials such as electrochemical property study with surface area is a gap in the existing research in the field of nitrides.

1.9 Aim of the study

Based on the extensive literature survey and existing gaps in the field of research for transition metal nitrides, following objectives will be focused in the current PhD thesis.

1. Synthesis of selected (Fe, Co, Ni based and V, W, Mo, Ti based) binary, substituted binary and ternary transition metal nitrides using novel chemical synthetic routes will be

done. Attempts will be taken for the synthesis of nano-crystalline and high surface area nitride materials for magnetic (Fe, Co, Ni based) and catalytic applications (V, Mo, W, and Ti based). During the synthesis, use of suitable chemicals, e.g. urea etc. and ammonia gas as nitrogen source will be employed. Depending upon the application, suitable chemical substitution will be performed.

2. Exhaustive characterizations will be performed using XRD, SEM, TEM and IR as required. A detailed study on solid state reactivity by XRD, IR investigations and morphology study by electron microscopy will be carried out. So that specific properties can be correlated to specific structures.

3. Fine-particle magnetism will be studied on Fe, Co and Ni based binary and ternary nitrides. The magnetic properties will be correlated to shape, size, morphology, and surface structures. We will attempt to synthesize magnetic materials with altered magnetic characteristics suitable for useful magnetic applications.

4. The nitrogen adsorption and desorption studies of V, Mo, W and Ti based binary and ternary materials will be carried out by BET method. The results will be analyzed with respect to high surface area and varied pore structure. Attempts will be taken in order to correlate the materials structure (which depends upon synthetic methodology) with adsorption parameters.

5. Depending upon materials systems under investigation electrical and electrochemical characterizations will be incorporated in order to explain the structure properties relation on magnetism and adsorption investigations, respectively.

Lay out of the thesis:

Chapter 1 describes general introduction, potential technological applications, crystal structure, common synthesis methods, characterization techniques, surface properties, magnetic phenomena in bulk and nano, literature survey, gaps in the existing research and objectives of the thesis.

Chapter 2 describes various available synthesis methods in detail with emphasis on the synthetic routes adopted in the thesis work. Advanced characterization techniques, sample processing and data interpretation have been presented in this chapter. Brief discussions on

BET and VSM techniques have been given for magnetism and physisorption properties analysis.

Chapter 3 describes magnetic properties of ε-$Co_xFe_{3-x}N$ ($0 \leq x \leq 0.4$) and γ′-$Ni_xFe_{4-x}N$ ($0 \leq x \leq 0.8$) nitride systems. This chapter includes synthesis of the nitride materials, structural characterization of the precursor and the nitrides, solid state reactivity study, electron microscopy study of the synthesized materials, magnetic properties study and analysis of results in correlation to the structure of the synthesized system of nitrides.

Chapter 4 deals with investigation on synthesis, characterization and surface properties study of vanadium nitride materials synthesized using various precursors obtained via alteration of reaction parameters and different nitridation sources. The observed properties of VN materials such as structural and surface properties have been correlated to the precursors, synthesis methods adopted and nitridation routes.

Chapter 5 focuses on synthesis of γ-Mo_2N and γ-$Co_{0.25}Mo_{1.75}N$ using novel synthesis techniques, structural characterization, surface and magnetic property studies. Novel precursor routes have been adopted using reducing agents like hydrazine and borohydride. Organic materials such as: solid urea and ethylene diamine have been used as nitrogen source for nitride synthesis. The reaction pathway and nature of the precursor are correlated to the structural and surface properties of nitride products.

Chapter 6 describes novel synthesis of binary β- W_2N and ternary $CoWN_2$ materials using citric acid assisted sol-gel route for the precursors and urea and ammonia gas as vectors for nitridation of the precursors, respectively. The materials have been characterized using various techniques such as: XRD, SEM, EDX and HRTEM. Surface and magnetic properties of the products have been studied using BET and VSM techniques, respectively.

Chapter 7 summarizes the thesis work with emphasis on the novelty and new findings. The future scope of the present work is also presented in the chapter.

References

1. G. M. Matenoglou, L. E. Koutsokeras, P. Patsalas, Appl. Phys. Lett. **94** (2009) 152108(1-3).

2. J. W. Orton, C. T. Foxon, Rep. Prog. Phys. **61** (1998) 1–75.

3. R. F. Davis, Proc. IEEE. **79** (1991) 702-712.

4. K. Takenaka, H. Takagi, Appl. Phys. Lett. **87** (2005) 261902(1)-(3).

5. A.-H. Lu, E. L. Salabas, F. Schuth, Angew. Chem. Int. Ed. **46** (2007) 1222 – 1244.

6. J. M. Daughton J. Magn. Magn. Mater.**192** (1999) 334-342.

7. A. Costales, M. A. Blanco, A. M. Pendas, A. K. Kandalam, R. Pandey, J. Am. Chem. Soc. **124** (2002) 4116-4123.

8. A. Fiedler, D. Schroder, S. Shaik, H. Schwarz, J. Am. Chem. Soc. **116** (1994)10734-10741.

9. B. Mazumder, A. L. Hector, J. Mater. Chem. **19** (2009) 4673–4686.

10. S. T. Oyama, J. Solid State Chem. **96** (1992) 442-445.

11. J. M. D. Coey, P. A. I. Smith, J. Magn. Magn. Mater. **200** (1999) 405- 424.

12. W. R.L. Lambercht, M. S. Miao, P. Lukashev, J. Appl. Phys. **97**(2005) 10D306(1)-(3).

13. M. Sifkovits, H. Smolinski, S. Hellwig, W. Weber, J. Magn. Magn. Mater. **204** (1999) 191-198.

14. S. F. Matar, J. Alloys Compd. **345** (2002) 72–76.

15. X. G. Ma, J. J. Jiang, P. Liang, J. Wang, Q. Ma, Q. K. Zhang, J. Alloys Compd. **480** (2009) 475–480.

16. H. Sun, J. M. D. Coey, Y Otani, D. P. F. Hurley, J. Phys. Condens. Matter. **2** (1990) 6465-6470.

17. Y. Tanabe, Y. Nishibayashi, Coord. Chem. Review. **257** (2012) 2551-2564.

18. J. S. J. Hargreaves, Appl. Petrochem. Research **4** (2014)3-10.

19. R. Kojima, K. Aika, Appl. Catal. A Gen. **215** (2001)149-160.

20. C. J. H. Jacobson, Chem. Commun. **12** (2000) 1057-1058.

21. R. B. Levy, M. Boudart, Science. **181** (1973)547-549.

22. S. T. Oyama, J. Solid State Chem. **96** (1992) 442-445.

23. M. S. Balogun, W. Qiu, W. Wang, P. Fang, X. Lu, Y. Tong, J. Mater. Chem. A **3** (2015) 1364–1387.

24. N.S. Gajbhiye, R. S. Ningthoujam, Mater. Res. Bull. **41** (2006) 1612–1621.

25. M. Yang, M. J. MacLeod, F. Tessier, F. J. Disalvo, J. Am. Ceram. Soc. **95** (2012) 3084–3089.

26. L. Toth, Refractory materials, A series of monograph, Academic Press, Newyork and London, volume 7, pp: 1-28.

27. E. Z. Fratczak, J. E. Prieto, M. E. Moneta, J. Alloys Compd. **586** (2014) 375-379.

28. S. F. Matar, G. Demazeau, B. Siberchicot, IEEE Trans. Magn. **26** (1990) 60-62.

29. R. N. Panda, N. S. Gajbhiye, Magnetics, IEEE Trans. Magn. **34** (1998) 542-548.

30. S. Kamiyama, K. Okamoto, T. Oyama, Energy Convers. Manage. **43** (2002) 281-287.

31. R. Loloee, J. Appl. Phys. **112** (2012) 023902(1)-(6).

32. S. Ramanathan, S. T. Oyama, J. Phys. Chem. **99** (1995)16365-16372.

33. C. Giordano, M. Antonietti, Nano Today. **6** (2011)366-380.

34. B. Song, X. Chen, J. Han, J. Jian,W. Wang, H. Zuo, X. Zhang, S. Meng, Inorg. Chem. **48** (2009) 10519–10527.

35. L. Wang, Q. Xin, Y. Zhao, G. Zhang, J. Dong, W. Gong, H. Guo, ChemCatChem. **4** (2012) 624-627.

36. F. Cardenas-Lizana, D. Lamey, N. Perret, S. Gomez-Quero, L. Kiwi-Minsker, M. A. Keane, Catal. Commun. **21** (2012) 46–51.

37. S. Kaskel, K. Schlichte, T. Kratzke, J. Mol. Catal. A: Chem. **208** (2004) 291–298.

38. W. F. Chen, J. T. Muckerman, E. Fujita, Chem. Commun. **49** (2013) 8896-8909.

39. Y. Y. Hua, H. P. Xian, D. Shanmu, Z. KeJun, Z. Chuanjian, S. C. Qun, C. G. Lei. Chin. Sci. Bull. **57** (2012) 4111-4118.

40. J. A. J. Rodrigues, G. M. Cruz, G. Bugli, M. Boudart, G. Djega-Mariadassou, Catal. Lett. **45** (1997) 1-3

41. C. H. Cheng, M. T. Nguyen, T. S. Leu, I. L. Chang, M. L. Liao, S. V. Panin, A. V. Panin Journal of Applied Mathematics, 2015, Article ID 238730,1- 9.

42. K. V. Chauhan, S. K. Rawal, Procedia Technology, **14** (2014) 430 – 437.

43. I. Jauberteau , A. Bessaudou , R. Mayet , J. Cornette, J. L. Jauberteau , P. Carles, T. Merle- Méjean, Coatings. **5** (2015) 656-687.

44. G. Hägg, Z. Phys. Chem. B. **12** (1931) 33−56

45. R. S. Ningthoujam, N. S. Gajbhiye, Prog. Mater Sci. **70** (2015) 50–154.

46. K. H. Jack, Proc. R. Soc. A. **208** (1951) 200.

47. S. Bhattacharyya, J. Phys. Chem. C. **119** (2015) 1601−1622.

48. N. S. Gajbhiye, R. N. Panda, R. S. Ningthoujam, S. Bhattacharya, Phys. Stat. Sol. (c). **1**(2004) 3252-3259.

49. D. Xue, F. Li, J. Yang, Y. Kong, M. Gao, J. Magn. Magn. Mater. **172** (1997) 165-172,

50. D. Andrimandroso, L. Fefilatiev, G. Demazeau, L. Fournes, M. Pouchard, Mater. Res. Bull. **19** (1984) 1187–1194.

51. B. Siberchicot, S. F Matar, L. Fournes, G. Demazeau, P. Hagenmuller, J. Solid State Chem. **84** (1990) 10–15.

52. K. H. Jack, Acta Cryst. **5** (1952)404

53. R. S. Ningthoujam, S. Bhattacharyya, Hyperfine Interact **164** (2005) 17–26.

54. J. G. Chen, Chem. Rev. **96 (**1996)1477-1498.

55. H. Jehn, P. Ettamayer, J. Less-Common Met. **58**(1978) 85-98.

56. V. Tagliazucca, M. Leoni, C. Weidenthaler, Phys. Chem. Chem. Phys. **16** (2014) 6182—6188.

57. R. A. Fischer, H. Parala, Metal-organic Chemical Vapour Deposition of Refractory Transition Metal Nitrides, in: A. C. Jones, M. L. Hitchman (Eds.), Chemical Vapour Deposition: Precursors, Processes and Applications, Royal Society of Chemistry, 2009, pp 414-450.

58. D. V. Suetin, I. R. Shein, A. L. Ivanovskii, J. Struct. Chem. **51**(2010) 199-203.

59. R. Niewa, F. J. Disalvo, Chem. Mater. **10** (1998) 2733-2752.

60. E. Enriquez, Y. Zhang, A. Chen, Z. Bi, Y. Wang, E. Fu, Z. Harrell, X. Lu, P. Dowden, H. Wang, C. Chen, Q. Jia, Appl. Phys. Lett. **109** (2016) 081907(1-5).

61. L. Volpe, M. Boudart, J. Solid State Chem. **59** (1985) 332-347.

62. A. Gomathi, Mater. Res. Bull. **42** (2007) 870-874.

63. J. Choi, E. G. Gillan, Inorg. Chem. **48** (2009) 4470-4477.

64. I. P. Parkin, G. S. Elwin, J. Mater. Chem. **11**(2001) 3120- 3124.

65. J. Pak, W. Lin, K. Wang, A. Chincore, M. Shi, D.C. Ingram, A.R. Smith, K. Sun, J. M. Lucy, A. J. Hauser, F.Y. Yang, J. Vac. Sci. Technol. A. **28** (2010) 536-540.

66. J. C. Caicedo, G. Zambrano, W. Aperador, L. Escobar-Alarcon, E. camps, Appl. Surf. Sci. **258** (2011) 312-320.

67. J. B. Claridge, A. P. E. York, A. J. Brungs, M. L. H. Green, Chem. Mater. **12** (2000) 132-142.

68. L. Lei, W. Yin, X. Jiang, S. Lin, D. He, Inorg. Chem. **52** (2013) 13356−13362.

69. R. Marchand, F. Tessiera, F. J. DiSalvo, J. Mater. Chem. **9** (1999) 297–304.

70. H. -M. Lee, G. H. Jeong, S. -W. Kim, C.-K. Kim, Appl. Surf. Sci. **400** (2017) 194–199.

71. Y. Qiu, L.Gao, J. Am. Ceram. Soc. **87** (2004)352-357.

72. J. W. Robinson, 'Atomic Absorption Spectroscopy' Report for analytical chemists. **32** (1960)17-29.

73. J. I. Goldstein, C.E. Lyman, D. E. Newbury, E. Lifshin, P. Echlin, L. Sawyer, D. C. Joy, J. R. Michael, Scanning electron microscopy and X-ray microanalysis : Third edition,2003, Springer science & Business media, 2012, pp.1-20

74. A. K. Cheetham, P. Day, Solid-State Chemistry : Techniques, Oxford University press,1987,pp72-74.

75. S. Utsunomiya, R. C. E Wing, Environ. Sci. Technol. **37** (2003) 786-791.

76. A. Dabrowski, Adv. Colloid Interface Sci. **93** (2001) 135-224.

77. J. C. Groen, L. A. A. Peffer, J. Perez-Ramirez, Microporous Mesoporous Mater. **60** (2003) 1–17.

78. K. S. W. Sing, D. H. Everett, R. A. W. Haul, L. Moscou, R. A. Pierotti, J. Rouquerol, T. Siemieniewska, Pure & Appl. Chem. **57** (1985) 603 - 619.

79. C. Kittel, Introduction to solid state physics, wiley edition, pp.417-440.

80. C. M. Hurd, Contemp. Phys. **23** (1982) 469-493.

81. U. Ozgur, Y. Alivov, H. Morkoc, J Mater Sci: Mater Electron. **20** (2009)789–834.

82. C. Wu, P. Yin, X. Zhu, C. O. Yang, Y. Xie, J. Phys. Chem. B, **110** (2006)17806-17812.

83. Z. M. Yuan, B. Liu, T. Zhou, C. K. Goh, C. L. Ong, C. M. Cheong, L. Wang, IEEE Trans. Magn. **45** (2009) 5038-5043.

84. Y. Ce, H. Yang-Long, G. Song, Chin. Phys. B **23** (2014) 057505 (1-8).

85. C. Kittel, Physical review. **70** (1946) 965-971.

86. J. L. Morin-Lopez, K. H. Bennemann, Phys. Rev. B. **23** (1981) 5978-5981.

87. M. Bailyn, Phys. Rev. **139**(1965) A1905-A1919.

88. D. J. Sellmyer, M. Zheng, R Skomski, J. Phys.: Condens. Matter. **13** (2001) R433–R460.

89. T. Moriya, J. Magn. Magn. Mater**. 100**(1991) 261-271.

90. F. E. Luborsky, J. Appl. Phys. **32**(1961)171S-183S.

91. G. Herzer, IEEE Trans. Magn. **25** (1989)3327-3329.

92. C. Liu, Z. J. Zhang, Chem. Mater., **13(**2001**)** 2092-2096.

93. J. P. Chen, C. M. Sorensen, K. J. Klabunde, G. C. Hadjipanayis, E. Devlin, A. Kostikas, Phys. Rev. B **54** (1996) 9288-9296.

94. K. V. P. M. Shafi, A. Gedanken, R. Prozorov, J. Balogh, Chem. Mater. **10** (1998) 3445-3450.

95. K. Haneda, A. H. Morrish, J. Appl. Phys. **63** (1988) 4258

96. F. Huang, G. L. Mankey, M. T. Kief, R. F. Willis, J. Appl. Phys. **73** (1993) 6760-6762.

97. Z. X. Tang, J. P. Chen, C. M. Sorensen, K. J. Klabunde, and G. C. Hadjipanayis, Phys. Rev. Lett. **68** (1992) 3114

98. K.T. Jacob, R. Verma, R. M. Mallya, J. Mater. Sci. **37** (2002) 4465-4472.

99. B. Vaidhyanathan, D. K. Agrawal, R. Roy, J. Mater. Res. **15(**2000) 974-981.

100. Y. Han, H. Wang, M. Zhang, M. Su,W. Li, K. Tao, Inorg. Chem. **47** (2008)1261-1263.

101. J. Theerthagiri, S. B. Dalavi, M. Manivel Raja, R. N. Panda, Mater. Res. Bull. **48** (2013) 4444–4448.

102. M. Minagawa, H. Yangihara, M. Kishimota, E. Kita, Material Transactions. **51** (2010) 2173-2176

103. H. Naganuma, R. Nakatani, Y. Endo, Y. Kawamura, M. Yamamoto, Sci. Technol. Adv. Mater. **5** (2004)101-106.

104. T. Liapina, A. Leineweber, E. J. Mittemijer, W. Kockelmann, Acta Mater. **52** (2004) 173-180.

105. S. Matar, B. Siberchicot, M. Pénicaud, G. Demazeau, J. Phys. I France. **2** (1992) 1819-1831.

106. V. F. Hlynsson, E. Skulason, A.L. Garden, J. Alloys Compd. **603** (2014) 172–179.

107. W. B. Mi, Z. B. Guo, X. P. Feng , H. L. Bai, Acta Mater. **61** (2013) 6387–6395.

108. L. L. Wang, X. Wang, W. T. Zheng, N. Ma, Q. F. Guan, J. Zhao, Y. Chen, S. H. Feng, Mater. Chem. Phys. **100** (2006)304-307.

109. N. S. Gajbhiye, R. S. Ningthoujam, J. Weissmuller, Hyperfine Interact. **156/157**(2004) 51-56.

110. N. S. Gajbhiye, S. Bhattacharya, Indian J. Pure Appl. Phys. **45** (2007)834-838.

111. R. N. Panda, N. S. Gajbhiye, J. Magn. Magn. Mater.**195** (1999)396-405.

112. F. Li, J. Yang, D. Xue, R. Zhou, Appl. Phys. Lett. **66** (1995) 2343-2345.

113. X. G. Diao, R. B. Scorzelli, H. R. Rechenberg, J. Magn. Magn. Mater. **218**(2000)81-90.

114. L. Chen, J. Magn. Magn. Mater.**303** (2006)266-269.

115. A. M. Glushenkov, D. Hulicova-Jurcakova, D. Llewellyn, G. Q. Lu, Y. Chen, Chem. Mater. **22** (2010) 914–921.

116. M. A. Roldan, V. López-Flores, M. D. Alcala, A. Ortega, C. Real, J. Eur. Ceram. Soc. **30** (2010) 2099–2107.

117. Y. C. Hong, H. S. Uhm, Scripta Mater. **59** (2008) 262–264.

118. M. Yang, W. T. Ralston, F. Tessier, A. J. Allen, F. J. DiSalvo, J. Solid State Chem. **197** (2013) 398–401.

119. X. Zhou, C. Shang, L. Gu, S. Dong, X. Chen, P. Han, L. Li, J. Yao, Z. Liu, H. Xu, Y. Zhu, G. Cui, ACS Appl. Mater. Interfaces. **3** (2011) 3058–3063.

120. X. Lu, M. Yu, T. Zhai, G. Wang, S. Xie, T. Liu, C. Liang, Nano Lett. **13** (2013) 2628−2633.

121. M. Yang, Z. Cui, F. J. Disalvo, Chem. Commun. **48** (2012) 10502-10504.

122. N. Y. Kim , J. H. Lee, J. A. Kwon, S. J. Yoo, J. H. Jang, H. J. Kim, D. H. Lim, J. Y. Kim, Journal of Industrial and Engineering Chemistry. **46** (2017) 298–303.

123. P. Rodriguez, J. L. Brito, A. Albornoz, M. Labadi, C. Pfaff, S. Marrero, D. Moronta, P. Betancourt, Catal. Commun. **5** (2004) 79–82.

124. J. Ma, Y. Du, J. Alloys Compd. **463** (2008) 196–199.

125. T. Kawashima, E. Takayama-Muromachi , P. F. McMillan, Physica C. **460–462** (2007) 651–652.

126. A. Gomathi, A. Sundaresan, C. N. R. Rao, J. Solid State Chem. **180** (2007) 291–295.

127. F. Cárdenas-Lizana, D. Lamey, S. Gómez-Quero, N. Perret, Catal. Today**. 173** (2011) 53– 61.

128. Z. Li, C. Chen, E. Zhan, N. Ta, W. Shen, Catal. Commun. **51** (2014) 58–62.

129. B. Cao, G. M. Veith, J. C. Neuefeind, R. R. Adzic, P. G. Khalifah, J. Am. Chem. Soc.**135** (2013)19186−19192.

130. D. Mckay, J. S. J. Hargreaves, J. L. Rico, J. L. Rivera, X.-L. Sun, J. Solid State Chem. **181** (2008) 325–333.

131. S. Wang, H. Ge, S. Sun, J. Zhang, F. Liu, X. Wen, X. Yu, L. Wang, Y. Zhang, H. Xu, J. C. Neuefeind, Z. Qin, C. Chen, C. Jin, Y. Li, D. He, Y. Zhao, J. Am. Chem. Soc. **137** (2015)4815−4822.

132. S. Wang, X. Yu, Z. Lin, R. Zhang, D. He, J. Qin, J. Zhu, J. Han, L. Wang, H. -K. Mao, J. Zhang, Y. Zhao, Chem. Mater. **24** (2012) 3023−3028.

133. D. Chen, H. Wen, T. Li, L. Yin , B. Fan, H. Wang , R. Zhang, X. Li , H. Xu , H. Lu, D. Yang, J. Sun, L. Gao, J. Solid State Chem.**184** (2011) 455–462.

134. S. Yin, L. Yang, L. Luo, F. Huang, Y. Qiang, New J. Chem. **37** (2013) 3976 -3980.

135. M. Zhang, Y. Qiu, Y. Han, Y. Guo, F. Cheng, J. Power Sources. **322** (2016) 163-168.

136. H. -C. Park, S. -J. Kim, M. -C. Kim, D. -M. Kim, K. -W. Park, Ceram. Int. **42** (2016)1933–1942.

137. L. Villaseca, B. Moreno, I. Lorite, J. R. Jurado, E. Chinarro, Ceram. Int. **41** (2015)4282–4288.

138. J. Shi , Z. Pu , Q. Liu , A. M. Asiri , J. Hu, X. Sun, Electrochim. Acta **154** (2015) 345–351.

139. C. Shi, A. M. Zhu, X. F. Yang, C. T. Au, Appllied catalysis A: General. **276**(2004) 223- 230.

Chapter 2

Materials and Methods

The current chapter presents various synthesis methods adopted in this thesis for nitride materials production. Also, advanced characterization techniques, basic principles, sample processing, sampling, data procurements and analytical methods for their interpretation have been presented.

2.1 Synthesis methods

A significant progress in the field of nitride chemistry has been observed in recent times leading to development of new synthetic approaches for nitrides. Synthesis of nitride materials is still difficult and complex because of the large thermodynamic barrier majorly due to lower decomposition temperature of the products [1]. Many of the nitrides especially those containing s-block elements, are sensitive to air and moisture and rapidly form oxides, hydroxides and ammonia upon contact with oxygen or moisture [1, 2]. These factors are responsible for low abundance of nitrides compared to oxides. The slow development of nitride chemistry compared to metal oxides can also be attributed to limited synthetic routes available. However, several methods are known in the literature and have been adopted for synthesis of metal nitrides and are mentioned as follows [1, 3-8].

(i) Passing of N_2(g) over metal powder/ film [1,3],
(ii) Passing of NH_3(g) over metal powder/ film/oxide/ halide/ sulphide [3,4],
(iii) Chemical vapour deposition method to form thin films of nitride [5],
(iv) Magnetron sputtering method to form coatings and films [6],
(v) Molecular beam epitaxy method to produce nanowires and interfaces [7],
(vi) Other methods include metathesis reaction (alkali, alkaline earth metal nitrides), solvothermal process, metal azide precursor, sol-gel processing etc.[1,3,8].

The direct route for the formation of nitride by the nitridation of elements using N_2(g) is limited due to the great strength of triple bond in dinitrogen molecule. Very often the nitridation process takes place at elevated temperatures. This means that only highly

thermally stable nitrides can be formed by this route [1]. Elemental combination often leaves metal impurity in the nitride. In part, this is because of restriction in N atom diffusion inside the metal or alloy lattices. This results in non-homogeneity in nitrogen atom distribution in the nitride product and often leaves metallic impurity. Further support comes from the fact that crystallite size is not restricted due to low temperature sintering of nitrides because the metal itself normally sinters readily at the reaction temperature by this process [4]. In the physical methods like vapour deposition [5], sputtering [7] and molecular beam epitaxy [7] etc., it is difficult to control the shape and size of the products [9]. It has been noted that synthesis of nitride using high temperature has a negative effect on the properties (e.g. magnetic, optical, mechanical etc.) of the final product [10]. In this regard, wet chemical methods are very useful in tuning the shape and size dependent properties of the product sample using novel precursor techniques feasible at relatively lower temperatures. Many physical and chemical properties like magnetic and electronic properties strongly depend upon the size, shape and structure of the materials. For example, magnetic properties of metal oxide nano structures can transform from ferro/ferri magnetic to superparamagnetic with reduction of size. In this regard, nano-scale design and process of synthesis can tune the size dependent properties of the products in an effective way. Similarly, the electronic properties also differ significantly with size. In case of semiconductors, the alteration of band gap is observed when the crystallite size is in the order of de Broglie wavelength of electrons (i.e. $\lambda = 1.23$ nm) [11]. In this thesis, a two step synthetic strategy was adopted for the synthesis of transition metal nitrides, (i) the first step being synthesis of precursor, while (ii) the later involves nitridation of the precursor. This novel synthesis techniques adopted are described in the below mentioned sub-sections.

2.1.1 Synthesis of precursor

2.1.1.1 Sol-gel method

Sol-gel methods are very useful for synthesis of oxide powder in nanocrystalline form. The basis of sol-gel routes rely on hydrolysis and condensation reactions between metal alkoxide and small amount of water in organic solvents. In this process, the breakage of a metal- oxygen bond is the rate limiting step, resulting in different kinetics for different metals involved in the form of metal alkoxides. The condensation results in the formation of

a sol, which transforms into a gel as the polymerization proceeds [12, 13]. Based on the above mentioned points, materials synthesis using sol-gel methods involve the following four steps:

STEP I: Preparation of colloidal solution of alkoxide species containing metal ions.

STEP II: Hydrolysis of alkoxide or nitrate precursors.

STEP III: Polycondensation of hydrolyzed products resulting in the formation of viscous gel with ease removal of simple molecules (Say solvent).

STEP IV: Materials processing of the 'gel' involving drying and/or heat treatment.

One further step modification has been done in our study involving sol-gel process. We have adopted citric acid assisted sol-gel method in our synthesis. In this method stoichiometric amount of the reagents in solution form are mixed with citric acid to form a homogeneous solution of metal(s) citrate complex. Next, the solution is refluxed for few hours and slowly evaporated below 100℃ to produce a xero-gel. The resulting gel is generally calcined about 300-500℃ for a duration of 1-3 hrs in order to produce a solid powder. The powder is ground well with the help of mortar and pestle and used as precursor for the nitridation reactions [10, 14, 15].

2.1.1.2 Co-precipitation method

Co-precipitation is an effective way to produce nanoparticles having homogeneous distribution of the constituent metal ions. In this method, compounds of metals are gradually precipitated from solution containing metal ions which were mixed together in an atomic scale. The precipitated solid is filtered out and calcined. Because of the high degree of homogenization, a lower formation temperature can be achieved by this technique. The method does not work well where (a) two reactants have very different solubility in solvent (say water) (b) the reactants do not precipitate at same rate (c) super saturated solutions occur[16, 17]. Although, it is very convenient method for materials synthesis and widely used for several systems, it is often not suitable for the preparation of highly pure and stoichiometric phases in certain complex materials systems involving more than one metal ion [16]. In addition to the above mentioned difficulties, synthesis of nano-structures with controlled shape and size is challenging. In the study, we have tried to stabilize newer synthesis routes by using various precipitation techniques. The methodology adopted involves the use of hydrazine ($NH_2NH_2 \cdot H_2O$) and borohydride ($-BH_4^-$) as reducing agents

for precipitation of metal ions from the metal complex solutions. The experimental details of the methods are described in the below mentioned sub-sections.

2.1.1.3 Borohydride reduction route

Over the past few years borohydride reduction of metal ions (M^{n+}) has been used extensively for production of metallic nano particles. In recent years its use has been extended for the synthesis of magnetic nano particles in oxide form with reduced oxidation states of the involved metal ions. Concentration, BH_4^-/ M^{n+} ion ratios, pH, method of mixing and rate of mixing can determine particle size and reactivity leading to product quality [18].

We have used potassium borohydride (KBH_4) as reducing agent to precipitate out the metal ions from a solution. Then the precipitate is collected, washed using ethanol and/ or ammonia water and distilled water, then dried well. The resulting solid is subjected to heat treatment under inert gas atmosphere or in air atmosphere, resulting solid precursors suitable for nitridation experiments [19, 20].

2.1.1.4 Other precursor methods: Use of metal and organic/inorganic chelator

(a) Vanadium oxide precursor method

Citrate is a natural chelator having active carboxylate ($-COO^-$) functionalities. Due to this reason it extends chemical reactivity towards a number of metal ions, such as: calcium, magnesium, vanadium, zinc and nickel. Among various metal ions, V^{6+} is a suitable target with regard to the complex formation capabilities with citrate chelator [21, 22]. In this method, a solution containing V^{6+} ions is taken, mixed with citric acid solution and refluxed at lower temperatures (less than or equal to 80℃ for 4h) in order to yield a vanadium citrate complex gel. After evaporating the liquid, the solid product is isolated, dried and calcined at various temperatures to produce vanadium oxide (V_2O_5) precursors which are used for subsequent nitridation reactions. In several cases, the as prepared solid precursors are heat treated at various temperatures in order to have new precursors for nitridation. As the structure of the precursor in solid state is sensitive towards nitridation, designing of the metal-citrate precursors and stabilizing for product formation have been attempted in this study.

(b) Ethylenediamine route

Ethylenediamine ($C_2H_4(NH_2)_2$) contains two amine groups and is capable of acting as chelating ligand. Ethylenediamine can be used to form complexes with the metal ions with ease. The resulting solid complex is used as precursor for the nitridation experiment directly, leading to corresponding metal nitride. The molar ratios of metal ions and ethylene diamine molecules in solution play a crucial role in controlling phase composition and nanostructured nature of the final products [23].

2.1.2 Nitridation of the precursors

(I) Nitridation of the precursors using ammonia (NH_3(g)) as nitridation source

The ammonolysis of oxides is one of the commonest routes for the synthesis of nanocrystalline and high surface area nitrides. Volpe and Boudart developed temperature programmed ammonolysis, which involves heating the metal oxide in a furnace through a temperature controlled reaction with NH_3(g) as the reactant gas [24]. In this process often a topotactic relationship between the reactants and the products exist and the product can be pseudomorphic with the reactant, i.e. crystallographic orientations and particle size and geometry of the reactants are retained in the product. The replacement of oxygen atoms by nitrogen during this transformation can also generate porous, lower density nitride materials [4]. Many literatures have reported synthesis of nitrides using this method [25-27]. Depending upon N content (i.e. z) in the nitride materials, different phases (stable and metastable) can be synthesized.

(II) Nitridation of the precursors using solid urea (NH_2CONH_2) as nitridation source

Use of nitrogen containing compounds instead of gaseous ammonia as nitrogen source, has already been known in the literature [22, 28, 29]. Urea ($(NH_2)_2CO$) can form metal–urea complex in the form of gel [29, 30]. The gel can be isolated as solid state precursors by simple materials processing techniques, such as washing with suitable solvent, drying in air/inert gas at room temperature or moderate temperature. The resulting gel is subjected to heat treatment using nitrogen/argon gas atmosphere in order to produce nano-structured nitrides/carbides at relatively lower temperature. In this procedure, urea acts as

stabilizing agent (necessary for the nanoparticle dispersion) in addition to its role as nitrogen source [3, 30, 31].

2.1.2.1 Solid-gas nitridation reactor

Two different reactors for nitridation of the precursors were used. The former was used for nitridation using gaseous ammonia while the later for nitridation using urea under nitrogen gas flow. In nitridation reactions using ammonia, samples were suspended vertically inside the quartz reactor tube. On the contrary, while carrying out the nitridation reactions using solid urea as nitridation source horizontal gas flow reactor was employed. The details of the experimental procedure have been described in the following sub-sections.

2.1.2.1.1 Nitridation using gaseous ammonia:

The typical sketch of the nitridation reactor, used for the nitridation using ammonia gas in order to synthesize nitride material is shown in figure 2.1. The reactor employs ammonia gas, which passes through a vertical quartz glass tube of 1cm diameter (inner). The flow of the gas is controlled by a flow controller. The precursor powder is suspended in the middle of the quartz tube with the help of a porous quartz wool plug, which allows passage of NH_3(g) through the solid (precursor). The vertical alignment of the reactor facilitates homogeneous distribution of NH_3(g) through the precursor powder which leads to pure product phase with better materials quality. Furnace controller is programmed to heat the precursor in different heating regimes and time intervals. The gas from the outlet is ventilated to the fumehood. The nature and quality of the product can be controlled by adjustment of reaction conditions; such as: precursor concentration, heating and cooling ramps, final holding temperature and time etc. [32].

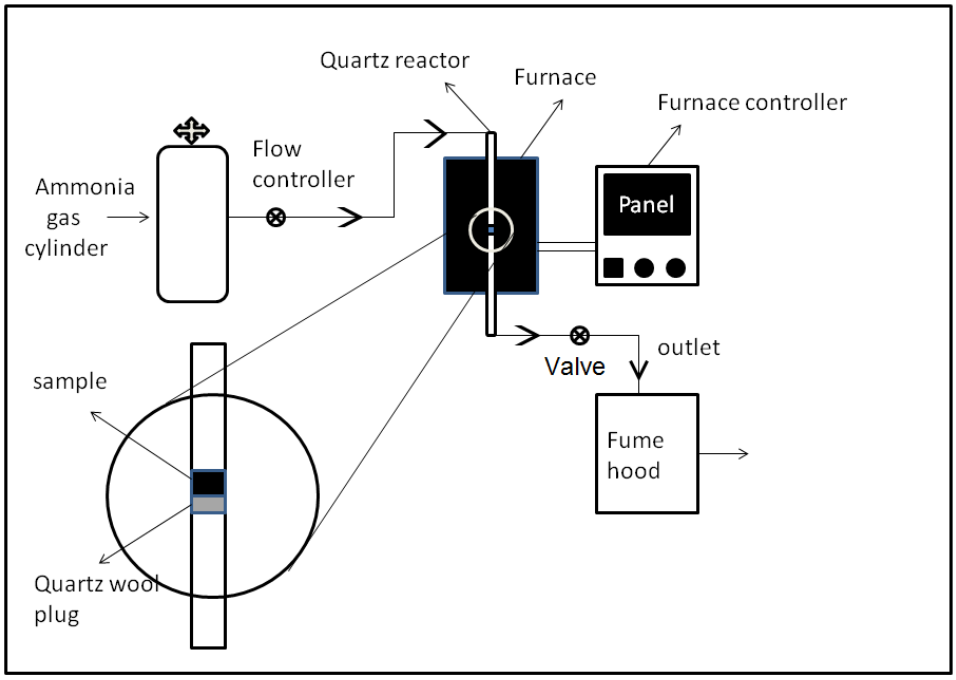

Figure 2.1 Schematic block diagram of vertical nitridation reactor. Enlarged view of the sample chamber is shown for clarity reason.

2.1.2.1.2 Nitridation using solid urea in N_2 (g) atmosphere

The solid-gas reactor is used for nitridation of solid state precursors using urea as nitrogen source in presence of N_2(g) gas flow atmosphere. Typical sketch of the nitridation reactor in order to synthesize nitride material is shown figure 2.2. A quartz tube of 10cm inner diameter is placed horizontally inside the furnace, which in turn connected with N_2 (g) inlet and outlet. The precursor material (about 1gm) is placed in an alumina boat placed horizontally inside towards the middle of the reactor tube. N_2(g) enters through the reactor tube, passes over the solid precursor material and comes out through the outlet. This arrangement allows the final product to cool down under the flow of N_2(g) until the furnace is cooled down to room temperature (298K).

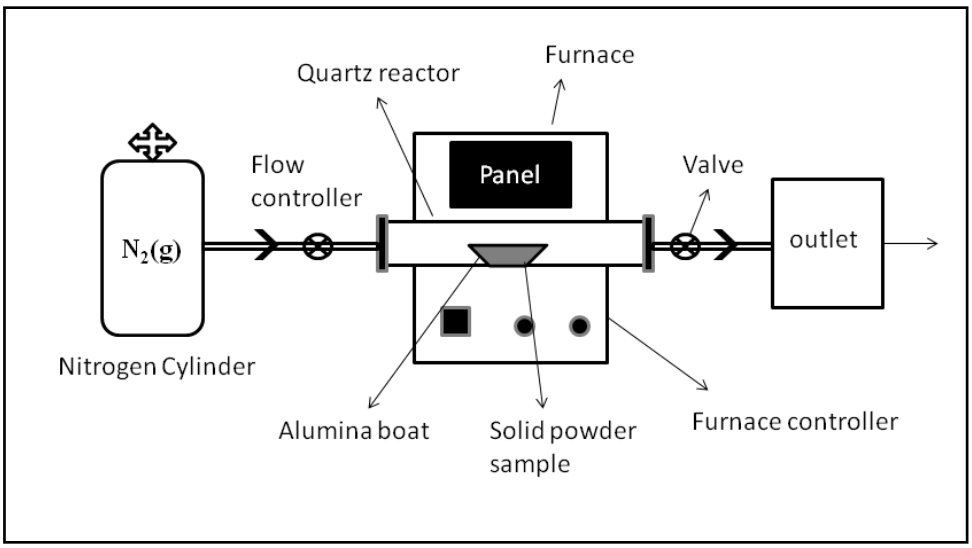

Figure 2.2 Schematic block diagram of horizontal nitridation reactor.

2.2 Elemental analysis

The synthesized nitride products were analyzed using different advanced instrumental techniques to determine their composition. These methods are summarized below.

2.2.1 Atomic absorption spectroscopy (AAS)

Atomic absorption spectroscopy (AAS) is an analytical tool for spectrophotometric determination of elements present in materials. The technique uses quantitative spectrophotometric absorption of optical radiation through free gaseous atoms. This technique can detect trace elements in the level of parts per million (ppm). The analytical application is based on the fact that metal atoms absorb radiation strongly at discrete and characteristic wave lengths which coincide with the emission spectra lines of the particular metal. Atomic absorption spectroscopy quantifies the absorption of ground state atoms in the gaseous state. Atoms absorb ultraviolet or visible light and make a transition to higher electronic state. The concentration of analyte is determined from the amount of absorption [33].

For analysis of the sample, it should be atomized. Various atomizers used are flames and electro thermal atomizers. The atoms should then be irradiated by optical radiation, and the radiation source could be either an element-specific line radiation source or a continuum

radiation source. The radiation then passes through a monochromator in order to separate the element-specific radiation from any other radiation emitted by the radiation source, which is finally measured by a detector [34]. The block diagram of the instrumental setup is given below in figure 2.3.

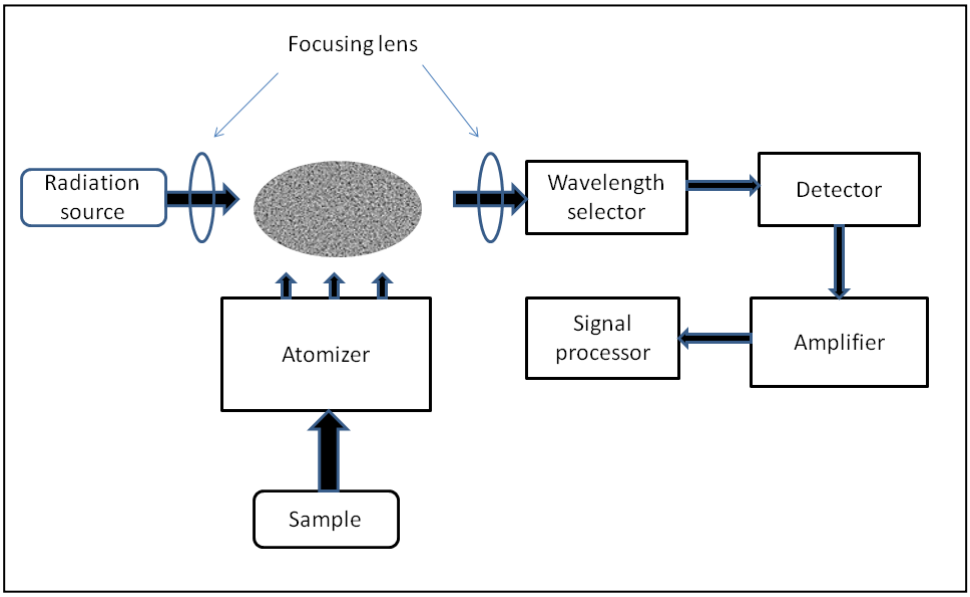

Figure 2.3 Block diagram illustrating experimental set up of atomic absorption spectroscope (AAS).

Sample preparation for atomic absorption spectroscopy study was done by chemical digestion methodology. In summary, 10 mg of the given sample was digested in dil. HCl and heated at 40^{o}C for about 4 hrs on a hot plate. 10 mg of this sample (the final solution after drying) was taken into a 10 ml standard flask and made up to 10 ml using H_2O to prepare a solution of strength 1000 ppm. 1 ml of 1000 ppm solution is taken into a 10 ml vol. flask and diluted with 9 ml H_2O to prepare 100 ppm solution. This 100 ppm solution was used as stock solution and diluted further in order to prepare solutions of strengths as low as 0.5 – 5 ppm (as the range of AAS instrument is from 0.5 ppm – 2 ppm).

2.2.2 Energy dispersive X-ray (EDX)

Energy dispersive X-ray (EDX) is an analytical technique for analysis of trace elements present in the solid sample. The number and energy of the X-rays emitted from a specimen can be measured by an energy-dispersive spectrometer. As the energies of the X-rays are characteristic of the difference in energy between the two shells and of the atomic structure

of the emitting element, EDX allows the elemental composition of the specimen to be measured. This EDX setup is attached with a scanning electron microscope, capable of doing raster scan of the sample to be studied. The focusing electron beam sweeps across the surface area of the specimen in a raster. In a SEM, the detector is placed near the specimen in the line of sight to detect the emitted X-rays from that [35].

The instrumental setup consists of (1) excitation source, (2) X-ray detector, (3) pulse processor and (4) analyzer. A detector is used to convert X-ray energy into voltage signal and the information is sent to pulse processor. The processor measures the signal and passes them to the analyzer for data analysis and display of spectrum [36]. In the EDX spectrum, characteristic peaks corresponding to all the elements are observed. For example, a typical EDX analysis of iron nitride (Fe-N) sample can show characteristic peaks due to elemental Fe and N at peak positions corresponding to 6.39 keV and 0.392 keV, respectively. By analyzing the integrated area of the peaks corresponding to Fe and N, one can estimate the elemental compositions of the materials.

2.3 Characterization

The characterization techniques employed in this thesis in order to probe the materials structure and properties are summarized in the following sub-sections.

2.3.1 Powder X-ray diffraction

X-ray diffraction is used to obtain structural information about crystalline solids. This is a major characterization tool for ascertaining phase purity, structural parameters, nano-size effects etc. in solid-state materials. The various aspects of the technique are described in the following sub-sections.

2.3.1.1 Basic principle

Crystals are considered as regular array of atoms and this can be used as a diffraction grating to diffract the X-ray beam. X-ray is used to produce the diffraction pattern because its wavelength 'λ' is typically the same order of magnitude (1 Å –100 Å) as the spacing *d* between planes in the crystal. Constructive interferences of two parallel X-ray beams have been shown in figure 2.4.

X-ray diffraction works on Bragg's law.

$$n\lambda = 2\,d \sin\theta \qquad \text{---------} \quad (2.1)$$

Where n = an integer, it refers to the order of the reflection. For first order reflection n=1,

λ = radiation wavelength, d =inter planar distance, θ = angle of incidence [37].

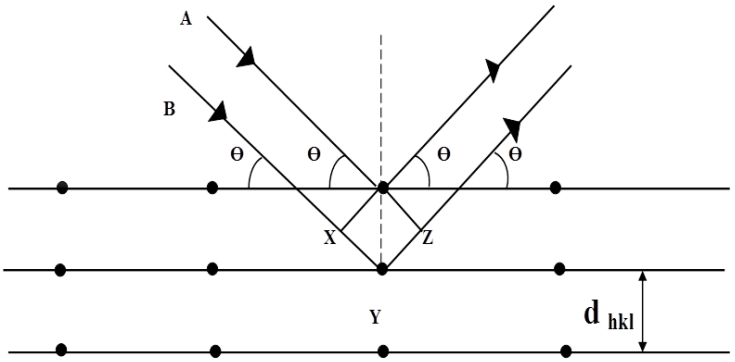

Figure 2.4 Representation of constructive interference of two parallel X-ray beams A and B, subjected to condition, when the path difference is a multiple of wavelength, λ.

2.3.1.2 Powder X-ray diffractometer

The block diagram of powder X-ray diffractometer is shown in figure 2.5 [16]. The major components of the X-ray tube are labeled as; (a) a source of electrons, (b) high accelerating voltage, (c) a metal target and (d) a detector. As the colliding electrons produce large amount of heat in the target so it has to be water-cooled to prevent melting. Most of the kinetic energy of colliding electron is converted into heat, less than one percent being transformed into X-rays. These X-rays can be detected by using fluorescent screens, photographic film and ionization devices (Guiger counter). The output from the detector system displays intensities (counts) as a function of diffraction angle (2θ).

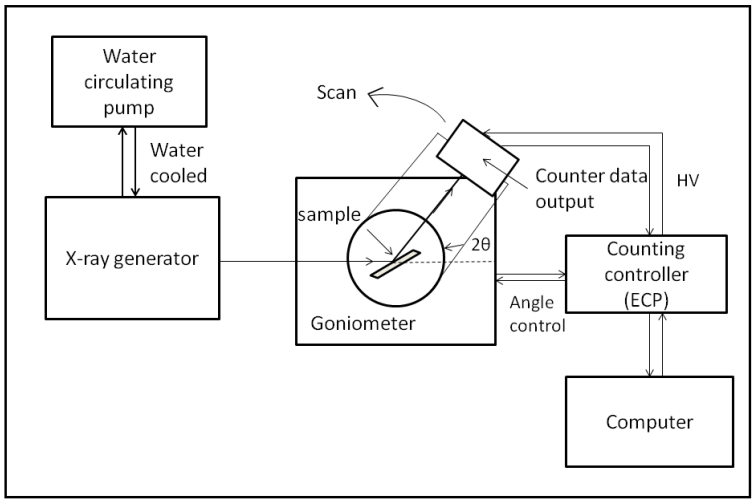

Figure 2.5 Block diagram of X-ray powder diffractometer

The powder sample in our study is spread on the indented section of the glass plate. XRD patterns were recorded using Cu K_α radiation ($\lambda = 0.15405$ nm) at a scan speed of ~3˚/ min. For shape profile analysis of the XRD patterns, lower scan speed of 1.2^o/min has been chosen.

2.3.1.3 Determination of structural parameters by using powder XRD

2.3.1.3.1 Determination of crystalline phase(s) and lattice parameters

Knowledge of crystal structure is important for understanding physical properties of a substance. The crystal structure of a substance determines the diffraction pattern of that substance. Geometry and dimension of the unit cell determines the angular positions of the diffraction lines. The observed relative intensities of the diffraction lines have their origins from the atomic arrangement within the unit cell. The below mentioned steps are followed to determine structural parameters of a sample [38].

Step I: The geometrical shape and size of the unit cell are deduced from the angular positions of the diffraction lines. An assumption is first made as to which of the seven crystal systems the unknown structure belongs to, and then, on the basis of this assumption, the correct Miller indices are assigned to each reflection. This step is called "indexing the pattern" and is only possible when the correct choice of crystal system has been made. Once this is done, the shape of the unit cell is known (from the crystal system), and its size is computable from the positions and Miller indices of the diffraction lines.

Step II: The number of atoms per unit cell is then computed from the shape and size of the unit cell, the chemical composition of the specimen, and its measured density. For example if the crystal is cubic in nature then the number of atoms per unit cell for simple cubic will be 8 × 1/8 =1, for body centered cubic will be 8×1/8 + 1= 2 and so on. In case, more than one element are presents in the crystal structure, the number of each kind of atoms present will distort the crystal lattice and give way for determination of chemical composition by extracting relevant X-ray parameters.

Step III: Finally, the positions of the atoms within the unit cell are deduced from the relative intensities of the diffraction lines. To be noted the relative intensities of the lines are sensitive to scattering of X-ray by atoms with varying atomic mass. Heavier atoms scatter more compared to the lighter ones. In practice, least square approach of Rietveld refinement the positions of the atoms can be calculated by using measured X-ray diffraction patterns [39].

2.3.1.3.2 Crystallite size measurement

It is possible to determine the average crystallite size in a powder sample from the x-ray diffraction data. The smaller is the particle size, the broader is the diffraction peak of the sample. From the width of the diffraction peak, one can get the particle size using scherrer equation [40].

$$t = \frac{0.9\lambda}{B\cos\Theta} \qquad \text{--------.(2.2)}$$

Where 't' is diameter of crystallite, 'λ' is wavelength of X-ray (1.5405Å for CuK_α line), 'Θ' is diffraction angle and 'B' is broadening of diffraction line measured at half its maximum intensity in radians (FWHM) [40]. 'Θ' is calculated as half of the diffraction angle corresponding to maximum intensity. The value of the average crystallite size, t, corresponds to the mean value of a crystallite size distributions.

2.3.2 Electron microscopy

Electron microscopy is a versatile technique for providing structural and microscopic details of the materials. The types of signals produced from the interaction of the electron beam with the sample include: secondary electrons, backscattered electrons, characteristic

X-rays etc. These signals are obtained from specific emission volumes within the sample and can be used to examine many characteristics of the sample (e.g. surface topography, crystallography, composition etc.)[35]. In case of SEM, the image of the sample is formed due to interaction of electron beam with the sample in raster scan. SEM technique is based on the scattered electrons whereas TEM is based on the transmitted electrons. TEMs are capable of imaging at a significantly higher resolution than light microscopes, owing to the small de Broglie wavelength of electrons. Thus, the structural information over a wide range of magnifications; i.e. upto 1,50000X for SEM and 3,00000X for TEM, can be achieved [41]. This enables the user to examine fine details on crystallographic parameters; e.g. single column of atoms which is thousands of times smaller than the smallest resolvable object in a light microscope. SEM is primarily used to study the surface structure of the bulk specimen whereas TEM provides information about internal structure of thin specimen.

2.3.2.1 Scanning electron microscopy (SEM)

2.3.2.1.1 Basic principle and instrumentation

A scanning electron microscope (SEM) is a type of electron microscope that produces images of a sample by scanning it with a focused beam of electrons. The most common mode of detection is the secondary electrons emitted by atoms excited by the electron beam. The number of secondary electrons is dependent on the function of the angle between the surface and the beam [42]. A typical block diagram of SEM with its different components has been presented in figure 2.6. The microscope consists of an electron source or gun to produce electrons, which accelerates with energy between 1keV and 30 keV. Two to three condensor lenses are there to demagnify the electron beam, so that it hits the specimen having a diameter of 2-10nm. The beam of electrons is scanned across the specimen by the scan coils. The detector counts the number of secondary electrons, given off from each point on the surface. Any radiation from the specimen may be used to provide the signal to modulate the cathod ray tube (CRT) and thus provide contrast in the image [42,43].

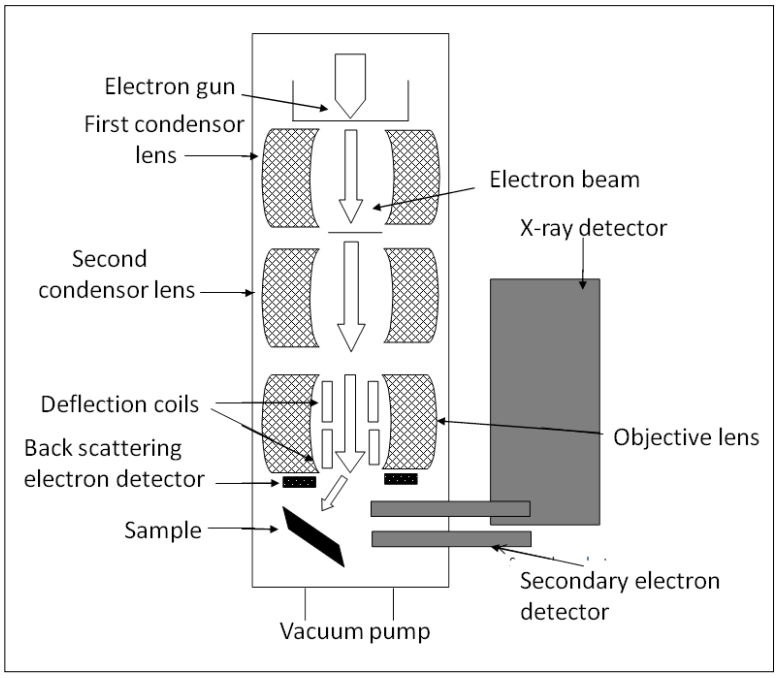

Figure 2.6 Block diagram of scanning electron microscope.

2.3.2.1.2 Sampling and determination of morphology and particle size

The sample to be analyzed using SEM, should be conducting. For non-conducting samples, charge accumulation may repel the incoming primary electrons, leading to a distorted image. In order to overcome the problem of charge accumulation, a thin conducting layer of metallic gold or carbon of about 10nm thickness is coated on the nonconducting specimens to be analyzed. The electrons interact with atoms in the sample, producing various signals that can be detected to build up an image of the sample surface which is displayed on the screen.The electron beam is generally scanned in a raster scan pattern (Sub-section 2.3.2) and the beam's position is combined with the detected signal in order to produce an image [42]. The dimensions of individual particles can be measured from the SEM picture. The average of the sizes gives an approximate value of the particle size which is generally referred as ‘SEM particle size’.

2.3.2.2 Transmission electron microscopy (TEM)

A. Conventional:

2.3.2.2.1 Basic principle and instrumentation

Transmission electron microscopy (TEM) is a microscopic technique in which a beam of electrons is transmitted through an ultra-thin specimen, thereby interacting with it as it passes through. An image is formed from the interaction of the electrons transmitted through the specimen; the image is magnified and focused onto an imaging device (e.g. a fluorescent screen or a layer of photographic film or to be detected by a sensor such as a CCD camera). The essential components of a TEM consists of an electron gun, condenser lenses, specimen chamber, objective and intermediate lenses, projector lens and the camera [43]. A typical block diagram of TEM instrument has been presented in figure 2.7.

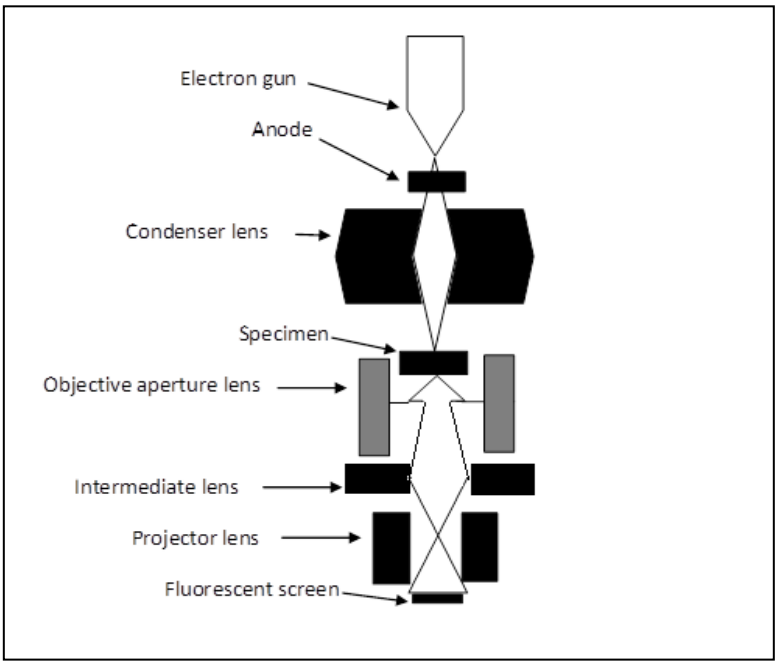

Figure 2.7 Block diagram of transmission electron microscope.

2.3.2.2.2 Sampling and determination of morphology and TEM particle size

The sample (nanoparticles) is dispersed in a solvent using ultrasonication using suitable solvents for a duration of 5-20 minutes. The charateristics of the solvent used are as follows: (a) should be chemically inert, (b) should not result in agglomeration of the nanoparticles, (c) should not leave carbon residues, and (d) should evaporate in a reasonable

time frame (~ 10-20 minutes) at room temperature.. Depending upon nature of our sample we have used either acetone or ethanol as solvent for dispersion experiments. TEM samples are mounted on a copper grid for analysis in our study. Copper grids are the most commonly used, though for high temperature work Mo grids are used. For nano particles and thin films a carbon film is used as support. A carbon film has low contrast in the TEM and does not obscure the contrast arising from the specimen[43]. The morphology can be depicted directly while the particle sizes were estimated using image soft-ware in a statistical averaging manner.

2.3.2.2.3 Interpretation of structural parameters from SAED pattern

A small area is selected and focused with the electron beam in a TEM instrument to measure SAED pattern of the sample. Depending on the samples, the patterns may take the form of diffuse rings (for amorphous system), bright spots (crystalline phase) or small spots making up rings (poly nanocrystalline). Each crystalline phase has a characteristic SAED pattern which corresponds to a set of lattice planes. The angular distribution of X-ray scattering can be displayed on the TEM screen. The observation of concentric rings indicates polycrystalline nature of the sample. The radius of the concentric ring corresponds to a particular interplanar spacing, d , of the cryatalline structure. The procedure adopted for calculation of 'd' values from SAED pattern are summarized as follows:

STEP I: The distance 2R of one ring across the centre is measured.

STEP II: The radius 'R' of the ring terms of 1/nm is found. This unit shows the distance is in reciprocal lattice.

STEP III: The interplanar distance 'd' in real space as 1/R in terms of the unit nm is obtained. This procedure can be repeated for all rings and 'd' can be calculated. The interplannar spacings can be compared to the literature reported 'd' values and the rings can be indexed in terms of Miller indices(hkl) [44].

B. High resolution transmission electron microscopy (HRTEM)

High resolution transmission electron microscopy is another useful technique for imaging of the materials at atomic scale with a resolution up to 0.5 Å. It can be also used to

characterize crystal structure, point defects, stacking faults, dislocations and surface structures etc. Basically, the instrumentation is similar to TEM, where the aberration has been corrected using a monochromator and Cs-corrector [45]. HRTEM uses both transmitted and scattered electron beam interference to form the image. This produces phase contrast image, which can be as small as the unit cell of a crystal. The sample preparation technique is similar to that of TEM for powdered samples (see sub-section: 2.3.2.2.2) and will not be described in this section. Good quality HRTEM images can be obtained only from thin specimens/nano-powder, since inelastic scattering will tend to degrade the image quality. The microscope must be aligned as accurately as possible and objective lens astigmatism must be minimized. The specimen should be carefully tilted so that the beam direction coincides with a crystallographic axis [43, 44].

2.4. Instrumental techniques for studying materials properties

The following materials properties, namely: Surface studies, magnetic properties and electrochemical studies were carried out in this thesis work. The methodologies involved are described in the following sub-sections.

2.4.1 BET surface area analyzer

2.4.1.1 Instrumentation

Knowledge of specific surface area and porosity of the synthesized materials are important tools for understanding the formation, structure and potential applications [46, 47]. Amongst the various theories on adsorption, Brunauer–Emmett–Teller (BET) theory explains the physical adsorption of gas molecules on a solid surface, satisfactorily. It is an important analytical technique for the measurement of the specific surface area of a material. The BET method is the most widely used procedure for the determination of the surface area of solid materials. The methodology is based on the use of the BET equation (Equation 2.3).

$$\frac{1}{W(\frac{P}{Po}-1)} = \frac{1}{WmC} + \frac{C-1}{WmC}\left(\frac{P}{Po}\right) \qquad \text{------- (2.3)}$$

Where, *W* is the weight of gas adsorbed at a relative pressure, P/P_o, and W_m is the weight of adsorbate constituting a monolayer of surface coverage. The term 'C' is the BET constant which is related to the energy of adsorption in the first adsorbed layer and consequently its

value is an indication of the magnitude of the adsorbent/adsorbate interactions [48]. The BET theory takes care of the possibility of multi layer adsorption, and usually adopts non-corrosive gases (like nitrogen, argon, carbon dioxide, etc.) as adsorbates for the determination of surface area.

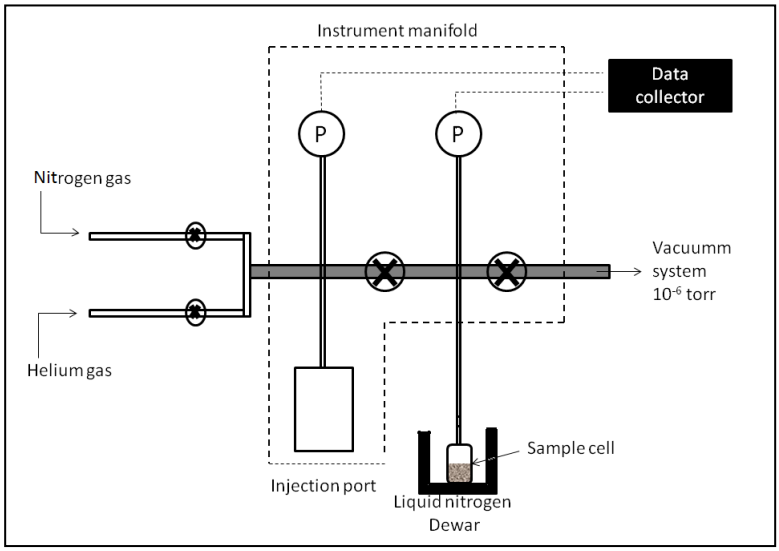

Figure 2.8 Block diagram of a BET surface area analyzer [48]

The block diagram of the BET surface area analyser has been shown in figure 2.8. The instrument consists of a degassing port, gas lines, heating mantle, Dewar(liquid nitrogen), sample holder and data collector, the degassing chamber is not shown.

2.4.1.2 Experimental procedure

The following steps are followed for determination of specific surface area of a sample.

1. Degas

   The sample is cleaned of any impurity present in it like water or organic vapours under a flow of inert and dry gas. The sample is placed in the degasing chamber for several hours. This is a very important step. For accurate determination of surface area selecting suitable time duration and temperature during degassing is necessary and is dependent on the natutre of the materials under study.

2. Adsorbate is introduced in to the manifold

3. The valve to the sample cell is opened allowing the adsorbate to interact with the sample material.
4. The pressure is repeatedly measured for the preset equilibration time, if the pressure drops dosing recurs and measurement proceeds until a stable reading is achieved.
5. The measurement is started after giving all the specifications in the programme and the data is saved. Finally an isotherm graph appears on the screen.

In our study we have activated the samples in the temperature range of 150-250^{o}C under inert gas atmosphere prior to measurements. The adsorption/desorption studies were carried out using N_2(g) as adsorbent at liquid nitrogen temperature (77K) using fixed known mass of the materials.

2.4.1.3 Interpretation of data for surface area and porosity

According to the width of pores, the materials can be classified in to following types as micropores < 2 nm, mesopores 2 ~ 50 nm, macropores > 50 nm. There are 6 types of isotherms (Type I-VI) as per IUPAC classification[48] . Similarly, all adsorption-desorption curves can be classified accordingly to four different types of hysteresis loops, i.e. H1, H2, H3 and H4 [48]. After sorption experiments, the BET isotherms are assigned according to its type and hysteresis loop and data are interptreted for surface area and pore size distribution.

2.4.2 VSM measurement

2.4.2.1 Basic Principles and instrumentation

Vibrating sample magnetometry (VSM) is based on Faraday's law, which states that an electromagnetic force is generated in a coil when there is a change in the flux linked through the coil. A typical setup for VSM instrument is presented in figure 2.9. A pair of detection coils is mounted inside an electromagnet that produces a uniform magnetic field, while the sample is attached to a vibrating sample holder that oscillates along the z-axis. When magnetized, the sample's magnetic flux moves with the sample, as it oscillates. This produces changes in the magnetic flux measured by the coils. The coils are connected and located so that, ideally, the signal due to the moving sample adds and any signal due to fluctuations of the field from the electromagnet subtracts and gets cancelled. The vibration

module is driven by a loudspeaker or equivalent mechanism connected to a small coil placed in the field of a permanent magnet. The system possesses another set of reference coils in order to maintain and rectify any error due to noise in the sample vibration so that measurements can be reproduced [49].

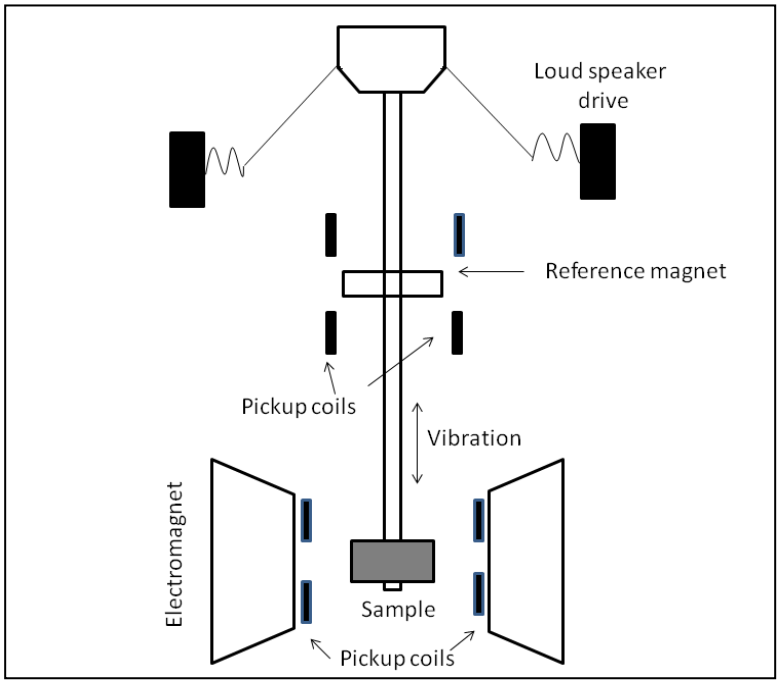

Figure 2.9 Schematic diagram representing principle involved in vibrating sample magnetometer [49].

2.4.2.2 Sampling and measurement of magnetic parameters

Weight of the powder sample can be as min as 30 mg for VSM measurement. The samples can be measured in terms of pellet and thin film also. Hysteresis loop gives the relation between the magnetization, M and applied field, H. Several useful magnetic parameters can be extracted from the hysteresis loop in order to characterize the magnetic properties of the materials. The parameters include saturation magnetization, M_s, Curie temperature,T_c, remnant magnetization, M_r and coercivity, H_c .

2.4.3 Electrochemical analysis

2.4.3.1 Basic principle and instrumentation

The electrochemical analysis yields specific information on the kinetics and thermodynamics of the reaction of solids that can be related to their structure and composition. In an electrochemical experiment, one can measure one or more of the following four parameters; (1) potential (E), (2) current (i), (3) charge (Q) and (4) time (t). The response of a system depends on the parameter, which is used as the excitation signal. In most electrochemical techniques, there are three electrodes; namely; working electrode, reference electrode and counter (or auxiliary) electrode. The three electrodes are connected to a potentiostat (an instrument which controls the potential of the working electrode and measures the resulting current). In a typical electrochemical experiment, potential is applied to the working electrode and the resulting current measured then plotted as a function of time. In another approach, the potential is varied and the resulting current is plotted as a function of applied potential. [50, 51]

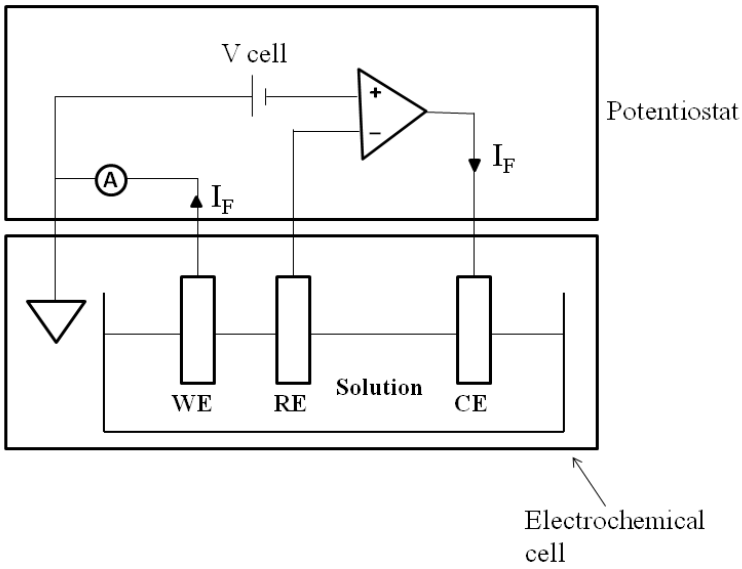

Figure 2.10 Block diagram of a typical electrochemical cell

2.4.3.2 Sampling and measurement of electrochemical parameters

The working electrode was prepared by mixing of 80 wt.% of synthesized active material, 10 wt.% of acetylene black and 10 wt.% of PVDF binder grinding together with NMP solvent to make a slurry. The prepared slurry was coated on stain less steel disc of area

$1cm^2$ and dried at 60˚C for 8h. All the electrochemical experiments were investigated using an 'Ivium stat electrochemical workstation' in a standard two-electrode assembly with the fabricated material on steel disc as a working electrode. The cyclic voltammetry measurements were in the potential ranging from 0 to -1.1 V. The specific capacitance (SC) of the fabricated electrode materials were estimated from CV curves using the equation (2.4). [52].

$$SC(CV) = \frac{Q(C)}{E(V)Xm(g)} \qquad \text{-------- (2.4)}$$

where SC is the specific capacitance (Fg^{-1}), Q is the cathodic charge in coulombs, E is the potential difference in volts, and m is the active material mass in grams.

The SC of the electrode materials were also evaluated from the charge-discharge curves by following equation (2.5).

$$SC = \frac{I\Delta t}{m\Delta V} \qquad \text{------ (2.5)}$$

where, *I*, t, V is the discharging current (A), time (s), potential difference (V), respectively [53].

References

1. M. S. Balogun, W. Qiu, W. Wang, P. Fang, X. Lu, Y. Tong, J. Mater. Chem. A. **3** (2015) 1364–1387.
2. E. Panabière, N. Emery, S. Bach, J. P. Pereira-Ramos, P. Willmann, Corros. Sci. **58** (2012) 237-241.
3. R.S. Ningthoujam, N.S. Gajbhiye, Prog. Mater Sci. **70** (2015) 50–154.
4. B. Mazumder, A. L. Hector, J. Mater. Chem. **19** (2009) 4673–4686.
5. I. P. Parkin, G. S. Elwin, J. Mater. Chem. **11** (2001)3120-3124.
6. J. C. Caicedo, G. Zambrano, W. Aperador, L. Escober-Alarcon, E. Camps, Appl. Surf. Sci. **258** (2011) 312-320.
7. J. Pak, W. Lin, K. Wang, A. Chinchore, M. Shi, D. C. Ingram, A. R. Smith, J. Vac. Sci. Technol., A. **28** (2010)536–540.
8. J. Choi, E. G. Gilan, Inorg. Chem. **48** (2009) 4470-4477.
9. T. Guo, M. S. Yao, Y. H. Lin, C. W. Nan, CrystEngComm. **17**(2015) 3551–3585.
10. C. Giordano, M. Antonietti, Nano Today. **6** (2011)366-380.
11. H. Weller, Adv. Mater. **5** (1993) 88- 95.
12. C. Lind, S D. Gates, N. M Pedoussaut, T. I. Baiz, Materials. **3** (2010)2567-2587.
13. L. L. Hench, J. K. West, Chem. Rev. **90** (1990) 33-72.
14. L. Gao, X. Wang, L. Fei, M. Ji, H. Zheng, H. Zhang, T. Shen, K. Yang, J. Cryst. Growth. **281**(2005) 463-467.
15. I. Bilecka, M. Niederberger, Electrochim. Acta. **55** (2010) 7717- 7725.
16. A. R west, Solid state chemistry and its applications, Wiley, Singapore, (2003) pp: 4-16.
17. I. M. Kolthoff, J. Phys. Chem. **36**(1932)860–881.
18. G. N. Glavee, K. J. Klabunde, C. M. Sorensen, G. C. Hadjapanayis, Langmuir. **8** (1992) 771-773.
19. R. N. Panda, N. S. Gajbhiye, J. Appl. Phys. **81** (1997)335- 339.
20. H. Wang, Z. Wu, J. Kong, Z. Wang, M. Zhang, J. Solid State Chem. **194** (2012) 238–244.
21. M. Tsaramyrsi, M. Kaliva, A. Salifoglou, C. P. Raptopoulou, A. Terzis, V. Tangoulis, J. Giapintzakis, Inorg. Chem. **40** (2001) 5772-5779.

22. R. N. Panda, S. B. Dalavi, J. Theerthagiri, Adsorpt. Sci. Technol. **30** (2012) 345-354.

23. J. Guo, Y. Hou, C.Yang, Y. Wang, L. Wang, Material letters. **67** (2012) 151-153.

24. L. Volpe, M. Boudart, J. Solid State Chem. **59**(1985) 332-347.

25. I. K. Milad, K. J. Smith, P. C. Smith, K. A. R. Mitchell, Catal. Lett. **52**(1998) 113-119.

26. P. P. Mishra, M. M. Raja, R. N. Panda, Mater. Res. Bull.**75** (2016) 127–133.

27. P. P. Mishra, M. M. Raja, R. N. Panda, J. Supercond. Nov. Magn. **29** (2016) 1347–1356.

28. A. Gomathi, Mater Res. Bull. **42** (2007)870-874.

29. C. Giordano, C. Erpen, W. Yao, B. Milke, M.Antonietti, Chem. Mater. **21** (2009) 5136-5144.

30. C. Giordano, C. Erpen, W. Yao, M. Antonietti, Nano Lett. **8** (2008) 4659-4663.

31. S. Podsiadlo, Thermochim Acta. **256** (1995) 375-380.

32. S. D. Krawiec, C. Aymonier, A. L. Serani, F. Weill, S. Gorsse, J. Etourneau, F. Cansell, J. Mater. Chem. **14** (2004) 228-232.

33. J. W. Robinson, Anal. Chem. **32** (1960) 17-29.

34. J. A. Van Loon, Analytical Atomic Absorption Spectroscopy: Selected Methods, Elsevier, 2012, pp :1-20.

35. J. I. Goldstein, C. E. Lyman, D. E. Newbury, E. Lifshin, P. Echlin, L. Sawyer, D. C. Joy, J. R. Michael, Scanning electron microscopy and X-ray microanalysis : Third edition,2003, Springer science & Business media, 2012, pp.1-20.

36. P. J. Goodhew, J. Humphreys, R. Beanland, Electron microscopy and analysis, Third edition, Taylor & Francis, pp:- 175.

37. B. D. Culity, Elements of X-ray diffraction, Addison-wesley, reading, Massachusetts, (1956) pp:84-85.

38. B.D Culity, Elements of X-ray diffraction, Addison-wesley, reading, Massachusetts, (1956) pp: 298-300.

39. D. B. Wiles, R. A.Young J. Appl. Crystallogr. **14** (1981) 149-151. ES and **R. A.**

40. B. D Culity, Elements of X-ray diffraction, Addison-wesley, reading, Massachusetts, (1956) pp:262-263.

41. R. Erni, M. D. Rossell, C. Kisielowski, U. Dahmen, Phys. Rev. Lett. **102** (2009) 096101(1)-(4).

42. A. R West, Solid state chemistry and its applications, Wiley, Singapore, (2003) pp: 47-101.

43. P. J. Goodhew, J. Humphreys, R. Beanland, Electron microscopy and analysis, Taylor & Francis, Third edition, pp: 66-167.

44. R. F. Egerton, Physical Principles of Electron Microscopy An Introduction to TEM, SEM, and AEM, Springer, pp: 93- 119.

45. M. Lentzen, Microsc. Microanal. **12** (2006) 191–205.

46. G. Limousin, J.-P. Gaudet, L. Charlet, S. Szenknect, V. Barthe`s, M. Krimissa, Appl. Geochem. **22** (2007) 249–2752.

47. R. S. Drago, C. E. Webster, J. M. McGilvray, J. Am. Chem. Soc. **120** (1998) 538-547.

48. K. S. W. Sing, D. H. Everett, R. A. W. Haul, L. Moscou, R. A. Pierotti, J. Rouquerol, T. Siemieniewska, Pure & Appl. Chem. **57**(1985) 603- 619.

49. C. D. Graham, J. Mater. Sci. Technol.**16** (2000) 97-101.

50. T. Grygar, F. Marken, U. Schroder, F. Scholz, Collect. Czech. Chem. Commun.**67** (2002)163-208.

51. F. Scholz, B. Meyer, Chem. Soc. Rev. **23** (1994) 341-347.

52. F. Cheng, C. He, D. Shu, H. Chen, J. Zhang, S. Tang, D. E. Finlow, Mater. Chem. Phys. 131 (2011) 268–273.

53. Y. Wang, M. Jiang, Y. Yang, F. Ran, Electrochim. Acta. **222** (2016)1914-1921.

Chapter 3

Magnetic Properties of ε-$Co_xFe_{3-x}N$ ($0 \leq x \leq 0.4$) and γ′-$Ni_xFe_{4-x}N$ ($0 \leq x \leq 0.8$) Nitride Systems

In this chapter, synthesis, characterization and magnetic properties of ε-$Co_xFe_{3-x}N$ ($0 \leq x \leq 0.4$) and γ′-$Ni_xFe_{4-x}N$ ($0.2 \leq x \leq 0.8$) materials have been investigated.

3.1 Introduction

Studies on potential applications of ε-Fe_3N and γ′-Fe_4N nitrides are reported in the literature [1-3]. Another noteworthy report includes the synthesis of ε-Fe_3N submicron rods via a modified ethane diamine route and its study on magnetism for magnetic resonance imaging [4]. In addition, several reports are available on development of new synthetic routes and properties studies on Co and Ni substituted ε-Fe_3N and γ′-Fe_4N nitrides including exploration of their technical applications [5-8]. Substitution of Co and Ni in iron nitrides can tailor the magnetic properties substantially. In fact, Co and Ni being ferromagnets, very little compromise on magnetic properties is expected. On the contrary, it can also give thermal stability to the substituted iron nitrides in epsilon (ε) and anti-perovskite γ′-Fe_4N phases. Synthesis of iron nitrides by nitridation of fine particles of α-Fe_2O_3 (size range: 10-20 nm) obtained via citrate precursor technique have been studied [9, 10]. It has been demonstrated that the process of nitridation occurs via several intermediate phases of iron oxides with reduced oxidation states of Fe which in turn converts to nitrides at higher temperatures [11, 12]. The details of the mechanistic aspects are not explored for the formation of above mentioned nitrides. In fact, use of various new synthetic strategies and processing parameters may lead to variable outcomes and needs further research. Effect of substitution of several transition metals in iron nitride phases have been attempted [5, 13, 14]. Reports on γ′-$Ni_xFe_{4-x}N$ nitrides are comparatively less in number due to synthetic challenges which may be evident from the occurrence of narrow regions of this phase in the Fe-N phase diagram [15]. Though the preparation of nitrides using oxalate precursor route is very common [5, 6], citrate precursor route is not well exploited.

In the present study, effects of Co and Ni substitution in Fe-N system on structural and magnetic properties have been studied. In this regard, development of citric acid based sol-gel method for the precursor synthesis and their nitridation reactions using ammonia gas for the synthesis of ε-$Co_xFe_{3-x}N$ ($0 \leq x \leq 0.4$) and γ′-Ni_xFe_{4-x} N ($0.2 \leq x \leq 0.8$) nitride materials is in order. This may ensure product quality with respect to nitrogen content and its distribution and hence merits further investigations. Therefore, based on the above mentioned lacuna, we have tried to explore new synthesis and processing strategy in order to develop high quality nitride materials. The solid state reactivity has been studied in order to explore the synthesis parameters for product formation. The details on the investigations of structural and magnetic properties have been studied.

3.2 Materials and methods

Citric acid based sol-gel route has been adopted for the synthesis of the nanocrystalline Co and Ni substituted iron nitride materials. We have concentrated on ε- and γ′- phases which are most extensively studied magnetic systems [9, 14]. Details of the synthesis strategies adopted have been summarized below.

3.2.1 Synthesis of ε-$Co_xFe_{3-x}N$ ($0 \leq x \leq 0.4$) and γ′-$Ni_xFe_{4-x}N$ ($0.2 \leq x \leq 0.8$) materials by direct nitridation of solid state precursors

3.2.1.1 Synthesis of iron based oxide and mixed metal oxide precursor(s)

Nanocrystalline ε-$Co_xFe_{3-x}N$ ($0 \leq x \leq 0.4$) phases were synthesized via citrate precursor route. The method includes thermal decomposition of metal (or mixed metal) citrate complex having desired metal atom ratios in air atmosphere. The novelty of the procedure have been described in chapter 2, subsection 2.1.1.1. In summary, the synthetic procedure can be described as follows: the aqueous solution of ferric nitrate, $Fe(NO_3)_3 \cdot 9H_2O$ (Molychem, 98%) and citric acid (anhydrous), $C_6H_8O_7$ (Qualigen, 99.5%) were mixed in a 400ml beaker with 1:3 molar ratio. The solution was transferred into a 2 neck round bottom flask and diluted to a total volume of 300ml. The resulting solution was refluxed and allowed to attain a constant temperature of 70°C while stirring continuously with the help of a magnetic stirrer. Next it was maintained at 70°C for 3h duration and allowed to cool down slowly. The resulting solution (sol) was evaporated slowly until a solid viscous gel (red

coloured) is obtained. With further continuation of heating, auto combustion of the gel takes place, resulting black coloured powder. In a similar manner, cobalt nitrate, $Co(NO_3)_2 \cdot 6H_2O$ or, Nickel Chloride, $NiCl_2 \cdot 6H_2O$, were added in different stoichiometric ratios with respect to $Fe(NO_3)_3 \cdot 9H_2O$ for preparing mixed metal citrate precursor(s). The resulting pre-fired black coloured powder was decomposed in air atmosphere at 673K in order to get ultrafine pure and Co or Ni substituted iron oxides.

3.2.1.2 Nitridation of oxide precursor

3.2.1.2.1 Nitridation of Co substituted Fe based mixed metal precursors

. Nitridation of iron oxide precursor was carried out in a vertical tubular furnace using a quartz reactor of 1cm diameter under flowing NH_3(g) in the temperature range 823K - 973K for 2h duration. After asserting the formation of pure phase ε-Fe_3N at 973 K, the mixed metal oxide precursors containing Co and Fe atoms in desired stoichiometry were nitrided at the same temperature in order to get ε-$Co_xFe_{3-x}N$ ($0 \leq x \leq 0.4$) material .The heating ramp was moderately high and kept at 3.8 K/min. The furnace was allowed to cool down naturally until room temperature (298K) was reached. During cooling, constant NH_3(g) flow rate was maintained. The resulting gray/black coloured nitride products were removed from the quartz reactor after completion of the experiment and exposed to air atmosphere. The summary of materials synthesized is listed in table 3.1 along with the synthesis and processing parameters.

Table 3.1 Materials, stoichiometric amount of reagents, nitridation temperature and heating ramp.

Materials	Stoichiometric amount of Reagents used (g)		Nitridation Temperature (K) /Nitridation Time(h)	Heating Ramp ($Kmin^{-1}$)
	$Fe(NO_3)_3 \cdot 9H_2O$	$Co(NO_3)_{2.} \cdot 6H_2O$		
ε-Fe_3N	6	---	973/2	3.8
ε- $Co_{0.1}Fe_{2.9}N$	5.819	0.145	973/2	3.8
ε- $Co_{0.2}Fe_{2.8}N$	5.656	0.291	973/2	3.8
ε- $Co_{0.3}Fe_{2.7}N$	5.417	0.433	973/2	3.8
ε- $Co_{0.4}Fe_{2.6}N$	5.20	0.580	973/2	3.8

3.2.1.2.2 Nitridation of Ni substituted Fe based mixed metal oxide precursors

All compositions of Ni substituted oxide precursors were nitrided at the same temperature, i.e. 973K in order to get γ′-$Ni_xFe_{4-x}N$ ($0.2 \leq x \leq 0.8$) materials. Details of the nitridation procedure and processing parameters followed are described in the preceding subsection 3.2.1.2.1. In short, every experimental parameters being similar, $Fe(NO_3)_3 \cdot 9H_2O$ and $Ni(NO_3)_2 \cdot 6H_2O$ were used for Fe and Ni source, respectively. The summary of the materials synthesized is listed in table 3.2 along with the synthesis and processing parameters. The material γ′-Fe_4N (x = 0) could not be synthesized in pure phase by using the present methodology and experimental parameters therein.

Table 3.2 Materials, stoichiometric amount of reagents, nitridation temperature and heating ramp.

Materials	Stoichiometric amount of Reagents used (g)		Nitridation Temperature (K) /Nitridation Time(h)	Heating Ramp ($Kmin^{-1}$)
	$Fe(NO_3)_3 \cdot 9H_2O$	$Ni(NO_3)_2 \cdot 6H_2O$		
γ′-$Ni_{0.2}Fe_{3.8}N$	5.656	0.166	973/2	3.8
γ′ $Ni_{0.4}Fe_{3.6}N$	5.400	0.353	973/2	3.8
γ′- $Ni_{0.6}Fe_{3.4}N$	5.099	0.530	973/2	3.8
γ′- $Ni_{0.8}Fe_{3.2}N$	4.799	0.706	973/2	3.8

3.2.2 Instrumental characterization

The X-ray powder diffraction (XRD) patterns were recorded using an X-ray diffractometer (model: Rigaku Mini Flex II, Japan) using $CuK\alpha_1$ radiation ($\lambda = 0.15405$ nm) at a scan speed of 3˚/min. The phase purity was ascertained using X-ray diffraction. Crystallite size was analyzed using Scherrer equation, $t = 0.9\lambda/B \cos\theta$, where 't' is the crystallite size, 'λ' is the wavelength of X-ray radiation, 'B' is the FWHM in radian and 'θ' is the diffraction angle[16] (chapter 2 subsection 2.3.1.3.2). The shape and morphology of the products were examined by scanning electron microscopy (SEM) (model: JEOL, JSM-6390) and transmission electron microscopy (TEM) (model: Philips- CM 200). Metal contents were determined using atomic absorption spectroscopy (AAS) (model: Shimadzu-AA 7000). The magnetization measurements (M vs. H characteristics) at room temperature (298K) were carried out on solid powder material using vibrating sample magnetometer (model: ADE VSM-EV9) which can provide a magnetic field up to 20 kOe.

3.3 Results and discussions

3.3.1 X-Ray diffraction analysis

The precursor material and the products have been characterized using X-ray diffraction for structure and materials phase analysis. The details of the results obtained are presented and discussed in the below mentioned subsections.

3.3.1.1 Precursor characterization

Several precursor materials having different metal atom ratios (e.g. Co:Fe and Ni:Fe :: 0.1:2.9, 0.2:2.8, 0.3:2.7, 0.4:2.6 and 0.2:3.8, 0.4:3.6,0.6:3.4, 0.8:3.2) were synthesized using citrate precursor technique including pure iron oxide. However, the precursor characterization of α-Fe_2O_3, $Co_{0.6}Fe_{2.6}O_4$ spinel and α- $Ni_{0.5}Fe_{1.5}O_3$ has been focused in a representative manner.

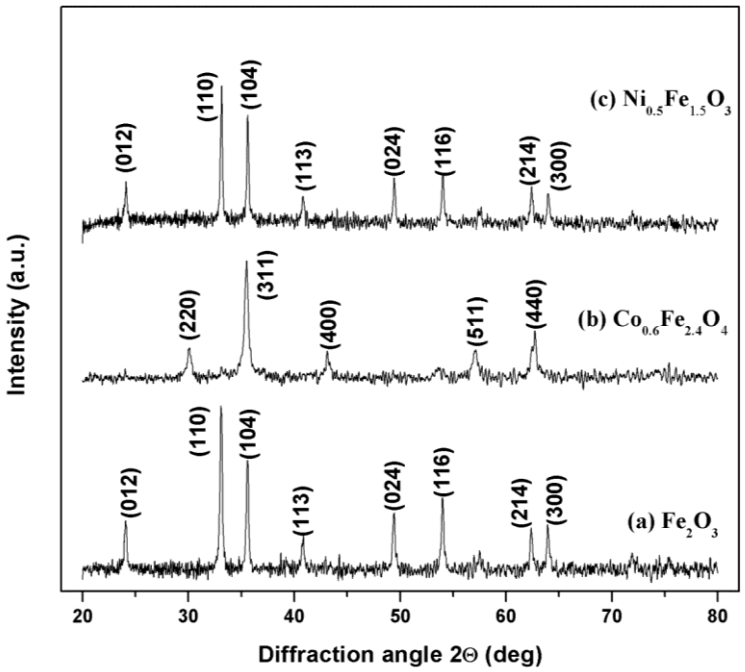

Figure 3.1 Indexed XRD patterns of various precursor materials; (a) α-Fe_2O_3, (b) $Co_{0.6}Fe_{2.4}O_4$ spinel and (c) α-$Ni_{0.5}Fe_{1.5}O_3$.

The X-ray diffraction patterns of iron oxide (α-Fe_2O_3) and Co (/Ni) substituted iron oxide precursors heat treated at 400˚C are presented in figure 3.1. It has been observed that substitution of Co and Ni in iron oxide leads to the formation of single phase solid state precursors instead of mixture of individual metal oxide phases. The precursor α-Fe_2O_3

(figure. 3.1(a)) crystallizes in cubic structure (ICDD PDF # 85-0599) with lattice parameters, a = 9.766(6) Å. Also, Co and Ni substituted iron oxide precursors crystallize in cubic structure (figure 3.1 (b) and (c)) (ICDD PDF # 03-0864, ICDD PDF # 85-0599). The estimated values of lattice parameters are found to be 8.367(3) Å and 8.244(3) Å, for Co-Fe and Ni-Fe oxides, respectively. These values are close to the values reported in the literature, i.e. 8.392 Å and 8.348 Å for $Co_{0.6}Fe_{2.4}O_4$ and $Ni_{0.8}Fe_{2.2}O_4$ materials, respectively [17, 18].

The materials, phase, interplanar distance, Miller indices, intensities and crystallite sizes of the precursor materials are presented in table 3.3. The diffraction peaks with very low intensities occurring at 2θ values of 57.5˚, 71.98˚ and 75.40˚ have not been emphasized in our study. The crystallite sizes of iron oxide and Co or Ni substituted iron oxide precursors are estimated using Scherrer equation and found to be 34nm, 19 nm and 36 nm, respectively. It can be easily seen that substitution of Co or Ni atoms in iron oxides results in alteration of crystallite sizes even when the synthesis and processing conditions are kept identical.

Table 3.3 Materials, Metal atom ratios, Phase, interplanar distance (d), Miller indices (hkl), relative intensities and crystallite sizes of various precursors.

Materials	Metal atom ratios	Phase	d- value	(h k l)	Relative Intensities	Avg. crystallite size (nm)
Precursor-1 α- Fe_2O_3	----	Cubic spinel	3.696(5)*	012	29	34±0.4
			2.700(8)	110	100	
			2.516(3)	104	67	
			2.208(8)	113	17	
			1.842(9)	024	33	
			1.695(2)	116	42	
			1.487(1)	214	24	
			1.455(8)	300	25	
Precursor-2 Co substituted α -Fe_2O_3	Co : Fe 0.6:2.4	Cubic	2.967(2)*	220	24	19±0.5
			2.522(9)	311	100	
			2.096(3)	400	27	
			1.611(5)	511	28	
			1.479(1)	440	35	
Precursor-3 Ni substituted α -Fe_2O_3	Ni : Fe 0.5:1.5	Cubic spinel	3.687(1)*	012	29	36±0.4
			2.704(4)	110	100	
			2.520(1)	104	77	
			2.212(6)	113	21	
			1.842(5)	024	32	
			1.697(4)	116	33	
			1.487(9)	214	26	
			1.454(1)	300	23	

*** Parentheses indicate accuracy in precision to the last decimal digit.**

3.3.1.2 Solid state reactivity study

In order to optimize the experimental parameters for the formation of various Co and Ni substituted iron nitrides and reaction conditions, α-Fe_2O_3 precursors were nitrided using various temperatures, heating ramp and time duration. The NH_3(g) gas flow rate during nitridation was adjusted suitably.

Figure 3.2 shows the indexed XRD patterns of α- Fe_2O_3 precursor nitrided at various temperatures, i.e. 550˚C, 600˚C and 700˚C. It can be observed that the oxide precursor transforms into Fe_3O_4 phase at 550˚C and 600˚C of nitridation temperature (ICDD PDF # 71- 4918) (figure 3.2(a), (b)). Formation of ε- Fe_3N phase occurs at 700˚C (figure 3.2(c)). The hexagonal ε- Fe_3N phase is indexed as per the ICDD PDF # 70-7409.

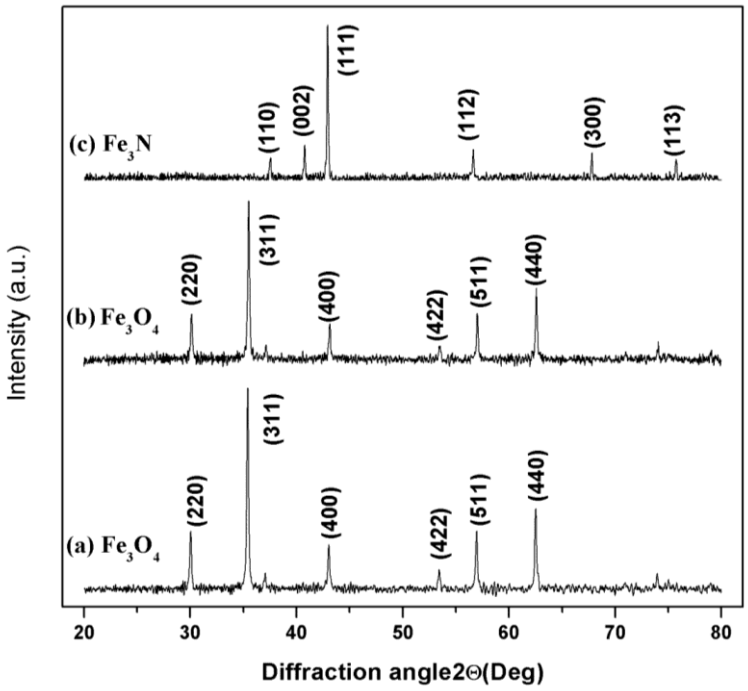

Figure 3.2 Indexed XRD patterns of products obtained via nitridation of α- Fe_2O_3 precursors at various temperatures; (a) 550˚C, (b) 600˚C and (c) 700˚C.

After optimization of the nitride formation temperature at 700˚C, different compositions of the bimetallic oxide precursors were nitrided at 700˚C. A series of ε-$Co_xFe_{3-x}N$ ($0.1 \leq x \leq 1.0$) nitride materials with varying values of 'x' were synthesized and the pure phases obtained with $0 \leq x \leq 0.4$ are tabulated (table 3.2).

Figure 3.3 shows indexed XRD pattern of products obtained from nitridation of α-$Ni_{0.2}Fe_{1.8}O_3$ precursor at various temperatures; (a) 550˚C, (b) 600˚C and (c) 700˚C. It is observed that the precursor transforms into Fe_3O_4 spinel phase up to 600˚C and converts into γ′-Fe_4N structure majorly, at a bit higher temperature, i.e. 700˚C (figure 3.3). With the increase in Ni content in the system, γ′-Fe_4N phase is stabilized.

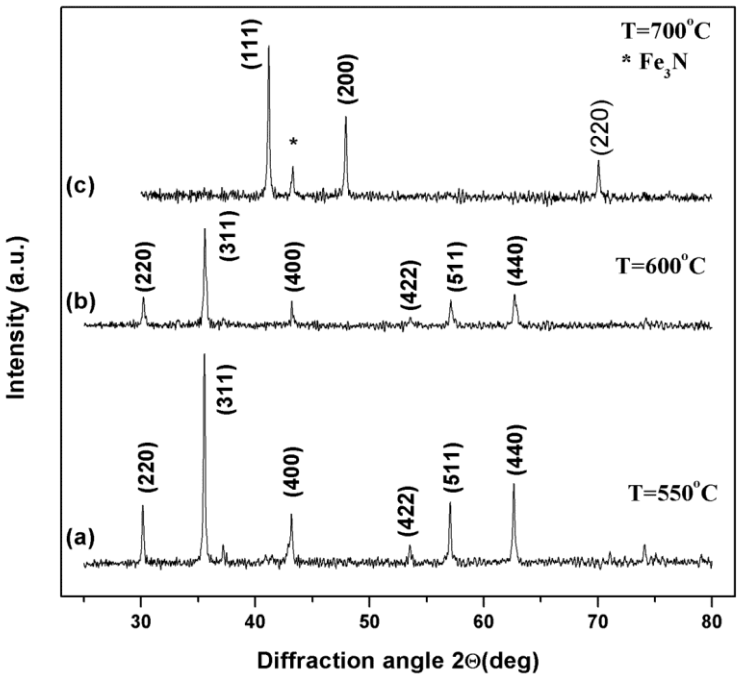

Figure 3.3 Indexed XRD patterns of products obtained via nitridation of α-$Ni_{0.2}Fe_{1.8}O_3$ precursor at various temperatures; (a) 550˚C, (b) 600˚C and (c) 700˚C.

3.3.1.3 XRD study of ε-$Co_xFe_{3-x}N$ ($0 \leq x \leq 0.4$)

The indexed XRD patterns of ε-$Co_xFe_{3-x}N$ ($0 \leq x \leq 0.4$) nitrides obtained by heating oxide precursors at 700˚C for 2h duration in continuous NH_3 (g) flow have been presented in figure 3.4. The results of powder XRD studies indicate the formation of hexagonal ε-Fe_3N phase (figure 3.4) (ICDD PDF # 70-7408). For 0.1 atomic weight % of Co, a mixture of ε-Fe_3N and γ′-Fe_4N was obtained. With further increase of cobalt content, i.e. x = 0.3 and 0.4 atomic weight %, small fraction of α-Fe precipitation was confirmed from XRD analysis of the materials. However, for Co content of 0.2 at. wt%, pure phase ε-Fe_3N was obtained.

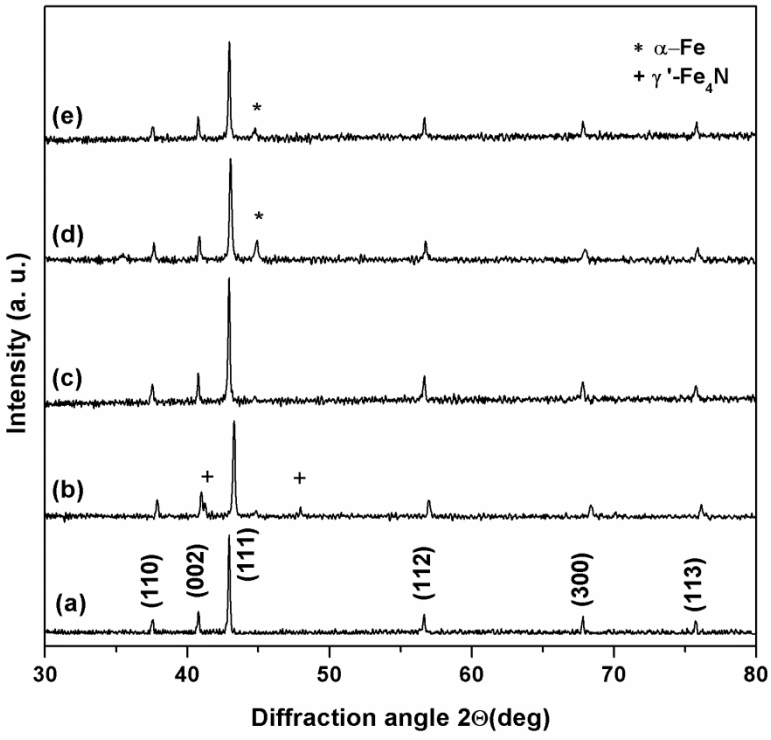

Figure 3.4 Indexed XRD patterns of ε-$Co_xFe_{3-x}N$ ($0.0 \leq x \leq 0.4$) materials synthesized at 700˚C; (a) x = 0, (b) x = 0.1, (c) x = 0.2, (d) x = 0.3 and (e) x = 0.4. Minor impurity phases corresponding to α-Fe and γ′-Fe_4N are marked with * and +, respectively.

In iron-nitrogen system, phase transformation kinetics between various phases, such as: ζ-Fe_2N, ε-Fe_3N, γ′-Fe_4N and α′- Fe_8N etc., are faster than processing parameters and are sensitive to the amount of N insertion in the crystal structure[19]. Therefore, with the small addition of Co (x = 0.1 at. wt.%) in the system cubic phase γ′-Fe_4N exists in small proportion along with the major hexagonal ε-Fe_3N phase. As the amount of Co atom substitution increases from x= 0.1 to x = 0.2 at. wt. %, hexagonal ε-Fe_3N phase is stabilized (figure 3.4(c)). There exists a diffraction peak corresponding to 2θ = 45˚ (with < 5 % intensity), which confirms α-Fe precipitation in ε-$Co_xFe_{3-x}N$ (x = 0.3, 0.4) system. Similar kind of observation has already been reported by Gajbhiye *et al.* [20]. With the progressive increase in Co content (x), fraction of α-Fe phase in the materials increases further. This may be due to the limited solubility of the corresponding binary phases of Co and Fe nitrides.

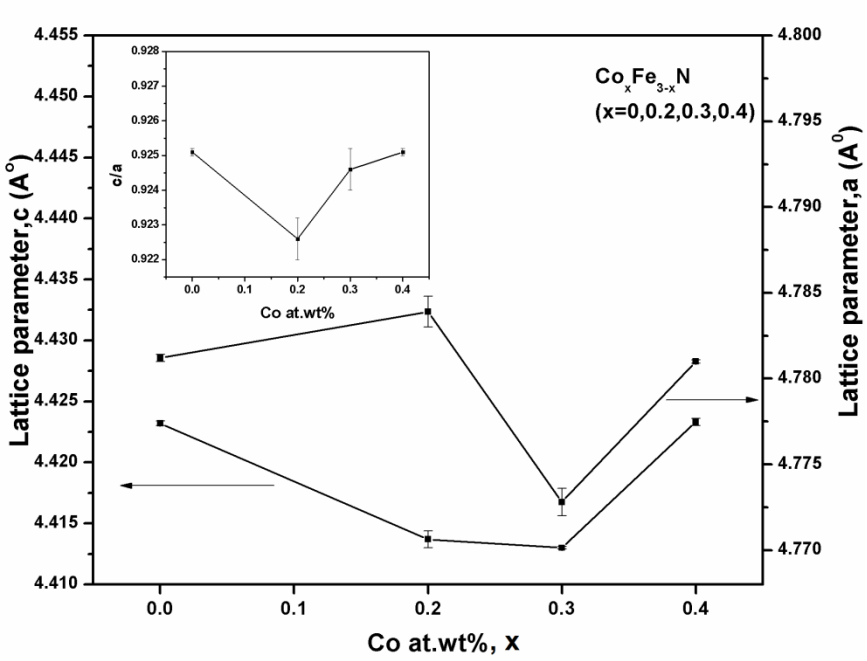

Figure 3.5 Variation of lattice parameters (a, c) with Co at. wt% in ε-$Co_xFe_{3-x}N$ (x=0, 0.2, 0.3 and 0.4) materials. Inset figure shows the variation of c/a ratios with various at. wt% of Co.

The crystal structure parameters derived from X-ray diffraction patterns are listed in table 3.4. The average crystallite sizes of the materials are in the range of 44±0.7 – 55±0.8 nm, presented in table 3.8. Small deviation in the lattice parameters (a and c) and c/a ratios were observed with the change in Co at.% (figure 3.5). The values of lattice parameters a = 4.781(2) Å and c = 4.423(2) Å are larger than the literature reported values i.e. a = 4.70 Å and c = 4.38 Å for ε-Fe_3N nitride [11, 21]. These results indicate that nitrogen content in our nitride products exceeds the stoichiometric values of 3:1 in the cobalt substituted ε-Fe_3N phase and could be assigned approximately as ε-$Co_xFe_{3-x}N_{1.37}$, by extrapolating the plot of lattice parameter 'a' vs. 'c' as reported by T. Liapina *et al.*[21]. The c/a ratio for ε-$Co_xFe_{3-x}N$ ($0 \leq x \leq 0.4$) shows initial drop at x = 0.2 and then increases with increasing Co at. % in the nitride materials (inset figure 3.5).

Table 3.4 Materials phase, Miller indices (hkl), observed (d_{obs}) and calculated interplanar distance (d_{cal}), lattice parameters (a, c) and c/a ratios of ε-$Co_xFe_{3-x}N$ ($0 \leq x \leq 0.4$) materials.

Materials phase	(hkl)	d_{obs} (Å)	d_{cal} (Å)	Lattice parameters(Å)	c/a ratio
ε-Fe_3N	(110)	2.392	2.390	a=4.781(2) * c=4.423(2) *	0.925(1) *
	(002)	2.214	2.211		
	(111)	2.102	2.103		
	(112)	1.622	1.623		
	(300)	1.380	1.380		
	(113)	1.253	1.253		
ε-$Co_{0.2}Fe_{2.8}N$	(110)	2.392	2.391	a=4.783(9) * c=4.413(7) *	0.922(6) *
	(002)	2.205	2.206		
	(111)	2.102	2.102		
	(112)	1.622	1.621		
	(300)	1.380	1.380		
	(113)	1.253	1.253		
ε-$Co_{0.3}Fe_{2.7}N$	(110)	2.387	2.386	a=4.772(8) * c=4.413(1) *	0.924(6) *
	(002)	2.207	2.206		
	(111)	2.100	2.099		
	(112)	1.620	1.620		
	(300)	1.377	1.377		
	(113)	1.251	1.252		
ε-$Co_{0.4}Fe_{2.6}N$	(110)	2.391	2.390	a=4.781(1) * c=4.423(3) *	0.925(1) *
	(002)	2.214	2.211		
	(111)	2.102	2.103		
	(112)	1.622	1.623		
	(300)	1.380	1.380		
	(113)	1.253	1.254		

*** Parentheses indicate accuracy in precision to the last decimal digit. For example, 0.925(1) can be 0.924 or 0.926.**

3.3.1.4 XRD study of γ′-$Ni_xFe_{4-x}N$ ($0.2 \leq x \leq 0.8$) materials

The indexed XRD patterns of γ′-$Ni_xFe_{4-x}N$ ($0.2 \leq x \leq 0.8$) nitrides obtained by heating oxide precursors at 700˚C for 2h duration in continuous NH_3 (g) flow have been presented in figure 3.6. Pure phase γ′-Fe_4N (x=0) could not be synthesized using the current synthetic strategy. However, addition of Ni stabilized γ′-Fe_4N phase gradually. The crystal structure parameters of γ′-$Ni_xFe_{4-x}N$ ($0.2 \leq x \leq 0.8$) derived from XRD study are presented in table 3.5. The average crystallite sizes of the materials are presented in table 3.9. The average crystallite sizes of the materials were found to decrease with increasing substitution of Ni at wt% (i.e. from x 0.2 to x=0.8) and is in the range of 31-45 nm.

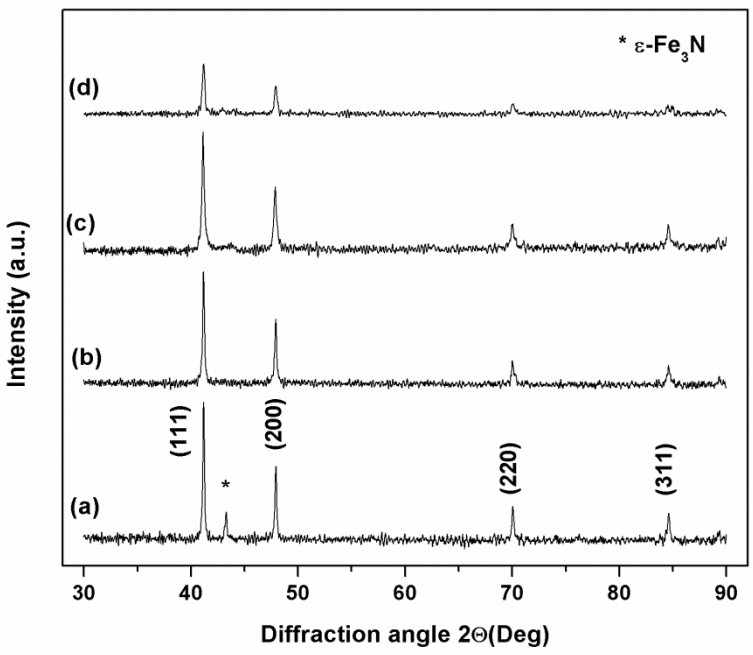

Figure 3.6 Indexed XRD patterns of γ′-$Ni_xFe_{4-x}N$ materials synthesized at 700˚C; (a) x = 0.2, (b) x = 0.4, (c) x = 0.6 and (d) x = 0.8. The impurity phase, ε-Fe_3N, has been marked as asterisk (*).

The lattice parameters of γ′-$Ni_xFe_{4-x}N$ (x=0.2, 0.4, 0.6, 0.8) system are found to be in the range of 3.792(2) Å-3.795(7) Å, which are in good agreement with the literature reported values of 3.787 Å-3.772 Å [22]. A slight increasing trend in the lattice parameters of the materials was observed with increase in Ni at wt% in our study up to x=0.6 and a decreasing trend thereafter (figure 3.7).The (inset) figure 3.7 shows the graphical representation (zoom plot) of the observed lattice expansion in our study.

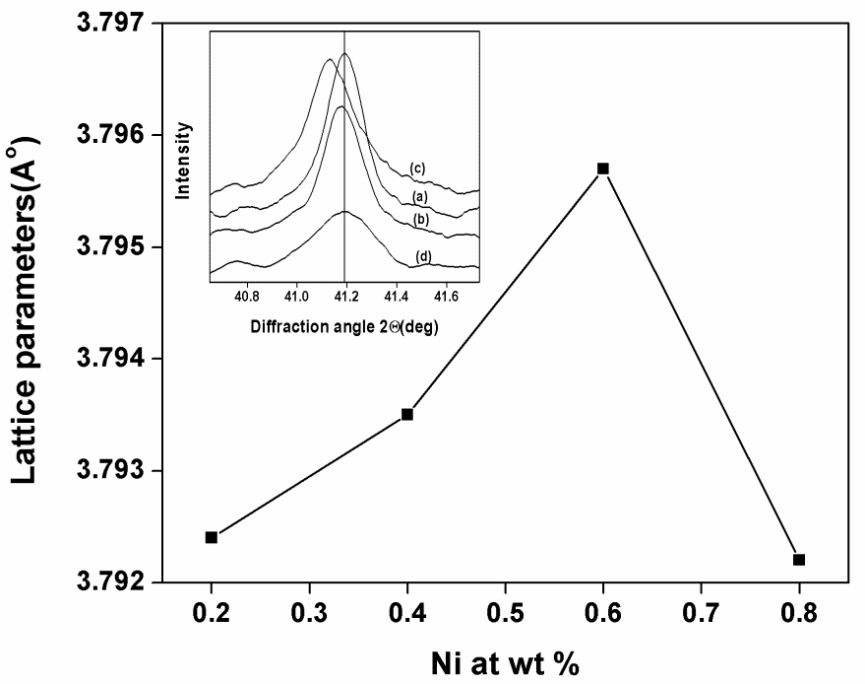

Figure 3.7 Composition dependent lattice parameters of γ′-$Ni_xFe_{4-x}N$ ($0.2 \leq x \leq 0.8$) materials. Inset figure shows change in (111) peak positions with various Ni content in γ′-$Ni_xFe_{4-x}N$ ($0.2 \leq x \leq 0.8$); x= (a) 0.2, (b) 0.4, (c) 0.6 and (d) 0.8.

The observed lattice expansion in γ′-$Ni_xFe_{4-x}N$(x=0.2, 0.4, 0.6, 0.8) system under our study, is in contrary to other studies reported in the literature [5, 23]. This expansion can be related to structural parameters of the nitride materials synthesized. One major factor for such anomaly may be lattice expansion of Ni nanoparticles with decrease in particle size [24]. The magnitude of the lattice parameter expansion is directly proportional to the reciprocal of the grain size. The lattice expansion is the combined result of the interfacial energy and surface tension due to mutual attraction of the Ni nanoparticles [24]. The effect of size-dependent lattice expansion in nanoparticles is very common [25]. The aforesaid effect arises due to a fundamental difference in the nature of expansion and contraction in nanoparticle systems [25].

Table 3.5 Materials phase, Miller indices (hkl), observed (d_{obs}) and calculated interplanar distance (d_{cal}) and lattice parameters of γ′-$Ni_xFe_{4-x}N$ (x=0.2, 0.4, 0.6, 0.8) nitrides.

Materials Phase	(hkl)	d_{obs} (Å)	d_{cal}(Å)	Lattice parameters(Å)
γ′-$Ni_{0.2}Fe_{3.8}N$	(111)	2.191	2.190	3.792(4)
	(200)	1.894	1.896	
	(220)	1.341	1.341	
	(311)	1.143	1.143	
	(222)	1.095	1.095	
γ′-$Ni_{0.4}Fe_{3.6}N$	(111)	2.188	2.190	3.793(5)
	(200)	1.897	1.896	
	(220)	1.342	1.341	
	(311)	1.143	1.143	
	(222)	1.095	1.095	
γ′-$Ni_{0.6}Fe_{3.4}N$	(111)	2.191	2.190	3.795(7)
	(200)	1.898	1.897	
	(220)	1.341	1.341	
	(311)	1.143	1.144	
	(222)	1.095	1.095	
γ′-$Ni_{0.8}Fe_{3.2}N$	(111)	2.191	2.192	3.792(2)
	(200)	1.897	1.898	
	(220)	1.341	1.342	
	(311)	1.145	1.144	
	(222)	1.097	1.096	

3.3.2 Elemental analysis of Fe-Co-N and Fe-Ni--N Nitrides

In this section, compositional analysis of the bimetallic nitride systems will be focused. As elemental analysis of nitrogen is difficult by AAS and approximate by EDX, care has been taken in order to estimate metal atom ratios along with the signature of the presence of the nitrogen. Co-Fe-N systems are analyzed by AAS whereas Fe-Ni-N systems by EDX and are presented as follows.

3.3.2.1 Atomic absorption spectroscopy of ε- $Co_xFe_{3-x}N$

The elemental composition of ε- $Co_xFe_{3-x}N$ material system was determined using atomic absorption spectroscopic technique. The values of absorbance were calibrated using pure metal chlorides of Fe, Co and Ni. The concentration of the solutions ranges for the standards were 0.5 – 2 ppm. The nitride materials were initially digested with hot HCl(aq.) and diluted for test solution preparation (2-5 ppm). Both theoretically and experimentally calculated weight % of the elements, i.e. Fe and Co, in ε-$Co_xFe_{3-x}N$ system are presented in

table 3.6. The concentration of the elements determined by AAS is lesser than the theoretically calculated values, however the stoichiometric trend while considering a range of compositions of varying Co and Fe atoms is evident from the estimation. This illustrates the insertion of Co atoms in ε-$Co_xFe_{3-x}N$ progressively, with the increase of Co content. The deviation of the experimental results from the theoretical value can be due to the presence of N, surface oxygen, organic content as the samples have been prepared via organometallic route. Furthermore, interferences of cationic and anionic species in the ppm level dilution may be a factor for error.

Table 3.6 Materials, Elements, Weight % calculated experimentally using AAS and theoretically.

Material	Elements	Weight %	
		Experimental (AAS)	Theoretical
ε- $Co_{0.1}Fe_{2.9}N$	Fe	70.16	89.13
	Co	3.06	3.18
ε- $Co_{0.2}Fe_{2.2.8}N$	Fe	62.01	85.96
	Co	5.45	6.35
ε- $Co_{0.3}Fe_{2.7}N$	Fe	61.2	82.80
	Co	8.39	9.52
ε- $Co_{0.4}Fe_{2.6}N$	Fe	66.15	79.64
	Co	7.82	12.69

3.3.2.2 EDX analysis of γ′-$Ni_xFe_{4-x}N$ ($0.2 \leq x \leq 0.8$) materials

The EDX spectra of the synthesized γ′-$Ni_xFe_{4-x}N$ ($0.2 \leq x \leq 0.8$) materials were recorded and the metal ratios were calculated experimentally. The metal ratios are presented in the table 3.7 given below and it corresponds well with the theoretically calculated metal weight % ratio.

Table 3.7 Materials, Elements, Atoms % calculated experimentally using EDX and theoretically.

Material	Elements	Atom %	
		Experimental (EDX)	Theoretical
ε- Fe_3N	Fe	89.83	75
	N	10.17	7.69
γ′-$Ni_{0.2}Fe_{3.8}N$	Fe	96.34	95
	Ni	3.66	5
	N	--	--
γ′-$Ni_{0.4}Fe_{3.6}N$	Fe	91.95	90
	Ni	8.05	10
	N	--	--
γ′-$Ni_{0.6}Fe_{3.4}N$	Fe	84.76	85
	Ni	14.44	15
	N	0.80	--
γ′-$Ni_{0.8}Fe_{3.2}N$	Fe	83.90	80
	Ni	16.10	20
	N	--	--

3.3.3 Electron microscopy studies of ε-$Co_xFe_{3-x}N$ ($0 \leq x \leq 0.4$) and γ′-$Ni_xFe_{4-x}N$ ($0.2 \leq x \leq 0.8$) materials

In order to probe the morphology (particle shape and size) and microstructure of ε-$Co_xFe_{3-x}N$ ($0 \leq x \leq 0.4$) and γ′-$Ni_xFe_{4-x}N$ ($0.2 \leq x \leq 0.8$) nitrides, SEM studies were performed. Various magnifications starting from 5000X to 30000X were attempted. Micrographs with magnifications higher than 30000X were not obtained with clear contrast and appear to be out of focus. The details of the experimental results are shown in the following sub-sections.

3.3.3.1 SEM studies of ε-$Co_xFe_{3-x}N$ ($0 \leq x \leq 0.4$) and γ′-$Ni_xFe_{4-x}N$ ($0.2 \leq x \leq 0.8$) materials

3.3.3.1.1 SEM studies of ε-$Co_xFe_{3-x}N$ ($0 \leq x \leq 0.4$)

Typical SEM micrographs of ε-$Co_xFe_{3-x}N$ ($0 \leq x \leq 0.4$) materials for x=0, x=0.2, x=0.3 and x=0.4 are shown in figure 3.8 ((a) –(h)) with two different magnification ranges, i.e. ~ 5000-10000X ((a), (c), (e) and (g)) and ~20000-25000X ((b), (d), (f) and (h)).

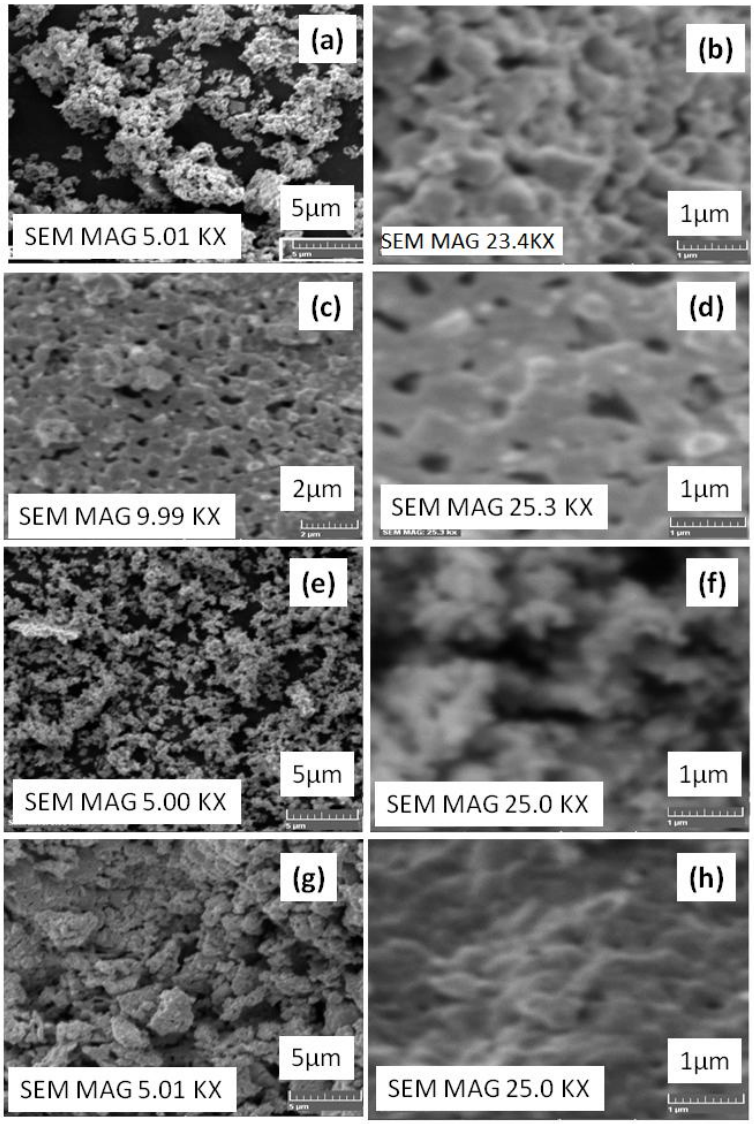

Figure 3.8 SEM micrographs of ε-Fe_3N ((a), (b)) and ε-$Co_xFe_{3-x}N$ ($0.2 \leq x \leq 0.4$) materials for x=0.2 ((c), (d)), x=0.3 ((e), (f)) and x=0.4 ((g), (h)).

The images with lower magnifications appear to be agglomerated clusters of several particles with hollow cavities. The figure also shows spherical nature of the particles with the particle sizes in the range 155-110 nm. The SEM particle sizes are tabulated in table 3.8.The observed SEM particle sizes are larger than the crystallite sizes i.e. 44-55 nm. These results indicate strong interparticle interactions towards formation of agglomerates in ε-Fe_3N and ε-$Co_xFe_{3-x}N$ ($0.2 \leq x \leq 0.4$) nitrides. Similar kinds of observations in Fe- and Co-based nano-particle systems synthesized by chemical routes have been well established [26, 27].

Table 3.8 Materials, Co at.wt% (x), Average crystallite sizes and SEM sizes of ε-Fe_3N (x=0) and ε-$Co_xFe_{3-x}N$ ($0.2 \leq x \leq 0.4$) materials.

Materials	Co at.wt% (x)	Average crystallite size(nm)	SEM particle size (nm)
ε-Fe_3N	--	54± 0.8	155±15
ε-$Co_xFe_{3-x}N$	0.2	54±0.8	144±9
	0.3	44±0.7	123±15
	0.4	55±0.8	110±10

3.3.3.1.2 SEM studies of γ′-$Ni_xFe_{4-x}N$ ($0.2 \leq x \leq 0.8$) materials

The SEM micrographs of γ′-$Ni_xFe_{4-x}N$ ($0.2 \leq x \leq 0.8$) materials have been presented in figure 3.9 with two different magnifications, i.e. 7500X and 20000X. Figure 3.9 ((a), (b)); ((c), (d)); ((e), (f)) and ((g), (h)) represent SEM micrographs with the values of Ni content, x = 0.2, 0.4, 0.6 and 0.8, respectively. The micrographs show aggregation of particulates in a non-uniform manner with several voids having dimension of several micrometer (μm) located in between the islands consisting of several particles. The SEM particle sizes are tabulated in table 3.9. The agglomeration of the nanoparticles in SEM micrographs can be due to its magnetic nature [27, 28]. The particles exhibit nearly spherical nature with sizes ranging between 155 nm to 250 nm, which are larger than the corresponding crystallite sizes of 45-31 nm because of the fact that a single particle may be consisted of several smaller crystallites.

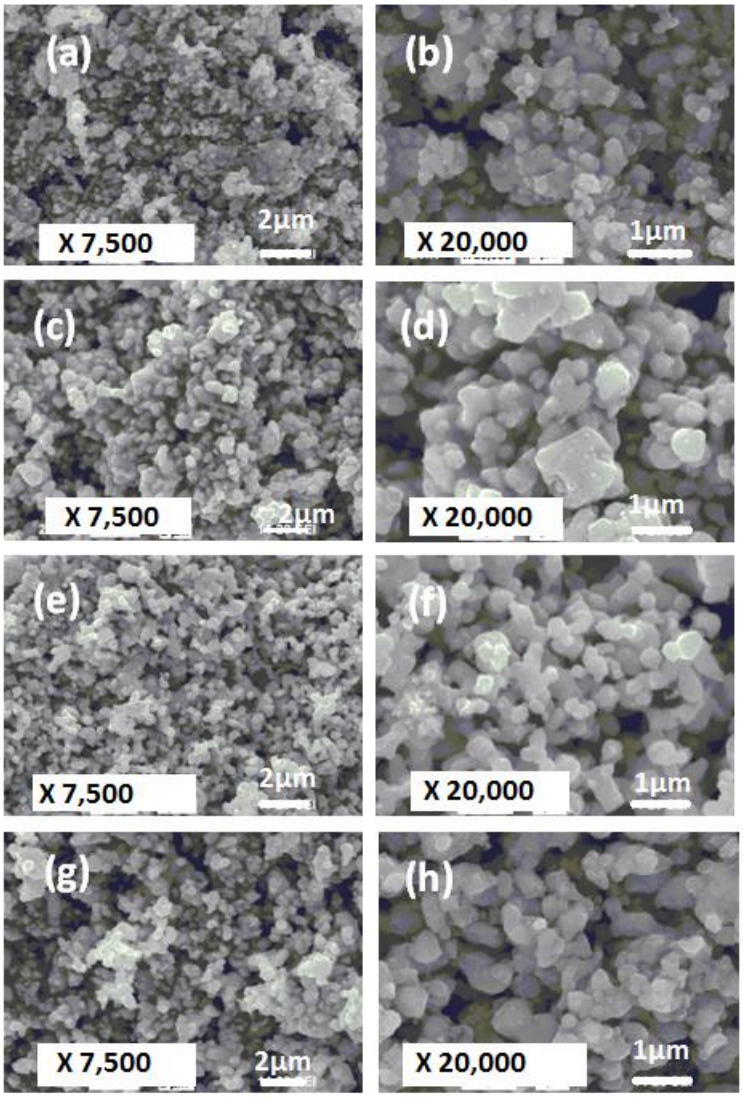

Figure 3.9 SEM micrographs of γ′-$Ni_xFe_{4-x}N$ ($0.2 \leq x \leq 0.8$) materials; ((a), (b)) x = 0.2, ((c), (d)) x = 0.4, ((e), (f)) x = 0.6 and ((g), (h)) x = 0.8.

Table 3.9 Materials, Ni at. wt%, Average crystallite size, SEM particle sizes of γ′-$Ni_xFe_{4-x}N$($0.2 \leq x \leq 0.8$) materials.

Material Phase	Ni at.wt%(x)	Average crystallite size(nm)	SEM particle size (nm)
γ′-$Ni_xFe_{4-x}N$	0.2	45±0.7	155±9
	0.4	43±0.6	210±17
	0.6	32±0.5	240±11
	0.8	31±0.5	250±14

3.3.3.1.3 EDX studies of ε-Fe_3N and γ′-$Ni_{0.4}Fe_{3.6}N$ nitride materials

In order to probe elemental composition and presence of nitrogen atoms in ε- and γ′-phase based iron nitride phases at micro-level, EDX studies have been performed on several selected nitride materials. Two representative nitride materials, i.e. pure hexagonal ε-Fe_3N and cubic γ′-$Ni_{0.4}Fe_{3.6}N$, are presented in this subsection.

The EDX spectra of ε-Fe_3N and cubic γ′-$Ni_{0.4}Fe_{3.6}N$ materials have been shown in figure 3.10 (a) and (b), respectively. Atomic percentage (at %) of the elements present (Fe, Ni, N etc.) are indicated in the above mentioned figure. Although, we could detect N atoms in the EDX spectra of both ε-Fe_3N and cubic γ′-$Ni_{0.4}Fe_{3.6}N$ phases, it was difficult to resolve the N peak in γ′- phase. The peak position corresponding to N in ε-Fe_3N was recorded at the energy value of 0.3 keV. The distinct peak position corresponding to N could not be resolved from the EDX spectrum of γ′-$Ni_{0.4}Fe_{3.6}N$ because of low energy cutoff [29]. This may also be due to presence of lower nitrogen content in γ′-$Ni_{0.4}Fe_{3.6}N$ nitride compared to ε-Fe_3N and alteration of bonding parameters including material disorder [29]. Similar kinds of results have already been reported in the literature for nitride materials in the form of thin film and nanowires [29- 31]. However, the Fe/Ni ratio, i.e. 11.5, obtained from EDX spectra of γ′-$Ni_{0.4}Fe_{3.6}N$ is significantly close to the stoichiometric ratios of the nitride materials. It should be noted that while estimating the metal ratios, total metal contents have been taken 100 wt % of the materials.

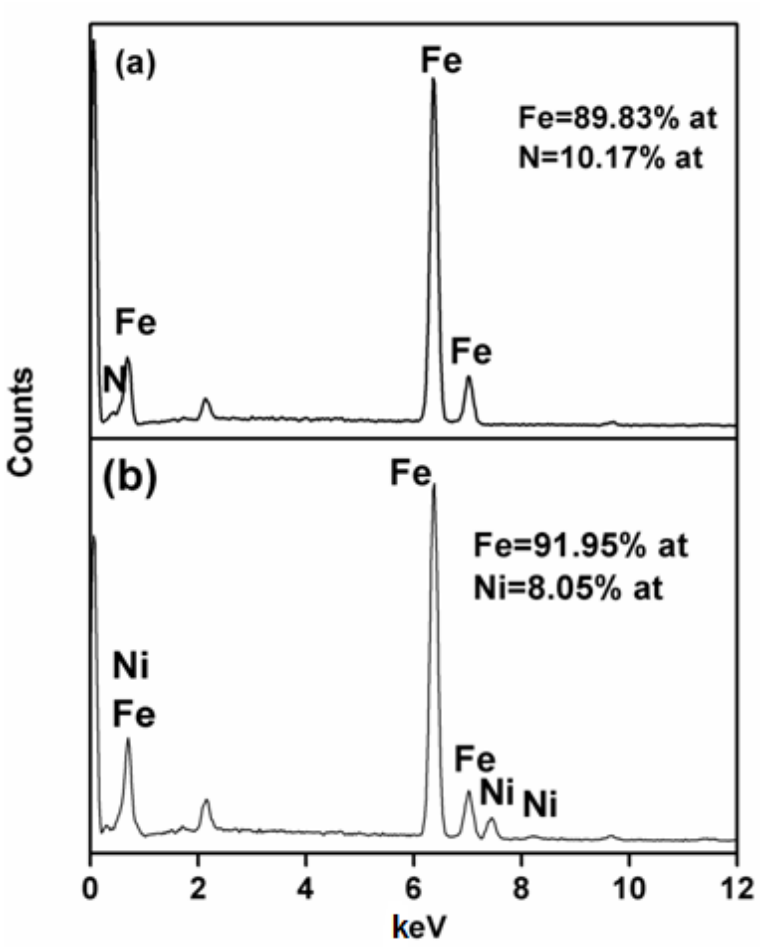

Figure 3.10 EDX spectra of (a) ε-Fe_3N and (b) γ′-$Ni_{0.4}Fe_{3.6}N$ Nitrides.

3.3.3.2 TEM studies of ε-Fe_3N and γ′-$Ni_xFe_{4-x}N$ ($0.2 \leq x \leq 0.8$) materials

In order to elucidate the nanostructure in more detail and to confirm the iron based interstitial nitride, TEM studies of selected samples have been carried out. As it has been observed that crystallite sizes are quite smaller than the observed SEM sizes due to agglomeration, a deeper understanding of the particulates constituting the agglomerates is necessary. In addition, studies on the diffraction pattern may give some insight regarding structure information including ordered arrangement of interstitial atoms. TEM studies of ε-Fe_3N and γ′-$Ni_xFe_{4-x}N$ ($0.2 \leq x \leq 0.8$) materials have been presented in the following subsections.

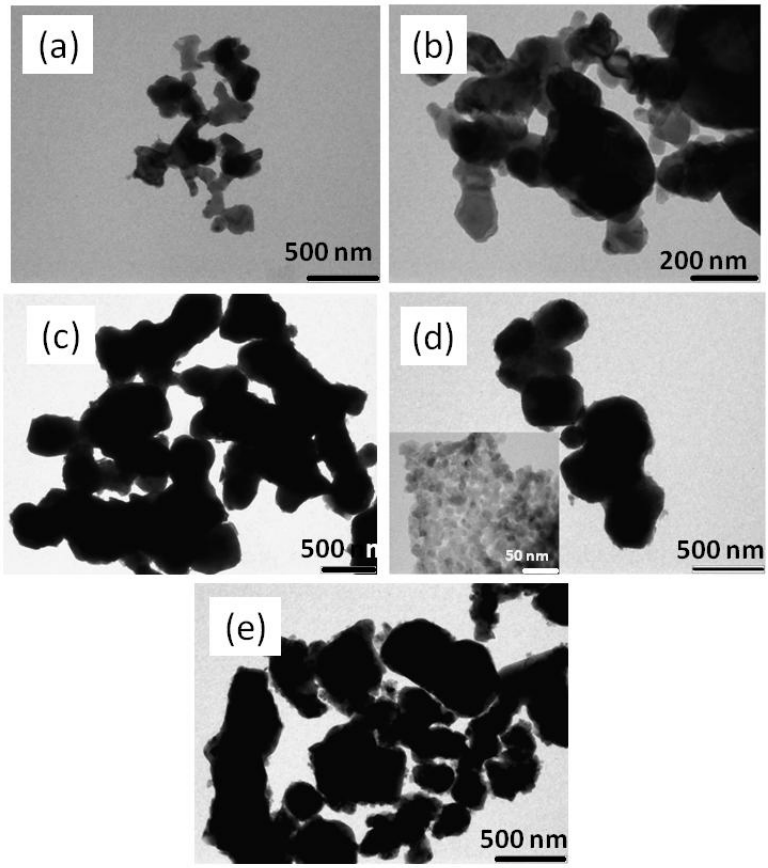

Figure 3.11 TEM micrograph of (a) ε-Fe_3N and γ′-$Ni_xFe_{4-x}N$ ($0.2 \leq x \leq 0.8$) materials; (b) x = 0.2, (c) x = 0.4, (d) x = 0.6 and (e) x = 0.8.

TEM micrographs of ε -Fe_3N and γ′-$Ni_xFe_{4-x}N$ ($0.2 \leq x \leq 0.8$) materials are depicted in figure 3.11. The figure shows chain like structure of agglomerated particles. As the particles are magnetic in nature, each magnetic particle is an assembly of spheroid microcrystallites. The particles show sphericity with measurable particle size up to 8 nm for γ′-$Ni_{0.6}Fe_{3.4}N$ material system.

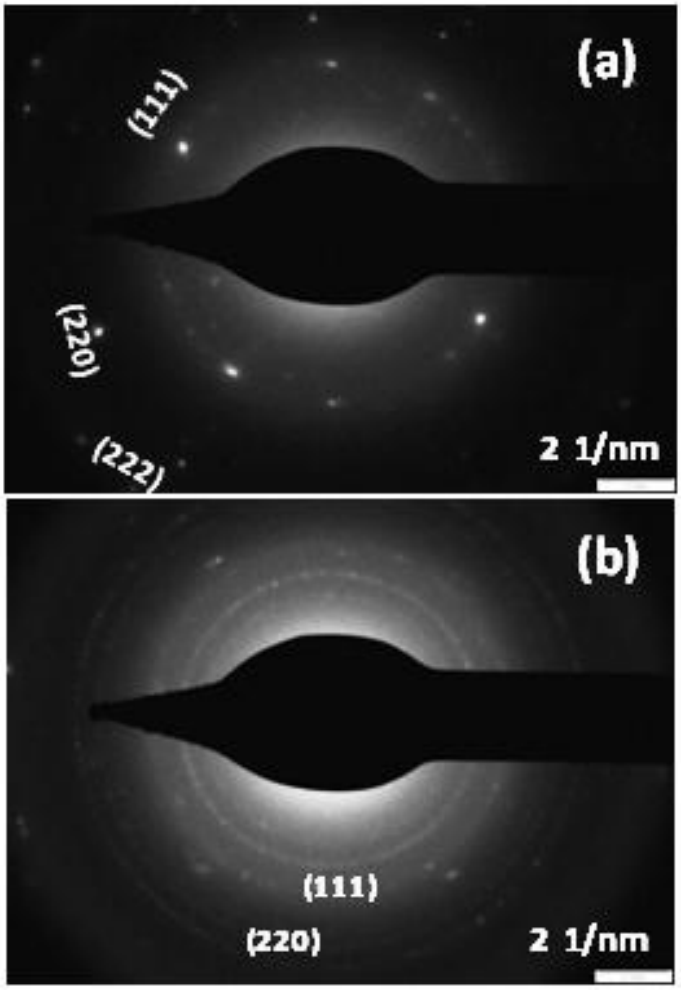

Figure 3.12 Selected area electron diffraction (SAED) patterns of γ′-$Ni_xFe_{4-x}N$ ($0.2 \leq x \leq 0.8$); (a) x= 0.4 and (b) x = 0.6 materials.

In order to probe the structural characteristics, two representative SAED patterns of γ′-$Ni_{0.4}Fe_{3.6}N$ and γ′-$Ni_{0.6}Fe_{3.4}N$ have been presented in figure 3.12. For γ′-$Ni_{0.4}Fe_{3.6}N$ materials the electron diffraction pattern consists of some bright Laue spots arranged in circular manner. Such kind of SAED pattern represents nano-crystalline nature of the synthesized sample. The diffraction rings corresponding to different crystallographic planes are indexed (figure 3.12(a)). The interplanar distance 'd' calculated from the diffraction patterns are found to be 2.098, 1.324 and 1.091 Å, which correspond well with the 'd' spacing of (111), (220) and (222) crystal planes.

Table 3.10 Materials, interplanar distance 'd', Miller indices and lattice parameters calculated from XRD and SAED patterns of γ′-$Ni_xFe_{4-x}N$(x = 0.4, 0.6) materials.

Materials	Interplanar distance 'd'(Å)		Miller indices (hkl)	Lattice parameter 'a'(Å)	
	XRD	SAED		XRD	SAED
γ′-$Ni_{0.4}Fe_{3.6}N$	2.188	2.098	(111)	3.793	3.633*
	1.342	1.324	(220)		---
	1.095	1.091	(222)		---
γ′-$Ni_{0.6}Fe_{3.4}N$	2.191	2.155	(111)	3.795	3.732*
	1.341	1.459	(220)		---

***Estimation of Lattice parameters from SAED pattern has been done considering (111) plane.**

For γ′-$Ni_{0.6}Fe_{3.4}N$ materials, electron diffraction pattern consists of several concentric bright rings made up by small bright spots, centered on a bright central spot representing the undiffracted electrons. Each spot arises from Bragg reflection of an individual crystallite corresponding to a particular set of planes. This indicates polycrystalline and ultrafine nature of the materials [32]. Also, each ring corresponds to a particular crystal plane with a fixed interplanar distance. The diffraction rings corresponding to different crystallographic planes are indexed in figure 3.12 (b). The calculated interplanar spacing 'd', Miller indices and lattice parameters calculated from SAED pattern are presented in table 3.10.

3.3.4 Magnetic properties study

The magnetic properties of ε-$Co_xFe_{3-x}N$ ($0 \leq x \leq 0.4$) and γ′-$Ni_xFe_{4-x}N$ ($0.2 \leq x \leq 0.8$) materials were studied at room temperature and analyzed in detail to correlate with other structural parameters using VSM technique. The results obtained are discussed in the following subsections.

3.3.4.1 Magnetic properties of ε-$Co_xFe_{3-x}N$ ($0 \leq x \leq 0.4$)

The field dependent magnetization plots for ε-$Co_xFe_{3-x}N$ ($0 \leq x \leq 0.4$) have been presented in figure 3.13(a, b, c, d). The plots of specific magnetization versus inverse of applied field have been shown in figure 3.14. M_s values for ε-$Co_xFe_{3-x}N$ ($0 \leq x \leq 0.4$) materials were estimated from the intercepts of the plots on the magnetization axis (figure 3.14) [9, 33]. The M_s values for ε-$Co_xFe_{3-x}N$ ($0 \leq x \leq 0.4$) materials lie in the range of 8-39 emu/g. The coercivity, H_c, was obtained as the negative intercept of magnetic hysteresis loop on applied field axis from the M vs. H plot. The coercivity values for ε-$Co_xFe_{3-x}N$ ($0 \leq$

$x \leq 0.4$) are in the range of 199- 219 Oe. The values of the saturation magnetization, M_s and coercivity, H_c, have been presented in table 3.11. The effect of Co substitution on the magnetization and coercivity of ε-$Co_xFe_{3-x}N$ ($0 \leq x \leq 0.4$) materials has been depicted in figure 3.15.

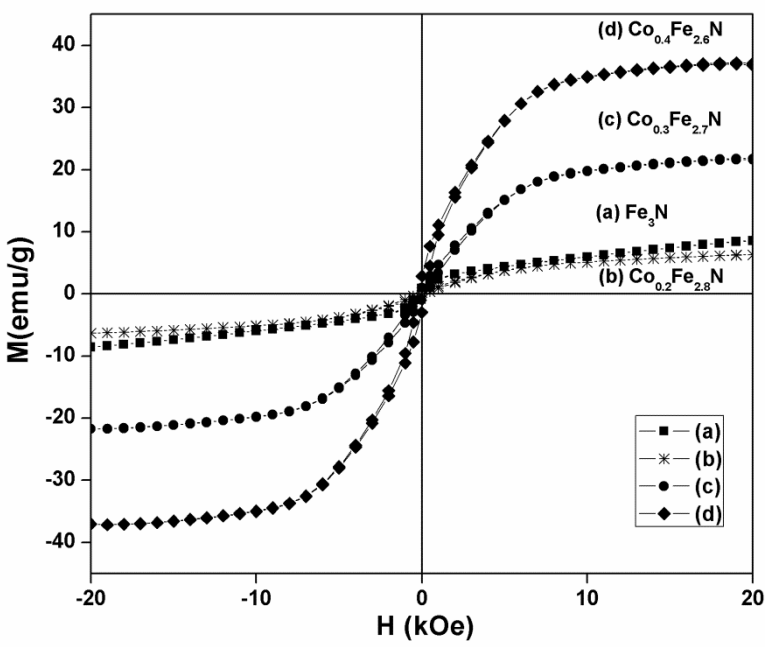

Figure 3.13 Plot of specific magnetization as a function of field for (a) ε-Fe_3N and ε-$Co_xFe_{3-x}N$ ($0.2 \leq x \leq 0.4$) materials; (b) x=0.2, (c) x=0.3 and (d) x=0.4.

The room temperature hysteresis loops of ε-$Co_xFe_{3-x}N$ ($0 \leq x \leq 0.4$) show that the plots do not get saturated even at applied field of 20 kOe. This observation implies that the synthesized materials are superparamagnetic in nature. Referring to the results obtained from XRD studies regarding expansion of the lattice volume, i.e. 101 $Å^3$, compared to the reported values of 96.75 $Å^3$ for stoichiometric composition, it can be concluded that nitrogen content in our sample is far beyond the stoichiometric, ε-Fe_3N, i.e. ε-$Fe_3N_{1.37}$ [11, 21].The value of M_s for ε-Fe_3N was obtained as 11 emu/g, which is quite less than the reported bulk value of 48emu/g for ε-$Fe_3N_{1.33}$ [15]. The large decrease of magnetization value, i.e. down to 11emu/g, as compared to theoretical reported value of 123 emu/g for bulk ε-Fe_3N [34] as a result of increase in nitrogen content has already been explained by the electron donor ability of N-2p states to Fe-3d states, thereby reducing the intrinsic magnetic moments of Fe atoms [15,35]. For Co content, x = 0.2 at wt%, the value of saturation magnetization is

slightly less than that of pure ε-Fe_3N, i.e. 8 emu/g. However, with the increase in Co content, enhancement of magnetization was observed up to 39 emu/g for x= 0.4 in ε-$Co_xFe_{3-x}N$ ($0 \leq x \leq 0.4$) system, which is evident from the figure 3.14. This observation is quite consistent with literature reported results [20, 36], the reason majorly being the generation of giant magnetic Fe phase. This result can be explained on the basis of structural alteration in the lattice due to Co atoms leading to high moment Fe atoms.

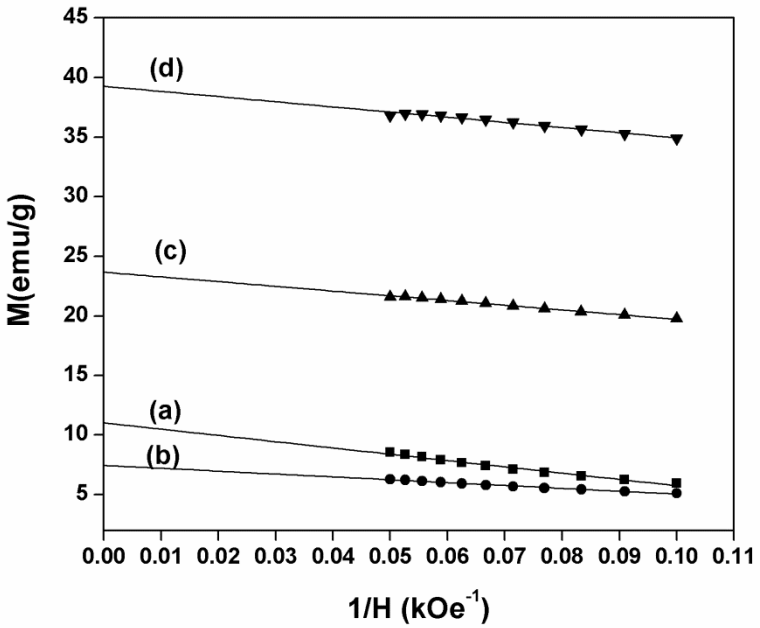

Figure 3.14 Plot of specific magnetization as a function of H^{-1} for ε-$Co_xFe_{3-x}N$ materials; (a) x=0, (b) x = 0.2, (c) x = 0.3 and (d) x = 0.4.

In our investigation, the increase of saturation magnetization as a function of increasing Co content can be mainly due to change in magnetic structure of the materials in the crystal lattice of ε-Fe_3N phase. In fact, ε-Fe_3N phases with higher nitrogen content are disordered in nature when compared with the stoichiometric ratios. The spin up and spin down states population in ε- Fe_3N phase are affected by nitrogen atom distribution in disordered state, thus affecting the magnetic moments of the Fe atoms [37]. Insertion of Co may result in: (1) change in structural parameters as a result of alteration of lattice parameter, (2) exchange interactions amongst the neighboring Fe atoms and (3) finally the shape and size of the materials. As the average crystallite sizes for various ε-$Co_xFe_{3-x}N$ ($0 \leq x \leq 0.4$) materials do not differ much, we anticipate the increasing trend in magnetization to the former two factors mentioned above.

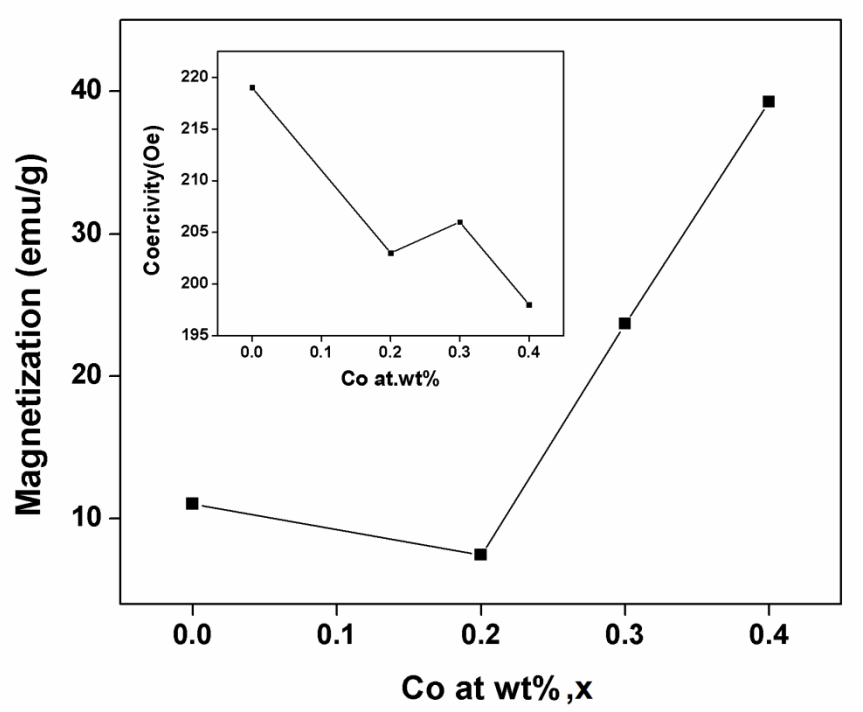

Figure 3.15 Plot of saturation magnetization vs. Co at.wt% of ε-$Co_xFe_{3-x}N$ (x=0, 0.2, 0.3, 0.4). Inset figure shows the plot of coercivities vs. Co at. wt%.

These results can also be correlated to initial decrease in c/a ratio up to x=0.2 and thereafter a gradual increase up to x=0.4 with lattice expansion [10]. The atomic radius of Fe, i.e. 1.56Å, being larger than the atomic radius of Co, i.e. 1.52 Å, one can expect contraction of lattice. The observed lattice expansion may be majorly due to distribution of nitrogen atoms inside the host hcp lattice in addition to nanosize effect. The values of saturation magnetization in ε-Fe_3N and ε-$Co_xFe_{3-x}N$ ($0.2 \leq x \leq 0.4$), i.e. 8-39 emu/g, at 300K are considerably smaller than the corresponding reported values of approximately 83-170 emu/g [38].

The decrease in the values of saturation magnetization at room temperature may be due to size and surface effect in our materials. With a decrease in size of the ferromagnetic materials, thermal effect, k_BT plays an important role in decreasing specific magnetizations as a result of superparamagnetic relaxation [10]. Furthermore, for fractions of materials found in the surfaces, different magnetic structures cannot be overruled [39]. Also, canted spin structures at the surface of the particles can reduce the values of saturation magnetization [26, 39]. The coercivity of the materials in ε-Fe_3N and ε-$Co_xFe_{3-x}N$ ($0.2 \leq x \leq$

0.4) almost remains constant with a gradual increase in the values of Co at %. The value of the H_c is dependent on magnetocrystalline anisotropy and shape and size of the materials. As ε-Fe_3N and ε-$Co_xFe_{3-x}N$ ($0.2 \leq x \leq 0.4$) materials crystallize in hexagonal close packed structure, shape and size of the materials are major factors for the origin of coercivity.

Table 3.11 Material, Co at.wt%, saturation magnetization (M_s) and coercivity (H_c) of ε-$Co_xFe_{3-x}N$ ($0.2 \leq x \leq 0.4$) nitrides.

Material	Co at.wt%	M_s (emu/g)	H_c (Oe)
ε-$Co_xFe_{3-x}N$	0	11	219
	0.2	8	204
	0.3	24	206
	0.4	39	199

In summary, the magnetic parameters in ε-Fe_3N and ε-$Co_xFe_{3-x}N$ ($0.2 \leq x \leq 0.4$) nano-crystalline system depend upon several factors, such as: nitrogen content, lattice expansion, enhancement of magnetic moments of atoms in the crystal structure, fine particle size, surface effects and spin canting at the surface of the nano-materials. The increasing trend in saturation magnetization in ε-$Co_xFe_{3-x}N$ ($0.2 \leq x \leq 0.4$) system is largely attributed to the cobalt content.

3.3.4.2 Magnetic properties of γ′-$Ni_xFe_{4-x}N$ ($0.2 \leq x \leq 0.8$) materials

The room temperature magnetic hysteresis plots for γ′-$Ni_xFe_{4-x}N$ ($0.2 \leq x \leq 0.8$) materials are presented in figure 3.16. The hysteresis plots do not get saturated even at applied field of 20 kOe, which signifies onset of superparamagnetism at 298K. The plot of specific magnetization versus inverse of field has been presented in figure 3.17. The values of M_s for γ′-$Ni_xFe_{4-x}N$ ($0.2 \leq x \leq 0.8$) materials are found to be in the range of 144-181emu/g. The coercivities of the materials are estimated to be in the range of 76-106 Oe. The variation of M_s and H_c with Ni content, x is presented in figure 3.18. The values of M_s and H_c of the corresponding material phase have been presented in table 3.12.

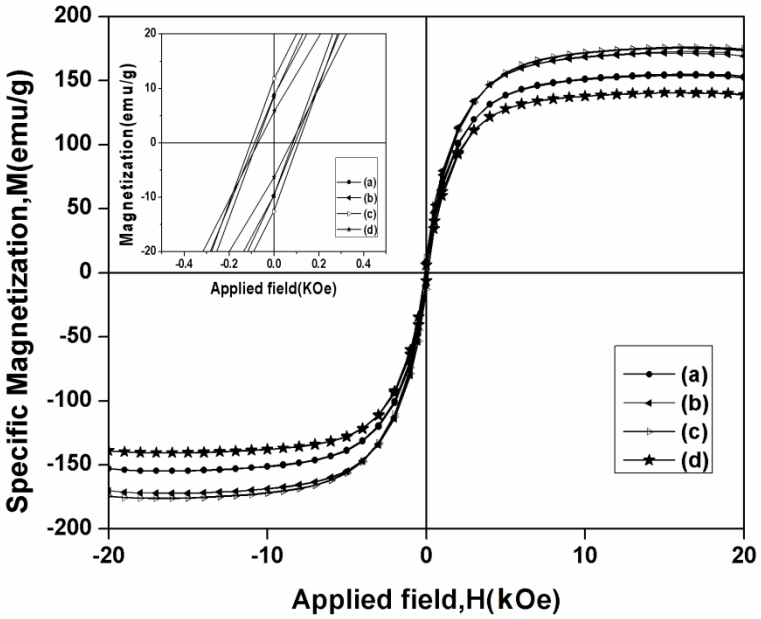

Figure 3.16 Plot of specific magnetization as a function of field for γ′-$Ni_xFe_{4-x}N$ ($0.2 \leq x \leq 0.8$) materials for (a) x = 0.2, (b) x = 0.4, (c) x = 0.6, (d) x = 0.8 materials. Inset shows zoom in plots near 0 kOe for clarity reason.

With progressive Ni substitution in the γ′- Fe_4N lattice, the value of saturation magnetization was found to increase from 158 emu/g for x = 0.2 to 181 emu/g for x = 0.6. The value of M_s decreased thereafter to 144 emu/g for x = 0.8. However, there is no significant alteration in the values of coercivities with the change in wt % of Ni(x).The larger values of M_s can be attributed to the nanosize effect of the synthesized materials. The M_s values for γ′-$Ni_xFe_{4-x}N$ ($0.2 \leq x \leq 0.8$) are larger but quite smaller than the reported M_s value of bulk γ′-Fe_4N, i.e. 208 emu/g at 0K [7, 9]. These observations can be correlated to the nanosize and surface effect along with Ni substitution.

Table 3.12 Material, Ni at.wt%, Saturation magnetization (M_s) and Coercivity (H_c) of γ′-$Ni_xFe_{4-x}N$ ($0.2 \leq x \leq 0.8$) nitrides

Material Phase	Ni at.wt%(x)	M_s (emu/g)	H_c (Oe)
γ′-$Ni_xFe_{4-x}N$	0.2	158	95
	0.4	176	82
	0.6	181	109
	0.8	144	76

There are several factors responsible for this kind of unusual trend in saturation magnetization with progressive Ni atoms substitution. It has been well known that addition of Ni in γ′- Fe_4N structure, induces magnetic dilution as the magnetic moment of Ni (55emu/g) is considerably less than that of α-Fe (222 emu/g) [28,40]. The second effect may be correlated to change in lattice volume leading to alteration of exchange interactions in the lattice, thereby marginal change in overall magnetization. The combined effect of both the factors explained above leads to overall decrease in magnetic moments with progressive increase in Ni wt %, and has been reported by several investigators with different synthesis and processing of the materials [22, 41]

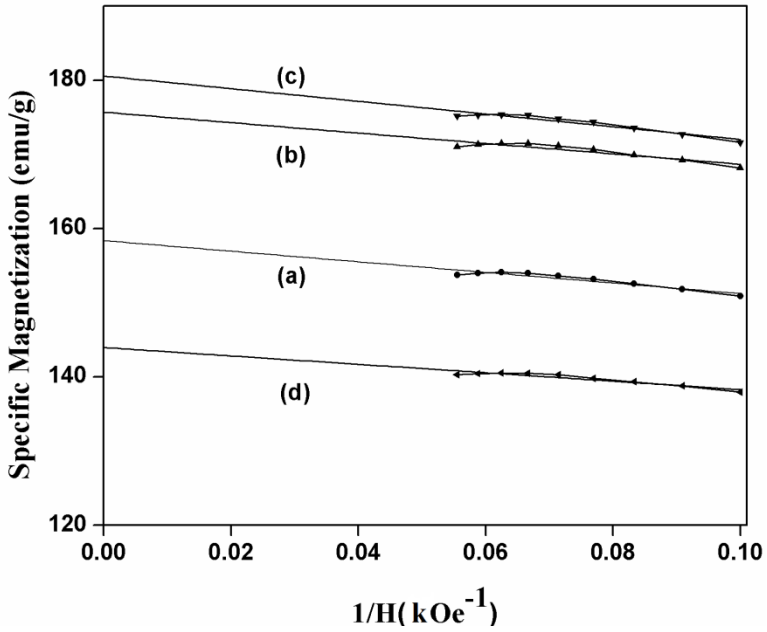

Figure 3.17 Plot of specific magnetization as a function of H^{-1} for γ′-$Ni_xFe_{4-x}N$ (a) x=0.2, (b) x= 0.4, (c) x =0.6, (d) x= 0.8 materials.

In addition, with progressive substitution of Ni, generation of high moment Fe atoms in the corner position of fcc lattice has been reported [7]. The magnitude of this enhanced magnetic moment may be dependent on particle size and lattice strain. Reduction of particle size may lead to enhancement in magnetic moment in appreciable amount. For example for a change of average particle size of 51.3-18.6 nm change of 0.117% volume expansion has been observed for Ni [25]. In our study, we have reduction of average crystallite size, i.e. 45 nm for x=0.2 sample to 31nm for x=0.8 sample. This may also contribute towards generation of high moment Fe atoms in addition to reduction of magnetization by size and

surface effects. As it can be seen from figure 3.7, materials having Ni content x=0.4 and 0.6, show lattice strain which can be evident from lattice expansion and non-Gaussian peak shapes. We believe, the lattice strain in γ′-$Ni_xFe_{4-x}N$ ($0.2 \leq x \leq 0.8$), for x=0.4 and 0.6, may be a responsible factor for the increase in magnetization [7].

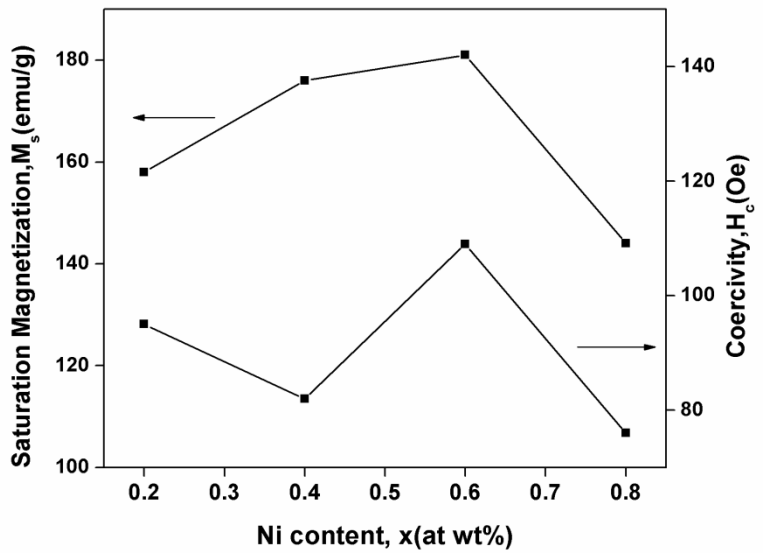

Figure 3.18 Plot of Ni at. wt% vs. saturation magnetization and coercivity of γ′-$Ni_xFe_{4-x}N$($0.2 \leq x \leq 0.8$) materials.

Above all, the change in magnetocrystalline anisotropy of different materials in the series γ′-$Ni_xFe_{4-x}N$ ($0.2 \leq x \leq 0.8$) along with size and surface effects may give rise to altered fractions of superparamagnetism which may contribute towards the values of saturation magnetizations at room temperature. The nearly comparable values of coercivities for γ′-$Ni_xFe_{4-x}N$ ($0.2 \leq x \leq 0.8$) series of materials, from 76-109 Oe, for the values of x=0.2-0.8 indicate that all the materials used in this study are well below the critical size range and are single domain in nature. The coercivities are of 'Stoner and Wohlfarth' type with magnetization reversal by spin rotation mechanism [42, 43]. This also indicates narrow particle size distributions, leading to no abrupt changes in the coercivities. In summary, we have succeeded in synthesizing γ′-$Ni_xFe_{4-x}N$ ($0.2 \leq x \leq 0.8$) nitride nano-materials with higher magnetic moments and reduced coercivities. The observed new trend in magnetizations as a function of Ni content has been explained in detail.

3.4 Conclusion

Nanocrystalline ε-$Co_xFe_{3-x}N$ ($0 \leq x \leq 0.4$) and γ′-$Ni_xFe_{4-x}N$ ($0.2 \leq x \leq 0.8$) materials have been synthesized via citrate precursor method. The nanocrystallites of ε-$Co_xFe_{3-x}N$ and γ′-$Ni_xFe_{4-x}N$ are in the size range of 44-54 nm and 31-45 nm, respectively. The synthesized materials have been characterized using XRD, SEM, EDX and VSM technique.

The XRD patterns confirm the evolution of hexagonal phase in ε-$Co_xFe_{3-x}N$ ($0 \leq x \leq 0.4$) system. With the increase in Co substitution in the iron nitride system, precipitation of α-Fe is observed, which is trapped in the nitride matrix. The values of lattice parameters are found to be in the range of a= 4.772(8) -4.783(9) Å and c = 4.413(7) - 4.423(2) Å for ε-$Co_xFe_{3-x}N$ ($0 \leq x \leq 0.4$) materials. The electron microscopy study of the materials exhibits greater particle sizes revealing possible agglomeration of the particles due to magnetic nature. The magnetization vs. field curves do not get saturated even at higher applied field strength and indicate superparamagnetic nature of the materials. The coercivity of ε-$Co_xFe_{3-x}N$ materials almost remains constant with a gradual increase in the values of x. The values of the saturation magnetizations are in the range of 8-39 emu/g for ε-$Co_xFe_{3-x}N$ ($0 \leq x \leq 0.4$) materials. The saturation magnetization is found to decrease slightly up to x= 0.2 in ε-$Co_xFe_{3-x}N$ ($0 \leq x \leq 0.4$) and there after increases with increase in Co at wt%. The results have been explained on the basis of altered structural and magnetic characteristics and fine particle size and surface effects.

γ′-$Ni_xFe_{4-x}N$ ($0.2 \leq x \leq 0.8$) nitrides crystallize in cubic structures. The estimated lattice parameters are found in the range of 3.792(2)-3.795(7) Å for γ′-$Ni_xFe_{4-x}N$ ($0.2 \leq x \leq 0.8$) materials. The values of lattice parameters for γ′-$Ni_xFe_{4-x}N$ ($0.2 \leq x \leq 0.8$) increase slightly up to x=0.6 and then decrease for x=0.8. The particles are spherical in nature and have SEM particle sizes in the range of 190-498nm. EDX measurement of the samples confirms the elemental composition present in the compounds. The values of the saturation magnetizations are in the range of 144-181 emu/g for γ′-$Ni_xFe_{4-x}N$ ($0.2 \leq x \leq 0.8$) materials. There is an increasing trend observed in the values of saturation magnetization for the γ′-$Ni_xFe_{4-x}N$ ($0.2 \leq x \leq 0.8$) materials for x= 0.2 to x= 0.6 and then decrease for x= 0.8. This observed new trend has been explained on the basis of size and surface effects in addition to lattice strain and surface effects.

References

1. W. Yin , D. Zhang , P. Zhang , X. Wang , W. Wang , X. Lei , Z. Shi , H. Yang, J. Alloys Compd. **688** (2016) 828-832.
2. Z. Schnepp, M. Thomas, S. Glatzel, K. Schlichte, R. Palkovits, C. Giordano, J. Mater. Chem. **21** (2011) 17760–17764.
3. R. Loloee, J. Appl. Phys. **112** (2012) 023902 (1-6).
4. P. Zhang, X. Wang, W. Wang, X. Lei, H. Yang, Dalton Trans. **45** (2016) 296-299.
5. D. Xue, F. Li, J. Yang, Y. Kong, M. Gao, J. Magn. Magn. Mater. **172** (1997) 165-172.
6. X. G. Diao, R. B. Scorzelli, H. R. Rechenberg, J. Magn. Magn. Mater. **218** (2000) 81-90.
7. F. Li, J. Yang, D. Xue, R. Zhou, Appl. Phys. Lett. **66** (1995) 2343-2345.
8. N. S. Gajbhiye, R. S. Ningthoujam, S. Bhattacharyya, Hyperfine Interact. **164** (2005) 17–26.
9. R. N. Panda, N. S. Gajbhiye, IEEE Trans. Magn. **34** (1998) 542–548.
10. R. N. Panda, N.S. Gajbhiye, J. Appl. Phys. **81** (1997) 335–339.
11. M. Minagawa, H. Yanagihara, M. Kishimoto, E. Kita, Mater. Trans. **51** (2010) 2173-2176.
12. D. Moszynski, I. Mozynska, W. Arabczyk, Material letters. **78** (2012) 32-34.
13. D. Andrimandroso, L. Fefilatiev, G. Demazeau, L. Fournes, M. Pouchard, Mater. Res. Bull. **19** (1984)1187–1194.
14. B. Siberchicot, S. F. Matar, L. Fournes, G. Demazeau, P. Hagenmuller, J. Solid State Chem. **84** (1990)10–15.
15. A. Leineweber, H. Jacobs, F. Hüning, H. Lueken, W. Kockelmann, J. Alloys Compd. **316** (2001) 21–38.
16. B. D. Cullity, Elements of X-ray Diffraction, Addison-Wesley, Reading, MA, 1956, p. 98
17. X. Jia, D. Chen, X. Jiao, T. He, H. Wang, W. Jiang, J. Phys. Chem. C **112** (2008) 911-917.
18. N. N. Mallikarjuna, A. Lagashetty, A. Venkataraman, J. Therm. Anal. Calorim. **74** (2003) 819–826.

19. M. Sifkovits, H. Smolinski, S. Hellwig, W. Weber, J. Magn. Magn. Mater. **204** (1999)191-198.

20. N. S. Gajbhiye, R. S. Ningthoujam, J. Weissmüller, Hyperfine Interact. **156/157** (2004) 51–56.

21. T. Liapina, A. Leineweber, E. J. Mittemeijer, W. Kockelman, Acta Mater. **52** (2004) 173–180.

22. R. N. Panda, N. S. Gajbhiye, J. Magn. Magn. Mater. **195** (1999) 396–495.

23. R. N. Panda, N. S. Gajbhiye, J. appl. Phys. **86** (1999)3295–3302.

24. Z. Wei, T. Xia, J. Ma, W. Feng, J. Dai, Q. Wang, P. Yan, Mater. Charact. **58** (2007) 1019–1024.

25. P. M. Diehm, P. Agoston, K. Albe, ChemPhysChem. **13** (2012) 2443–2454.

26. S. B. Dalavi, J. Theerthagiri, M. ManivelRaja, R.N. Panda, J. Magn. Magn. Mater. **344** (2013) 30–34,

27. Y. Zhang, S. -W. Or, Z. Zhang, Advances in Materials Physics and Chemistry. **1**(2011) 7-13.

28. J. Theerthagiri, S. B. Dalavi, M. M. Raja, R. N. Panda, Mater. Res. Bull. **48** (2013) 4444–4448.

29. J. Pak, W. Lin, K. Wang, A. Chinchore, M. Shi, D. C. Ingram, A. R. Smith, J. Vac. Sci. Technol. A. **28** (2010) 536-540.

30. F. Z. Mammeri, L. Chekour, N. Rouag, Acta. Phys. Pol. A. **123** (2013) 294-295.

31. J. Liu, X. M. Meng, Y. Jiang, C. S. Lee, I. Bello, S. T. Lee, Appl. Phys. Lett. **83** (2003) 4241-4243.

32. Y. Han, H. Wang, M. Zhang, M. Su,W. Li, K. Tao, Inorg. Chem. **47** (2008) 1261-1263.

33. C. P. Bean, I. S. Jacobs, J. Appl. Phys. **31**(1960) 1228–1230.

34. M. Robbins, J. G. White, J. Phys. Chem. Solids **25** (1964) 717-720.

35. G. M. Chen, N. K. Jaggi, J. B. Butt, E. B. Yeh, L. H. Schwartz, J. Phys. Chem. **87** (1983)5326-5332.

36. N. S. Gajbhiye, R. N. Panda, R. S. Ningthoujam, S. Bhattacharyya, Phys. Status Solidi C. **1**(2004) 3252-3259.

37. S. F. Matar, J. Alloys Compd. **345** (2002) 72–76.

38. M. Yang, Z. Cuiz, F.J. DiSalvo, Chem. Commun. **48** (2012) 10502–10504.

39. A. H. Morrish, K. H. Haneda, J. Magn. Magn. Mater. **35** (1983) 105–113.

40. J. H. Hwang, V. P. Dravid, M. H. Teng, J. J. Host, B. R. Elliott, D. L. Johnson, T. O. Mason, J. Mater. Res. **12** (1997)1076-1082.

41. L. L.Wang, W. T. Zheng, T. Ana, N. Mab, J. Gong, J. Alloys Compd. **495** (2010) 265–267.

42. E. C. Stoner, E. P. Wohlfarth, Phil. Trans. Roy. Soc. London A **240** (1948) 599-642.

43. P. J. van der Zaag, P. J. van der Valk, M. Th. Rekveldt, Appl. Phys. Lett. **69** (1996) 2927- 2929.

Chapter 4

Structural Characterization and Surface Properties Study of vanadium nitride Synthesized using Novel Chemical Methods

The current chapter deals with investigation on synthesis, characterization and surface properties study of vanadium nitride materials synthesized using various precursors and nitridation sources.

4.1 Introduction

The scientific merit of studying VN as a topic of research interest can be realized from the following examples. VN holds a great promise as electrode material for asymmetric supercapacitor due to its large specific capacitance, high electrical conductivity and wide operation window in the potential range [1, 2]. VN supported Pd catalyst exhibits significant catalytic activity for formic acid oxidation [3]. VN nanofiber membrane performs as a highly stable support for Pt catalyzed oxygen reduction reaction with much higher durability [4]. VN exhibits supercapacitive behaviour with high value of specific capacitance. This is because of its high value of electronic conductivity (σ_{bulk} = 1.67×10^{6} $\Omega^{-1}m^{-1}$) and possibility to offer various oxidation states of vanadium (II-V) in nitrides. The former characteristic is associated with the high rate charge- discharge while the later for pseudocapacitance behaviour [5, 6].

The importance of preparation techniques (chemical / physical) for obtaining quality product of vanadium nitride in nanoscale has been reported [7, 8]. Krawiec *et al.* have shown that very high specific surface area and nanostructured nitrides can be obtained by nitridation of chemically synthesized V_2O_5 foam precursor in a high flow of NH_3(g) by employing low heating rates, i.e. 100-300 K/h [9,10]. VN has been synthesized by VCl_4 and $NaNH_2$ at room temperature by Chen *et al.* [11]. A low temperature direct method in order to obtain mesoporous VN via one-step chemical precipitation route by using vanadium tetrachloride and urea has been reported by Lee *et al.* [12]. A number of transition metal nitrides including VN have been synthesized using urea, cyanamide and melamine as the

nitrogen sources [6, 13, 14]. Their results prove that use of organic based nitrogen containing compounds as nitrogen source plays an important role in the formation of nitride materials with smaller particle sizes. Thus, optimizing synthesis methodology and synthetic parameters in order to achieve desired properties of VN has become important topic of research. Therefore, extending the scope of available synthetic strategies is crucial with respect to properties tuning. Nano-dispersed material which has control over particle shape is highly desirable for various applications of interest.

Amongst the reported methods of synthesis in literature (described above), the low temperature methods for the preparation of compounds are important to obtain a pure phase, strain free, fine particle with controlled morphologies. Temperature programmed reaction (TPR) using ammonia with chemically synthesized V_2O_5 is a simple alternative procedure for the synthesis of VN in porous and high surface area form [15]. Also, for the preparation of nanocrystalline VN with high specific surface area, a proper precursor of the vanadium source along with suitable nitriding agent is very important. Urea can be selected as a nontoxic nitrogen source for the synthesis of nitrides. Therefore in the present chapter different synthetic routes have been explored. The effect of different nitriding sources and precursors with variable crystallinity and size on the physical properties of nitride products have been investigated and summarized in detail.

The current chapter deals with investigation on synthesis, characterization and surface properties study of vanadium nitride materials. The materials were synthesized via nitridation of nanocrystalline vanadium oxide, V_2O_5, precursor which was obtained via citric acid assisted sol-gel technique (details have been described in Chap. 2, subsection 2.1.1.1). The nitridation reactions were carried out via two different routes i.e. use of (1) ammonia (NH_3(g)) and (2) solid urea (NH_2CONH_2) as nitrogen sources. Different precursors have been synthesized with alteration of reaction parameters for the nitridation process. The experimental parameters were standardized in order to obtain pure phase VN product via different precursors and nitrogen sources. The effect of precursors and nitridation routes (for the formation of VN product) on various properties such as: structural, morphological, surface properties etc. have been investigated in detail. The properties and characterizations

using advanced instrumental techniques for VN products have been summarized in the present chapter.

4.2 Materials and methods

Citric acid based sol-gel method has been adopted for the synthesis of V_2O_5 precursor in nanocrystalline form. The resulting precursor is nitrided using two different nitrogen sources, i.e., (1) urea and (2) ammonia, for the synthesis of vanadium nitride product. The details of the synthesis procedure adopted have been described in the following subsections.

4.2.1 Preparation of V_2O_5 precursor by citric acid based sol-gel method

In a typical synthesis, 2.514g of ammonium vanadate (NH_4VO_3) (SDFCL) and 8.981g of anhydrous citric acid (Fisher Scientific, India) (1:2 molar ratio) were taken. NH_4VO_3 (s) was dissolved in 80 ml of distilled water in a round bottom flask and stirred on oil bath maintained at 80˚ C for half an hour. Then citric acid was dissolved in 20 ml of distilled water and was slowly added to the solution of NH_4VO_3. The colour of the solution changed from brown to blue- black. The solution was stirred at 80˚C for 4 h in oil bath using magnetic stirrer. Next, it was evaporated on a hot plate which resulted in a solid vanadium citrate complex. Approximately, 5.95g of the vanadium citrate complex was obtained in the form of xerogel. The solid product was heat treated in air atmosphere at various temperatures and time in order to get nanocrystalline V_2O_5 precursor. V_2O_5 precursors obtained by heat treatment of the xerogel at 350˚C and 550˚C for 4 h duration were selected for nitridation experiments after proper characterization. The precursors were named as V_2O_5 (350) and V_2O_5 (550) for denoting heat treatments at 350^{o}C and 550^{o}C, respectively, else otherwise stated.

4.2.2 Synthesis of VN by urea route

In order to synthesize VN materials, the synthesized precursors (V_2O_5) containing V^{5+} ions were mixed with solid urea in different molar ratios and heat treated in inert gas atmosphere of nitrogen. The synthesis procedure was standardized by employing different metal : urea molar ratios, i.e. 1:6 to 1:22, for nitridation at various reaction temperatures and

time durations (3-12h) in N_2(g) atmosphere. The pure product formation was ascertained by XRD for the molar ratios of 1:18 and 1:15 for V_2O_5 precursors obtained at 350^{o}C and 550^{o}C, respectively (table 4.1). Therefore, in our synthesis 0.4g of V_2O_5 precursors, synthesized at 350˚C and 550^{o}C were mixed thoroughly with 2.38 g and 1.98 g of urea in the molar ratio of 1:18 and 1:15, respectively. The resulting mixture was heated in an alumina boat which was placed in quartz tubular furnace in N_2 (g) atmosphere at 700^{o}C for 3h time duration. The selected summary of the nitridation experiments are presented in table 4.1.

Table 4.1 Summary of nitridation process.

Precursor(Temp^{o}C)	**Precursor: urea**	**Nitridation Temp/Ramp (˚C/Kmin^{-1})**	**Holding time (h)**	**Product (s)/ phase**
V_2O_5 (350)	1:15	700/3.8	3	VN/cubic
	1:18	700/3.8	3	VN/cubic
V_2O_5 (550)	1:18	650/3.6	3	VN/cubic
	1:18	700/3.8	3	VN/cubic
	1:15	650/3.6	3	VN/cubic
	1:15	700/3.8	3	VN/cubic

4.2.3 Synthesis of VN by nitridation using NH_3(g)

Several batches of synthesized V_2O_5 precursors (0.45g each) obtained at 350˚C and 550˚C were loaded in the quartz tubular reactor of 1cm diameter (inner) and kept in the vertical furnace. The precursor materials were suspended in the middle of the quartz tubular reactor with the help of porous ceramic wool and NH_3(g) was passed through the solid materials in a controlled way. The precursors were nitrided using NH_3(g) flow at various temperatures (650 - 800^{o}C) and time durations (2-6 h). The heating rate was varied between 1.9 – 3.3˚ C/ min during all the preparations. The furnace was cooled naturally to room temperature (298K) under flowing ammonia atmosphere before exposing to the air atmosphere.

4.2.4 Instrumental characterization

The XRD patterns were recorded using a powder X-ray diffractometer (Miniflex-II) using Cu-Kα_1 radiation (1.5405Å) at a scanning speed of 3˚/min. The phase purity was ascertained using XRD. The crystallite size was analyzed using Scherrer equation, $t = 0.9\lambda/(B \cos\theta)$, where t is the crystal size; λ is the wave length of X-ray; B is the full width at half maximum (FWHM); θ is the diffraction angle [16]. The shape, size and morphology of the

VN materials were examined by SEM (Jeol JSM 6390) and by TEM (model: Philips- CM 200). Nitrogen physisorption experiments were performed using a physisorption apparatus (Micromeritics Gemini VII). The VN samples were activated at 250˚C for 6 hrs using high-purity He (g)/N_2(g) gas mixture. Electrochemical properties were tested using Ivium stat electrochemical workstation. The potential is varied between -1V to 1V with a scan rate of 20mV/s and a potential step of 30mV.

4.3 Results and discussions

The synthesized product VN was characterized using XRD, SEM, TEM and BET surface area analysis. The results obtained are presented and discussed in the following subsections.

4.3.1 X-ray diffraction studies

4.3.1.1 Precursor characterization

Figure 4.1 represents the indexed XRD patterns of V_2O_5 precursor synthesized at (a) 350˚C and (b) 550˚C. The XRD patterns are indexed according to JCPDS card # 89–2483 as reported in the literature [17]. Minor peaks with integrated intensities less than 5 % have not been indexed in the XRD patterns. The XRD patterns show phase purity and nanocrystalline nature of V_2O_5 precursor. The nanocrystalline nature is evident from the observed line broadenings of the powder XRD lines. The crystallite sizes were estimated using Scherrer equation (Chapter 2 subsection 2.3.1.3.2) and are found to be 27±0.3 nm and 39±0.1 nm for V_2O_5 materials, synthesized at 350˚C and 550˚C, respectively. The crystallite size of V_2O_5 is bigger, i.e., 39±0.1 nm, when heat treated at higher temperature of 550˚C. This can be majorly due to the grain growth of the smaller crystallites at elevated temperatures.

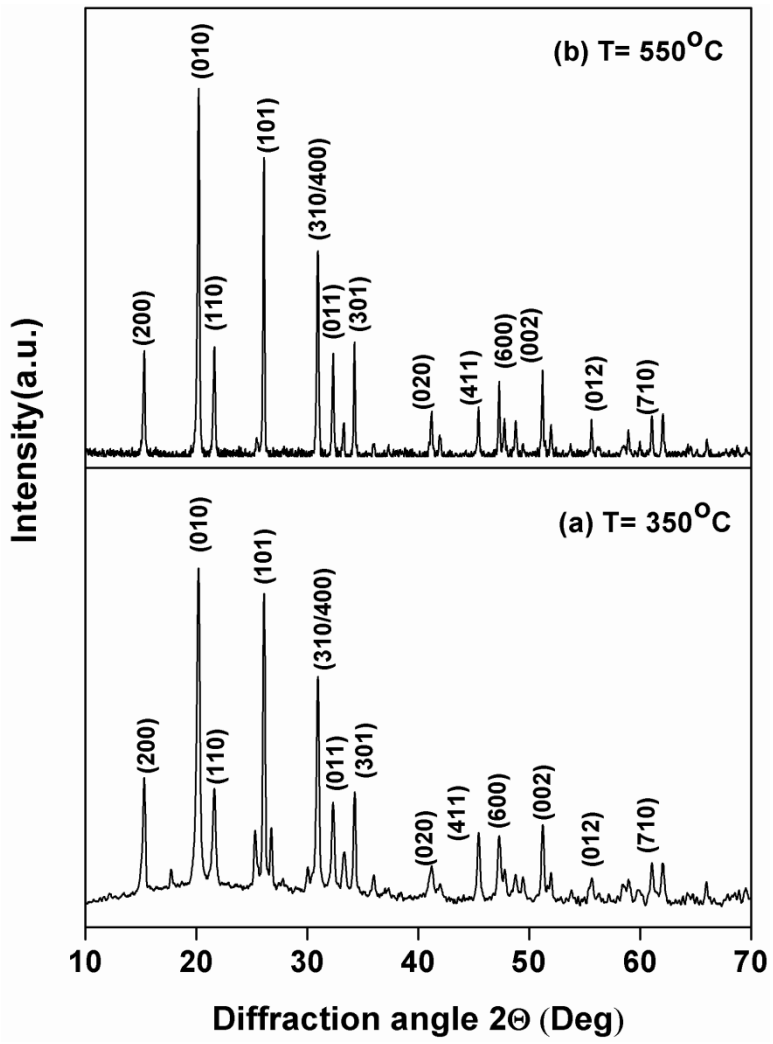

Figure 4.1.Indexed XRD patterns of V_2O_5 precursor materials synthesized by citric acid–assisted sol–gel method at various temperatures; (a) 350 °C and (b) 550 °C.

The XRD parameters; such as: Miller indices, observed interplanar distance and lattice parameters, for V_2O_5 precursors are presented in table 4.2. The values of the estimated lattice parameters (a, b and c) for V_2O_5 precursors synthesized at 350^{o}C and 550^{o}C are quite similar (see table 4.2). These results indicate absence of lattice distortion in both the precursors even though the crystallite sizes are remarkably different.

Table 4.2 Materials, Miller indices, observed interplanar distance and calculated lattice parameters for V_2O_5 precursors synthesized at 350°C and 550°C.

Precursor Materials	Miller indices (hkl)	Interplanar distance 'd' (Å)	Lattice parameters (Å)
V_2O_5 (350°C)	(200)	5.802	a=11.547(17) b=4.389(8) c=3.564(6)
	(010)	4.397	
	(110)	4.099	
	(101)	3.415	
	(400)	2.881	
	(011)	2.763	
	(301)	2.615	
	(411)	1.992	
	(600)	1.920	
	(002)	1.780	
V_2O_5 (550°C)	(200)	5.773	a=11.543(10) b=4.390(5) c=3.568(3)
	(010)	4.397	
	(110)	4.099	
	(101)	3.415	
	(400)	2.891	
	(011)	2.763	
	(301)	2.615	
	(411)	1.996	
	(600)	1.920	
	(002)	1.783	

4.3.1.2 Solid state reactivity study

4.3.1.2.1 Solid state reactivity study of VN formation via urea route

For studying solid state reactivity of VN formation via urea route, we have chosen nanocrystalline V_2O_5 precursors synthesized at 550^{o}C (V_2O_5 (550)). The precursor materials were well crystallized having crystallite size of ~39 nm. The precursor materials were mixed with solid urea with different molar ratios, i.e. V_2O_5 : urea ratios of 1:15 and 1:18 and are nitrided at various temperatures ranging from 650^{o}C to 800^{o}C. Figure 4.2 represents the XRD patterns of the nitridation products obtained via urea route at two different temperatures, i.e. at 650˚C [(a) and (c)] and at 700˚ C [(b) and (d)] from V_2O_5 (550) precursor. The nitridation products obtained at 650^{o}C using V_2O_5 : urea molar ratios of 1:15 and 1:18 were found to be single phase of VN. However, the low intensity peaks corresponding to lattice planes (311) and (222) which occur at high diffraction angles were absent. This could be due to poor crystallinity of the synthesized VN nanocrystals along the (311) and (222) crystal planes. Further, it can be observed from the figure 4.2 that all peaks of cubic phase VN are present in the XRD pattern synthesized at 700^{o}C. The observed broad

peaks in the XRD pattern indicate nanocrystalline nature of the synthesized materials. Figure 4.2(d) has been indexed according to ICDD PDF# 35-0768. Therefore, in our study, we have taken the flexibility of choosing V_2O_5 : urea molar ratios of 1:15 and nitridation temperature of 700^oC for the formation of VN using V_2O_5 (550) precursors. However, pure phase VN was obtained at 700^oC from V_2O_5 (350) precursor for V_2O_5 : urea molar ratios of 1:18.

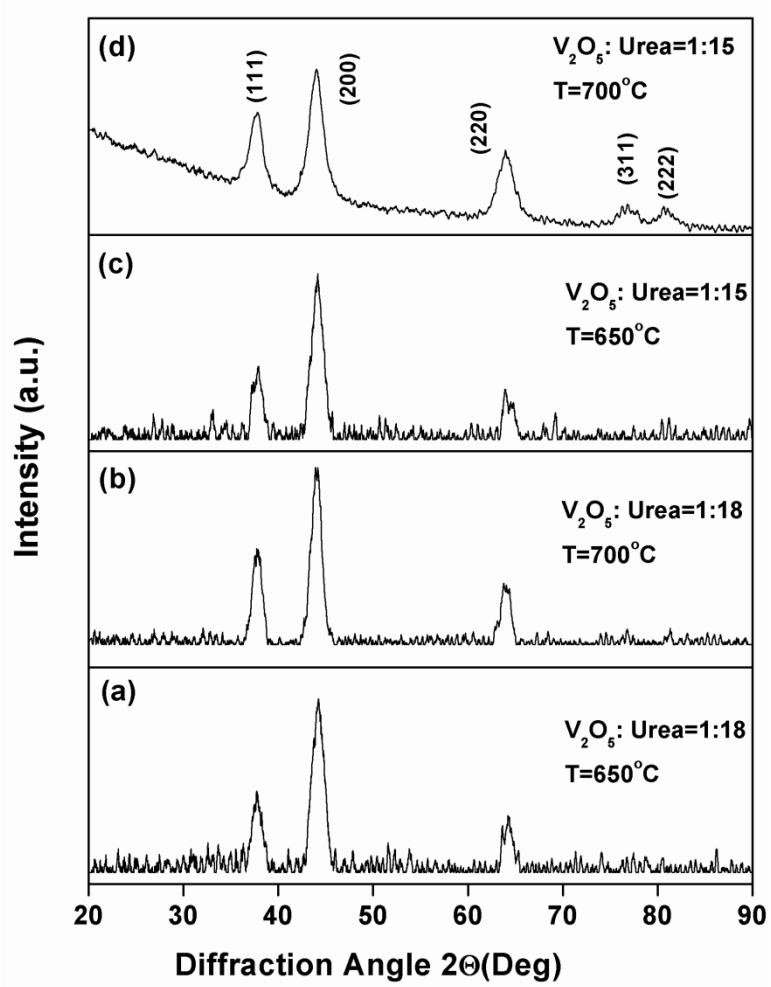

Figure 4.2 Indexed XRD patterns of products obtained via nitridation of V_2O_5 precursor synthesized at 550˚C via urea route at (a) 650˚C and V_2O_5 : urea = 1:18 (b) 700˚ C temperature and V_2O_5 : urea = 1:18 (c) 650˚C and V_2O_5 : urea = 1:15 (d) 700˚C and V_2O_5 : urea = 1:15.

4.3.1.2.2 Solid state reactivity study of VN formation via NH_3(g) route

Solid state reactivity of VN formation using commercial and synthesized V_2O_5 precursors is well known [18]. It has been predicted by analysis of the intermediate products obtained during nitridation that the reaction is topotactic in nature. The reaction products at intermediate steps indicate chemical reduction of V_2O_5 in to several oxides with reduced oxidation states, such as: V_2O_3, VO etc., which on further nitridation at higher temperatures results VN product [18]. Formation temperature of VN depends upon precursors used for nitridation experiments. For example: VN synthesized using commercial V_2O_5 powder occurs at temperature range of 800 - 900˚C, whereas using metallo-organic precursors it can be done in one step at around 450 - 600˚C [18]. Gajbhiye *et al*. have reported formation of VN via decomposition and nitridation of $[VO(NH_2O)_2Gly]H_2O$ complex in NH_3(g) gas at 973 K [19]. As we have followed similar synthesis procedure using nanocrystalline V_2O_5 as precursor, synthesized via sol-gel route, nitridation experiments were carried out at 700˚C-800˚C. During the nitridation experiments at fixed temperatures, the precursors were subjected to several heating ramps (1.9 - 3.3 K/min) and nitridation durations (4 - 6 hrs). It has been observed that faster heating rate and reduced nitridation time results in mixture of two phases, i.e. pure VN and V_2O_5, as examined by X-ray diffraction studies. We could optimize the formation of pure phase VN product at 700^{o}C with ramp of 1.9 K/min. The flow rate of ammonia gas was kept nearly uniform, i.e. ~100 cc/min, for all experiments.

4.3.1.3 X-Ray Diffraction study of VN synthesized by urea and ammonia routes

The X-ray diffraction patterns of VN synthesized from V_2O_5 precursor synthesized at 350˚C and 550˚C via urea route and ammonia route have been presented in figure 4.3 and figure 4.4, respectively. The Miller indices, observed and calculated interplanar distances and lattice parameters are presented in table 4.3. The observed and calculated values of the d-spacings match well in our calculation considering cubic symmetry. The crystallite sizes are presented in table 4.4. The XRD patterns are indexed according to ICDD PDF # 35-0768.

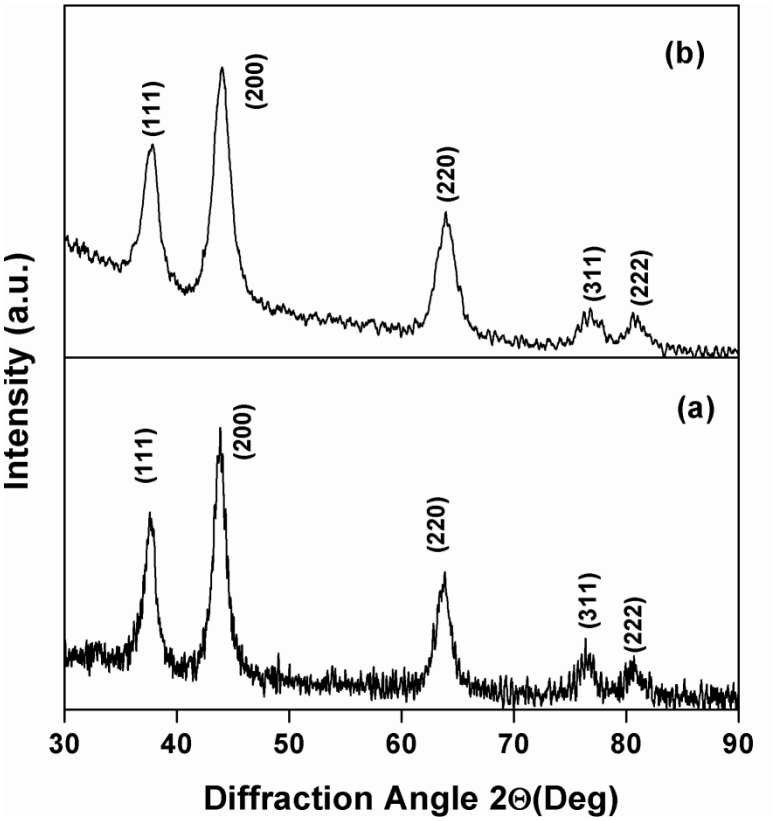

Figure 4.3 Indexed XRD patterns of VN synthesized at 700˚C from V_2O_5 precursor obtained at (a) 350˚C and (b) 550˚C via urea route.

The indexed XRD figure depicts broad peaks indicating ultra fine nature and absence of extra XRD peaks confirms phase purity of the synthesized nitride products. VN crystallizes in cubic structure with space group *Fm3m* [6]. The lattice parameters of VN are 4.126(6) Å and 4.113(6) Å prepared via urea route from V_2O_5 precursor heat treated at 350˚C and 550˚C.

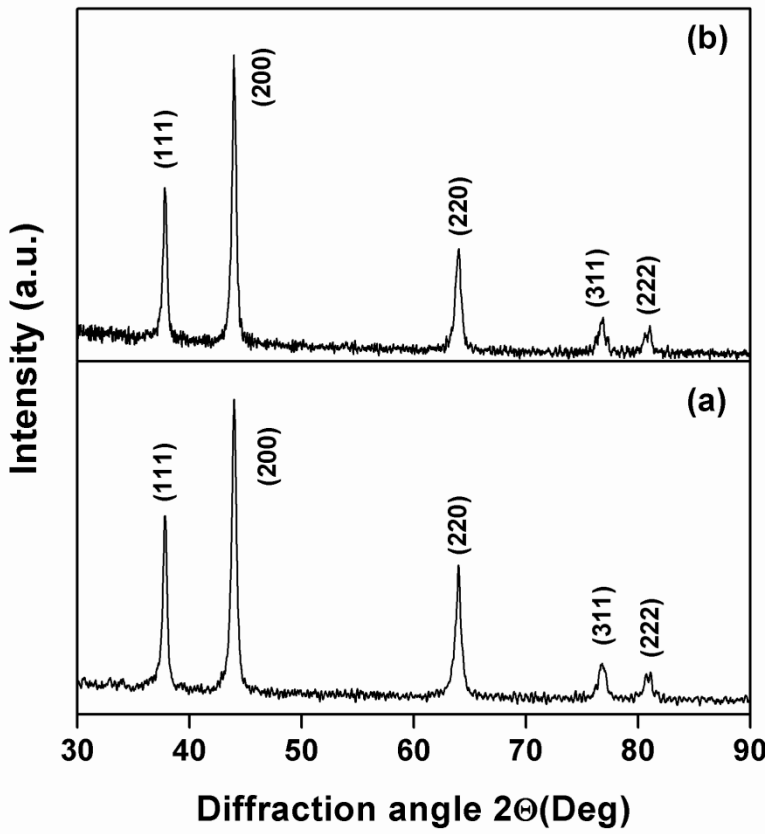

Figure 4.4 Indexed XRD patterns of VN synthesized at 700˚C from V_2O_5 precursor obtained at (a) 350˚C and (b) 550˚C via ammonia route.

The lattice parameters are estimated to be 4.112(5) Å and 4.112 Å for VN synthesized via ammonia route from V_2O_5 precursor obtained at temperature 350˚C and 550˚C (table 4.3). The observed values of lattice parameters, i.e. in the range of 4.112 - 4.126 Å, are slightly less but comparable with the value of 4.139 Å for stoichiometric VN material [6]. The reason for such decrease in the lattice parameters may be due to strain effects and fine particle size and surface distortions [20, 21]. Further, it may be noted that that the lattice parameter 'a' is very sensitive to the N content in the material and the possibility of slight deviation from ideal stoichiometry, i.e. 1:1 for VN, cannot be overruled [20, 22].The crystallite sizes of the VN synthesized via urea route from V_2O_5 precursor obtained at 350˚C and 550˚C are found to be 9±0.6 nm and 7±0.2 nm, respectively. Similarly, the crystallite sizes of VN synthesized via ammonia route are 22 nm and 28±0.3 nm under similar heat treatment conditions, i.e. 350˚C and 550˚C for 4h durations, respectively. These results indicate that urea route is more effective in producing smaller size nanocrystals in addition

to its ease in synthesis compared to ammonia route. The average crystallite sizes are presented in table 4.4.

Table 4.3 Materials, precursors, routes, Miller indices, observed and calculated interplanar spacing and lattice parameters of VN nano materials.

Material	Precursor	Route	Miller indices (hkl)	d_{obs}	d_{cal}	Lattice parameters(Å)
VN	V_2O_5 (350)	Urea	(111)	2.386	2.382	4.126(6)
			(200)	2.063	2.063	
			(220)	1.459	1.458	
			(311)	1.241	1.244	
			(222)	1.192	1.191	
		Ammonia	(111)	2.378	2.374	4.112(5)
			(200)	2.057	2.056	
			(220)	1.451	1.454	
			(311)	1.239	1.239	
			(222)	1.187	1.187	
VN	V_2O_5 (550)	Urea	(111)	2.377	2.375	4.113(6)
			(200)	2.055	2.056	
			(220)	1.454	1.454	
			(311)	1.239	1.240	
			(222)	1.188	1.187	
		Ammonia	(111)	2.377	2.374	4.112(0)
			(200)	2.055	2.056	
			(220)	1.454	1.453	
			(311)	1.239	1.239	
			(222)	1.185	1.187	

4.3.2 Electron microscopy study

In order to probe the micro structure, shape and size of the VN products scanning and transmission electron microscopy were carried out. Composition analysis was done from the EDX study of the VN material. TEM and SAED patterns provided more insight into the electronic configuration and atomic structure of the synthesized VN product.

4.3.2.1 SEM study of VN

The typical SEM micrographs of VN nanomaterials synthesized by urea route and ammonia route by using different precursors synthesized at 350˚C and 550˚C are depicted in figure 4.5 (a) ,(b),(c) and (d) . SEM micrographs of VN samples synthesized by urea route

show elongated particle morphology. Figure 4.5(a) shows oval shaped particles having average SEM particle size 115nm, where as figure 4.5(c) shows elongated particles having average dimension: 300 nm×15 nm. Figure 4.5(b) shows SEM micrograph of VN nanoparticles having spherical particle size with average diameter 111nm.Figure 4.5(d) shows spherical particle with average diameter 68 nm. The SEM particle sizes are found to be bigger than the estimated crystallite sizes (table 4.4), because of the fact that several crystallites can form agglomerates. Such kinds of observations have already been reported and are not uncommon in the literature [23, 24].

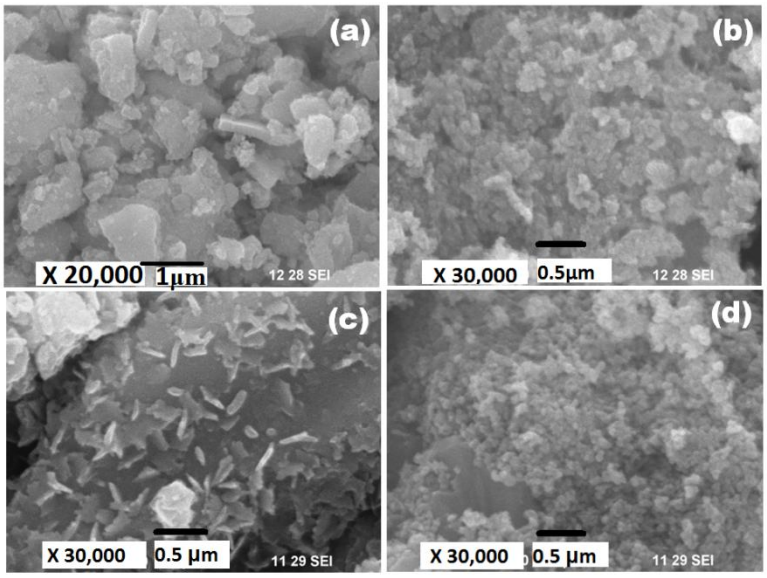

Figure 4.5 SEM micrographs of VN synthesized via urea route ((a), (c)) and ammonia route ((b) and (d)) obtained by nitridation of V_2O_5 precursors heat treated at 350 °C and 550°C, respectively.

4.3.2.2 TEM study of VN

In order to probe the structural and microscopic properties (such as: interplanar distance, lattice parameters, crystallinity, grain size and shape etc.) of the synthesized materials in detail, TEM studies were carried out. TEM micrographs of VN nitrides at different magnifications synthesized via urea route from V_2O_5 precursors obtained at 350 °C (a), (b) and 550 °C (c), (d) are presented in figure 4.6. Similarly, TEM micrographs of VN nitrides at different magnifications synthesized via ammonia route from V_2O_5 precursors obtained at 350°C (a), (b) and 550°C (c), (d) are presented in figure 4.7. The SAED patterns of VN materials have been presented in figure 4.8 (a), (b), (c) and (d), representing VN

synthesized via urea route from V_2O_5 precursors obtained at (a) 350°C and (b) 550˚C and via ammonia route using V_2O_5 precursors obtained at (c) 350˚C and (d) 550°C. It can be seen from figure 4.6 that VN materials synthesized via urea route possess particles with rod shaped morphology whereas VN synthesized via ammonia route crystallizes in nearly spherical morphologies. The SAED patterns of VN nitrides indicate varieties of material structures including amorphous, partly crystalline and well defined polycrystalline nature. The observed rings in the SAED patterns have been indexed in terms of Miller indices (hkl). The above mentioned observations are sensitive to synthetic route and heat treatment temperatures of the vanadium pentoxide precursors.

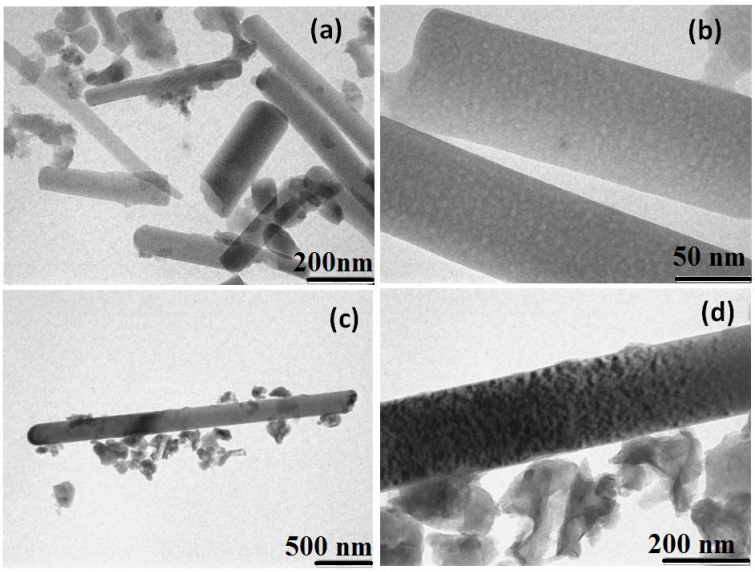

Figure 4.6 TEM micrographs of VN nitrides at different magnifications synthesized via urea route from V_2O_5 precursors obtained at 350 °C ((a), (b)) and 550 °C ((c), (d)).

The elongated rod shaped structures in figure 4.6 (a) and (b) have dimensions ranging from (320 nm ×72nm) to (540 nm × 82nm). It can be seen that some of the VN nanorods overlap each other with small nanoparticles embedded in it (figure 4.6(a) and (b)). Some oval shaped particles are also found along with the rods in the TEM picture of VN prepared via urea route from the V_2O_5 precursor obtained at 350˚C. Vanadium nitride rod structures depicted in figure 4.6 (c) and (d) have dimensions in the range of (1.2μ ×192 nm) to (3μ × 261 nm). These pictures also show small embedded clusters of nanoparticles with some distorted spherical morphology (dia: ≈ 104 nm) on the surface of submicron VN rod. The TEM

particle sizes of the synthesized VN products are given in the table 4.4. It can be observed that both the precursors nitrided via urea route produced rod shaped morphology. The preferential growth of VN material along a particular axis may be due to the synthetic route adopted, i.e. urea route, in our case. The chemical reaction between solid urea and V_2O_5 precursors at high temperature range (RT-700^oC) in nitrogen atmosphere is quite complex and leads to varieties of intermediate products depending upon temperature. We believe that the precursor geometry before nitride formation (~ say 600^oC) is remaining intact in product morphology [15]. The mechanism can be understood based on the fact that the growth along a particular crystal face can occur preferentially leading to nano-rod formation.

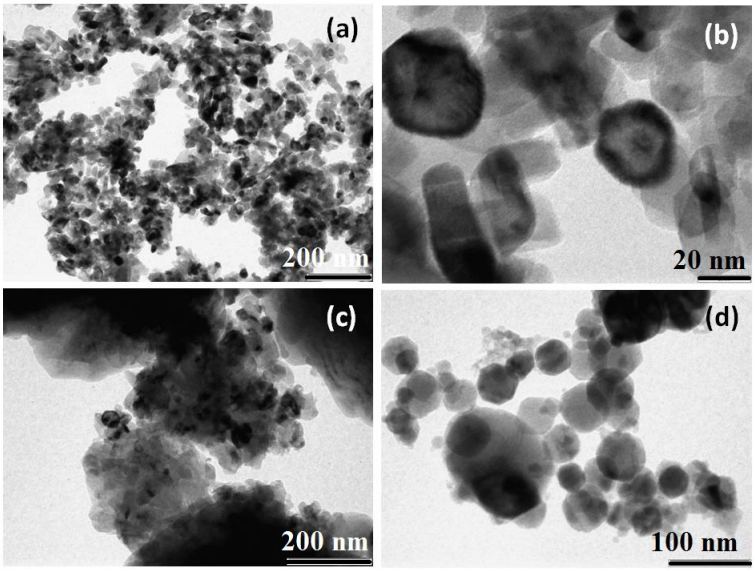

Figure 4.7 TEM micrographs of VN nitrides at different magnifications synthesized via ammonia route from V_2O_5 precursors obtained at 350 °C ((a), (b)) and 550 °C ((c), (d)).

Figure 4.7 (a), (b), (c) and (d), represents well organized dispersed cluster structures of synthesized VN product at various magnifications, i.e. (a), (c) with lower and (b), (d) with higher magnification. The particles in figure 4.7 (a) and (b) (synthesized from V_2O_5 precursors heat treated at 350^oC) are nearly spherical or oval shaped in nature. The average TEM particle sizes were calculated by selecting a number of particles in the micrographs and averaging their diameters. The estimated average TEM particle size is found to be 22 nm which agrees well with the crystallite size obtained from XRD measurements (table 4.4).

Similar results were found in the TEM studies on VN nitride synthesized using V_2O_5 precursor at 550^oC, except slight change in particle size and their distributions (figure 4.7 (c) and (d)). The average TEM particle size for the VN synthesized from V_2O_5 heat treated at 550˚ C is estimated to be 32 nm, nearly equal to the crystallite size 28±0.3 nm. Also, one can observe few lumps of large agglomerated clusters within the matrix of smaller crystallites. This can be due to the precursor structures having larger crystallite sizes obtained via annealing of the materials at higher temperatures, i.e. 550^oC, used for nitridation. The average TEM particle sizes have been listed in table 4.4. Thus, TEM results confirm that smaller sized VN materials are obtained when nitridation involves the use of smaller size V_2O_5 precursors. [14, 25]. The TEM particle size distributions have been presented in figure 4.9 (a) and (b).

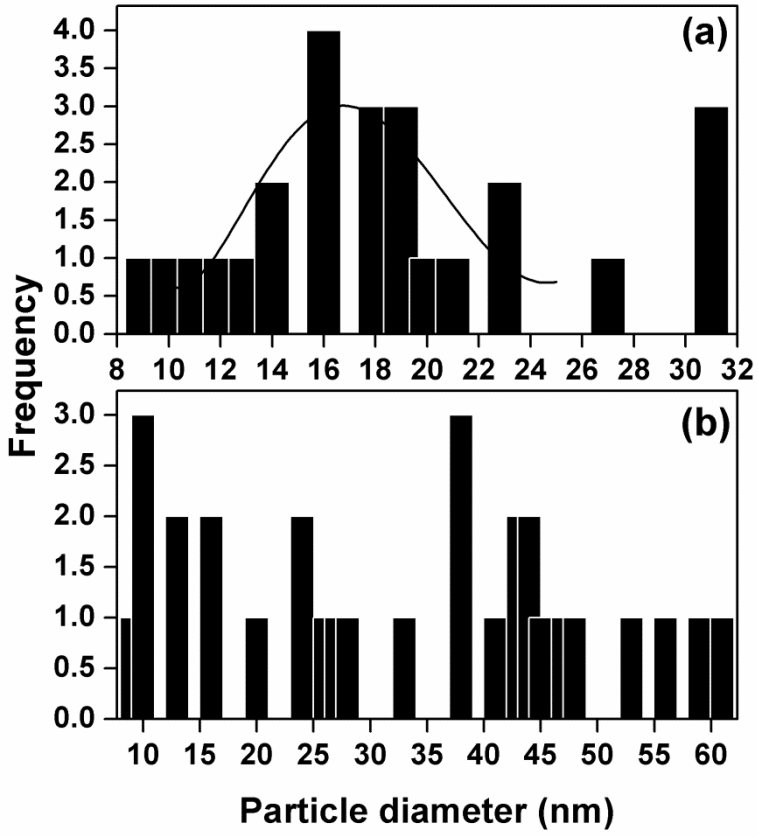

Figure 4.8 TEM particle size distributions of VN nitrides synthesized via ammonia route from V_2O_5 precursors obtained at different temperatures; (a) 350˚C and (b) 550˚C.

One can see from the figure that VN nitride obtained using precursor synthesized at lower temperature possess narrow size distribution (10-32 nm with peak centered around 16 nm)

compared to that synthesized at higher temperatures (10-60 nm distributed with more or less equal occurrence throughout).

Table 4.4 Materials, precursors, routes, average crystallite sizes, TEM and SEM particle sizes of VN materials synthesized via different routes.

Material	Precursor	Route	Crystallite size (nm)	Average TEM particle size (nm)	Average SEM particle size (nm)
VN	V_2O_5 (350)	Urea Ammonia	9±0.6 22	540X72 22	115 111
VN	V_2O_5 (550)	Urea Ammonia	7±0.2 28±0.3	1266 X261 32	300X15 68

SAED patterns corresponding to various VN products are presented in figure 4.9 (a), (b), (c) and (d). Figure 4.9 (a), (b) and (d) indicate weakly crystalline structure along with amorphous nature of the materials having diffused rings and few bright spots located randomly. Figure 4.9(c) represents well defined polycrystalline nature of the VN product having concentric rings made up of bright spots. It has been observed that several reflections which are observed in SAED patterns are absent in the XRD patterns and vice versa. These results can be understood as difference in orientations of the planes during TEM and XRD measurements. The values of the interplanar distances calculated from the SAED patterns have been presented in table 4.5.

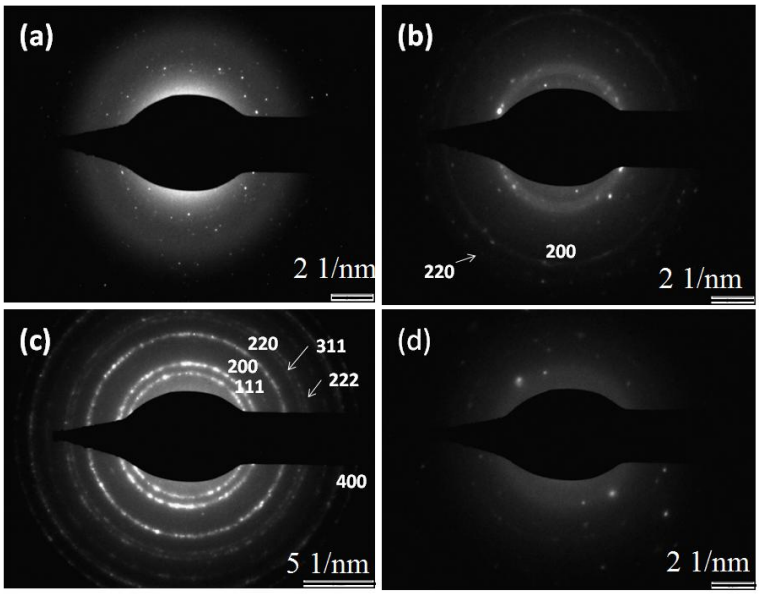

Figure 4.9 SAED patterns of VN nitrides synthesized via urea ((a), (b)) and ammonia ((c) and (d)) routes. The patterns ((a), (c)) and ((b) and (d)) are recorded from VN nitride synthesized via V_2O_5 precursors heat treated at 350 °C (V_2O_5 (350)) and 550 °C (V_2O_5 (550)), respectively.

The values of interplanar spacing obtained from SAED have been compared with those obtained from the XRD measurements and are found to be in good agreement. As more % of crystallinity is related to larger grains compared to partially crystalline or amorphous materials, one can expect larger surface areas for materials having lesser crystallinity. The above mentioned arguments are confirmed from our surface area studies (subsection 4.3.3) where amorphous products do have larger surface areas compared the crystalline samples (table 4.5).

Table 4.5 Materials, Synthesis routes, Precursors, Interplanar Spacings and Miller indices (hkl) of VN Materials.

Material	Synthesis Route	Precursors	Interplanar Spacing 'd' (Å)		(hkl)
			SAED	XRD	
VN	Urea	V_2O_5 (550)	1.792	2.056	200
			1.497	1.45	220
VN	Ammonia	V_2O_5 (350)	2.145	2.375	111
			1.926	2.056	200
			1.371	1.454	220
			1.176	1.239	311
			1.120	1.187	222
			0.875	---	400

4.3.2.3 EDX study of VN

Two representative EDX spectra of VN materials, synthesized via urea route and ammonia route from V_2O_5 precursor obtained at 350°C have been shown in figure 4.10 (a) and (b), respectively. The spectra confirm the presence of metallic V, N and/or C as elements. The presence of C and N in interstitials form is also evident from the observed peak position at ~0.05 keV. As we have synthesized the materials at high temperature (800^oC) under the nitrogen flow, we believe that minimum amount of C contamination is present in our sample. It has been already observed in the literature that EDX spectra of some nitride materials obtained via organometallic precursors show the presence of peak at very low energy values (say < 0.1 keV) [26]. In addition, we observed EDX peak position at ≈ 0.469 keV in both the spectra. This has been attributed to the presence of N and metallic V in elemental form in the VN crystal structure. Similar interpretations of the EDX results have been derived in the literature [7, 27, 28]. The broad peak position observed at 0.469 keV may correspond to Kα peak of N (0.392 keV) and Lα peak of V (0.573 keV) (figure 4.8) [27, 28]. The other prominent peak position of V Kα line centered at 4.936 keV corresponds well with the reported value [7, 28]. The occurrence of altered values of peak positions for N atom specifically in doped systems has also been proved in N-doped TiO_2 system [29]

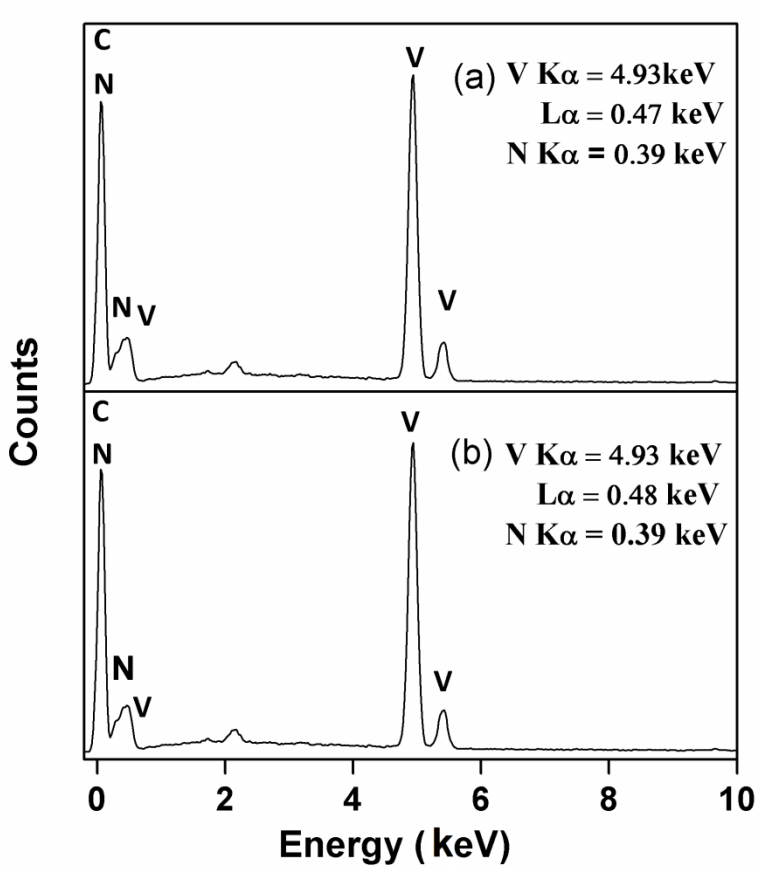

Figure 4.10 EDX spectra of VN synthesized at 700˚C via (a) urea route and (b) ammonia route from V_2O_5 precursor obtained at 350 °C.

4.3.3 BET adsorption and desorption studies

4.3.3.1 BET surface area study

The specific surface area of VN samples synthesized by urea route obtained from V_2O_5 precursors heat treated at temperature 350^{o}C and 550^{o}C are found to be 57m^2/g and 11m^2/g. The BET surface area for VN samples prepared by ammonia route using V_2O_5 precursors heat treated at temperature 350^{o}C and 550^{o}C are found to be 15 m^2/g and 39 m^2/g. We could succeed in synthesizing high surface area VN nitride having maximum surface area of 57 m^2/g using V_2O_5 (350) precursor via urea route. However, VN prepared via same urea route from the precursor V_2O_5 obtained at 550˚C possesses moderate surface area of 11m^2/g. On the contrary, VN synthesized via ammonia route from V_2O_5 precursor heat treated at 550^{o}C possesses high surface area of 39m^2/g, whereas that obtained from V_2O_5 precursor heat treated at 350^{o}C has a surface area of 15 m^2/g.

The particle sizes of VN can be calculated from the specific surface area, assuming spherical nature of the particles, using the relation:

$$d = \frac{6}{\rho s} \times 1000 \qquad \text{……. eq. (4.1)}$$

where 'd' is the average diameter (nm) of the particle, 'ρ' is the density(g/cc) and 's' is the specific surface area (m^2/g) [30]. Substituting theoretical value of 6.13 g/cc for density 'ρ' of VN [31] , particle diameters for the sample prepared by urea route and ammonia route are 17nm, 89nm and 65nm, 25nm, using V_2O_5 precursors heat treated at temperature 350^{o}C and 550^{o}C, respectively. The BET particle sizes were larger than the XRD crystallite size and smaller than SEM particle size (table 4.4, table 4.6). It can be seen from the tables that the calculated BET particle sizes do not correspond well to the observed XRD crystallite sizes and SEM sizes. This can be attributed to the presence of agglomerates and different pore structures in the VN material. The lattice strain can also produce additional broadening in the XRD pattern.

Table 4.6 Materials, precursors, route, pore volume, BET surface area, BET particle size and average pore size of VN materials.

Material	Precursors	Route	Pore volume (cc/g)	BET surface area (m^2/g)	BET Particle size(nm)	Average Pore size (nm)
VN	V_2O_5 (350)	Urea	9.245	57	17	4
		Ammonia	3.150	15	65	33
VN	V_2O_5 (550)	Urea	0.010	11	89	189
		Ammonia	0.088	39	25	9

In summary, it is observed that use of different precursors and different synthetic strategies lead to different specific surface area and surface properties. It has been already reported that temperature programmed reaction of V_2O_5 is a simple procedure to produce high surface area materials [15, 32]. Synthesis of high surface area material also depends upon the heating ramp employed during the temperature programmed reaction. We could obtain surface area of 57 m^2/g and 39 m^2/g by employing heating ramp of 3.8 K/min. We anticipate that decreasing the heating ramp may produce very high surface area material. To be noted a specific surface area of 90 m^2/g has already been obtained by using low heating

rate of 1.66 K/min and high flow rate of ammonia [9]. On the above, the use of nano-crystalline V_2O_5 precursor having particle dimensions of 27nm and 39nm obtained by heat treating the sample at 350^{o}C and 550^{o}C may attribute to the production of high surface area materials in our study.

4.3.3.2 Sorption isotherm and porosity

Figure 4.11 (a), (b), (c) and (d) and figure 4.12 (a), (b), (c) and (d) represent the adsorption - desorption isotherms and pore diameter distribution obtained at 77K for VN synthesized by urea route and ammonia route, from V_2O_5 precursors heat treated at temperature 350˚C and 550˚C, respectively. The N_2 adsorption at low relative pressure is negligible. Therefore, the micropore contribution to the total pore volume can be lower.

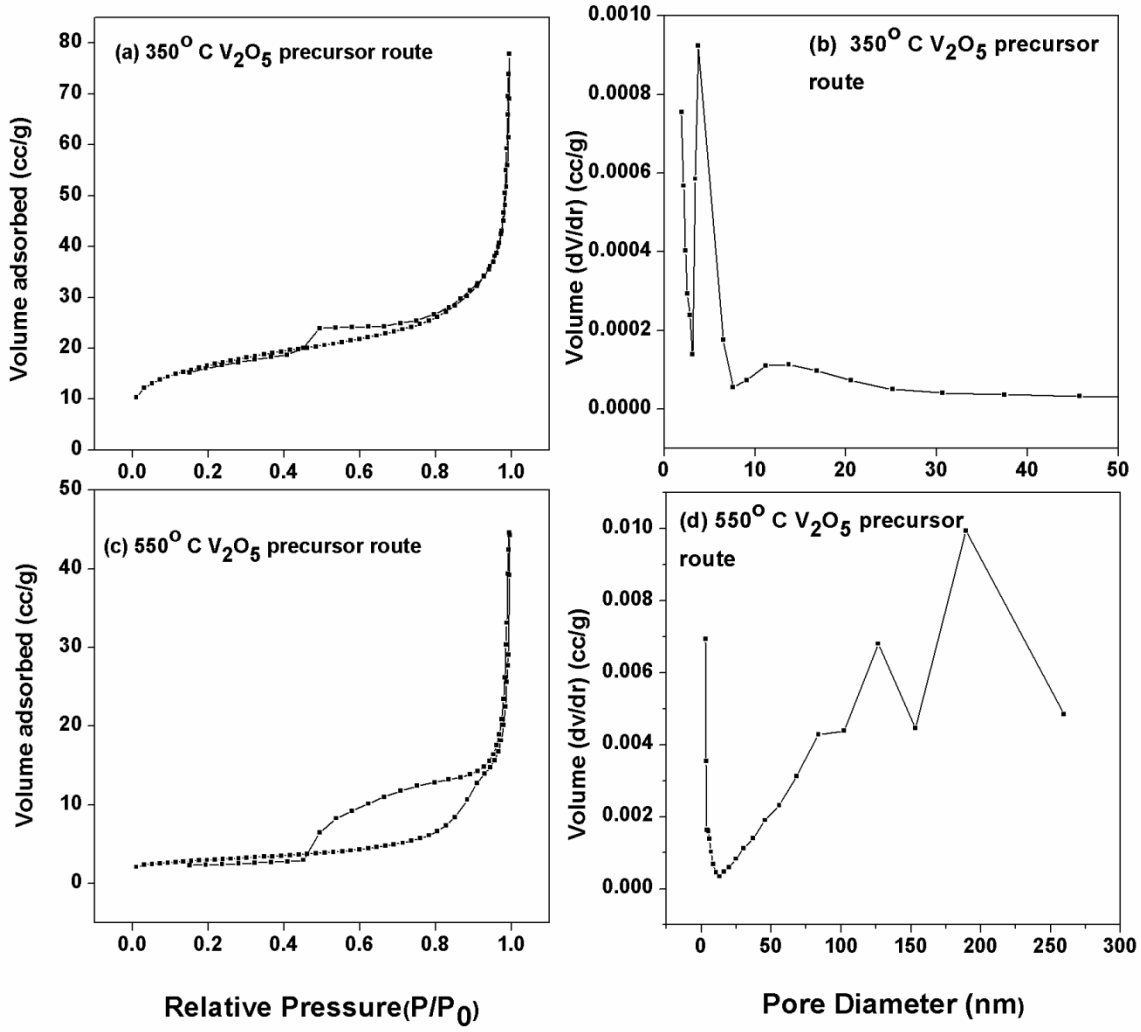

Figure 4.11 Adsorption–desorption isotherms and pore-size distribution plots of VN materials prepared via urea route from V_2O_5 precursors obtained at 350˚C ((a), (b)) and 550˚C ((c), (d)), respectively.

The isotherms show typical type-IV type with H2 hysteresis behaviour which is the characteristics for the mesoporous behaviour [2, 7, 33, 34]. The mesoporous behaviour is accompanied by initial stiff increase in the value of sorption having inflation point, approximately at P/P_0 = 0.5 and thereafter a linear increase up to 0.99. However for VN synthesized by urea route, the jump occurs at higher value of P/P_0 i.e. 0.9 (figure 4.11). The jump at approximately, P/P_0 = 0.5, corresponds to capillary condensation and the presence of hysteresis in the isotherm shows interparticle mesoporosity.

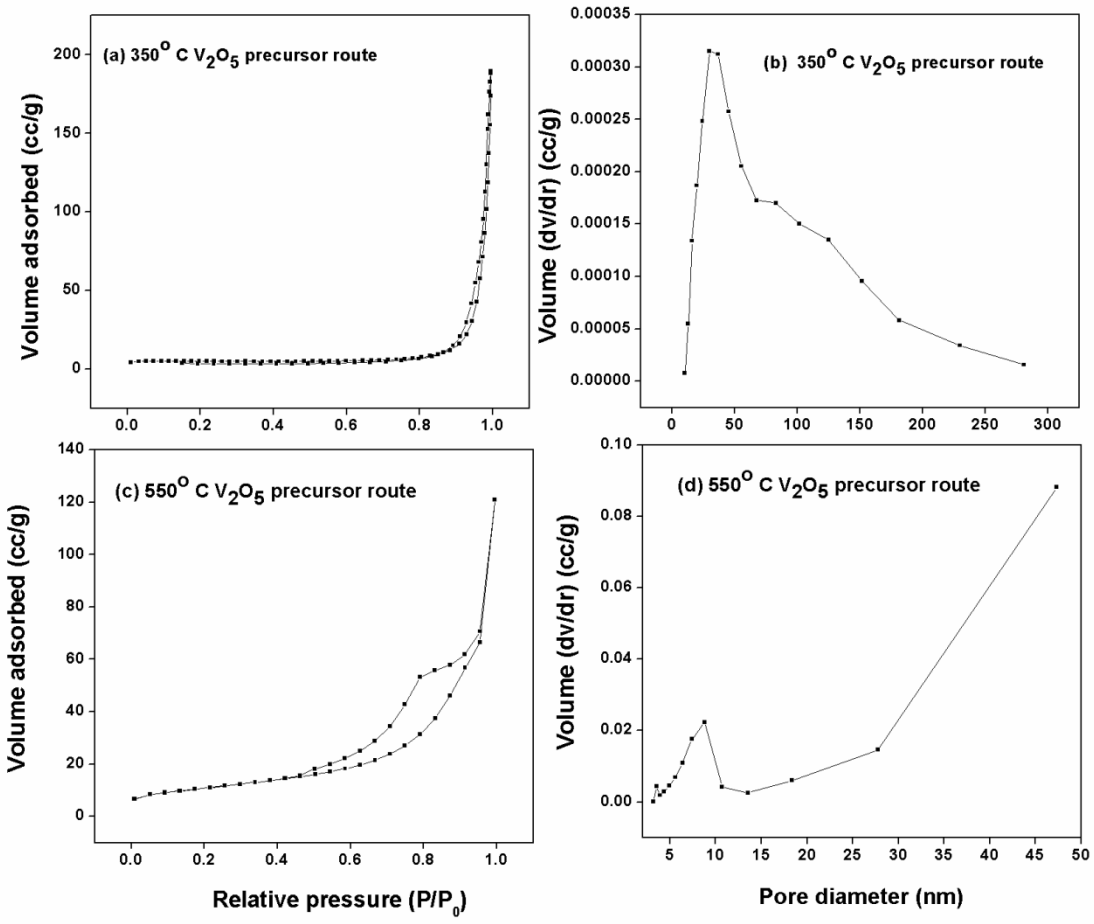

Figure 4.12 Adsorption–desorption isotherms and pore-size distribution plots of VN materials prepared via ammonia route from V_2O_5 precursors obtained at 350˚C ((a), (b)) and 550˚C ((c), (d)), respectively.

The pore diameter distribution curve for VN samples synthesized by urea route (figure 4.11(b), (d)) shows the presence of macropores (50-250 nm) [35]. The peak positions in the pore size distribution curves are depicted in the figure (4.11(b), (d)) and are centered

at 4 nm and 189 nm for VN synthesized by urea route from V_2O_5 precursors heat treated at temperature 350^oC and 550^oC, respectively. The abundance of mesopores for VN sample synthesized by ammonia route is in the range of 2-10 nm and 10-50 nm (figure. 4.12 (b), (d)). The peaks are centered at 33 nm and 9 nm for VN synthesized by ammonia route from V_2O_5 precursors heat treated at temperature 350˚C and 550˚C, respectively. All the above stated results confirm the mesoporous behaviour of our materials. The mesoporous structure might be due to the nitridation reaction and the presence of carbon impurity in the precursor materials [36]. These results also indicate that production of high surface area VN materials is dependent on chemically synthesized precursor. Further, the sorption results can be correlated to the observation of macropores in the material. For example, the absence of macropores in the VN product leads to high surface area materials irrespective of the synthetic routes and precursors used.

4.3.4 Electrochemical properties of VN Nitride

Electrochemical properties (V vs. I) of the selected nitride materials were tested by CV measurements. Several samples have been tested and the results are different for samples synthesized via different routes and having altered size, surface structure, porosity and morphologies. Various nitride products have been studied using the method described earlier (Chapter 2, Subsection 2.4.3) for CV measurement. A typical result of the CV measurements for VN synthesized via ammonia route using V_2O_5 (350) precursor has been presented in figure 4.13. As it can be seen the figure, typical hysteresis loops which are characteristics of supercapacitor properties are observed. Using the standard formula the specific capacitance (SC), the SC value for VN material is calculated to be 31 kF/g. In conclusion, our studies on electrochemical properties indicate potentiality of our synthesis methods for nano-structured nitride formation which are useful for supercapacitor applications including tuning of properties.

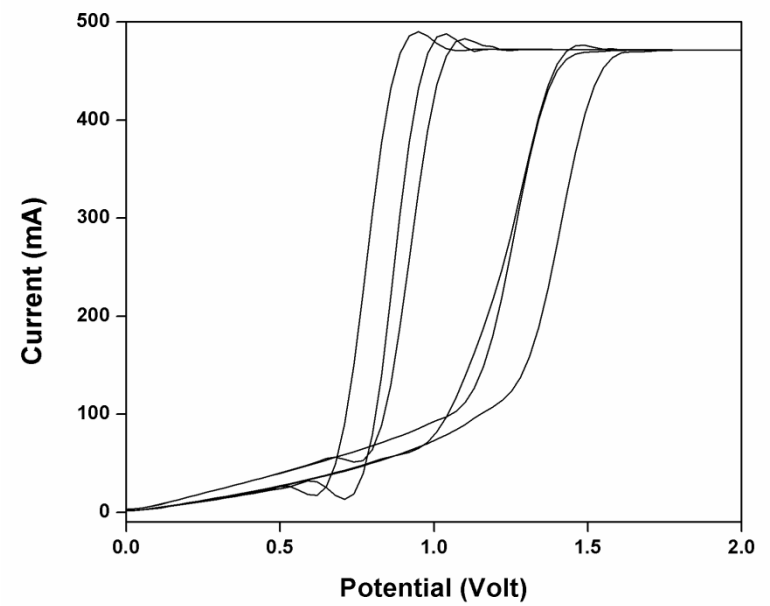

Figure 4.13 Cyclic voltametry plots of VN prepared via ammonia route from precursor V_2O_5(350).

4.4 Conclusion

High surface area nanocrystalline VN samples have been prepared via chemical synthesis route. The XRD patterns show formation of pure cubic phase samples of VN having lattice parameters 4.113(6) Å and 4.126(6) Å for urea route and 4.112(0) Å and 4.112(5) Å for ammonia route, using V_2O_5 precursors heat treated at temperature 550^{o}C and 350^{o}C respectively. The SEM micrographs show agglomerates of dimension 300×15 nm and 115 nm for urea route, 68nm and 111nm for ammonia route from V_2O_5 precursors heat treated at temperature 350^{o}C and 550^{o}C, respectively. TEM micrographs reveal that VN materials synthesized via urea route possess particles with rod shaped morphology whereas VN synthesized via ammonia route crystallizes in nearly spherical morphologies. The SAED patterns of VN nitrides indicate varieties of material structures including amorphous, partly crystalline and well defined polycrystalline nature. The BET isotherms show the typical type-IV with H2 hysteresis and indicate mesoporous behavior. The maximum BET surface area for VN sample was found to be 57 m^2/g for the material synthesized via ammonia route from V_2O_5 precursors heat treated at temperature 350^{o}C. In summary, we have synthesized porous VN with remarkable high surface area by a newer precursor route. The method may be useful for production of several other VN based bimetallic nitrides with high surface area and enhanced porosity.

References

1. X. Lu, M. Yu, T. Zhai, G. Wang, S. Xie, T. Liu, C. Liang, Y. Tong, Y. Li, Nano Lett. **13** (2013) 2628-2633.

2. Z. -H. Gao, H. Zhang, G. -P. Cao, M. -F. Han, Y. -S. Yang, Electrochim. Acta. **87** (2013) 375-380.

3. M. Yang, Z. Cui, F. J. Disalvo, Chem. Commun. **48** (2012) 10502-10504.

4. N. Y. Kim , J. H. Lee, J. A. Kwon, S. J. Yoo, J. H. Jang, H. J. Kim, D. H. Lim, J. Y. Kim, Journal of Industrial and Engineering Chemistry. **46** (2017) 298–303.

5. M. R. Wixom, D. J. Tarnowski, J. M. Parker, J. Q. Lee, P. L. Chen, I. Song, L. T. Thompson, Mater. Res. Soc. Symp. Proc. **496** (1998) 643.

6. F. Cheng, C. He, D. Shu, H. Chen, J. Zhang, S. Tang, D. E. Finlow, Mater. Chem. Phys. **131** (2011) 268-273.

7. Z. Zhao, Y. Liu, H. Cao, J. Ye, S. Gao, M. Tu, J. Alloy Compd. **464** (2008) 75-80.

8. Y. C. Hong, D. H. Shin, H. S. Uhm, Mater. Chem. Phys. **101** (2007) 35-40.

9. P. Krawiec, P. L. De Cola, R. Glaser, J. Weitkamp, C. Weidenthaler, S. Kaskel, Adv. Mater. **18** (2006) 505-508.

10. P. Krawiec, R. N. Panda, E. Kockrick, D. Geiger, S. Kaskel, J. Solid State Chem.**181** (2008) 935-942.

11. L. Chen, Y. Gu, L. Shi, Z. Yang, J. Ma, Y. Qian, Solid State Commun.**132** (2004) 343-346.

12. H. -M. Lee, G. H. Jeong, S. -W. Kim, C. -K. Kim, Appl. Surf. Sci. **400** (2017)194-199.

13. C. Giordano, C. Erpen, W. Yao, B. Mike, M. Antonietti, Chem. Mater. **21**(2009) 5136-5144.

14. J. Buha, I. Djerdj, M. Antonietti, M. Niederberger, Chem. Mater. **19** (2007) 3499-3505.

15. A. M. Glushenkov, D. Hulicova-Jurcakova, D. Llewellyn, G. Q. Lu, Y. Chen, Chem. Mater. **22** (2010) 914-921.

16. B. D. Cullity, Elements of X-ray Diffraction, Addison-Wesley, Reading, MA, 1956. p. 98.

17. L. Gao, X. Wang, L. Fei, M. Ji, H. Zheng, H. Zhang, T. Shen, K. Yang, J. Cryst. Growth. **281** (2005) 463–467.

18. P. Rodriguez, J. L. Brito, A. Albornoz, M. Labadi, C. Pfaff, S. Marrero, D. Moronta, P. Betancourt, Catal. Commun. **5** (2004) 79-82.

19. N. S. Gajbhiye, R. S. Ningthoujam, Mater. Res. Bull. **41** (2006) 1612–1621.

20. M. A. Roldan, V. López-Flores, M. D. Alcala, A. Ortega, C. Real, J. Eur. Ceram. Soc. **30** (2010) 2099–2107.

21. M. D. Agues, A. M. Nartowski, I. P. Parkin, M. Mackenzie, A. J. Craven, J. Mater, Chem. **8** (1998) 1875-1880.

22. G. Kothleitner, M. Rogers, A. Berendes, W. Bock, B. O. Kolbesen, Appl Surf Sci. **252** (2005) 66–76.

23. K. C. Dewangan, R. S. Ningthoujam, S. Kuriyan, N. S. Gajbhiye, Hyperfine Interact. **183** (2008) 185-191.

24. J. Theerthagiri, S. B. Dalavi, M. M. Raja, R. N. Panda, Mater. Res. Bull. **48** (2013) 4444–4448.

25. Y. Yang, K. Shen, Y. Liu, Y. Tan, X. Zhao, J. Wu, X. Niu, F. Ran, Nano-Micro Lett. **9** (2017) 6-15.

26. T. Palaniselvam, R. Kannan, S. Kurungot, Supplementary Material (ESI) Chem. Commun. **47** (2011) 2910–2912.

27. D. A. Wollman, S.W. Nam, G. C. Hilton, K. D. Irwin, N. F. Bergren, D. A. Rudman, J. M. Martinis, D. E. Newbury, J. Microsc. **199** (2000) 37-44.

28. D. Zhao, Z. Cui, S. Wang, J. Qin, M. Cao, J. Mater. Chem. A, **4** (2016)7914–7923.

29. T. S. Le, Q. B. Ngo, V. D. Nguyen, H. C. Nguyen, T. H. Dao, X. T. Tran, E. N. Kabachkov, I. L. Balikhin, Adv. Nat. Sci: Nanosci. Nanotechnol. **5** (2014) 015017 (1)-(6).

30. S. Brunauer, P. H. Emmett, E. Teller, J. Amer. Chem. Soc. **60** (1938) 309 -319.

31. C. L. Yeh, H. C. Chuang, E. W. Liu,Y. C. Chang, Ceram. Int. **31**(2005) 95-104.

32. H. Kwon, S. Choi, L. T. Thompson, J. Catal. **184** (1999) 236-246.

33. C. R. Theocharis, C. Attipa, E. Hapeshi, A Tillirou, R. Kokkinofta, Adsorpt. Sci. Technol. **26** (2008) 643-650.

34. Z. S. Wu, Y. Sun, Y. Z. Tan, S. Yang, X. Feng, M. Klaus, J. Am. Chem. Soc. **134** (2012) 19532-19535.

35. K. S. W. Sing, D. H. Everett, R. A. W. Haul, L. Moscou, R. A. Pierotti, J. Rouquerol, T. Siemieniewska, Pure Appl. Chem. **57** (1985) 603-619.

36. X. Zhou, C. Shang, L. Gu, S. Dong, X. Chen, P. Han, L. Li, J. Yao, Z . Liu, H. Xu, Y. Zhu, G. Cui, ACS Appl. Mater. Interfaces **3** (2011) 3058-3063.

Chapter-5

Novel Synthesis, Characterization and Studies on Nanocrystalline γ-Mo_2N and γ-$Co_{0.25}Mo_{1.75}N$ Nitrides

This chapter focuses on the synthesis of γ-Mo_2N and γ-$Co_{0.25}$ $Mo_{1.75}$ N nitrides via nitridation using various chemically synthesized precursors. The nitride products have been characterized and studied for magnetic and surface properties in details.

5.1 Introduction

Development of alternative materials which can replace noble metal catalyst is a very important topic of research. Nanocrystalline, porous Mo_2N material is an efficient catalyst in a number of reactions such as oxygen reduction reaction, dehydrogenation of aromatic alcohols, ammonia synthesis and hydrodechlorination etc. [1-4]. The phase, morphology and structure of Mo_2N influence the ammonia synthesis activity and reduction characteristics [3, 5]. Due to layered crystal structure of γ-Mo_2N, it is effective in charge storage capacity. In recent years, molybdenum nitride (MoN_x) has been used as active electrode material owing to its high electrochemical activity, chemical stability, good electrical conductivity above 0.2 S cm^{-1} and good resistance towards electrochemical decomposition in aqueous electrolytes. It can be used as an electrode material in Li-ion batteries [6] γ-Mo_2N materials show very good superconducting properties with superconducting transition in the temperature range of 4–12K [7-9]. Cobalt molybdenum nitride with nanoscale morphology has been used to produce a highly active and stable electrocatalyst for the hydrogen evolution reaction (HER) [10].

Volpe *et al*. have shown temperature-programmed reaction between MoO_3 with NH_3(g) is an effective way to prepare Mo_2N powders with specific surface area as high as 220m^2/g [11]. Use of solid urea as a non-toxic nitrogen source has been reported to control the crystallinity and growth of the nitride products [12].The composition of molybdenum nitride as well as the structures and properties depend on the parameters of the process used

to synthesize the product. For example: transformation of MoO_3 into γ-Mo_2N is topotactic in nature, as the crystallographic planes (100) of γ-Mo_2N are produced parallel to the parent MoO_3 (010) planes [13]. The psuedomorphous γ-Mo_2N product consists of low density and highly porous nitride products [13]. Based on the above discussions, development of newer precursor routes (chemical) in order to obtain quality nanocrystalline products of Mo based nitrides and studies on their structural, surface, magnetic, electrochemical and mechanical properties are important topics of research.

The present chapter focuses on synthesis of Mo and Co-Mo based precursors through various synthetic routes and their transformation into nitrides using different nitrogen sources. This study involves development of newer precursors via facile chemical routes and their subsequent nitridation in order to obtain nitride products. The synthesis routes involve the use of hydrazine and potassium borohydride as reducing agents and ethylenediamine as complexing agents for the synthesis of different batches of precursors, separately. Ammonia gas and solid urea as nitrogen sources have been used for the nitridation experiment. The solid state reactivity, exhaustive characterization for surface structure, electron microscopy and magnetic properties of Co-Mo based nitrides have been investigated. The chemical nature of the precursors, nitrogen sources and parameters for nitridation reactions are correlated to the structural, surface and magnetic properties of nitride products.

5.2 Materials and methods

Three different chemical based precursor routes have been adopted during the synthesis of nitride products. Based on the feasibility, one of the two different nitrogen sources; namely: NH_3(g) and solid urea, are used during nitridation reactions. In summary, reducing agents like hydrazine and potassium borohydride have been used for the synthesis of molybdenum oxide and cobalt substituted molybdenum oxide precursors, respectively. The different precursors synthesized, were subjected to nitridation using ammonia as nitrogen source. Ethylenediamine is also used for the synthesis of molybdenum based organometalic complex (solid) which on subsequent nitridation via urea route produces γ-Mo_2N. The details of synthesis procedure adopted have been described in the following subsections.

5.2.1 Synthesis of γ-Mo_2N and γ-$Co_{0.25}Mo_{1.75}N$ nitrides via nitridation using NH_3(g)

5.2.1.1 Synthesis of molybdenum oxide via hydrazine route

For the preparation of oxide precursor, 5g of ammonium paramolybdate, $(NH_4)_6Mo_7O_{24}\cdot 4H_2O$ (Molychem) was dissolved in 50ml of distilled water and stirred with magnetic stirrer. After complete dissolution of the solid, 7.5ml of 15% hydrazine hydrate ($NH_2NH_2\cdot H_2O$) (Qualigen) solution was added drop wise at room temperature (298K) until the colour of the solution becomes brown. The resulting solution was refluxed at 70˚C for 30 min in air atmosphere. The resulting coarse precipitate was filtered out, washed with distilled water and ethanol several times and air dried at 298K for 12hrs. The dried precipitate was collected and heated separately under N_2(g) flow at two different temperatures (300˚C and 500˚C) for 2h duration. The violet coloured amorphous powder (precursor) obtained at 300˚C is used for nitridation experiment while the blue colored product obtained at 500^{o}C is used for studying precursor characteristics.

5.2.1.2 Synthesis of Co-Mo based bimetallic oxides via borohydride route

For the synthesis of γ-$Co_{0.25}Mo_{1.75}N$, stoichiometric amounts of Co and Mo sources $(NH_4)_6Mo_7O_{24}.4H_2O$ and $Co(NO_3)_2.6H_2O$) were dissolved in 40ml of distilled water and stirred. 10ml of 0.1N aqueous ammonia was added in order to make the solution basic. Next 15ml of 0.04M KBH_4 was added to it and agitated using a magnetic stirrer for 1h at 298K in order to get a pinkish white solid precipitate. The solid was collected, washed with aqueous ammonia, ethanol and cooled down to 298K then dried at 80˚C in air for a duration of approximately 72hrs. The resulting solid was heated at 200˚C for 2h duration under N_2(g) flow. After cooling down to 298K, the resulting solid was crushed well and used for nitridation experiments.

5.2.1.3 Synthesis of γ-Mo_2N and γ-$Co_{0.25}Mo_{1.75}N$ via ammonia route

The solid precursors obtained in the previous subsections (5.2.1 and 5.2.2) via hydrazine and KBH_4 routes, respectively, were used as precursors for nitridation in order to synthesize γ-Mo_2N and γ-$Co_{0.25}Mo_{1.75}N$ nitrides**.** Approximately, 0.6g of oxide precursors was loaded in the middle of a quartz reactor of 1m length. The tube containing precursor is placed inside a vertical tubular furnace. NH_3 (g) is purged for 1h to remove any residual oxygen from the reactor. Then furnace is programmed to heat the precursor up to 700˚C in

4h with the heating ramp of 2.9˚C /min and maintained at the final temperature (700˚C) for 2h. The furnace was allowed to cool down naturally under the flow of NH_3 (g) till room temperature was reached. The resulting final products are subjected to characterization and properties studies.

5.2.2 Synthesis of γ-Mo_2N nitrides via nitridation using solid urea

5.2.2.1 Synthesis of molybdenum - ethylenediamine complex

We have tried to synthesize literature reported ethylenediammonium trioxomolybdate (VI)-μ- oxotrioxoethylenediaminemolybdate (VI) (enH_2) [O_3Mo-O-Mo(en)O_3]) precursor using modified synthetic strategy [14]. Further, the possibility of nitride formation using the above precursor has been explored. The procedure adopted may be summarized as follows: commercially available molybdenum trioxide (MoO_3) (Molychem 99.5%) and ethylenediamine ($NH_2CH_2CH_2NH_2$) (Fisher Scientific, 99%) were taken in 1: 25 equivalence of molar ratios in a 500ml beaker. In real practice, approximately, 4g of MoO_3 was taken in a beaker and 120 ml of distilled water was added. 4.6 ml of ethylenediamine was added to the resulting suspension in order to obtain a clear solution. After stirring for 5 min. at room temperature, Conc. HCl (aq.) was added drop wise till white precipitate was formed. This is heated at 100˚C for 5h with constant stirring and reflux on oil bath. The precipitate formed is then filtered out using a filter paper and dried at room temperature for 48- 72h. The white colored dried precipitate was then collected, crushed and used as the precursor for nitridation.

5.2.2.2 Synthesis of γ-Mo_2N via urea route

The organometallic precursor (0.7g) (as described in sub-section 5.2.2.1) and solid urea (1.057g) were taken in 1:9 molar equivalences and mixed well using a mortar and pestle. The mixture was taken in an alumina boat and placed inside the tubular furnace. Initially, N_2(g) was purged for 1-2h to remove any residual oxygen present in the sample chamber and to make the reaction in inert atmosphere. Next, the furnace was programmed to heat the reactant mixture in a controlled manner under the flow of N_2(g). The precursor was heated up to 650˚C inside the furnace in 3h duration with a heating rate of 3.6˚C/ min. The furnace was maintained at the final temperature for the reaction to take place for 3h duration. After that the reactor was allowed to cool down naturally under N_2(g) flow until

room temperature was reached. The sample was removed from the reactor and exposed to air at room temperature.

5.2.3 Instrumental characterization

The XRD patterns were recorded using a powder X-ray diffractometer (Rigaku Miniflex-II) using Cu-Kα radiation at a scanning speed of 3˚/min. The phase purity was ascertained using XRD. The shape and morphology of the products were examined by scanning electron microscopy (SEM) (model: JEOL, JSM-6390), transmission electron microscopy (TEM) (model: Philips- CM 200) and HRTEM (model : Tecnai G2,F30). Nitrogen physisorption experiments were performed using BET measurement (Model: Micromeritics Gemini VII, USA). The samples were activated at 250˚C/1h using high purity N_2.The magnetization measurements (M vs. H characteristics) were carried out on solid powder material using vibrating sample magnetometer (model: Lakeshore VSM 7410) which can provide a magnetic field up to 20 kOe.

5.3 Results and discussions

The synthesized γ-Mo_2N and γ-$Co_{0.25}Mo_{1.75}N$ materials were characterized using XRD, TEM, HRTEM, BET and VSM techniques. The obtained results of structural, surface and magnetic properties of Mo and Co-Mo based materials have been presented and analyzed in detail in the following subsections.

5.3.1 γ-Mo_2N synthesized via ammonia route

X-ray diffraction studies have been used to characterize the precursor and different final products were obtained at various reaction temperatures. Phase analyses and various XRD parameters have been studied for selected precursor materials and nitride products obtained at various temperatures.

5.3.1.1 XRD studies of γ-Mo_2N

5.3.1.1.1 Precursor characterization

The precursor material prepared via hydrazine route was used for nitridation using NH_3(g) in order to prepare nanocrystalline γ-Mo_2N. The precursors were heated at various temperatures and time intervals in order to ensure crystalline phase and ultrafine nature.

Figure 5.1 represents the precursor materials (synthesized at 200°C) heat treated at 300˚C and 500˚C under the flow of high purity N_2(g).

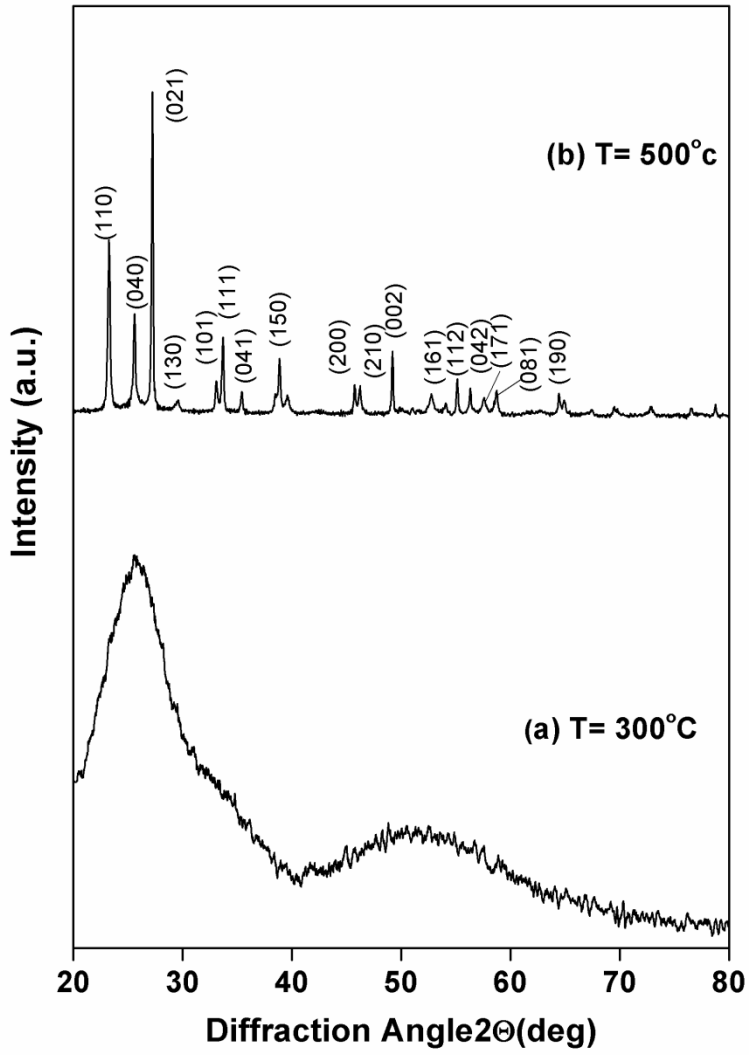

Figure 5.1 Indexed XRD patterns of precursors, heat treated at (a) 300˚C and (b) 500˚C for 2hrs duration. The precursors were prepared via hydrazine route.

The heat treated precursor at 300˚C shows nearly amorphous structure with two broad peaks centered at 2Θ values of nearly 26˚ and 52˚ (figure 5.1(a)). With the increase of heat treatment temperature up to 500˚C, the phase-pure orthorhombic α-MoO_3 is formed (figure 5.1(b)). The XRD pattern of orthorhombic α-MoO_3has been indexed as per ICDD PDF # 05-0508 and is shown in the figure 5.1 (b). The XRD parameters along with crystallographic parameters have been summarized in table 5.1. The lattice parameters of α-MoO_3 are estimated to be a = 3.980(5) Å, b = 13.932(9) Å and c = 3.699(3) Å (see table

5.1), comparable to the reported values of a = 3.962 Å, b = 13.858 Å and c = 3.697 Å [15]. The above results support the evolution of α-MoO_3 phase using the current synthesis method. However, we have taken the amorphous form of crystalline α-MoO_3 as precursor presuming it might have enhanced reactivity for nitride formation.

Table 5.1 Materials, Miller indices (hkl), observed and calculated interplanar spacings (d_{obs} and d_{cal}) and lattice parameters (a, b, c) of α-MoO_3 synthesized via hydrazine route and heat treated at 500°C.

Material	(hkl)	d_{obs}(Å)	d_{cal}(Å)	Lattice parameters* (Å)
α-MoO_3	(110)	3.818	3.827	a=3.980(5) b=13.932(9) c=3.699(3)
	(040)	3.485	3.483	
	(021)	3.279	3.267	
	(101)	2.714	2.709	
	(111)	2.654	2.659	
	(150)	2.318	2.282	
	(002)	1.852	1.849	
	(161)	1.735	1.763	
	(112)	1.665	1.665	
	(042)	1.632	1.633	
	(081)	1.569	1.575	

*** The material crystallizes in orthorhombic crystal structure.**

5.3.1.1.2 Solid state reactivity study on formation of γ-Mo_2N

The amorphous product prepared via hydrazine route at 300˚C was taken as the precursor for nitridation reaction using NH_3(g) as nitrogen source. The reaction temperature and experimental parameters for γ-Mo_2N formation were standardized by using XRD technique. Figure 5.2 represents the XRD patterns of various nitridation products obtained at various temperatures ranging from 650°C-700°C.

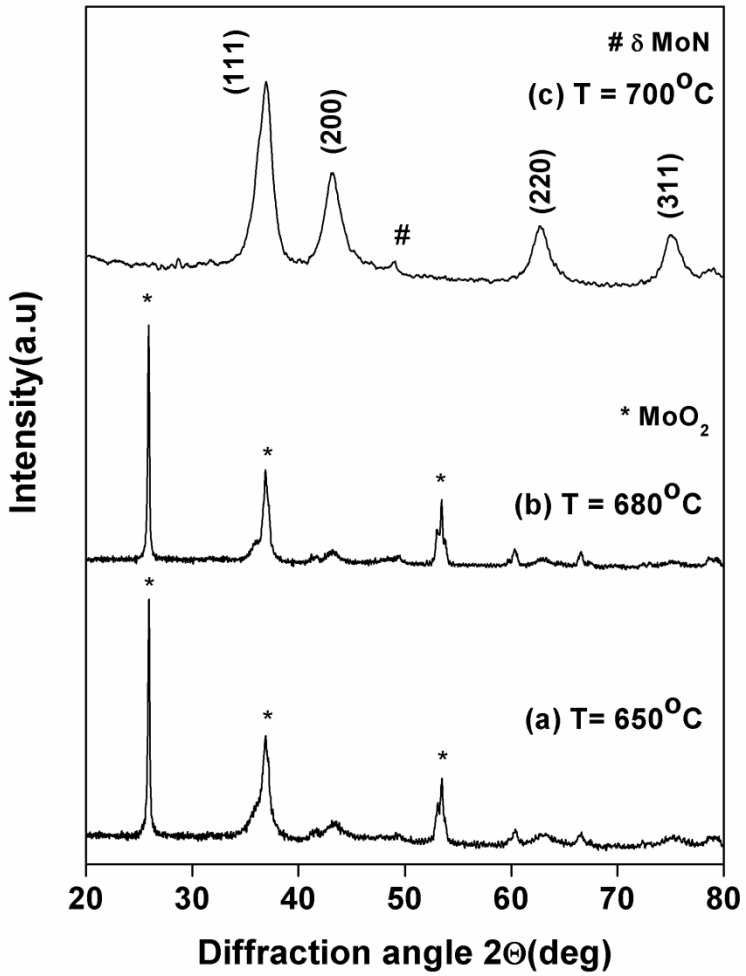

Figure 5.2 Indexed XRD patterns of nitridation products obtained at various temperatures; (a) 650˚C, (b) 680˚C and (c) 700˚C. * and # indicate minute impurity phases present in the materials.

With the gradual increase in nitridation temperatures, i.e. up to 680˚C, the XRD patterns show MoO_2 oxide phases majorly along with minor peaks of γ-Mo_2N phase (figure 5.2(a), (b)). With further increase of nitridation temperature up to 700˚C, formation of pure phase γ-Mo_2N takes place (figure 5.2(c)). Hence, the reaction temperature was optimized at 700˚C for nitridation of Mo based and Co substituted Mo based precursors obtained via various routes in our study. Increase of reaction temperature beyond 750^{o}C, results in the decomposition of the nitride phases (as confirmed by XRD study, figure not shown). The above results were supported by published literature [16, 17]. Therefore, in our study higher reaction temperature (i.e. > 750˚C) was avoided in order to avoid decomposition of the nitride products in to varieties of phases; such as: metal, alloys, nitride etc. [17]. Such kind

of observations may be understood on the basis of lower nitrogen solubilities in the nitride materials at elevated temperatures and/or thermodynamic instability of the nitride product [18].

5.3.1.1.3 X-ray diffraction study of γ-Mo_2N

The XRD pattern of nitride product γ-Mo_2N obtained via nitridation using NH_3 (g) at 700° C is presented in figure 5.3 and indexed as per ICDD PDF # 25-1366. The XRD peaks are broad indicating nanocrystalline nature of the product. The interplanar distance, Miller indices, lattice parameters and average crystallite size of the product are presented in table 5.2.

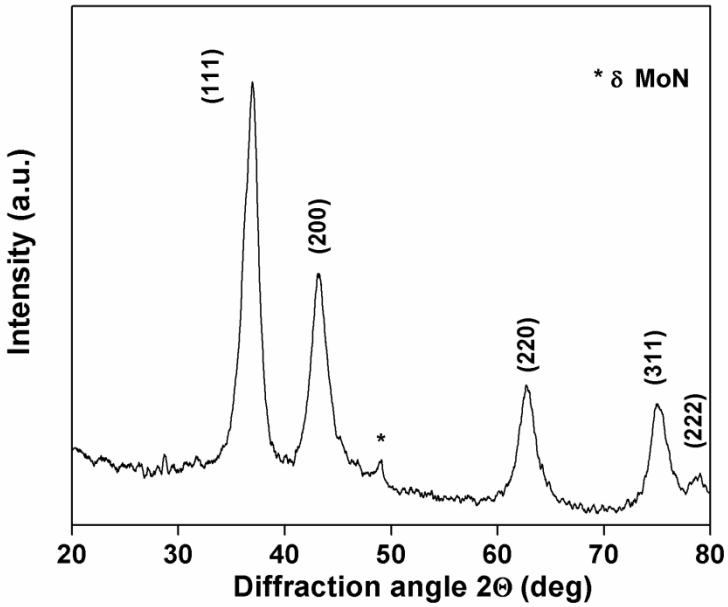

Figure 5.3 Indexed XRD pattern of γ-Mo_2N synthesized via ammonia route at 700°C. * indicates presence of minute amount of δ-MoN phase in the product.

A minor peak of δ-MoN was detected in the XRD pattern of γ-Mo_2N (figure 5.3). The values of average crystallite size and lattice parameter for γ-Mo_2N are 6±0.8 nm and 4.193(5) Å, respectively (table 5.2). The value of lattice parameter is slightly higher than the literature reported values of 4.161 Å [19]. The value obtained indicates lattice expansion of the synthesized material γ-Mo_2N in our study. These kinds of observations are already reported for nanostructured nitrides [20, 21]

Table 5.2 Material, Miller indices, observed and calculated interplanar distance, lattice parameter and average crystallite size of γ-Mo_2N.

Material	(hkl)	d_{obs}(Å)	d_{cal}(Å)	Lattice Parameter (Å)	Average crystallite size(nm)
γ-Mo_2N	(111)	2.430	2.421	4.193(5)	6±0.8
	(200)	2.091	2.096		
	(220)	1.478	1.482		
	(311)	1.262	1.264		
	(222)	1.213	1.210		

5.3.1.2 Electron microscopic studies of γ-Mo_2N synthesized via ammonia route

The synthesized sample of γ-Mo_2N was characterized using TEM and HRTEM for its morphology and structural arrangement study. The details of the study are described below.

5.3.1.2.1 TEM studies of γ-Mo_2N

The TEM micrographs and SAED pattern of γ-Mo_2N have been presented in the figure 5.4(a), (b), (c) and (d), respectively. The particles show spherical morphology with narrow size distribution. The average TEM size for γ-Mo_2N is found to be 5nm and is listed in table 5.3. The observed TEM particle size corresponds well with the crystallite size of the material (6nm). The SAED pattern for γ-Mo_2N (figure 5.4(d)) shows diffused ring type structures.

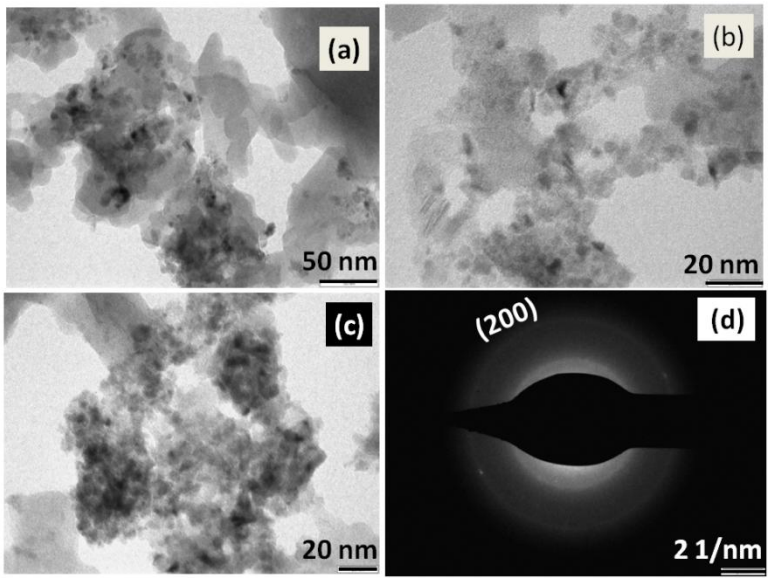

Figure 5.4 TEM micrographs at various magnifications (a)-(c) and SAED pattern (d) of γ-Mo_2N.

This result indicates poor crystallinity or amorphous nature of the product. The values of interplanar distance obtained from SAED pattern are presented in table 5.3. The ring with interplanar distance of 1.999Å corresponds to crystal plane (200) which can be well matched with the value of d- spacing of 2.091Å, calculated from XRD. The particle size distributions were estimated by plotting the size range versus frequency of occurrence and analyzed by Gaussian fit. The size distributions calculated were found to be in the range of 3- 9 nm for γ-Mo_2N material (figure 5.5). These results signify ultrafine nature of synthesized product with narrow particle size distribution.

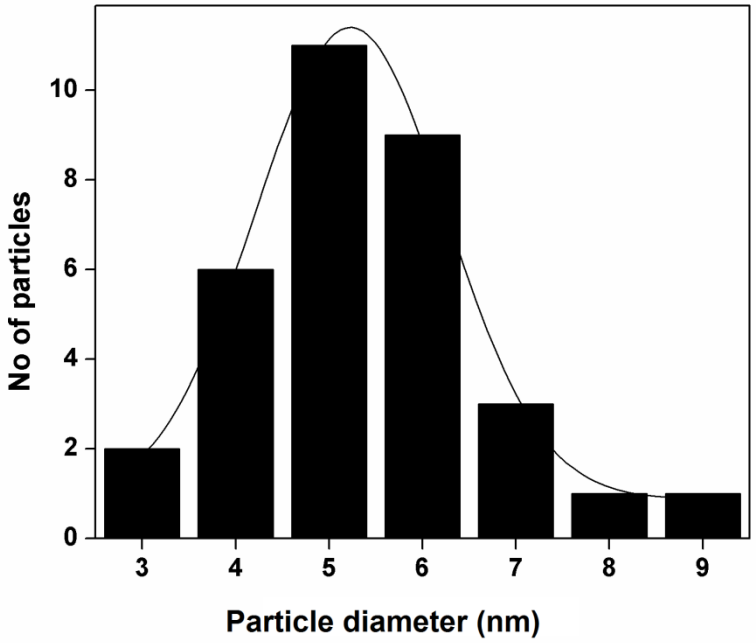

Figure 5.5 TEM particle size distributions for γ-Mo_2N materials.

Table 5.3 Average TEM particle size, interplanar distance, Miller indices and lattice parameters observed from SAED pattern of γ-Mo_2N.

Material	Average TEM particle size(nm)	Interplanar distance 'd'(Å)		Miller indices (hkl)	Lattice parameters 'a'(Å)	
		SAED	XRD		SAED	XRD
γ-Mo_2N	5	3.125 1.999	-- 2.091	(200)	-- 3.998	-- 4.193(5)

5.3.1.2.2 HRTEM studies of γ-Mo_2N

HRTEM study of γ-Mo_2N is carried out for structural analysis and representative figure is present below in figure 5.6.The micrograph shows the development of crystalline

periodicity corresponding to lattice spacing of nearly 2.1 Å for γ-Mo_2N. The stacking of atoms along (200) plane can be concluded from the observed lattice spacing. HRTEM image for γ-Mo_2N shows regions of amorphous like structures having non-periodicity, surrounding the crystalline regions and patterning structure with periodic spacing of 4.496 Å.

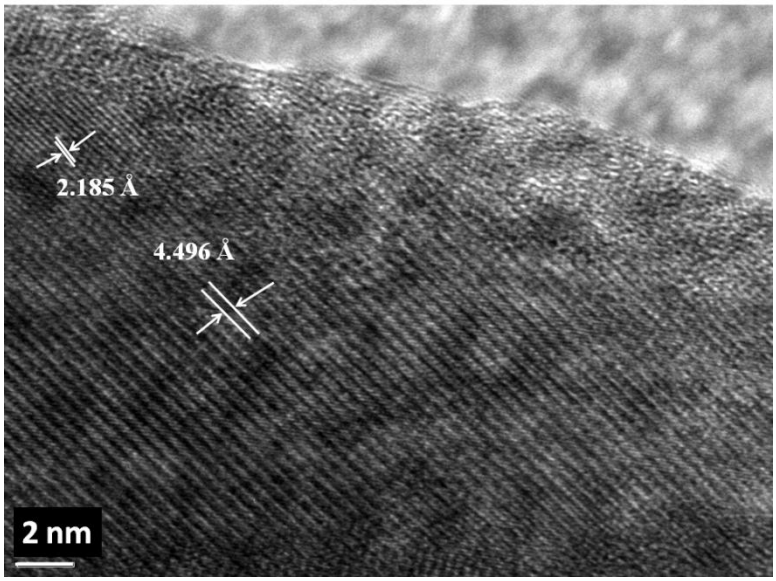

Figure 5.6 HRTEM micrograph of γ-Mo_2N synthesized via ammonia route at 700˚ C

These results are in accordance with literature reported analysis of HRTEM of fcc γ-Mo_2N phase grown inside thin film or hybrid structure [22, 23].

5.3.1.3 BET surface area study of γ-Mo_2N

In order to probe surface area and porosity, sorption studies were carried out using BET method for γ-Mo_2N nitrides and the results are presented in figure 5.7 (a) and (b) . Figure 5.7(a) represents nitrogen adsorption-desorption isotherm while figure 5.7 (b) shows pore size distribution plot of γ-Mo_2N material. The volume of nitrogen adsorbed in the region of low pressure ($0 \leq P/P_o \leq 0.2$) is not significantly higher (i.e. 15 % of that adsorbed at saturation pressure) for γ-Mo_2N. These results indicate that the micropore contribution to the total adsorption is negligible. The adsorption plots are accompanied by an inflation point at $\approx P/P_o = 0.47$ with a faster increase in adsorption rate thereafter up to a value of P/P_o very close to 1.0. This phenomenon is similar to a mesoporous behaviour with type IV isotherm and H2 hysteresis. This can be also interpreted as interparticle mesoporosity. These results can be correlated with the presence of partially crystalline structures having voids irregularly

scattered in the precursor material. Similar kinds of reports already exist in the literature for some other material systems [24]. High surface area of 53m^2/g is obtained for γ-Mo_2N using BET method.

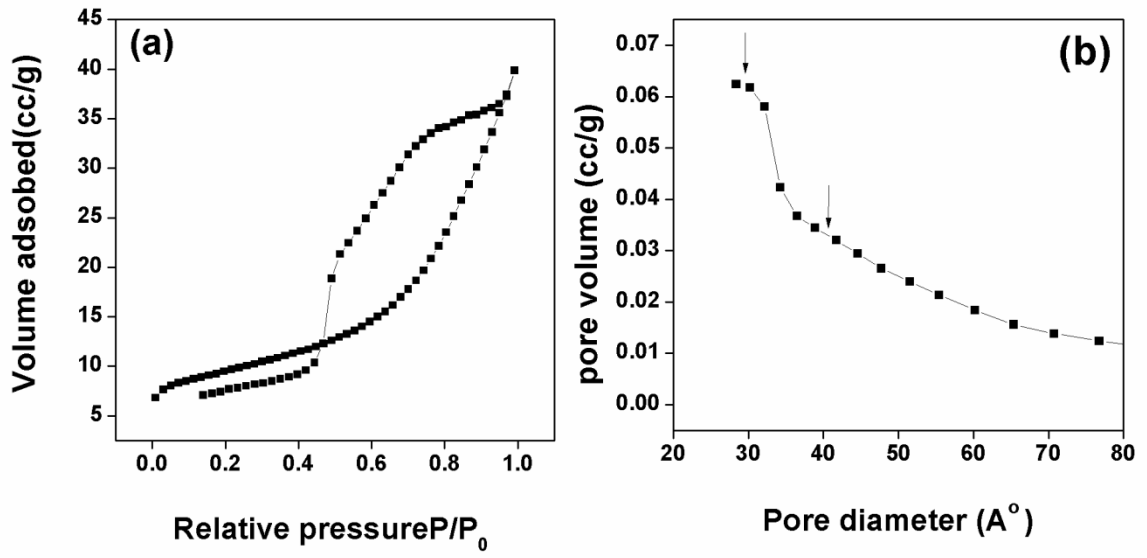

Figure 5.7 (a) Adsorption - desorption isotherm and (b) pore size distribution plots of γ-Mo_2N measured at 77K.

The pore size distributions obtained from BJH analysis of the desorption data in γ-Mo_2N shows two distinct pore structures in the mesoporous region which are centered at ≈ 2.8 (major) and ≈ 3.9 nm having narrow size distributions. The adsorption and desorption plots do not coincide at lower pressure region. This indicates the existence of non-equilibrium conditions leading to decrease in desorption rate compared to adsorption rate. We believe that these kinds of behaviour can be due to strong interaction of nitrogen gas with the nano-structured materials and some sort of restriction in diffusion process during the sorption processes.

5.3.1.4 Magnetic studies of γ-Mo_2N

The field dependent magnetization hysteresis plot of γ-Mo_2N has been shown in figure 5.8. M vs. H characteristic plot shows ferromagnetic behaviour with specific magnetizations in the order of 10^{-2} emu/g with faster increase in magnetization in the lower

field region (0 < H < 2 kOe) with finite coercivities. For γ-Mo_2N, at higher field regions (5 kOe – 15 kOe) the magnetization values tend to decrease after reaching saturation. This decrease can be due to dominant dia-magnetic contributions arising from the sample holder during the measurement compared to contribution from samples at higher fields (> 5 kOe). The specific magnetization of γ-Mo_2N at the field strength of 5 kOe is estimated to be 0.03 emu/g. The magnetic parameters obtained for synthesized γ-Mo_2N in our study are well supported by the literature reported results of Sidana *et al*. [25].

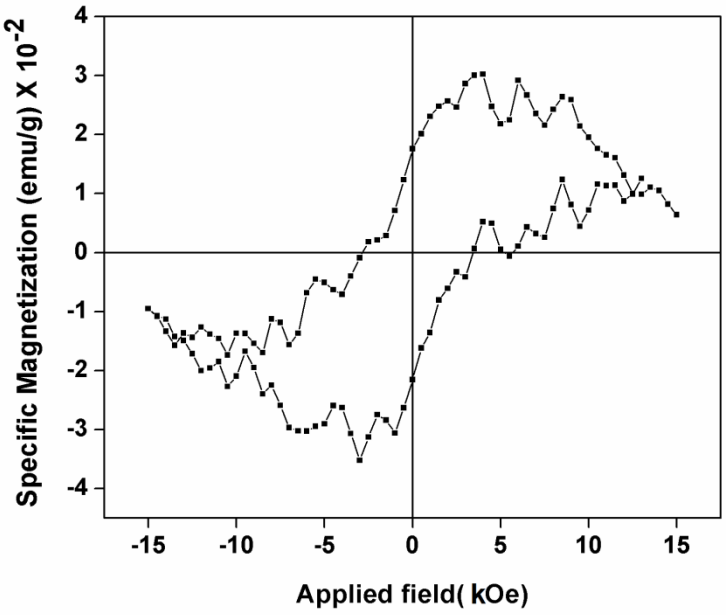

Figure 5.8Plot of specific magnetization vs. field of γ-Mo_2N measured at room temperature.

The values of coercivities for γ-Mo_2N materials are found to be 2838 Oe. Unexpectedly, a higher value of coercivity is observed for γ-Mo_2N nitrides. These results can be attributed to the disordered structural parameters in the synthesized materials using the current synthetic strategy. This kind of high coercivity has already been reported for single domain iron and cobalt particles with elongated shape [26, 27]. The observed high coercivity can be explained by noncoherent magnetization reversal mechanism [27, 28].

5.3.2 γ-$Co_{0.25}$ $Mo_{1.75}N$ synthesized via ammonia route

In order to study the effect Co atom substitution on physical properties of γ-Mo_2N, γ-$Co_{0.25}$ $Mo_{1.75}N$ nitride material has been synthesized. The structural, morphological, surface and magnetic properties of the product γ-$Co_{0.25}$ $Mo_{1.75}N$ have been investigated and compared with those corresponding to γ-Mo_2N material. The synthesized product has been characterized using XRD, TEM, HRTEM, BET and VSM techniques and the results have been presented in the following subsections.

5.3.2.1 X-ray diffraction studies of γ-$Co_{0.25}$ $Mo_{1.75}N$

The X- ray diffraction patterns of the precursor and the final nitride product have been presented and analyzed in detail in this section.

5.3.2.1.1 Precursor characterization

Figure 5.9 represents the XRD patterns of the precursors at different heat treatment temperatures, obtained using borohydride route. The XRD structure of the precipitate obtained after drying it at 80˚C and 200˚C are presented in figure 5.9(a) and (b). Figure 5.9(a) shows the poor crystalline nature of the as dried product at 80˚C, having XRD peaks in the 2θ values ranging from 25˚ - 40˚. The XRD pattern could not be indexed as per the existing JCPDS data files. However the pattern is quite similar to the standard XRD pattern of $MoO_3.H_2O$, synthesized by non-traditional route [29]. With the increase of heat treatment temperature to 200˚C, surprisingly evolution of orthorhombic α-MoO_3 phase occurs with varying interplanar spacing and intensities of certain crystal planes due to preferential growth. Non-existence of any Co-based oxides or $CoMoO_4$ indicates that Co atoms have been incorporated in the crystal structure of α-MoO_3. Evolution of α-MoO_3 crystal phase at relatively lower temperature, i.e. 200˚C, in borohydride route is note worthy. It has been already known that α-MoO_3 crystallizes in orthorhombic structure at much higher temperature, i.e. nearly 500˚C, when synthesized using different chemical methodologies [15, 21].

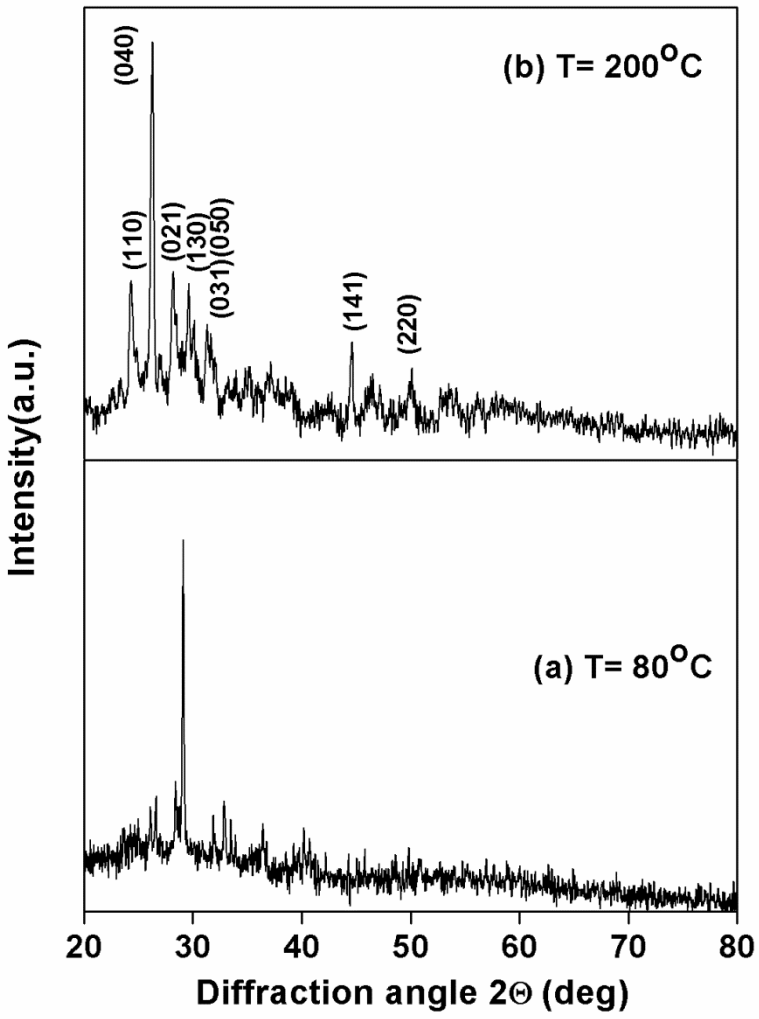

Figure 5.9 XRD patterns of the α-$Co_{0.12}Mo_{0.88}O_3$ precursors obtained via borohydride route and heated at different temperatures (a) 80°C (as prepared) and (b) 200°C.

α-$Co_{0.12}Mo_{0.88}O_3$ material crystallizes in orthorhombic structure with lattice parameters; a = 3.788(2) Å, b= 13.599(5) Å and c = 3.563(8) Å having lattice volume of 183.5 $Å^3$. The observed values of lattice parameters are comparable but less than those of α-MoO_3, i.e. a = 3.980 Å, b = 13.932 Å and c = 3.699 Å and the literature reported values by Wongkrua *et al*. for 450° C annealed samples [15, 30]. Further the estimated lattice volume of α-$Co_{0.12}Mo_{0.88}O_3$, i.e. 183.5 $Å^3$, is significantly less than that of α-MoO_3, i.e. 202.9 $Å^3$. This result may be explained on the basis of substitution of Co atoms with atomic radius of 1.25 Å in place of Mo with atomic radius of 1.40 Å and confirms Co atom incorporation in the lattice of α-MoO_3. The estimated average crystallite size of α-$Co_{0.12}Mo_{0.88}O_3$ precursor is 27 nm.

5.3.2.1.2 XRD study of γ-$Co_{0.25}$ $Mo_{1.75}$ N

Figure 5.10 represents the X-ray diffraction pattern of Co substituted γ-Mo_2N synthesized at 700˚C using NH_3(g) from mixed metal oxide precursor obtained via borohydride reduction route. A minor impurity of MoO_3 was detected in the XRD pattern of γ-$Co_{0.25}$ $Mo_{1.75}$ N. The XRD peaks are broad indicating nanocrystalline nature of the material. The XRD pattern is indexed as per the ICDD PDF # 25-1366. The values of the interplanar spacing, Miller indices (hkl), lattice parameters and crystallite size etc. are listed in table 5.4.

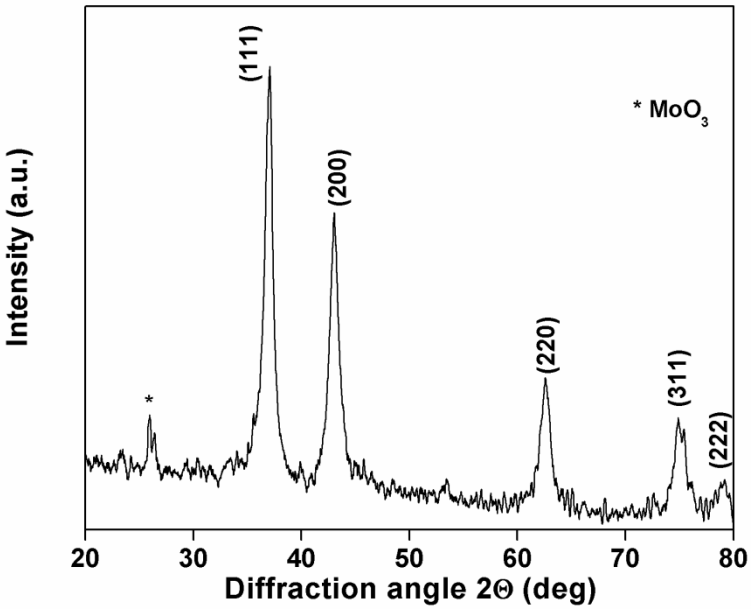

Figure 5.10 Indexed XRD pattern of γ-$Co_{0.25}$ $Mo_{1.75}$ N synthesized at 700˚C. * indicates minute MoO_3 as impurity phase.

The material γ -$Co_{0.25}$ $Mo_{1.75}$ N crystallizes in face centered cubic structure with lattice parameter value of 4.198(2) Å. The observed value of lattice parameter is comparable, but slightly greater than the reported value of 4.161 Å for γ-Mo_2N [19]. Thus, an expansion of crystal lattice is observed in our synthesized materials. The average crystallite size is estimated to be 11±0.5 nm for γ-$Co_{0.25}$ $Mo_{1.75}$ N material which is significantly greater than the value of γ-Mo_2N i.e. 6±0.8 nm. These results prove that insertion of Co into γ-Mo_2N matrix dilates the host lattice.

Table 5.4 Material, Miller indices (hkl), observed and calculated interplanar spacings (d_{obs} d_{cal}), lattice parameter and average crystallite size of γ- $Co_{0.25}Mo_{1.75}N$ nitride.

Material	(hkl)	d_{obs}(Å)	d_{cal}(Å)	Lattice parameter(Å)	Average crystallite size(nm)
γ- $Co_{0.25}Mo_{1.75}N$	(111)	2.428	2.423	4.198(2)	11±0.5
	(200)	2.099	2.099		
	(220)	1.482	1.484		
	(311)	1.264	1.265		
	(222)	1.211	1.211		

5.3.2.2 Microstructural characterization of γ-$Co_{0.25}Mo_{1.75}N$ synthesized via ammonia route

Structural analysis of γ-$Co_{0.25}Mo_{1.75}N$ was carried out using TEM and HRTEM techniques in detail. The micrographs with different resolution and the selected area diffraction pattern (SAED) have been presented and analyzed in the following subsections.

5.3.2.2.1 TEM studies of γ-$Co_{0.25}Mo_{1.75}N$

TEM micrographs with various resolutions and SAED patterns of γ-$Co_{0.25}Mo_{1.75}N$ material are presented in figure 5.11. γ-$Co_{0.25}Mo_{1.75}N$ materials are found to possess nearly spherical morphology with remarkably narrow particle size distributions.

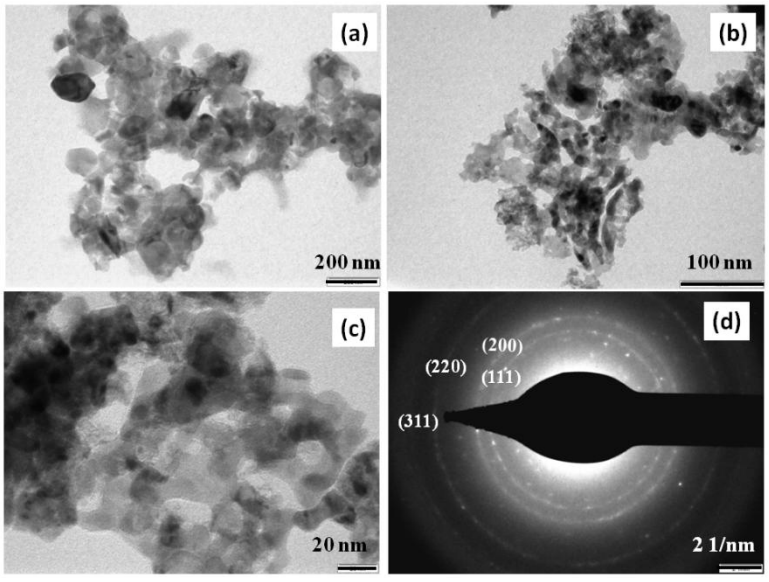

Figure 5.11 TEM micrographs with various resolutions ((a), (b) and (c)) and SAED pattern (d) of γ-$Co_{0.25}Mo_{1.75}N$.

The average TEM particle size for γ-$Co_{0.25}Mo_{1.75}N$ materials is found to be 12±0.2 nm, which is well matched with the average crystallite size of the material, 11±0.5 nm estimated from XRD analysis. SAED patterns of γ -$Co_{0.25}Mo_{1.75}N$ show well intense diffraction rings at inter planar spacing of 2.317 Å, 1.999 Å, 1.421 Å and 1.229 Å and corresponds to (111), (200), (220) and (311) planes, respectively. The average TEM particle size, obtained interplanar distance from SAED pattern, corresponding Miller indices and lattice parameters are presented in table 5.5.

Table 5.5 Material, Average TEM particle size, interplanar distance calculated from SAED and XRD, Miller indices and lattice parameter calculated from SAED and XRD pattern of γ-$Co_{0.25}Mo_{1.75}N$ material.

Material	Average TEM particle size(nm)	Interplanar distance 'd'(Å)		Miller indices (hkl)	Lattice parameter* 'a'(Å)	
		SAED	XRD		SAED	XRD
γ-$Co_{0.25}Mo_{1.75}N$	12±0.2	2.512	--	--	4.013(1)	4.198(2)
		2.317	2.428	(111)		
		1.999	2.099	(200)		
		1.421	1.482	(220)		
		1.229	1.264	(311)		

*** The lattice parameter corresponding to (111) peak calculated from SAED pattern has been presented**.

The particle size distributions calculated were found to be in the range of 7 nm - 20 nm for γ-$Co_{0.25}Mo_{1.75}N$ nitride (figure 5.12). As it can be seen from the figure, the most probable average value lies at 10 nm and beyond 14 nm small fraction of particles with bigger size present as tail of the Gaussian peak (non-uniform distributions).

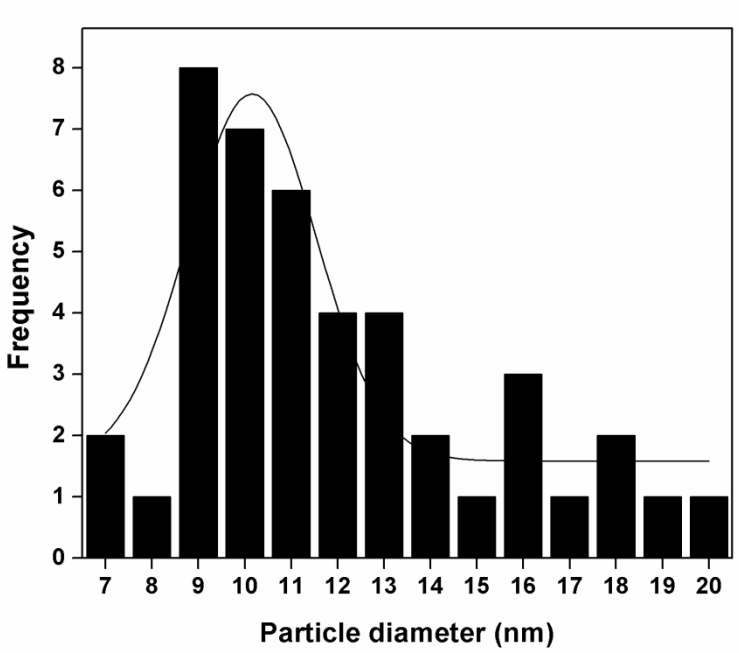

Figure 5.12 TEM particle size distributions for γ-$Co_{0.25}Mo_{1.75}N$ material.

However, considering the statistical average of all particles we have taken 12 nm as average particle size in our further analysis of results. The average TEM particle size calculated above is larger than that of γ-Mo_2N (5 nm). Such kind of non-uniform distributions of particle sizes may be due to non-uniformity in experimental conditions. A study with similar findings which can support our results has also been reported in molybdenum nitrides synthesized via urea route [9].

5.3.2.2.2 HRTEM studies of γ-$Co_{0.25}Mo_{1.75}N$

High resolution transmission micrograph of γ-$Co_{0.25}Mo_{1.75}N$ material has been presented in figure 5.13. The micrograph shows the development of crystalline periodicity with the estimated values of lattice spacing as 1.791 Å**,** 1.788 Å and 1.742 Å for γ-$Co_{0.25}Mo_{1.75}N$ product**.** The observed interplanar distance of 1.791 Å may correspond to (200) lattice plane having 'd' value of 2.099 Å**.** Therefore, it can be concluded that stacking of atoms along (200) plane occurs in our synthesized material. Further, the observed lattice spacing of 1.79 Å from HRTEM study is comparable with that observed in the TEM study (1.999 Å).

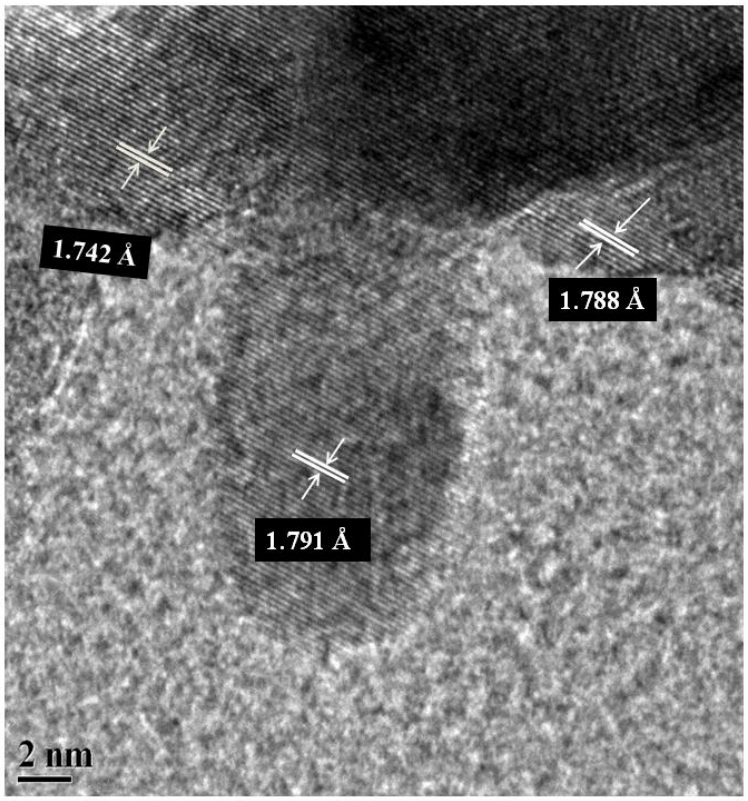

Figure 5.13 HRTEM image of γ-$Co_{0.25}Mo_{1.75}N$.

5.3.2.3 BET surface area study of γ-$Co_{0.25}Mo_{1.75}N$

The nitrogen adsorption- desorption plot for γ-$Co_{0.25}Mo_{1.75}N$ material has been presented in figure 5.14. The hysteresis plot shows mesoporous behaviour with type IV isotherm and H2 hysteresis [31] (Chapter 1, subsection 1.5.4). The adsorption plot is accompanied by an inflation point at ≈ P/P_o = 0.47 with a faster increase in adsorption rate thereafter up to a value of $P/P_o \rightarrow 1.0$. The estimated BET surface area is found to be 12 m^2/g for γ -$Co_{0.25}$ $Mo_{1.75}$ N. Two distinct pore structures centered around 2.8 nm and 3.9 nm are observed (indicated by arrow) in figure 5.14. The pore volume is estimated to be 0.0185 cc/g. There is a reduction of surface area due to Co atom substitution in γ-Mo_2N, i.e. from 53 m^2/g for pure γ-phase to12 m^2/g for γ-$Co_{0.25}Mo_{1.75}N$.

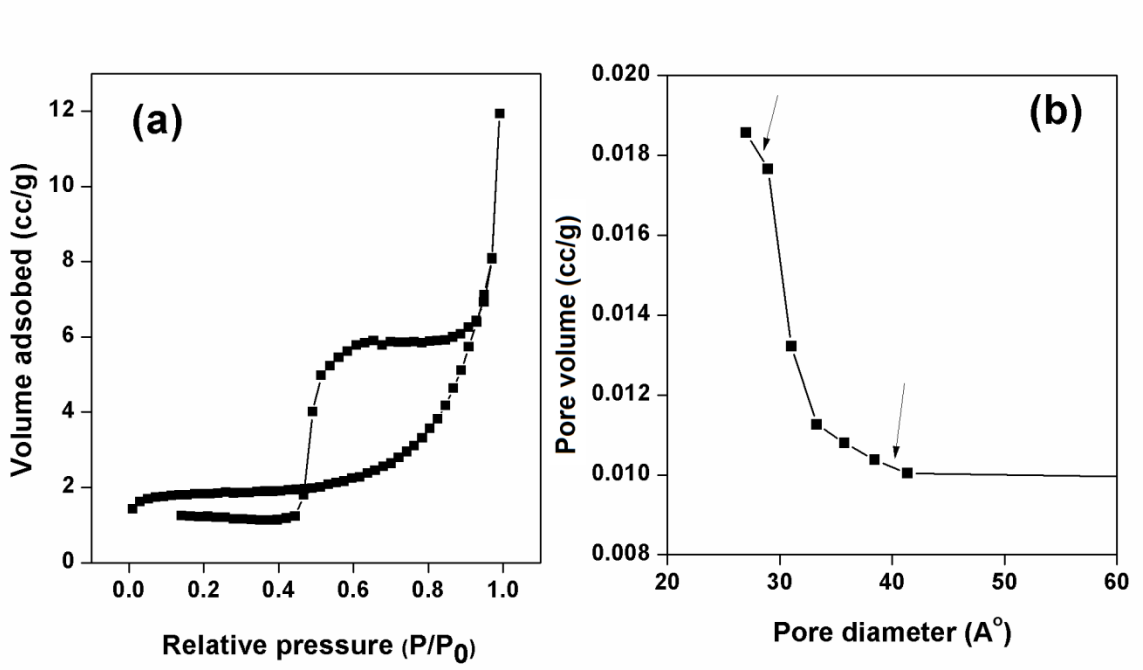

Figure 5.14 Plots of adsorption - desorption isotherm (a) and pore size distribution (b) for γ-$Co_{0.25}$ $Mo_{1.75}$ N material.

5.3.2.4 VSM studies of γ-$Co_{0.25}Mo_{1.75}N$

The room temperature field dependent magnetization plot of γ-$Co_{0.25}$ $Mo_{1.75}$ N has been presented in figure 5.15. The hysteresis plot shows ferromagnetic behaviour with faster increase in magnetization in the lower field region (0 < H < 2 kOe) with finite values of coercivities. The hysteresis plot does not get saturated even at an applied field of 15 kOe. This observation may be attributed to nano size and surface effect of our synthesized material. The values of saturation magnetization (M_s) are obtained by extrapolating the M vs. 1/H plot on magnetization axis from the values of specific magnetizations at higher field regions (10 kOe – 15 kOe) [32].

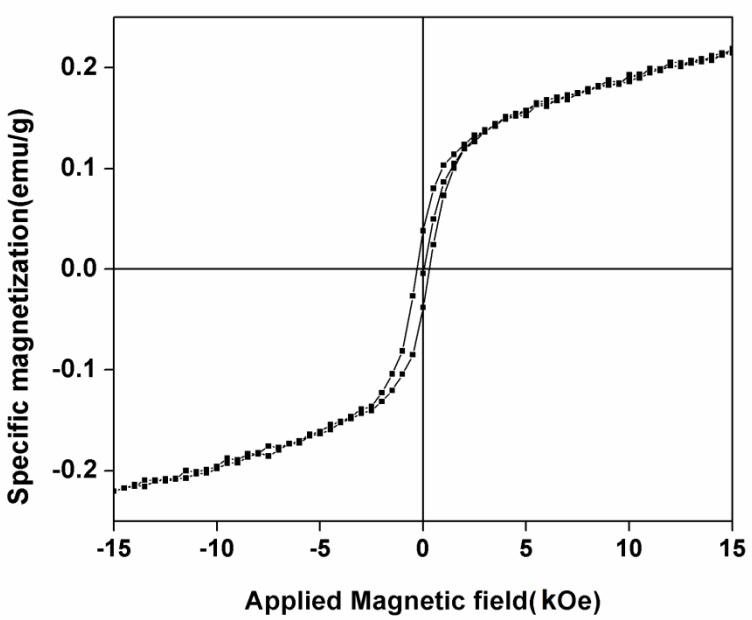

Figure 5.15 Plot of specific magnetization vs. applied field of γ-$Co_{0.25}Mo_{1.75}N$ materials synthesized at 700°C.

Therefore, higher value of M_s, i.e. 0.268 emu/g, for γ-$Co_{0.25}Mo_{1.75}N$ is in accordance with the contributions from higher atomic moments of Co in the nitride confirming bimetallic nature. Taking into consideration that Co atoms are the only contributor towards net magnetic moment in the samples, one can calculate the 0.037 μ_B contribution per atom of Co in the crystal lattice of γ-$Co_{0.25}Mo_{1.75}N$. The value is at par with the same order of magnitude of magnetic moments observed for weak itinerant ferromagnetic nitride materials, such as: Fe_3Mo_3N, Co_3Mo_3N, Co_6Mo_6N etc [33-35]. The origin of weak ferromagnetism in the crystal lattice may be due to presence of intrinsic magnetic moments which are susceptible to long range ordering in the crystal structure. These results are also supported by XRD phase analysis and significant decrease of surface area of the γ-$Co_{0.25}Mo_{1.75}N$ compared to γ-Mo_2N. The value of coercivity for γ-$Co_{0.25}Mo_{1.75}N$ material is found to be 296 Oe, (figure 5.14). The coercivity for γ-$Co_{0.25}Mo_{1.75}N$ material is in the soft ferromagnetic range.

5.3.3 γ-Mo_2N synthesized via urea route

γ-Mo_2N has been successfully synthesized via urea route and characterized for different properties study using XRD, SEM, HRTEM and VSM. The results obtained are presented and discussed in detail in the following subsections.

5.3.3.1 X-ray diffraction studies of γ–Mo_2N

X-ray diffraction pattern of γ-Mo_2N has been presented in figure 5.16. The pattern shows broad peaks indicating nanocrystalline nature of the synthesized nitride product. The absence of any extra line in the XRD pattern confirms the phase purity of the synthesized sample. The XRD pattern is indexed in accordance with the ICDD PDF # 25-1366. The average crystallite size is found to be 5±0.4 nm. The lattice parameter value is estimated to be 4.162(17) Å, which is in well agreement with the literature reported value of 4.161 Å [19, 36].

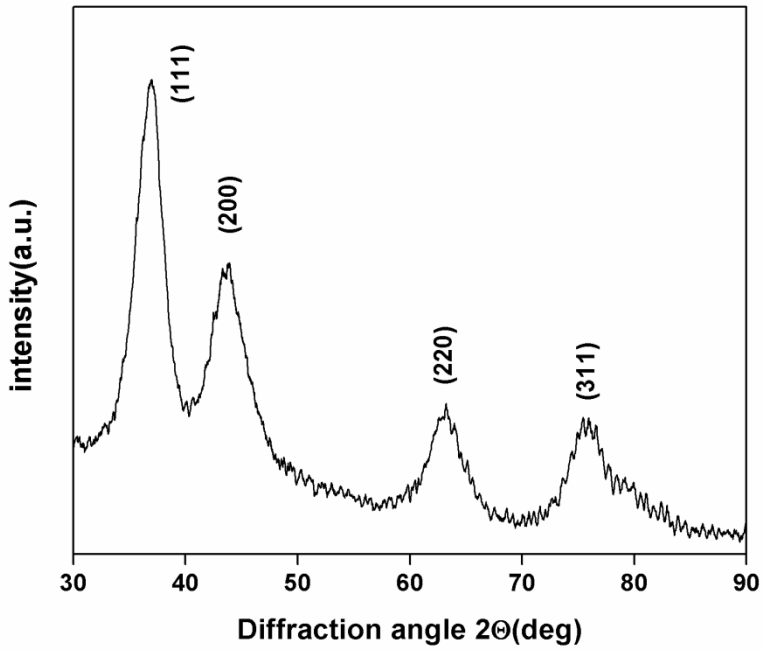

Figure 5.16 Indexed XRD pattern of γ–Mo_2N synthesized at 700˚C via urea route.

The XRD parameters such as average crystallite size, Miller indices, interplanar distance and lattice parameters are tabulated in table 5.6. γ-Mo_2N material crystallizes in fcc structure with space group Fm3m [36, 37].

Table 5.6 Material, Miller indices, observed and calculated interplanar distance, lattice parameter and average crystallite size of γ -Mo_2N synthesized via urea route.

Material	(hkl)	d_{obs}(Å)	d_{cal}(Å)	Lattice Parameter (Å)	Average crystallite size(nm)
γ-Mo_2N	(111)	2.430	2.403	4.162(17)	5±0.4
	(200)	2.064	2.081		
	(220)	1.469	1.471		
	(311)	1.252	1.254		

5.3.3.2 Structural characterization of γ-Mo_2N synthesized via urea route

The structural arrangement, shape, size and composition of the product materials were studied in detail using SEM, EDX and HRTEM techniques. The results obtained and the analysis is presented below.

5.3.3.2.1 SEM and EDX studies of γ-Mo_2N

The scanning electron micrographs (SEM) of γ -Mo_2N synthesized via urea route have been presented in figure 5.17 ((a), (b), (c) and (d)) having different magnifications. The SEM pictures show rod like elongated structures along with some spherical particles of γ-Mo_2N. The average dimension of γ-Mo_2N nanorods is found to be approximately (295 nm x 83 nm) (table 5.8).

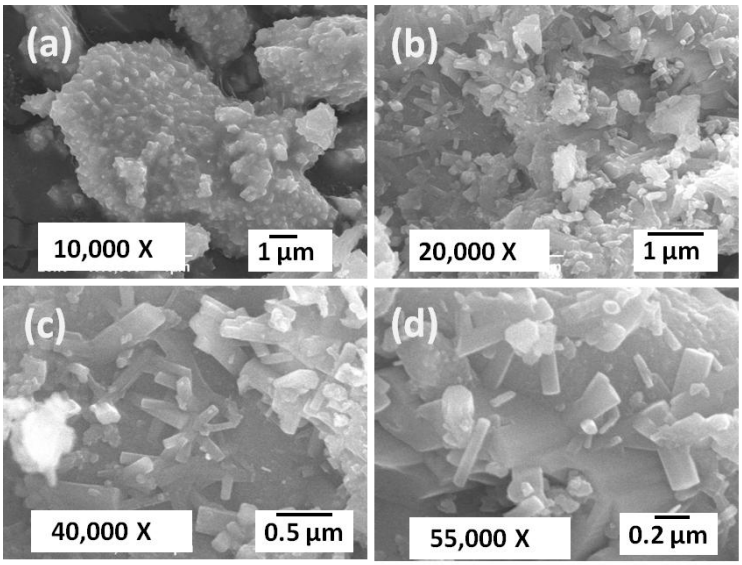

Figure 5.17 SEM micrographs of γ-Mo_2N synthesized via urea route at 700° C with different magnifications(X); (a) 10000X, (b) 20000X, (c) 40000X and (d) 55000X.

The EDX pattern of the sample is presented in figure 5.18. The spectrum shows characteristic peaks indicating the presence of Mo and O atoms. The weight % of molybdenum (Mo) and oxygen (O) are calculated to be 67.59 and 32.41, respectively. This result indicates surface oxidation of the synthesized material due to its ultrafine nature. However, the presence of N in the product could not be determined by EDX in our study.

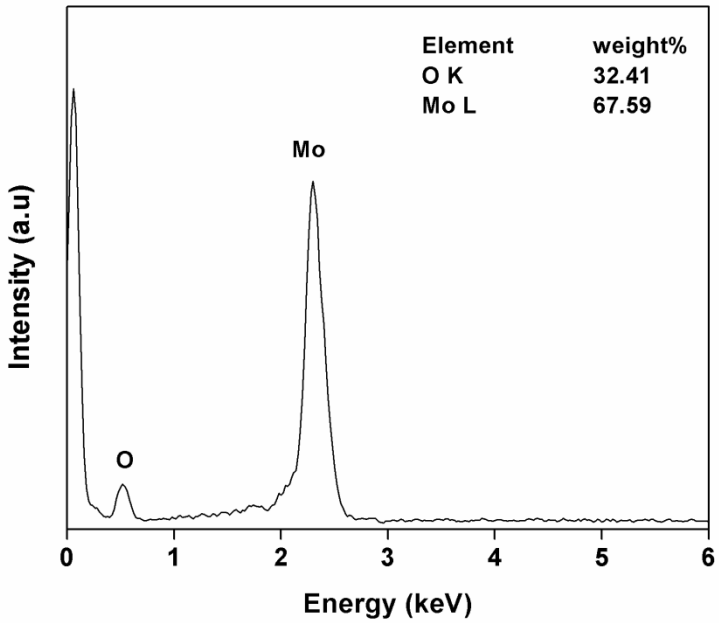

Figure 5.18 EDX spectrum of γ-Mo_2N synthesized via urea route at 700° C.

5.3.3.2.2 HRTEM studies of γ-Mo_2N

The high resolution TEM micrographs and the SAED pattern of γ-Mo_2N prepared via urea route at 700˚C has been presented in figure 5.19 ((a) and (b)). The HRTEM picture shows good crystallinity of the product material. Four different lattice stackings with interplanar distances corresponding to 2.222Å, 2.030Å, 1.960 Å and 2.096 Å are observed in γ-Mo_2N crystalline materials (figure 5.19(a)). The interplanar distances were calculated from the fringe widths of the HRTEM micrographs. The obtained value of 2.096 Å, corresponds to interplanar distance of 2.081 Å along (200) plane. The obtained SAED pattern for γ-Mo_2N product depicts orderly arranged bright Laue spots (figure 5.19(b)). This observation confirms that the synthesized product is single phase and nanocrystalline in nature.

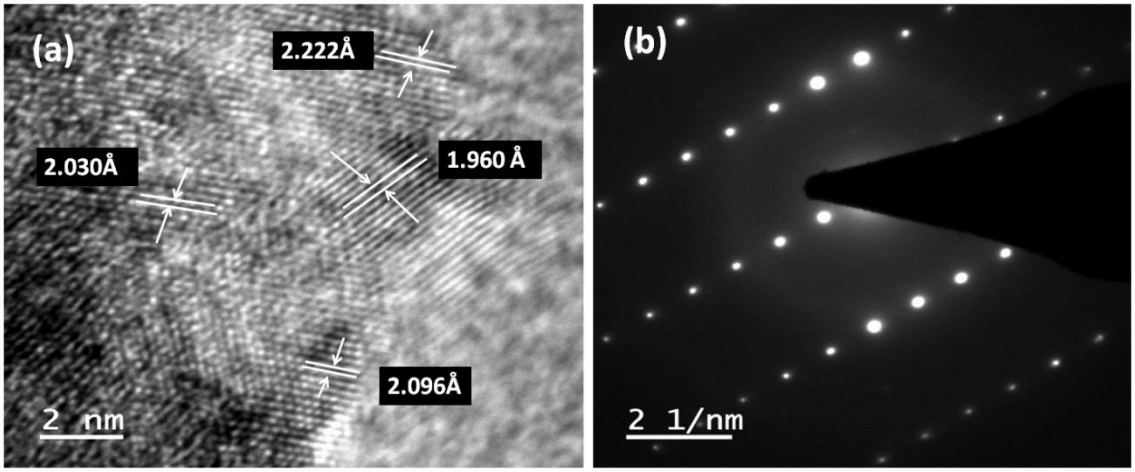

Figure 5.19 HRTEM image (a) and corresponding SAED pattern (b) of γ-Mo_2N synthesized via urea route at 700°C.

The interplanar distance and lattice parameter calculated from HRTEM and XRD with corresponding Miller indices have been presented in table 5.7. The lattice parameter value calculated from the HRTEM, d- spacing corresponding to (200) plane is found to be 4.192 Å, which is slightly higher than the value of 4.162 Å, obtained from the XRD parameters (table 5.6)

Table 5.7 Materials, average SEM particle size, interplanar distance from SAED pattern, Miller indices and corresponding lattice parameters of γ-Mo_2N material synthesized via urea route.

Materials	Average SEM particle size(nm)	Interplanar distance 'd'(Å)		Miller indices (hkl)	Lattice parameter 'a'(Å)	
		SAED	XRD		SAED	XRD
γ-Mo_2N	295x83	1.960	--	--	4.192(0)	4.162(17)
		2.030	--	--		
		2.096	2.081	200		
		2.222	--	--		

5.3.3.3 VSM studies of γ-Mo_2N synthesized via urea route

The field dependent magnetization plot of γ-Mo_2N has been presented in figure 5.20. The hysteresis plot does not get saturated even after applying field of 15 kOe. This indicates superparamagnetic nature of the synthesized material. The value of the saturation magnetization and coercivity are found to be 0.019 emu/g and 880 Oe, respectively. Around field strengths of 5 kOe the value of specific magnetization is found to be 0.011emu/g,

where as in case of γ-Mo_2N obtained via ammonia route corresponding specific magnetization value is observed to be 0.03emu/g. The slight decrease in the value of magnetization of γ-Mo_2N may be attributed to the synthetic strategy adopted, leading to variation in the crystallinity and morphology of the product in addition to size and shape. However, the observed value of the specific magnetization is in accordance with the literature reported value [25]. The observed value of the coercivity (880 Oe) for this product is quite lower than the value (2838 Oe) obtained for γ-Mo_2N prepared via ammonia route (subsection 5.3.4). The value of coercivity is dependent on particle size. So there is significant difference in values of coercivities obtained for different particle sizes of γ-Mo_2N prepared via different routes [28].

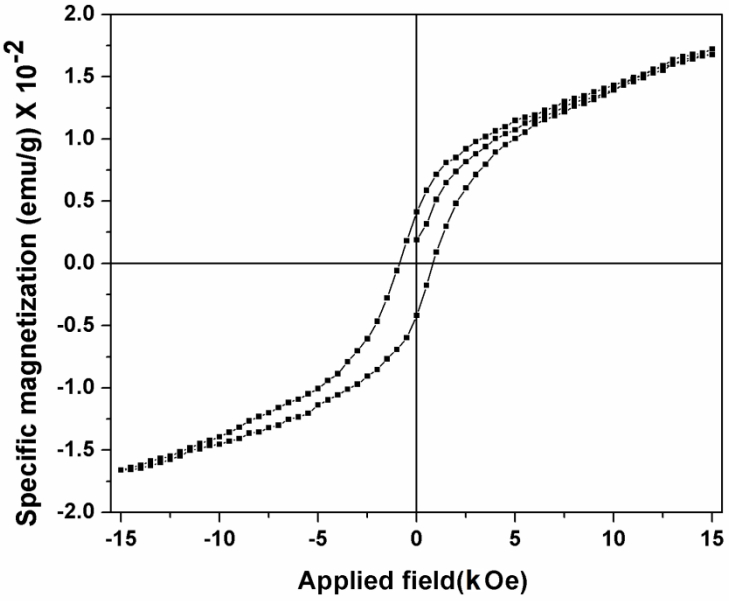

Figure 5.20 Field dependent magnetization plot of γ-Mo_2N synthesized via urea route measured at room temperature.

5.4 Conclusion

Nanocrystalline phase pure γ-Mo_2N and Co substituted γ-Mo_2N have been prepared using novel chemical synthetic methods. The synthesized products were characterized using XRD, SEM, TEM, HRTEM for structural and morphological studies. Surface and magnetic properties are studied using BET and VSM techniques. The synthetic methodologies have been optimized studying the solid state reactivity of the precursors in the subsequent

nitridation routes. The methodologies involve the use of reducing agents, namely: hydrazine and borohydride and organic source: ethylene diamine in order to synthesize precursors for transition metal nitrides. Ammonia (NH_3) (g) and solid urea both have been used as nitriding sources. We could optimize the formation temperature of the γ-Mo_2N and γ-$Co_{0.25}Mo_{1.75}N$ nitride to be 700^oC, by using the precursors obtained via aforesaid novel chemical route. XRD patterns indicate nanocrystalline nature of the synthesized materials with distinct peak broadening. The nitride products crystallize in face centered cubic structure with lattice parameter values of 4.193(5) Å, 4.198(2) Å and 4.162(17) Å for γ-Mo_2N and γ-$Co_{0.25}Mo_{1.75}N$ synthesized via ammonia route and γ-Mo_2N synthesized via urea route, respectively. Lattice expansion is observed for γ-Mo_2N synthesized via ammonia route. Insertion of Co into host lattice alters the crystal structure. TEM studies confirm the narrow distribution of particles in γ-Mo_2N and γ-$Co_{0.25}Mo_{1.75}N$ nitrides about 5nm and 12 nm, respectively. HRTEM study for nitride products confirms well crystallinity of the synthesized product. The surface properties study for γ-Mo_2N and γ-$Co_{0.25}Mo_{1.75}N$ nitride materials synthesized via ammonia route indicate high and moderate surface areas with mesoporous structures, i.e. 53 and 12 m^2/g, respectively. Magnetic hysteresis study indicates weak ferromagnetic behaviour of γ-Mo_2N and γ-$Co_{0.25}Mo_{1.75}N$ (ammonia route) and γ-Mo_2N (urea route) materials having coercivities 2838 Oe, 880 Oe and 296 Oe, respectively. The results were analyzed on the basis of structure-properties correlations.

References

1. K. -H. Lee, Y. -W. Lee, D. -H. Kwak, J. -S. Moon, A. -R. Park, E. -T. Hwang, K. -W. Park, Mater. Lett. **124** (2014) 231–234.

2. Z. Li, C. Chen, E. Zhan, N. Ta, W. Shen, Catal. Commun. **51** (2014) 58–62.

3. D. Mckay, J. S. J. Hargreaves, J. L. Rico, J. L. Rivera, X.-L. Sun, J. Solid state Chem. **181** (2008)325-333.

4. S. Jujjuri, F. Ca´rdenas-Lizana, M. A. Keane, J. Mater. Sci. **49** (2014) 5406–5417.

5. L. Volpe, M. Boudart, J. Phys. Chem. **90** (1986) 4874-4877.

6. Y. Xie, F. Tian, Mater. Sci. Eng., B. **215** (2017) 64–70.

7. B. T. Matthias, J. K. Hulm, Phys. Rev. **87** (1952) 799–806.

8. C. L. Bull, P.F. McMillan, E. Soignard, K. Leinenweber, J. Solid State Chem. **177** (2004) 1488–1492.

9. A. Gomathi, A. Sundaresan, C. N. R. Rao, J. Solid State Chem.**180** (2007) 291–295.

10. B. Cao, G. M. Veith, J. C. Neuefeind, R. R. Adzic, P. G. Khalifah, J. Am. Chem. Soc. **135** (2013) 19186−19192.

11. L. Volpe, M. Boudart, J. Solid State Chem. **59** (1985) 332-347.

12. C. Giordano, C. Erpen, W. Yao, B. Milke, M. Antonietti, Chem. Mater. **21** (2009) 5136–5144.

13. R. Marchand, F. Tessier, F. J. Disalvo, J. Mater. Chem. **9** (1999) 297-304.

14. P. Roman, A. Luque, J. M. Gutierrez-Zorrilla, S. Garcia-Granda, Polyhedron. **10** (1991) 2057-2064.

15. P. Wongkrua, T. Thongtem, S. Thongtem, J Nanomater. **2013** (2013) 1-8, Article Id702679.

16. B. Mazumder, A. L. Hector, J. Mater. Chem. **19** (2009) 4673–4686.

17. J. C. Fitzmaurice, A. L. Hector, I. P. Parkin, J. Chem. Soc., Dalton Trans.**0**(1993) 2435-2438.

18. E. G. Gillan, R. B. Kaner, Chem. Mater. **8** (1996) 333-343.

19. J. Ma, Y. Du, J. Alloys Compd. **463** (2008) 196-199.

20. A. Hojabri, F. Hajakbari, A.E. Meibodi, J. Theor. Appl. Phys. **9** (2015) 67–73.

21. N. R. Dighore, S. P. Jadhav, S. T. Gaikwad, A. S. Rajbhoj, Int. J. Eng. Res. Appl. **4** (2014) 135–139.

22. J. Chaudhuri, L. Nyakiti, R. Lee, Y. Ma, P. Li, Q. L. Cui, L. H Shen, Mater. Lett. **61** (2007)4763-4765.

23. Y. Xiao, Z. Fu, G. Zhan, Z. Pan , C. Xiao, S. Wu, C. Chen, G. Hu, Z. Wei, J. Power Sources. **273** (2015) 33-40.

24. Z. Wu, Y. Sun, Y. Tan, S. Yang, X. Feng, K. Müllen, J. Am. Chem. Soc. **134** (2012) 19532-19532.

25. H. K. Sidana, R. A. Mir, O. P. Pandey, J. Alloys Compd. **736** (2018) 255-265.

26. I. S. Jacobs, C. P. Bean, Phys. Rev. **100** (1955) 1060 -1067**.**

27. K. Gandha, J. Mohapatra, J. P. Liu, J. Magn. Magn. Mater. **438** (2017) 41-45.

28. F. E. Luborsky, J. Appl. Phys. **32** (1961)171S-183S.

29. T. H. Chiang, H. C. Yeh, Materials. **6** (2013) 4609-4625.

30. P. P Mishra, M. Manivel Raja, R. N. panda, Mater. Res. Bull. **75** (2016) 127–133.

31. K. S. W. Sing, D. H. Everett, R. A. W. Haul, L. Moscou, R. A. Pierotti, J. Rouquerol, T. Siemieniewska, Pure & Appl. Chem. **57** (1985) 603 – 619.

32. R. N. Panda, N. S. Gajbhiye, J. Appl. Phys. **81** (1997) 335-339.

33. R. N. Panda, N. S. Gajbhiye , J. Alloys Compd. **256** (1997) 102-107.

34. T. Waki, S. Terazawa, Y. Umemoto, Y. Tabata, Y. Murase, M. Kato, K. Hirota, H. Nakamura, Journal of Physics: Conference Series **344** (2012) 012017.

35. S. M. Hunter, D. Mckay, R. I. Smith, J. S. J. Hargreaves, D. H. Gregory, Chem. Mater. **22** (2010) 2898–2907.

36. T. Kawashima, E. Takayama - Muromachi, P. F. McMillan, Physica C. **460-462** (2007) 651-652.

37. V. Tagliazucca, M. Leoni, C. Weidenthaler, Phys.Chem.Chem.Phys. **16** (2014) 6182-6188.

Chapter 6

Novel Synthesis, Characterization and Properties Study of W and Co-W based Binary and Ternary Nitride Materials

This chapter describes novel synthesis of binary β-W_2N and ternary $CoWN_2$ materials using nitridation of the precursors synthesized via citric acid assisted sol-gel route. During the nitridation, solid urea and ammonia gas have been used as nitrogen sources. The materials have been characterized using various techniques such as: XRD, SEM, EDX and HRTEM. Surface and magnetic properties of the products have been studied using BET and VSM techniques, respectively.

6.1 Introduction

Amongst varieties of transition metal nitrides, tungsten nitrides (β-W_2N, WN, WN_2, W_3N_2 etc.) are characterized by high melting point, high hardness, good chemical and thermal stability, good electrical conductivity and a relatively low band gap (2.2 eV) [1-3]. These unique properties of tungsten nitride and related tungsten based ternary nitrides have wide applications in micro electronics [4,5], wear resistant coatings [3.], catalyst for NO dissociation and reduction with hydrogen [6,7], photo catalyst for water decomposition using solar light [2.] and cathode catalyst for fuel cells [8] etc. Several applications of the W-based nitrides are vested on their availability as high surface area form [6, 9]. These materials are obtained from chemically synthesized precursor in high surface area form along with controlled shape and size by using these non-traditional approaches of synthesis [10, 11].

Tungsten nitrides, however, are intrinsically difficult to prepare primarily because the incorporation of nitrogen into metallic tungsten lattice is thermodynamically unfavourable at atmospheric pressure [12]. As a result, most of the materials in the W-N binary system are produced as thin films with low crystallinity [13, 14]. However, W-based binary and ternary nitrides can be synthesized in nanoparticle form at moderate reaction

temperature using protecting atmosphere (e.g. NH_3, N_2 etc.). Several reports are available on synthesis of β-W_2N using N_2/H_2 or NH_3/N_2 gas mixtures [11, 15]. Therefore, development of novel chemical methods for tungsten nitride materials in nanocrystalline form with tunable properties by controlling the precursor nature is highly desirable.

In this chapter development of chemical based novel synthesis method for β-W_2N and $CoWN_2$ materials have been studied. Structural and morphological characterizations along with studies on surface and magnetic properties have been carried out.

6.2 Materials and methods

Binary β-W_2N and ternary $CoWN_2$ materials have been prepared from chemically synthesized precursors via urea route and ammonia route, respectively. The synthesized materials have been characterized for various properties study using advanced instrumental techniques. The details of the methodology and characterization techniques have been presented in the following subsections.

6.2.1 Synthesis of β-W_2N

The synthesis of β-W_2N involves two steps: (1) synthesis of precursor and (2) nitridation of precursor. The details of the synthetic procedure adopted have been described below.

6.2.1.1 Precursor synthesis

The precursor for β-W_2N material was synthesized via citric acid assisted sol-gel route. The details regarding the experimental procedure have been presented in chapter 4 sub section 4.2.1 for VN materials. In summary, the modified procedure adopted can be described in the following part of this paragraph. For the synthesis, 2.44g of ammonium tungsten oxide hydrate ($(NH_4)_6W_{12}O_{39}\cdot$ x H_2O) (Alfa Aesar) and 1.92g of anhydrous citric acid ($C_6H_8O_7$) (Fisher scientific) were taken in 1:1 molar ratio and dissolved in 300ml of distilled water in order to get clear solution. Next, the solution was taken in a round bottom flask and refluxed at 80˚C for 1h. The resulting clear solution was then placed in a fume hood for evapouration at a controlled temperature of 80-90˚C. After 3h, light brown colored viscous gel was obtained. The cooled gel turned greenish in colour and was heat treated

again at 90˚C in air atmosphere for 24h. The dried crystal gel was then prefired at a temperature of 150˚C for 30 min. It was then collected, crushed well and stored as precursor for nitridation.

6.2.1.2 Nitridation of precursor via urea route

The prefired precursor, obtained after heat treatment at 150˚C, was used for nitridation to yield β-W_2N using urea as nitrogen source. For the nitridation experiment, the precursor and solid urea were taken in a molar ratio of 1:12, crushed well mechanically using an agate mortar and pestle for 15-20 mins. The solid mixture was placed inside the middle of a horizontal reactor of the furnace taken in an alumina boat. Initially, N_2 (g) was purged through the reactant mixture to expel any residual oxygen and to make the reaction environment inert. Then, the furnace was programmed to heat the reactants in a controlled manner up to a range of 700- 750˚C in duration of 3h-4h. The reaction temperature was held for 2h duration, followed by natural cooling of the product in the flow of N_2 (g). The product was removed at room temperature, after cooling and used for further characterization.

6.2.2 Synthesis of $CoWN_2$

The two step synthetic methodology for the preparation of ternary $CoWN_2$ has been adopted in this study. The first step involves synthesis of $CoWO_4$ precursor while the second step is nitridation of the synthesized precursor. The details of the experimental procedure are described below.

6.2.2.1 Synthesis of cobalt tungstate, $CoWO_4$, precursor

In a typical synthesis of precursor, i.e. $CoWO_4$, 0.8162g of ammonium tungsten oxide hydrate ($(NH_4)_6W_{12}O_{39}\cdot xH_2O$) (Alfa Aesar, United States) and 0.9701g of cobalt nitrate ($Co(No_3)_2\cdot 6H_2O$)) (Molychem, India) were taken in 1:1 molar ratio. Cobalt and tungsten salts were dissolved separately in distilled water and added to aqueous solution containing 5g of citric acid. The resulting solution was taken in a 500 ml round bottom flask and diluted to 300 ml using distilled water. Next, the solution was stirred and refluxed at 80˚C for 3h duration using magnetic stirrer. At the end a pink coloured solution was obtained. This solution was placed in the fume hood for evapouration using a hot plate. The

evapouration was continued until approximately 5-10 ml of the viscous gel was left. The gel was collected and heated in air atmosphere at 90˚C overnight. After drying, it was scratched, crushed, freed from moisture and heated again at 400˚C in air atmosphere for 3h to yield $CoWO_4$, precursor. Finally, the heat treated precursor was ground several times with the help of mortar and pestle and subjected to nitridation and/ or characterization.

6.2.2.2 Nitridation of precursor via ammonia route

The synthesized $CoWO_4$ precursor was nitrided using NH_3(g) as nitrogen source to produce $CoWN_2$ nitride material. For the nitridation experiment, approximately 0.6g of the oxide precursor was taken, placed in the middle of the vertical tubular furnace with the help of porous ceramic wool. The quartz reactor containing the precursor material is placed inside the tubular furnace vertically. Initially, NH_3 (g) was purged for 2h duration in order to expel any residual oxygen and make the reaction environment filled with gaseous ammonia. Then, the furnace was programmed to heat the precursor up to 700˚C in 4h duration with a heating ramp of 2.9 K/min. The reaction temperature of 700˚C was maintained for 2h duration inside the furnace, followed by natural cooling under continuous flow of NH_3 (g). The product was removed after 24h when the reactor temperature reached 298K. The resulting product was characterized for further study.

6.2.3 Instrumental characterization

XRD patterns were recorded using a powder X-ray diffractometer (Rigaku Miniflex-II) using Cu-Kα_1 (1.5405 Å) radiation at a scanning speed of 3˚/minute. The phase purity was ascertained using XRD. CHN analysis was done by using Elementar, variomicrocube. The shape and morphology of the products were examined by scanning electron microscopy (SEM) (model: JEOL, JSM-6390), high resolution transmission electron microscopy HRTEM (model: Tecnai G2, F30). Nitrogen physisorption experiments were performed using BET measurement (Model: Micromeritics Gemini VII, USA). The samples were activated at 250˚C for 1h using high purity He/N_2 gas mixture. Magnetization measurements (M vs. H characteristics) were carried out on solid powder material using vibrating sample magnetometer (model: Lakeshore VSM 7410) which can provide a magnetic field up to 20 kOe.

6.3 Results and discussions

6.3.1 β-W_2N synthesized via urea route using WO_3 precursor

The results of structural characterization, surface and magnetic properties of β-W_2N have been presented and analyzed in detail in the following subsections.

6.3.1.1 X- ray diffraction analysis of β-W_2N

X-ray diffraction studies have been used to characterize the precursor and different intermediate products obtained via nitridation of the precursor at various reaction temperatures and time durations. The phase analysis of the precursor and products is studied as a function of reaction temperature.

6.3.1.1.1 Precursor characterization

Figure 6.1 (a), (b), (c), (d) represent the XRD patterns of precursor materials subjected to different heat treatment conditions in air atmosphere. The XRD pattern of 'as dried powder' recorded using viscous sticky gel prefired at 150°C for half an hour in air atmosphere is presented in figure 6.1(a). The prefired powder heat treated at 300°C for 2h is presented in figure 6.1(b). These XRD patterns indicate amorphous nature of the materials with low crystallinity. However, the XRD pattern of 'heat treated gel' shows prominent broad peaks centered at around 2θ values of 23° in both the figures, i.e. 6.1(a) and 6.1 (b), and can be identified with evolution of amorphous tungsten trioxide (WO_3). In addition, we have observed broad peaks centered around 2θ values of 27° (Figure 6 (a) and (b)) which may correspond to prefired W-citrate complex [16,17]. With increase of heat treatment temperature up to 400°C, evolution of WO_3 phase occurs (figure 6.1(c)). With further increase of temperature up to 500°C, formation of well crystalline WO_3 phase is observed (figure 6.1(d)). It appears that the observed diffraction peaks can be attributed to monoclinic or orthorhombic crystal structures (monoclinic: ICDD PDF# 43- 1035 and orthorhombic: ICDD # 20-1324). It has been reported that monoclinic phase appears in the XRD patterns of WO_3 which is crystallized from solution and heat treated below 320^0C. Further, increase of temperature results in the stabilization of orthorhombic structure up to 750^0C beyond which it transforms into tetragonal phase [18-21]. Therefore, we have indexed the XRD

patterns in accordance with orthorhombic crystal structure and estimated the XRD parameters for the chemically synthesized WO_3, heat treated at 500^oC.

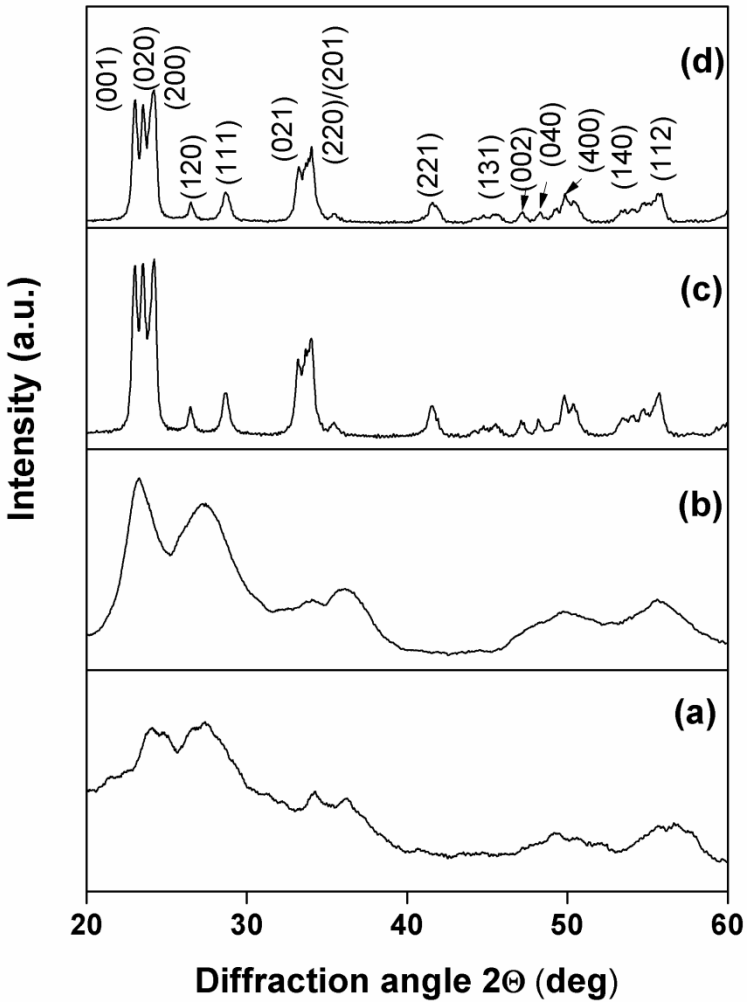

Figure 6.1 XRD patterns of precursor heat treated at various temperatures; (a) 150°C, (b) 300°C, (c) 400°C and (d) 500°C in air atmosphere. The XRD pattern recorded for 500°C heat treated sample has been indexed.

The estimated values of lattice parameters of WO_3 are found to be a=7.363(2) Å, b=7.556(7) Å and c=3.783(1) Å and are comparable with the values noted in the ICDD PDF # 20-1324. The average crystallite size of the material, heat treated at 500^o C is estimated to be 21±0.4 nm. The XRD parameters derived from the XRD analysis such as Miller indices (hkl), interplanar spacing, lattice parameters and average crystallite size of precursor material (WO_3) are presented in the table 6.1.

Table 6.1 Material, Phase, Average crystallite size, Miller indices (hkl), interplanar spacings (d) and lattice parameters of WO_3 precursor.

Material	Phase	Average crystallite size(nm)	Miller indices (hkl)	Interplanar distance 'd'(Å)	Lattice parameters (Å)
WO_3	Orthorhombic	21±0.4	(001)	3.861	a=7.363(2) b=7.556(7) c=3.783(1)
			(020)	3.778	
			(200)	3.675	
			(120)	3.360	
			(111)	3.112	
			(021)	2.696	
			(220)	2.634	
			(221)	2.171	
			(131)	1.990	
			(002)	1.924	
			(040)	1.883	
			(400)	1.845	
			(140)	1.811	
			(112)	1.651	

6.3.1.1.2 Solid state reactivity and XRD study of β-W_2N

Figure 6.2 (a), (b) and (c) show XRD patterns of the reaction products obtained after nitridation via urea route (ratios of precursor (150°C) : urea :: 1 : 12) at various temperatures and time durations. The X-ray diffraction pattern of the product obtained at 700°C is amorphous in nature with a broad hump centered around 2θ value of 36° (figure 6.2(a)) corresponding to (111) peak of β-W_2N. The pure phase β-W_2N (ICDD PDF # 25-1257) product is obtained at 750°C (figure 6.2(b)) (run 1). The broad peaks obtained in the XRD pattern signify the ultra fine size of the synthesized β- W_2N particles. Figure 6.2(c) shows the XRD pattern of β-W_2N obtained during the nitridation at 750^{o}C, in a different experimental run (run 2). As it can be seen from the figure (6.2 (c)), the resulting product, namely: β-W_2N, crystallizes fractionally and three major broad peaks centered at 2θ value of 37.4, 61.9 and 74.6 ^{o} corresponding to (111), (220) and (311) lattice planes, respectively, are found. This indicates the presence of very small crystallites in β-W_2N materials synthesized in second run. To be noted, the motivation in developing materials with poor crystallinity lies in obtaining nitride products with higher surface areas having structural deformation.

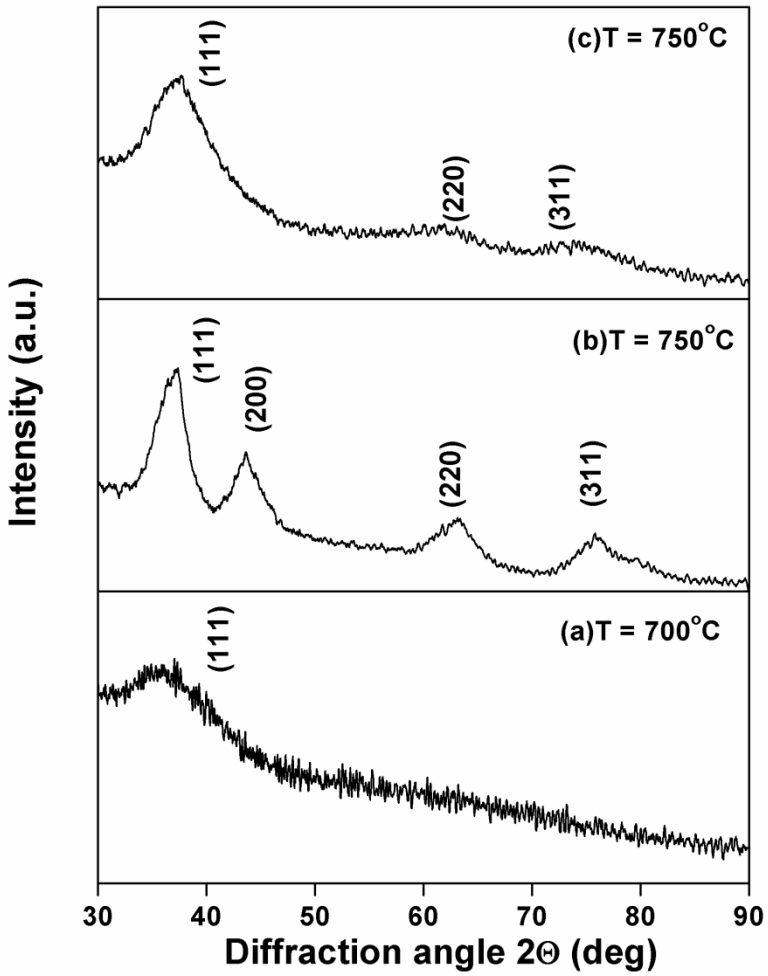

Figure 6.2 Indexed XRD patterns of the nitridation products obtained from prefired amorphous precursor, WO_3, at (a) 700°C and (b), (c) 750 °C.

The indexed XRD pattern of phase pure β-W_2N (figure 6.2 (b)) synthesized at 750°C has been analyzed for XRD study. The XRD parameters such as interplanar distance, Miller indices and lattice parameters are presented in table 6.2. The significantly broad peaks in the diffraction pattern indicate nanocrystalline nature of the synthesized product. The nitride product, β-W_2N, crystallizes in cubic structure with space group *Pm3m* [22]. The estimated crystallite size and lattice parameter of β-W_2N product are found to be 3±0.2 nm and 4.155(4) Å, respectively. This value is slightly higher than the reported value of lattice parameter for β-W_2N, i.e. 4.127 Å, and indicates lattice expansion [23]. The observed expansion in lattice volume in our study may be attributed to the incorporation of excessive nitrogen atoms in the interstitial sites of fcc β-W_2N lattice. This kind of observation is already reported in the literature for β-W_2N thin film systems [24, 25].

Table 6.2 Material, Phase, Miller indices, observed and calculated interplanar spacing, crystallite sizes and lattice parameter of β-W_2N.

Material	Phase	(hkl)	d_{obs}(Å)	d_{cal}(Å)	Average crystallite size(nm)	Lattice parameter(Å)
β- W_2N	fcc cubic	(111)	2.404	2.399	3±0.2	4.155(4)
		(200)	2.073	2.077		
		(220)	1.466	1.469		
		(311)	1.253	1.252		

6.3.1.2 Microstructural characterization of β-W_2N

The synthesized β-W_2N nitride was characterized using SEM and HRTEM for its morphology and structural arrangement study. The details of the studies are described below.

6.3.1.2.1 SEM studies of β-W_2N synthesized at various temperatures

The scanning electron micrographs (SEM) of β-W_2N synthesized at various temperatures have been presented in figure 6.3 (a), (b) and (c). The SEM image of amorphous product obtained at 700°C shows big flakes type morphology with dimensions of several micrometer (figure 6.3 (a)). Figure 6.3(b) shows the micrograph of pure phase β-W_2N particles with nearly spherical particle morphology. SEM image of the particles having partly crystalline β-W_2N product obtained at 750°C is presented in figure 6.3(c). It shows bigger flakes of several micrometer dimension of the product. SEM particle size calculation is difficult for SEM micrograph of β-W_2N with flakes morphology of various dimensions. However, SEM particle size of pure and well crystallized β-W_2N phase having spherical morphology is estimated to be 234±17 nm. The SEM particle sizes are significantly larger than the calculated crystallite sizes, i.e. ≈ 3 nm, which indicates agglomeration of crystallites/smaller particles. Varieties of SEM morphologies of β-W_2N nitride have also been reported in the literature [9, 26]. The observed morphologies are quite sensitive to the synthetic approaches used in order to prepare the products. Several papers describe micrographs with distinct lumps (consisting of several particulates) with different shapes and sizes [9.].

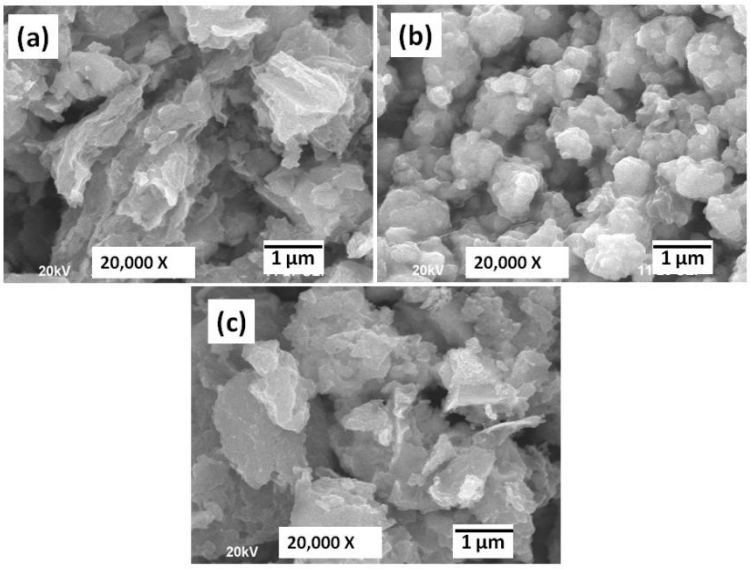

Figure 6.3 SEM micrographs of β-W_2N synthesized at various temperatures; (a) 700°C, (b)750°C (run 1)and (c) 750°C(run 2).

6.3.1.2.2 HRTEM studies of β-W_2N synthesized at 750°C

In order to examine the microstructural details with 'Å' level resolution, we have carried out HRTEM study of crystalline β-W_2N nitride synthesized at 750^oC. Figure 6.4 represents the typical HRTEM images and SAED pattern of β-W_2N material synthesized at 750^oC. The HRTEM image depicts lattice fringes with interplanar spacing of 1.576Å and 3.014Å corresponding to (220) and (110) of β-W_2N structure, respectively (figure 6.4(a) and (c)) [26]. The occurrence of such fringes corroborates well with the XRD and SAED studies mentioned above. In addition, lattice fringe with interplanar spacing corresponding to 3.54 Å is observed (figure 6.4 (b)), which is attributed to (002) plane of crystalline carbon (graphite) [27, 28]. The possibility of existence of carbon in our nitride can be understood as we have used the prefired precursor for nitridation using solid urea in inert atmosphere. The result has also been confirmed by our CHN analysis where we could estimate 5.98 wt % of carbon in the material under HRTEM investigation. The SAED pattern of β-W_2N consists of two diffused concentric rings around the central spot indicating amorphous nature of the material (figure 6.4 (d)). The radii of the diffused rings are estimated to be 2.186 Å and 1.298 Å, approximately. These rings correspond to the interplanar distance of 2.073 Å and 1.253 Å of (200) and (311) crystal planes, respectively. These results are well matched with the observed interplanar spacing calculated from powder XRD study.

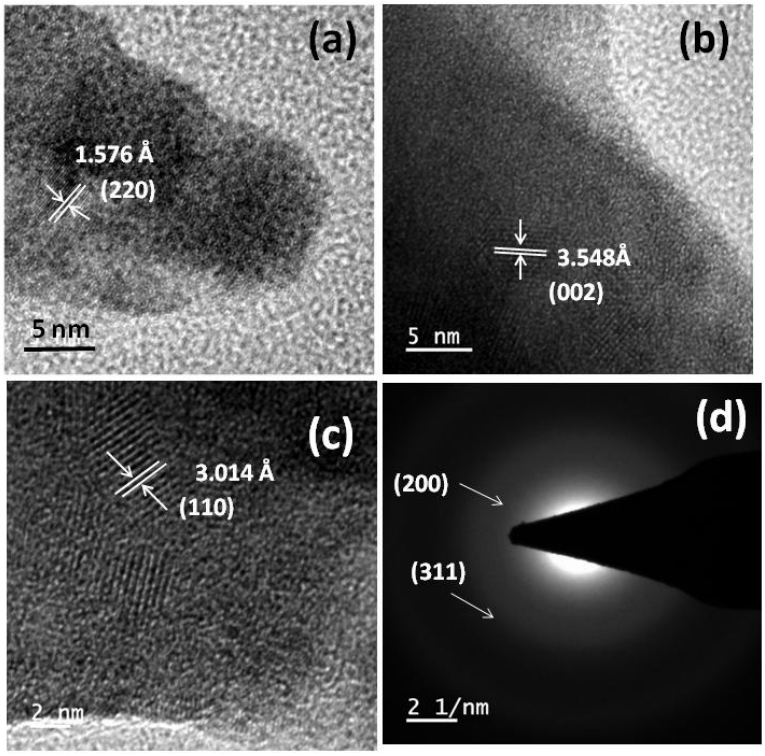

Figure 6.4 (a), (b) and (c) HRTEM micrographs of β- W_2N nitride synthesized at 750°C and (d) SAED pattern of β-W_2N.

6.3.1.2.3 EDX study of β-W_2N synthesized via urea route:

Figure 6.5 represents the EDX spectra of several β-W_2N materials synthesized at 700°C and 750°C. Figure 6.5(a) and (c) represent the EDX spectra of partly crystalline form of β-W_2N synthesized at 700°C and 750°C, respectively. While figure 6.5(b) represents well crystallized and pure phase β-W_2N synthesized at 750°C. The spectra show the presence of expected characteristic peaks for tungsten (W), nitrogen (N) and oxygen (O). The presence of O in the synthesized nitride products may be due to the surface oxidation of the materials because of their ultra fine nano size nature. Also, the presence of minute quantity of oxygen in the EDX spectra could be due to the residual oxygen in the high vacuum chamber associated with SEM set up.

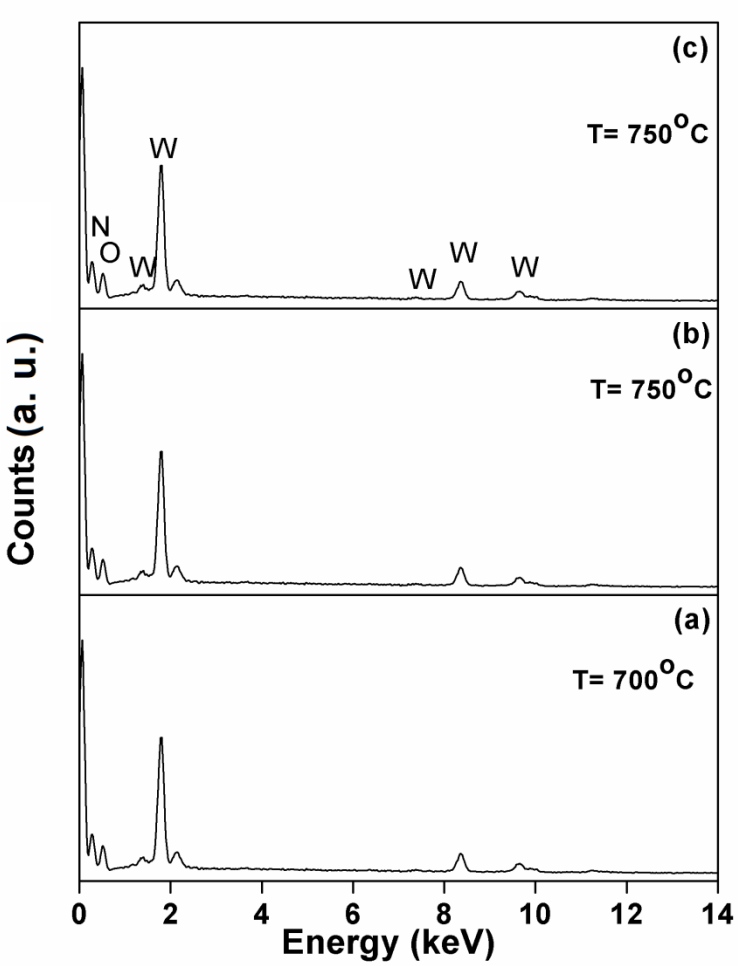

Figure 6.5 EDX spectra of β-W_2N synthesized at various temperatures; (a) 700°C and (b), (c) 750°C.

6.3.1.3 BET surface area study of β-W_2N synthesized via urea route

Nitrogen adsorption–desorption isotherms of β-W_2N materials synthesized at two different temperatures, i.e. 700°C and 750°C via urea route have been presented in figure 6.6 (a) and (b), respectively. Also, the surface area, pore volume and average pore sizes of the materials are summarized in table 6.3. The isotherms are nearly of type IV nature with finite hysteresis.

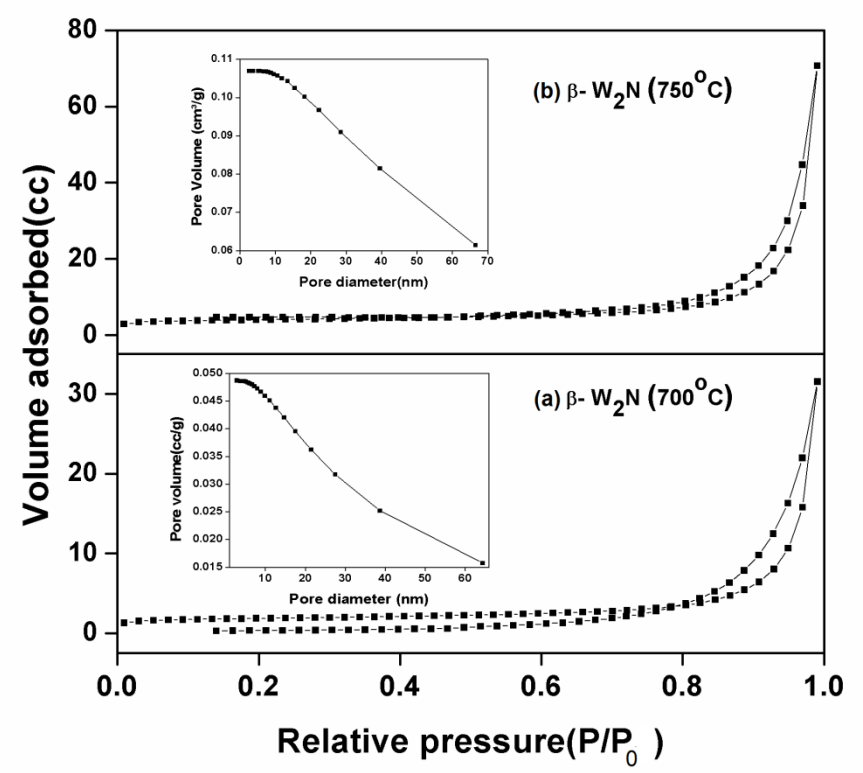

Figure 6.6 BET adsorption- desorption isotherms of β-W_2N synthesized at (a) 700°C and (b) 750°C. Inset shows corresponding pore size distribution plots.

The estimated surface areas are found to be 6m^2/g and 13 m^2/g for β-W_2N materials synthesized at 700°C and 750°C, respectively. The estimated pore volumes are 0.048 cc/g and 0.109 cc/g for β-W_2N synthesized at 700°C and 750°C, respectively. Pore size analysis calculated from BJH desorption plots estimates the values of average pore sizes as 260 Å and 335 Å for β-W_2N materials synthesized at 700°C and 750°C, respectively (figure 6.6 (a) and (b)). This result indicates that high surface area and porous β-W_2N material can be synthesized using the current methodology adopted by us.

Table 6.3 Materials, Nitridation temperature, BET surface area, pore volume and average pore sizes of β-W_2N materials.

Material	Nitridation Temperature(^{o}C)	BET surface area(m^2/g)	Pore volume (cc/g)	Average Pore size(Å)
β-W_2N	700	6	0.048	260
β-W_2N	750	13	0.109	335

6.3.1.4 Magnetic studies of β-W_2N

The room temperature field dependent magnetization plot of β-W_2N material synthesized at 750°C has been presented in figure 6.7. The hysteresis plots show gradual increasing trend of specific magnetization with the increase in applied magnetic field and do not get saturated up to 15 kOe, also. The values of saturation magnetization and coercivity are estimated to be 0.031 emu/g and 759 Oe for β-W_2N nitride. This result indicates the origin of ferromagnetism in addition to the expected paramagnetism. This conclusion can be drawn from the fact that the magnitude of saturation magnetization is in the order of 10^{-2} emu/g which is well above the values originating from Pauli paramagnetism. In addition, the observation of finite coercivities, i.e. 759 Oe, confirms our argument. Such kind of behaviour has already been explained in γ-Mo_2N system (see chapter 5, subsection 5.3.1.4).

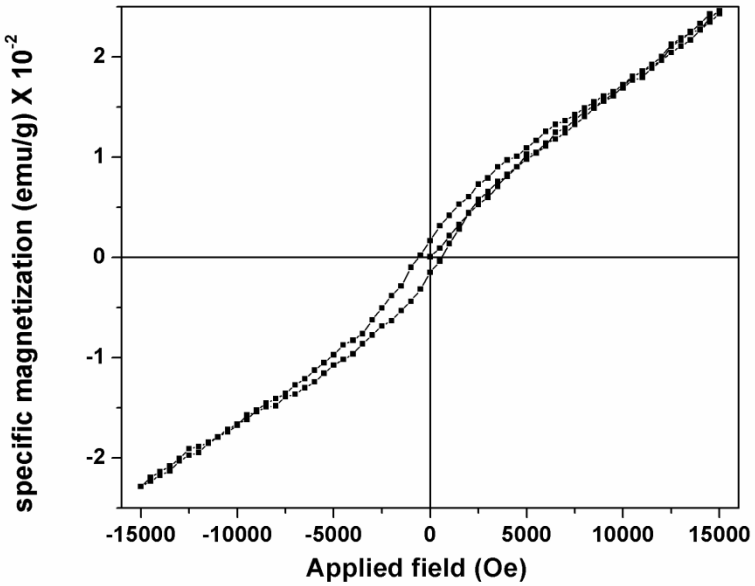

Figure 6.7 Field dependent magnetization plot of crystalline β-W_2N material synthesized at 750°C (run 1).

6.3.2 $CoWN_2$ synthesized via nitridation of $CoWO_4$ using NH_3(g)

The synthesized ternary nitride $CoWN_2$ was characterized using XRD for structural analysis and phase purity. SEM and EDX analysis were carried out for size and shape morphology and elemental composition, respectively. Magnetic properties have been investigated in detail. The results are presented and interpreted in the subsections below.

6.3.2.1 X- ray diffraction analysis of $CoWN_2$

The precursor material has been characterized using XRD study, synthesized at different temperatures. Solid state reactivity of $CoWN_2$ formation has been investigated at various temperatures and reaction parameters. The X-ray diffraction pattern has been analyzed for determination of structural parameters like lattice constant, interplanar distance and structural phase of $CoWN_2$ material.

6.3.2.1.1 Precursor characterization

Figure 6.8 (a) and (b) represent the XRD patterns of as dried and heat treated precursors at 90°C and 400°C in air atmosphere, respectively. Figure 6.8(a) indicates some crystalline peaks which indicate development of some crystallinity in the as dried precursor at 90°C.

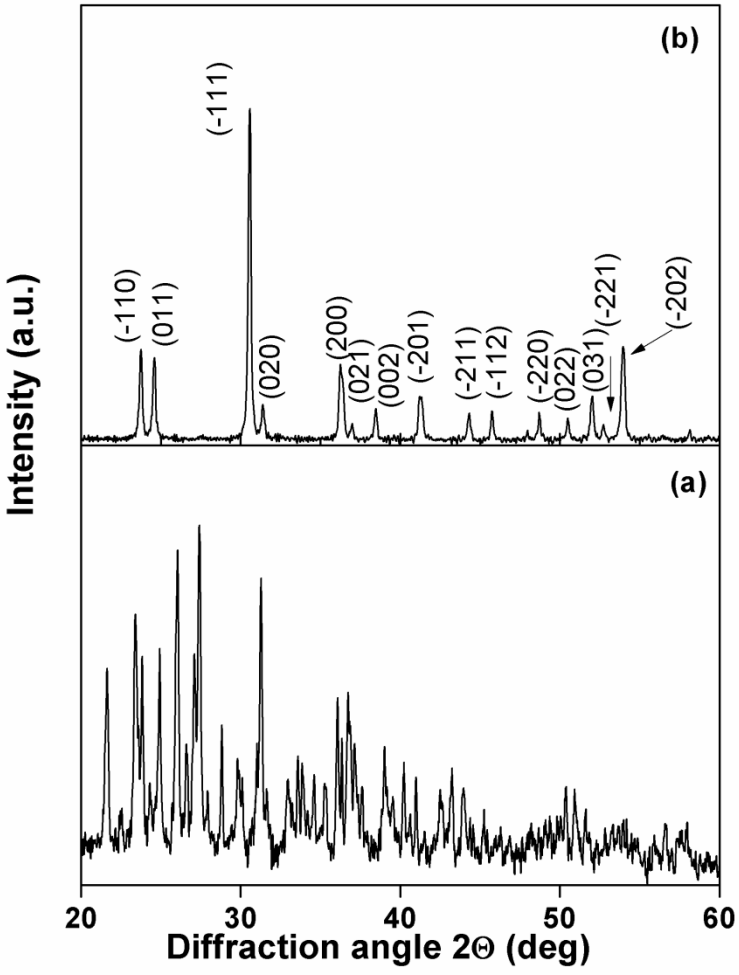

Figure 6.8 XRD pattern of precursor material heat treated at various temperatures (a) as dried at 90°C and (b) 400°C in air atmosphere.

However, the patterns could not be indexed as per the available JCPDS cards. The XRD pattern of as dried precursor heated at 400°C in air atmosphere matches well with monoclinic $CoWO_4$ phase with space group P2/c (figure 6.8(b))(ICDD PDF# 15-0867) [29, 30].The XRD parameters extracted from the pattern of $CoWO_4$ precursor materials are presented in table 6.4. The lattice parameters of $CoWO_4$ are estimated to be a = 4.954(5) Å, b = 5.690(4) Å and c = 4.680(4) Å which are comparable with the literature reported values of a = 4.947 Å, b = 5.682 Å and c = 4.669 Å [31]**.** The average crystallite size of the material was found to be 38 nm calculated from (-111) peak of the XRD pattern. The highly intense peaks in the XRD pattern of the material signify well-crystalline nature of the material.

Table 6.4 Material, Miller indices (hkl), observed interplanar distances (d), lattice parameters and average crystallite size of $CoWO_4$.

Material	(hkl)	Interplanar distance 'd'(Å)	Lattice parameter(Å)	Average crystallite size(nm)
$CoWO_4$	(-110)	3.745	a= 4.954(5) b=5.690(4) c= 4.680(4)	38±0.4
	(011)	3.619		
	(-111)	2.922		
	(020)	2.847		
	(200)	2.477		
	(021)	2.428		
	(002)	2.338		
	(-201)	2.188		
	(-211)	2.042		
	(-112)	1.982		
	(-220)	1.868		
	(022)	1.808		
	(031)	1.756		
	(-221)	1.736		
	(-202)	1.698		

6.3.2.1.2 Solid state reactivity and XRD study

The formation of β-W_2N using commercial WO_3 and NH_3(g) has been investigated. Figure 6.9 shows the XRD pattern of β-W_2N synthesized at 700°C via ammonia route from commercial WO_3 precursor (Alfa Aesar, 99.8%). After ascertaining pure β-W_2N phase formation of at 700°C via ammonia route, the synthesis of ternary $CoWN_2$ nitride has been tried, with incorporation of Co in the W_2N lattice.

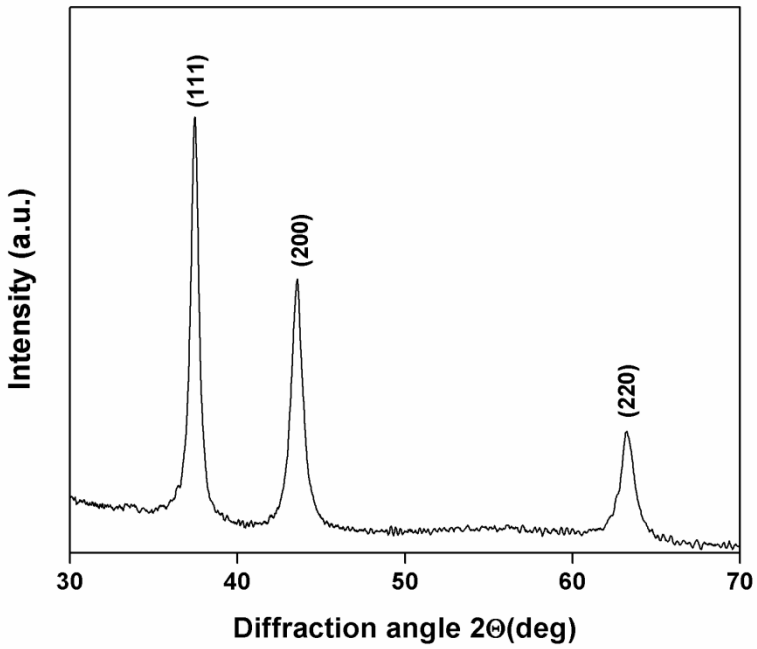

Figure 6.9 Indexed XRD pattern of β-W_2N synthesized at 700°C via ammonia route from commercial WO_3 precursor.

Figure 6.10(a), (b) and (c) represent the solid state reactivity of formation of $CoWN_2$ material at various nitridation temperatures; such as: (a) 650°C, (b) 700°C and (c) 750°C. Figure 6.10 shows the formation of $CoWN_2$ phase with increase of nitridation temperature from 650°C to 700°C **(**figure 6.10(b)**)**. With further increase of reaction temperature to 750°C, $CoWN_2$ phase becomes more crystalline with intense XRD peaks (figure 6.10(c)). Higher reaction temperature beyond 750°C was avoided in order to prevent grain growth and decomposition of the nitride products.

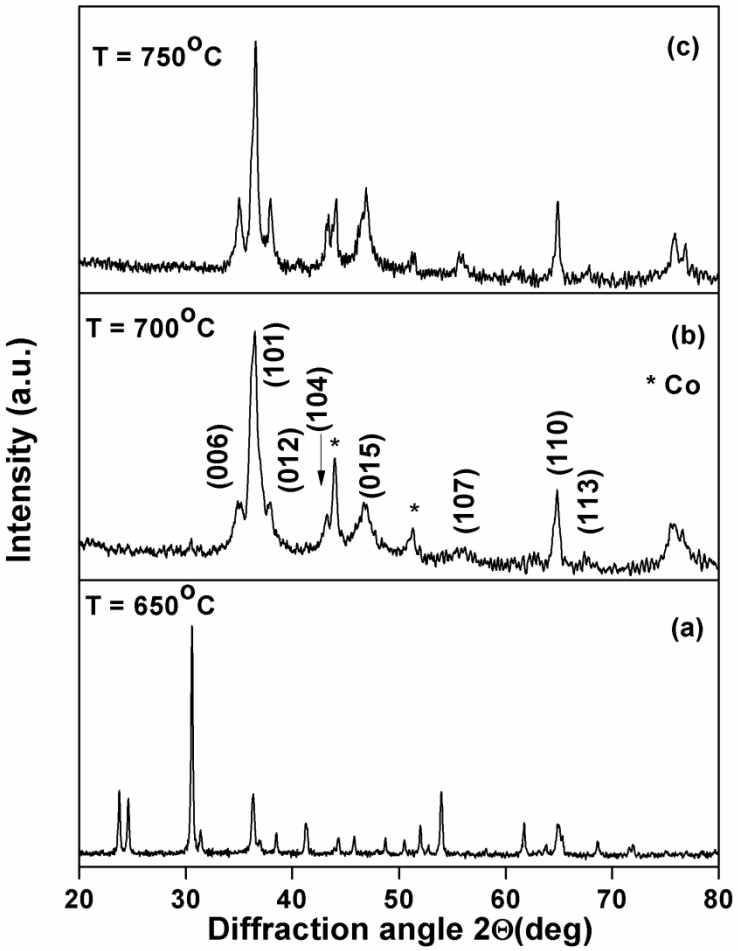

Figure 6.10 Indexed XRD pattern of nitridation products heat treated at various temperatures (a) 650°C (b) 700°C and (c) 750°C. * indicates Co as impurity phase.

Figure 6.10 (a),(b) represents the X-ray diffraction patterns of $CoWN_2$ products synthesized at (a) 700°C and (b) 750°C via ammonia route from chemically synthesized $CoWO_4$ precursor. The products are indexed as per the literature [32]. $CoWN_2$ materials crystallize in hexagonal structure. The lattice parameters of the materials are estimated to be a=2.876(7), b = 2.876(6) Å, c=15.372(48) Å and a=2.872(3) Å, b=2.872(2) Å, c=15.381(21) Å for $CoWN_2$ products synthesized at 700°C and 750°C**,** respectively. These values of calculated lattice parameters are quite comparable to the literature reported values [32].The average crystallite sizes are estimated to be 11 nm and 16±0.2 nm for $CoWN_2$ products synthesized at 700°C and 750°C**,** respectively. The estimated XRD parameters are summarized in table 6.5.

Table 6.5 Materials, Nitridation temperature, Miller indices, observed and calculated interplanar distances, lattice parameters and average crystallite size of $CoWN_2$ materials synthesized at various temperatures.

Material	Nitridation temperature (℃)	(hkl)	d_{obs} (Å)	d_{cal} (Å)	Lattice parameters (Å)	Average crystallite size(nm)
$CoWN_2$	700	(006)	2.567	2.562	a=2.876(7) b=2.876(6) c=15.372(48)	11
		(101)	2.458	2.458		
		(012)	2.368	2.369		
		(104)	2.088	2.090		
		(015)	1.943	1.935		
		(107)	1.635	1.647		
		(110)	1.436	1.438		
		(113)	1.388	1.384		
$CoWN_2$	750	(006)	2.559	2.563	a=2.872(3) b=2.872(2) c=15.381(21)	16±0.2
		(101)	2.454	2.455		
		(012)	2.368	2.366		
		(104)	2.091	2.088		
		(015)	1.934	1.934		
		(107)	1.650	1.646		
		(110)	1.435	1.436		
		(113)	1.379	1.382		

6.3.2.2 Microstructural (SEM and EDX) characterization of $CoWN_2$

6.3.2.2.1 SEM studies of $CoWN_2$

Figure 6.11((a), (b) and (c) and (d)) represent the SEM micrographs of ternary $CoWN_2$ materials synthesized at 700°C and 750°C with low and high resolutions, respectively. The particles show nearly spherical morphology with average SEM particle sizes of 97±5 nm and 67±4 nm for the products obtained at 700°C and 750°C, respectively.

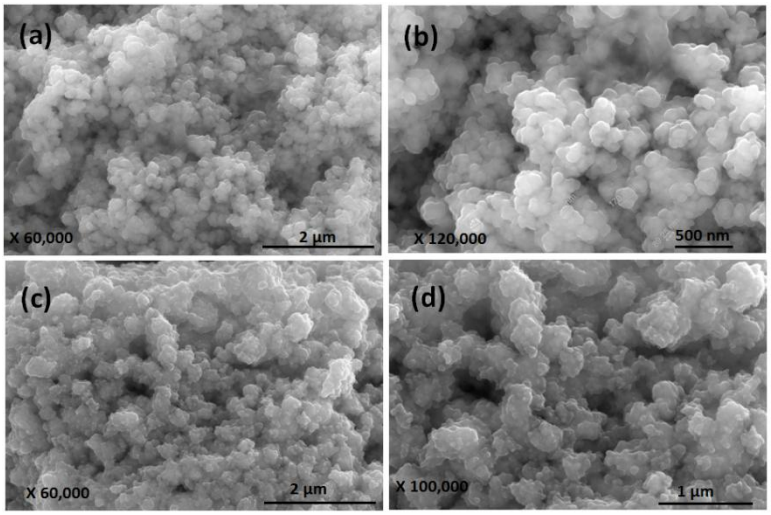

Figure 6.11 SEM micrographs of $CoWN_2$synthesized at 700°C (a), (b) and 750°C (c), (d) with various magnifications.

6.3.2.2.2 EDX studies

Figure 6.12 (a), (b) represents the EDX spectra of synthesized product $CoWN_2$ at temperature 700°C and 750°C, respectively. The weight % and atomic % of the elements present in the nitride products have been shown in the corresponding EDX spectrum.

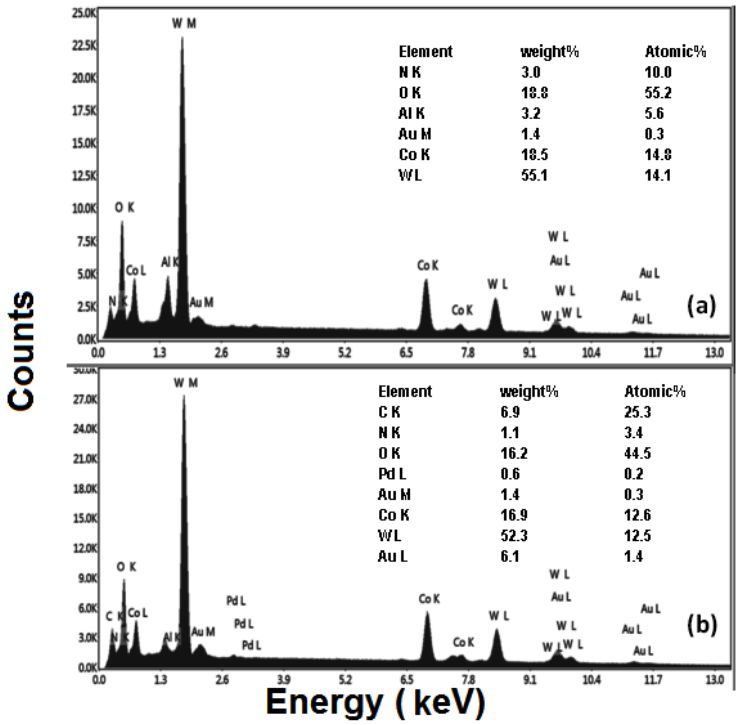

Figure 6.12 EDX spectra of $CoWN_2$ synthesized at (a) 700°C and (b) 750°C.

6.3.2.3 Magnetic studies of $CoWN_2$

The room temperature field dependent magnetization plot of β-W_2N materials synthesized at 750°C has been presented in figure 6.13. The values of M_s and H_c are estimated to be 1.71emu/g and 375Oe, respectively. The hysteresis plot shows ferromagnetic behaviour with faster increase in magnetization up to 3000 Oe, in the lower field region with finite coercivity. The M vs. H plot does not get saturated even at the applied field strength of 15 kOe. This result indicates the origin of weak ferromagnetism in $CoWN_2$. Insertion of Co atoms having intrinsic magnetic moments might be a reason for enhanced values of saturation magnetization, i.e. M_s = 1.71 emu/g, in $CoWN_2$ nitride. However, ferromagnetic couplings are considered to be weak which may be understood as lack of effective distance required for coupling of Co^{2+} ions in the lattice structure. Observation of finite coercivity, i.e. 375 Oe, in the magnetic study for $CoWN_2$ confirms our interpretation. Such kind of magnetic behaviour has already been explained by us in the literature on Mo_2N system [33].

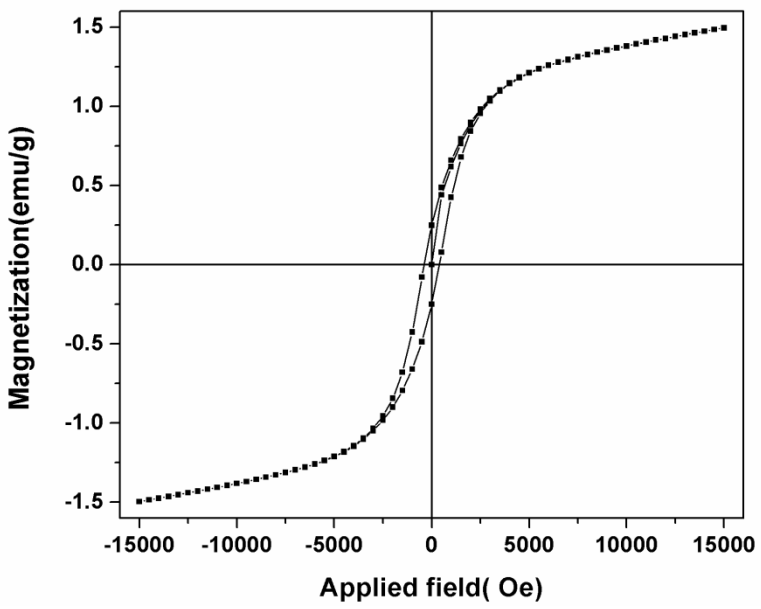

Figure 6.13 Field dependent magnetization plot of $CoWN_2$ measured at room temperature.

6.4 Conclusion

Binary β-W_2N and ternary $CoWN_2$ materials have been synthesized using novel chemical methods. Citric acid assisted sol-gel method has been adopted for synthesis of oxide precursors. Solid urea and NH_3 (g) have been used as nitrogen sources for the nitridation reactions. X-ray diffraction patterns show phase pure nanocrystalline nature of the materials. The lattice parameter and crystallite size for β-W_2N were estimated to be 4.155(4) Å and 3±0.2 nm, respectively. The lattice parameters are found to be a=2.876(7) Å, b=2.876(6) Å, c=15.372(48) Å and a=2.872(3) Å, b=2.872(2) Å, c=15.381(21) Å for $CoWN_2$ materials synthesized at 700°C and 750°C, respectively. The crystallite sizes were found to be 11nm and 16±0.2 nm for $CoWN_2$ materials obtained at 700°C and 750°C, respectively. BET surface area of β-W_2N materials were estimated to be 6m^2/g and 13 m^2/g synthesized at 700°C and 750°C, respectively. The values of the saturation magnetization, M_s and coercivity, H_c are estimated to be 0.031emu/g ,759 Oe and 1.71 emu/g, 375Oe, for β-W_2N and $CoWN_2$ materials, respectively.

References

1. Y. Ma, Q. Cui, L. Shen, Z. He, J. Appl. Phys. **102**(2007)013525.

2. V. Chakrapani, J. Thangala, M. K. Sunkara, Int. J. Hydrogen Energy. **34** (2009) 9050-9059.

3. T. Polcar, N. M. G. Parreira, A. Cavaleiro, Wear. **265** (2008)319-326.

4. B. H. Lee, K. Yong, J. Vac. Sci. Technol. B. **22**(2004)2375-2379.

5. J. S. Becker, R. G. Gordon, Appl. Phys. Lett. **82** (2003) 2239-2241.

6. C. Shi, X. F. Yang, A. M. Zhu, C. T. Au, Catal. Today. **93–95** (2004) 819–826.

7. Z. W. Yao, H. T. Dong, Appl. Surf. Sci. **255**(2008)2259-2264.

8. H. Tominaga, M. Nagai, Electrochim. Acta. **54** (2009)6732-6739.

9. L. Villaseca, B. Moreno, I. Lorite, J. R.Jurado, E. Chinarro, Ceram. Int. **41**(2015)4282–428.

10. C. Giordano, C. Erpen, W. Yao, M. Antonietti, Nano Lett. **8** (2008)4659-4663.

11. R. N. Panda, S. B. Dalavi, J. Theerthagiri, Adsorpt. Sci. Technol. **30** (2012) 345-354.

12. S. Wang, X. Yu, Z. Lin, R. Zhang, D. He, J. Qin, J. Zhu, J. Han, L. Wang, H.-K. Mao, J. Zhang, Y. Zhao, Chem. Mater. **24** (2012) 3023−3028.

13. S. H. Mohamed, Surf. Coat. Technol. **202** (2008) 2169-2175.

14. Y. Ma, Q. Cui, L. Shen, Z. He, J. Appl. Phys. **102** (2007)013525.

15. S. Yin, L. Yang, L. Luo, F. Huang, Y. Qiang, H. Zhang, Z. Yan , NewJ.Chem. **37** (2013) 3976-3980.

16. J. H. Ryu, J. Yoon, C. S. Lim, W. Oh, K. B. Shim, Ceram. Int. **31**(2005) 883 -888.

17. R. Zhang, X. Zhou, S. Xiao, Z. Zhou, Inorg. Chim. Acta. **391** (2012) 224-228.

18. K. Kalantar-Zadeh, A. Z. Sadek, H. D. Zheng, V. Bansal, S. K. Bhargava, W. Wlodarski, J. M. Zhu, L. S. Yu, Z. Hu, Sens. Actuators B. **142** (2009)230–235.

19. M. Gillet, K. Aguir, C. Lemire, E. Gillet, K. Schierbaum, Thin Solid Films. **467 (**2004) 239–246.

20. M. Karimi-Nazarabad, E. K. Goharshadi, M. H. Entezari, P. Nancarrow, Microfluid Nanofluid. **19** (2015) 1191–1202.

21. H. Zheng, Y. Tachibana, K. Kalantar-zadeh, Langmuir. **26** (2010)19148–19152.

22. D. Chen, H. Wen, T. Li, L. Yin, B. Fan, H. Wang, R. Zhang, X. Li, H. Xu, H. Lu, D. Yang, J. Sun , L. Gao, J. Solid State Chem. **184** (2011) 455–462.

23. Joint Committee for Powder Diffraction Standards, Powder Diffraction.File No. 25-1257 (JCPDS International Center for Diffraction Data, 1982).

24. C. W. Lee, Y. T. Kim, Appl. Phys. Lett. **65** (1994) 965-967.

25. M. H. Tsai, S. C. Sun, H. T. Chiu, S. H. Chuang, Appl. Phys. Lett. **68**(1996) 1412-1414.

26. H. Park, S. Kim, M. Kim, D. Kim, K. Park, Ceram. Int. **42**(2016)1933–1942.

27. M. Kalyva, S. Kumar, R. Brescia, S. Petroni, C. L. Tegola, G. Bertoni, M. D. Vittorio, R. Cingolani, A. Athanassiou, Nanotechnology **24** (2013) 035707(1-9).

28. A. Tambre, J. Henocque, M. Clin, International Journal of Spectroscopy. 2011, Article ID 186471,1-6.

29. S. Sagadevan, J. Podder, I. Das, J Mater Sci: Mater Electron. **27** (2016) 9885-9890.

30. J. Deng, L. Chang, P. Wang, E. Zhang, J. Ma, T. Wang, Cryst. Res. Technol. **47** (2012) 1004–1007.

31. B. Sun, H. Li, L. Wei, P. Chen, CrystEngComm. **16** (2014) 9891–9895.

32. P. S. Herle, N.Y. Vasanthacharya, M.S. Hegde, J. Gopalakrishnan, J. Alloys Compd. **217** (1995) 22-24.

33. P. P. Mishra, M. Manivel Raja, R. N. Panda, Mater. Res. Bull. **75** (2016) 127–133.

Chapter 7

Summary and Future Scope

7.1 Summary

Transition metal nitrides are important class of materials because of their unique physical and chemical properties. However, there is intrinsic difficulty in synthesis of the nitride products in nano form due to making and breaking of strong bonds associated with N≡ N. Further, many nitrides are moisture and air sensitive. Therefore, those are synthesized in bulk form in micron size or as protected/coated thin films. Based on the above mentioned facts, development of alternative, cost effective, novel chemical synthetic routes, useful in fine tuning the important properties of nano crystalline transition metal nitrides, merits further investigation. The present study involves development of novel synthetic routes for various transition metal nitrides, binary, substituted binary and ternary nitrides such as: ε-$Co_xFe_{3-x}N$, γ′-$Ni_xFe_{4-x}N$, VN, γ-Mo_2N, γ-$Co_xMo_{2-x}N$, β-W_2N, $CoWN_2$ and investigations on their magnetic and surface properties study.

Chapter 1 provides the general introduction to the thesis work. This chapter reviews the potential technological applications and crystal structure of the transition metal nitrides, which are of importance to the present study. A brief discussion on the available synthetic methods and their merits and demerits has been presented. This chapter also describes a brief overview of various characterization techniques; such as: elemental analysis, powder X-ray diffraction and electron microscopy, etc. The general terminology and definitions of physisorption isotherms and its classification for sorption behaviour analysis is also presented in this chapter. For the proper understanding of magnetic behaviour of particles in bulk and nano form, a discussion on various forms of magnetism has been presented. The effects of fine particle magnetism such as size and surface effects on various magnetic properties (M_s, H_c, K and T_c) have been specifically emphasized. The magnetic phenomena like superparamagnetism and spin canting at nanoscale have been described in this chapter. The literatures available on transition metal nitrides with reference to the materials included in the present thesis have been reviewed. Finally, well defined objectives based on the existing gaps in the field of research have been presented in chapter 1.

Chapter 2 describes details of various synthesis methods, sample processing and characterization techniques involved in this thesis work. Available synthetic routes for the nitride systems have been reviewed with additional focus on their merits and demerits. The importance of modern methods over traditional methods has been highlighted. Next, the newer/modified synthetic routes adopted in the present thesis have been justified. Composition or elemental analysis techniques such as atomic absorption spectroscopy (AAS) and energy dispersive X-ray (EDX) techniques have been elaborated. The instrumental techniques such as XRD, SEM, TEM and HRTEM have been discussed for solid state reactivity study and structural characterizations. The instrumental technique, basic principle and data interpretation for BET method has been described. The details of VSM technique has been described for magnetic measurements and analysis in chapter 2.

Chapter 3 includes details of the novel chemical synthesis of ε-$Co_xFe_{3-x}N$ ($0 \leq x \leq 0.4$) and γ′-$Ni_xFe_{4-x}N$ ($0 \leq x \leq 0.8$) nitride systems. Citric acid assisted sol-gel method for the synthesis of precursor followed by nitridation using ammonia gas has been adopted for the synthesis of nitride materials. X-ray diffraction analysis of precursor characterization, solid state reactivity study towards nitride formation and the nitride product phase analysis have been presented for both Co and Ni substituted iron nitride systems. Also, magnetic properties are investigated in detail and correlated to structural parameters as described below:

(i) **ε-$Co_xFe_{3-x}N$**: XRD pattern confirms evolution of hexagonal phase for ε-$Co_xFe_{3-x}N$ ($0 \leq x \leq 0.4$) system of materials. Precipitation of α-Fe is observed in the XRD pattern for ε-$Co_xFe_{3-x}N$ ($0 \leq x \leq 0.4$) system with gradual increase in Co substitution, beyond cobalt content, x = 0.2. The values of the lattice parameters (a and c) for ε-$Co_xFe_{3-x}N$ ($0 \leq x \leq 0.4$) materials are found to be in the range of 4.772(8) - 4.783(9) Å and 4.413(7) - 4.423(2) Å for ‘a’ and ‘c’, respectively. The observed values for lattice parameters are greater than the reported values for ε-Fe_3N. This result may be attributed to higher nitrogen concentration in our synthesized products exceeding stoichiometric ratio of 3:1 and can be assigned as ε-$Co_xFe_{3-x}N_{1.37}$ on the basis of observed lattice expansion. The average crystallite sizes of the nitride products are in the range of 44±0.7 - 55±0.8 nm. However, SEM study provides

particle sizes in the range of 110±10 -155±15 nm with spherical morphology indicating possible agglomeration of crystallites due to their magnetic nature. Maximum M_s value of 39 emu/g was achieved for cobalt content, x = 0.4, in ε-$Co_xFe_{3-x}N$ ($0 \leq x \leq 0.4$) series of materials. The synthesized nitride products show superparamagnetic behaviour at room temperature. The magnetization values follow an increasing trend with the gradual increase of Co content (x) in ε-$Co_xFe_{3-x}N$ system except a slight initial decrease for x = 0.2 at wt%. This observation can be correlated with the formation of giant magnetic phase of Fe atoms due to structural alteration induced by Co atoms substitution in the crystal lattice.

(ii) **γ′-$Ni_xFe_{4-x}N$**: γ′-$Ni_xFe_{4-x}N$ ($0.2 \leq x \leq 0.8$) materials crystallize in cubic phase with lattice parameter values in the range of 3.792(2) Å- 3.795(7) Å. The values of lattice parameters increase slightly up to x=0.6 and then decrease for x=0.8. An increasing trend in the values of lattice parameter, i.e. a=3.792(4) for x = 0.2 to a=3.795(7) for x = 0.6, is observed for γ′-$Ni_xFe_{4-x}N$ ($0.2 \leq x \leq 0.8$) materials, which is explained on the basis of nanosize and surface effects along with strain effect. The average crystallite sizes are in the range of 31±0.5 nm – 45±0.7 nm for γ′-$Ni_xFe_{4-x}N$ ($0.2 \leq x \leq 0.8$) nitrides. Electron microscopy studies of the synthesized nitride products indicate presence of magnetic clusters in the size range of 155±9 - 250±14 nm consisting of several crystallites. Magnetic studies reveal superparamagnetic nature of the synthesized products having coercivity in the range of 76-109 Oe. A maximum value of M_s , i.e. 181 emu/g, was achieved for Ni content, x = 0.6, in γ′-$Ni_xFe_{4-x}N$ ($0.2 \leq x \leq 0.8$) materials system. The unusual increasing trend in M_s for γ′-$Ni_xFe_{4-x}N$ materials has been explained on the basis of size and surface effects in addition to lattice strain effects. Existence of finite values of coercivities indicates either deformed structures or presence of bigger crystallites well beyond the superparamagnetic size limit. In this study, achievement of high saturation magnetization with low coercivity and reduced particle size is particularly useful for soft magnetic applications.

Chapter 4 deals with development of novel chemical methods for the synthesis, characterization and surface properties study of vanadium nitride materials. Synthesis of different precursor materials with alteration of reaction parameters, followed by nitridation

using two different nitrogen sources (viz. solid urea and ammonia gas) have been investigated. The observed properties of the materials have been correlated to the nature of the precursors and the nitridation sources employed. XRD patterns confirm phase pure nano crystalline nature with average crystallite size in the range of 7±0.2 – 28±0.3 nm of the nitride products obtained via different precursors and nitridation routes. The synthesized VN products crystallize in cubic phase having lattice parameters in the range of 4.112(5) Å – 4.126(6) Å. These observed values of lattice parameter are less than that corresponding to the stoichiometric value, i.e. 4.139 Å. The observed lattice contraction can be explained on the basis of strain effects, fine particle size and surface distortions in addition to deviation of N content from the ideal stoichiometry in our synthesized product. Electron microscopy studies confirm elongated rod like morphology of the VN materials synthesized via urea route from both the precursors of V_2O_5 obtained at 350^{o}C and 550^{o}C. On the contrary, VN products obtained via ammonia route are of nearly spherical morphology. A maximum surface area of 57 m^2/g was estimated using BET method for the VN obtained via urea route from the V_2O_5 precursor synthesized at 350^{o}C. The values of specific surface area for other VN products are moderate to high (i.e. in the range of 11-39 m^2/g). The average pore diameters of the VN materials are in the range of 4-189 nm. The sorption isotherms of VN products are of type IV nature with H2 hysteresis signifying mesoporousity of the materials. The observed properties of the synthesized VN products are variable, depending upon nature of the precursor and the reaction parameters. It is observed that nitridation using urea route facilitates smaller particle formation with elongated rod like morphology when compared with materials synthesized via ammonia route.

Chapter 5 focuses on synthesis of Mo and Co-Mo based precursors through various synthetic routes and their transformation into nitrides using different nitrogen sources. This study involves use of hydrazine ($NH_2NH_2{\cdot}H_2O$) and potassium borohydride (KBH_4) as reducing agents and ethylenediamine ($NH_2CH_2CH_2NH_2$) as organic source for the synthesis of different precursors. Ammonia gas and solid urea have been used for the nitridation experiment as nitrogen sources. The effect of various precursor routes and nitridation sources on the physical properties such as surface and magnetic properties of nitrides have been studied in detail. The nitride products crystallize in fcc structure with lattice parameter values of 4.193(5) Å, 4.198(2) Å and 4.162(17) Å for γ-Mo_2N and γ-$Co_{0.25}Mo_{1.75}N$

synthesized via ammonia route and γ-Mo_2N synthesized via urea route, respectively. Lattice expansion is observed for γ-Mo_2N nitride synthesized via ammonia route. Insertion of Co into host lattice of γ-Mo_2N alters the crystal structure. The average crystallite sizes of γ-Mo_2N and γ-$Co_{0.25}Mo_{1.75}N$ synthesized via ammonia route and γ-Mo_2N synthesized via urea route are estimated to be 6±0.8 nm, 11±0.5 nm and 5±0.4, respectively. TEM and HRTEM studies confirm nanocrystalline nature of the materials. The surface properties study for γ-Mo_2N and γ-$Co_{0.25}Mo_{1.75}N$ nitride materials synthesized via ammonia route indicate high and moderate surface areas i.e. 53 and 12 m^2/g, respectively. The study confirms mesoporous nature of the materials. Room temperature VSM study indicates weak ferromagnetic behaviour of γ-Mo_2N and γ-$Co_{0.25}Mo_{1.75}N$ (ammonia route) and γ-Mo_2N (urea route) materials having coercivity values of 2838 Oe, 880 Oe and 296 Oe, respectively.

Chapter 6 describes novel synthesis of binary β- W_2N and ternary $CoWN_2$ materials using citric acid assisted sol-gel route for the precursors. Solid urea and NH_3(g) gas are used as vectors for nitridation of the precursors, separately. Pure phase nanocrystalline nitride products have been prepared with crystallite sizes 3±0.2 nm for β- W_2N and in the range of 11- 16 nm for $CoWN_2$ materials prepared at two different temperatures, i.e. 700°C and 750°C, respectively. It is observed that the nitridation temperature plays an important role in variation of structural parameters and properties of the resulting products. β- W_2N material crystallizes in fcc structure with lattice parameter, 4.155(4) Å. The synthesized $CoWN_2$ materials crystallize in hexagonal structure. The lattice parameter values are estimated to be a=2.876(7) Å, b=2.876(6) Å, c=15.372(48) Å and a=2.872(3) Å, b=2.872(2) Å, c=15.381(21) Å for the products obtained at 700°C and 750°C, respectively. Electron microscopy studies indicate spherical morphology of the particles. The average SEM particle size for β-W_2N materials is estimated to be 234±17 nm and 97±5 nm and 67±4 nm for $CoWN_2$ materials synthesized at700°C and 750°C, respectively. The specific surface areas of β-W_2N materials obtained via urea route are estimated to be 6 m^2/g and 13 m^2/g, synthesized at 700°C and 750°C, respectively. The values of the saturation magnetization, M_s and coercivity, H_c, are estimated to be 0.031emu/g and 759 Oe, respectively for crystalline β-W_2N synthesized at 750°C. The values of M_s and H_c of $CoWN_2$ synthesized at 750°C are estimated to be 1.71emu/g and 375Oe, respectively.

In summary, the present doctoral thesis describes various novel chemical synthesis routes for the preparation of nanocrystalline transition metal nitrides. Structural, microstructural, surface and magnetic properties of the synthesized nitride products have been investigated in detail. Substitution of transition metals into the binary nitride system has been attempted successfully and its effect on various physical properties has been studied. Use of various nitridation routes and varieties of precursors for the synthesis of nitride product has been explored in this study. Magnetic material systems such as ε-Fe_3N and γ′-Fe_4N have been synthesized and the effect of transition metal substitution into the lattice has been studied in detail. Highly magnetic Ni substituted γ′-Fe_4N material having magnetization 181 emu/g has been achieved. High surface materials such as: VN, γ-Mo_2N, β-W_2N and $CoWN_2$ which are of potential technological importance have been synthesized and studied in detail in the present thesis. We are successful in synthesizing high surface area VN and γ-Mo_2N materials having surface area values of 57 m^2/g and 53 m^2/g, respectively.

7.2 Future Prospects

Transition metal nitrides have received increasing attention, as an important class of functional materials. These materials are mainly important having unique physical and chemical properties, which can be useful for varied applications: as high temperature ceramics, magnetic materials, superconductors, optoelectronic devices or catalysts and so on. Despite the very interesting and unique properties of transition metal nitrides, there are several issues still need to be investigated. Development of novel synthetic methods for the binary and ternary nitrides has become significant as the properties of the nitrides are dependent on the synthetic route employed and the nature of the precursor. For example, for catalytic applications the nitride powders with high specific surface area need to be synthesized at moderate temperature condition. However, a facile route to metal nitrides in large scale is still a challenge and should be developed in order to meet the increasing demands of nitrides from variety fields of potential application. Ternary nitrides have not been studied much in the literature because of their challenges in synthesis, which involve low decomposition temperatures. Therefore, research on nitrides has become more intensive focusing mainly on new ternary and higher order transition metal nitrides. In future, research

on innovative low temperature synthetic routes, solid state reactivity of phase formation and kinetics may provide more information into nitride chemistry. The optimization of reaction parameters for different size and shape of the material is of significance in fine tuning various structure dependent properties of nitride materials in nanoscale. Research on structure dependent properties of nanocrystalline nitrides is an interesting future scope. The production of hybrid or composite nitrides is considered as a next important step in the field of these nanosystems. Further, more detailed structural characterization using advanced characterization techniques is crucial for understanding the relationship among structural, electronic and catalytic property of the nitride materials.

Although many nitrides in the iron nitride family are well studied, some of the metastable pure phases are still not produced in bulk form due to fundamental difficulties. The large magnetization or the giant magnetic moment of α″- $Fe_{16}N_2$ is incompatible with band theory. Because of the controversy upon the widely different observations of magnetic properties in terms of thin films and bulk form, it seems desirable to measure the magnetic properties of pure bulk α″- $Fe_{16}N_2$. Doping of other elements like Ga, Cr, Mn, Ni and Cu in the ferromagnetic Fe-N lattice breaks the long range ordering and introduces localized nonmagnetic or antiferomagnetic interactions. These mixed magnetic phases give rise to short range ordering like spin glass with alteration in magnetic and exchange anisotropy. Extensive research on magnetic property of binary and substituted binary nitrides may lead to development of candidates for high density magnetic recording, biomedical and catalytic applications.

V, Mo and W based materials are well known to have high surface area useful for catalytic applications. Development of porous structures with high surface area is an important topic of research interest useful for commercial and industrial applications. Also, due to high surface area of nano materials, they can be used in biomedical field for drug delivery. The future research scope for development of newer/ novel synthetic strategies of these nitride materials may be worthy scientific contribution. Exploring the effects of variable particle size, surface treatment and composition is an interesting future scope for further research on these materials. Nitride materials are excellent electrode materials and energy storage devices used in Li ion batteries and super capacitors. Their performance is

restricted due to low stability. Further research can be done in this field to overcome the problem of instability using coating, hybrid and composite nitride materials. Fabrication of electrode materials with high energy density has become a vital challenge. TiN and VN have been proved to be favourable candidates in this regard. However further research on electrochemical properties of metal nitrides is an important future prospect for super capacitor applications.

List of publications

1. **Pragnya P. Mishra**, J. Theerthagiri and Rabi N. Panda "Mesoporous Vanadium Nitride Synthesized by Chemical Routes" *Adsorption Science & Technology* **32** (2014) 465-474.
2. **Pragnya P. Mishra** and Rabi N. Panda "Development of novel chemical synthetic routes for nanocrystalline VN, Mo_2N and W_2N nitride materials" *AIP Conference Proceedings* **1665** (2015) 050030 (1–3).
3. **Pragnya P. Mishra**, M. Manivel Raja and Rabi N. Panda "Novel Synthesis and Nanostructure Controlled Magnetic Characteristics of ε-Fe_3N and γ'-$Ni_xFe_{4-x}N$ ($0.2 \leq x \leq 0.8$) Nitrides" *Journal of Superconductivity and Novel Magnetism* **29** (2016) 1347 -1356.
4. **Pragnya P. Mishra,** M. Manivel Raja and Rabi N. Panda "Enhancement of magnetic moment in Co substituted Nanocrystalline ε -$Co_xFe_{3-x}N$ ($0.2 \leq x \leq 0.4$) synthesized by modified citrate precursor route" *Materials Research Bulletin* **75** (2016) 127–133.
5. **Pragnya P. Mishra** and Rabi N. Panda "Novel synthesis, characterization and magnetic properties of nano-structured γ-Mo_2N and γ-$Co_{0.25}Mo_{1.75}N$ nitrides" *Materials Research Bulletin* **86**(2017) 241-247.

List of publications other than thesis work

1. Rabi N. Panda, Shankar B. Dalavi and Pragnya P. Mishra "Tuning of Magnetic Properties of Ni, Fe-Co, Co-Ni, FeCoN and FeNiN Nano-structured Materials Developed by Novel Synthetic Strategies" to be submitted.
2. Shankar B. Dalavi, Pragnya P. Mishra, Tomy Cherian, M. Manivel Raja and Rabi N. Panda "Synthesis, Characterization, Magnetic and Mössbauer studies on Nanocrystalline $CoCr_xFe_{2-x}O_4$ ($0 \leq x \leq 1$)" to be submitted.

Conferences attended

1. Pragnya Paramita Mishra and Rabi Narayan Panda "Development Of Novel Chemical Synthetic Routes For Nanocrystalline VN, Mo_2N, And W_2N Nitride Materials" presented poster in DAE SSPS-2014 organized by BARC Mumbai held in VIT Vellore during 16th Dec-20th Dec,2014
2. Pragnya Paramita Mishra and Rabi Narayan Panda "Novel Synthesis and Characterization of Nanocrystalline VN, Mo_2N, And W_2N Nitride Materials for Catalytic Applications" presented poster in Indian science congress association -2015 held in Mumbai university during 3rd Jan – 7th Jan 2015.

Brief Biodata of the Candidate

Name Pragnya Paramita Mishra

Date of birth 10-07-1986

Education MSc (Physics)
Khallikote University, Brahmapur, Odisha (2009)
BSc (Physics)
Utkal University, Bhubaneswar, Odisha (2006)

Email mamappm@gmail.com

Research experience

- Worked as Project Assistant-II in DST project from March, 2013 to November, 2014.

Research publications

- 05 publications in international journals

Conferences attended

- 02 national conferences

Work experience

- Worked as Lecturer in Physics at Gayatri Science College, Bhubaneswar from August, 2009 to August, 2010.
- Worked as Lecturer in Electronics at KIIT Science College, Bhubaneswar from August, 2010 to May, 2011.
- Worked as Asst. Prof. in Physics at Girijabai Sail Institute of Technology, Karwar from August, 2012 to March, 2013.

Honors and Awards

Recipient of best science graduate and best lady graduate during BSc.

Brief Bio-data of Supervisor

Name Prof. Rabi Narayan Panda

Date of Birth 01/09/1970

Current position Associate Professor
Department of Chemistry
Birla Institute of Technology and Science-Pilani,
K. K. Birla Goa Campus
Zuarinagar-403726, Goa, India.

Education Ph. D. (Chemistry) IIT Kanpur, UP (1998)
M. Sc. (Chemistry) Sambalpur University, Odisha (1993)

Post doctoral experience

- 1998-1999: Senior Project Associate, Department of Physics and Center for Laser Technology, Indian Institute of Technology, Kanpur, India.
- 1999-2000: Research Associate, Surface Physics Division, Saha Institute of Nuclear Physics, Calcutta, India.
- 2000 - 2002: Post-doctoral researcher at National Science Council, Taiwan, worked in the field of Material Science at National Tsing Hua University, Taiwan.
- 2002-2003: Post-doctoral researcher at Max-Plank Institute fur Kohlenforschung, Muelheim an der Ruhr, Germany, worked in the field of Heterogeneous Catalysis.
- 2003 - 2004: Post-doctoral researcher as **Alexander Von Humboldt** Fellow, worked on nano-materials at the Institute of nanotechnology, Forschungszentrum Karlsruhe (Now KIT), Germany.
- 2004-2005: Post Doctoral researcher in DST sponsored project at Indian Institute of technology, Kanpur,India.

- 2005: Post-doctoral researcher at National Science Council, Taiwan, worked on Spintronics at Department of Physics, National Taiwan University,Taipei, Taiwan.

No. of Sponsored Research Projects

Completed projects as PI (02)

(i) 'Magnetic Properties of Metallic nano-particles' sponsored by CSIR, India.

(ii) 'Synthesis and characterization of binary and ternary transition metal nitrides' sponsored by DST, India

No. of research Publications

(i)	Publications in international journals	42 (h-index : 15, i-10-index: 22)
(ii)	No. of Conference Proceedings	21
(iii)	No. of Invited Talk and Seminars	13

Honors and Awards

(i) 1991-1993: Recipient of national scholarship during M. Sc. at Sambalpur University.

(ii) 1993: Qualified Graduate Aptitude Test in Engg. (GATE) conducted by IITS, India.

(iii) 1994: Qualified National Eligibility Test (NET) in Chemical Science conducted jointly by University Grant Commission (UGC) and Council of Scientific and Industrial Research (CSIR), INDIA.

(iv) 2000: Awarded a post doctoral fellowship from National Science Council, Taiwan.

(v) 2003: Awarded Alexander Von Humboldt Fellowship.

(vi) 2005: Awarded post doctoral fellowship from National Science Council, Taiwan.

Reviewer and Editor in international journals

Reviewer	Nano-Scale Research Letter, Materials Science and Engg. B, Materials Lett. , Journal of Magn. Magn. Mater., Dalton transactions, etc.
Guest Editor	J. Nanomaterials (2014-15), Special Issue: Advanced Nanoporous Materials: Synthesis, properties and applications.